

UNIVERSITY OF SZEGED
FACULTY OF SCIENCE AND INFORMATICS
DOCTORAL SCHOOL OF GEOSCIENCES
DEPARTMENT OF MINERALOGY, GEOCHEMISTRY, AND PETROLOGY

**HYDROGEOPHYSICAL AND HYDROGEOCHEMICAL CHARACTERIZATION OF
VOLCANIC AQUIFERS IN NORTHWEST ETHIOPIA**

PhD Thesis

MULUGETA CHANIE FENTA

SUPERVISOR
Dr. habil. János Szanyi
Assistant professor

Szeged, Hungary
2022

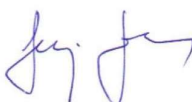
© copyright 2022 by Fenta Mulugeta Chanie.

This copy of the PhD thesis has been supplied in consultation to the author. Its copyright rests with the author, and the use of any data or pieces of information resulting from this work must be in accordance with the current copyright law. Moreover, any citations from this work must include full recognition.

Declaration of the supervisor

As the supervisor of MULUGETA CHANIE FENTA I declare that the doctoral thesis entitled HYDROGEOPHYSICAL AND HYDROGEOCHEMICAL CHARACTERISATION OF VOLCANIC AQUIFERS IN NORTHWEST ETHIOPIA is based on the independent work of the candidate. He had a significant role in achieving the research results presented in the thesis. The content of the dissertation is scientifically sound; thus, I propose to accept the thesis.

Szeged, 24 January 2022


.....
(Dr. János Szanyi, supervisor)

PREFACE

The doctoral thesis results and main findings are mainly derived from these papers, and the thesis is mainly based on 1–3 listed published papers. However, other published research papers, book chapters, conference proceedings, and abstracts have been accomplished during the PhD study period, and they are listed as 4–13.

List of publications in Scopus and web of sciences indexed journals

1. **Fenta, M.**, Anteneh, Z. , Szanyi, J., & Walker, D. (2020). Hydrogeological framework of the volcanic aquifers and groundwater quality in Dangila Town and the surrounding area, Northwest Ethiopia. *Groundwater for Sustainable Development*, 11, 1–13. <https://doi.org/10.1016/j.gsd.2020.100408>.
2. **Fenta, M.**, Anteneh, Z., Szanyi, J., & Walker, D. (2020). Hydrochemical data on groundwater quality for drinking and irrigation use around Dangila town, Northwest Ethiopia. *Data in Brief*, 31, 1–11. <https://doi.org/10.1016/j.dib.2020.105877>.
3. **Fenta, M.**, Potter, D., & Szanyi, J. (2021). Fibre Optic Methods of Prospecting: a Comprehensive and Modern Branch of Geophysics. *Surveys in Geophysics*. 42, 551–584. <https://doi.org/10.1007/s10712-021-09634-8>.
4. Anteneh,Z.,Alemu,M.,Bawoke,G.,Kehali,A.,**Fenta,M.**,&Desta,M.(2022).Appraising potential groundwater zones using geospatial and multi-criteria decision analysis(MCDA) techniques in Andasa-Tul watershed, Upper Blue Nile Basin, Ethiopia. *Environmental Earth sciences*, 81(14). <https://doi.org/10.1007/s12665-021-10083-0>.
5. Ingle, K., **Fenta, M.**, Harada, K., Ingle, A., Ueda A. (2021). Wastewater treatment plants advantage to combat climate change and help sustainable water management. In the book 'Water Resource Management and Environmental Sustainability,' Edited Book (Springer Series): Advances in Geographical and Environmental Sciences, Series Ed by R.B. Singh. Chapter -3,Pp.
6. Ingle, K., Polikovsky, M., **Fenta, M.**, Ingle, A., Golberg, A.(2022): Integrated multitrophic aquaculture approach with marine energy projects for management and restoration of coastal ecosystems of India. *Ecological Engineering*,176.1-13. <https://doi.org/10.1016/j.ecoleng.2021.106525>.

List of Conference Proceedings and Abstracts

7. **Fenta, M.,** Liyew, Z., Heincz, A., Szanyi, J. (2018). Hydrogeophysical characterization of shallow volcanic aquifers around Dangila town, Northwest Ethiopia. In: Meeting of Young Geoscientists(6-7 April 2018). Hajdúszoboszló, Hungary (conference Abstracts): p. 75
8. **Fenta, M.** (2018). Vertical electrical sounding geophysical survey in volcanic terrains for groundwater exploration at semi-desert area of southern Ethiopia. In: Constantin Gh. Popa Poster & Paper Contest 10th Edition. Ploesti oil and gas University, Ploesti, Romania (Conference Abstract): p.1
9. **Fenta, M.,** Lewi, E., Hail, T., Fisseha, S. (2019). High precision gravity assisted with a differential global positioning system (DGPS) and geomagnetic surveys for mapping groundwater reservoir potential in volcanic terranes of south Ethiopia. In: Geophysical Research: EGU General Assembly 2019. Vinea, Austria (conference Abstracts): 303, P1.
10. **Fenta, M.,** Szanyi, J. (2019). Integrated near surfaces geophysical survey and interpretations to map potential geothermal sites at Mecsek fault zone, Southwest Hungary. In 10th European Geothermal PhD Day. Potsdam, Germany (conference abstract): p. 33.
11. **Fenta, M.** (2019). Fibre optical methods as a comprehensive and modern oil and gas exploration and management technique: A review. In Proceedings: 6th edition of Annual Student Energy Congress. Zagreb, Croatia (Conference preceding). pp. 9-13.
12. Ingle, K., Polikovsky, M., **Fenta , M.,** Ingle A., Golberg, A. (2019). Ecological Risk Management with Integrated Multi-Tropic Aquaculture Approach for Marine Energy Projects in India (2019). 1st International Conference on Advanced Production and Processing. Novi Sad, Serbia (Poster presentation).
13. **Fenta, M.** (2022). Geo-Physics and its benefit for humanity. International Conference on Global Trends in Science, Technology, Humanities, Commerce & Management 2022 (ICGTSTHCM 2022). SSBT's College of Engineering and Technology, Bambhori- Jalgaon, Maharashtra, India (Expert Lecture).

ABSTRACT

The pursuit of meeting the critical needs for clean water of Ethiopia's citizens depends on groundwater resources. However, the geology, rainfall, physiography, and other factors make it challenging to manage resources without conducting intensive, efficient investigations. The variable physiographic area surrounding the town of Dangila in northwest Ethiopia has been occasioned by incessant borehole failure and low yield over the past four decades. The Oligocene – Miocene and the recent Quaternary timing of volcanic eruption yielded a highly complex groundwater reservoir. The variable groundwater reservoir of rainfall causes variations in groundwater occurrence, quality, quantity, and aquifer parameters within hundreds of meters. Volcanic aquifers supplying freshwater in Ethiopian highlands have imposed various challenges on sustainable management that have prompted groundwater research.

In my study, the intricate nature of volcanic aquifers demands a multi-investigation approach that uses survey data and information from diverse sources. Numerous investigative approaches have been utilized, comprising analysis of existing boreholes, rock outcrops, and hydrochemistry as well as water-stable isotope analysis, surveys of near-surface geomagnetic and vertical electrical sounding, and pump test analysis techniques. Additionally, the extent of the possibility of utilizing new fiber optical technologies to understand the complex geometry of aquifers systems has been assessed. As a result, in this study, the aquifer's groundwater reservoir characteristics, hydraulic parameters, water quality, and suitability for drinking and irrigation use have been investigated. The influencing factors for groundwater chemistry, the sources of ions in the groundwater, the rock–water interactions, and groundwater evolution have been examined. Furthermore, the sources of precipitation for recharge, the recharge and discharge areas, the potential areas for further borehole drilling, and the governing features for groundwater occurrence and movement have been investigated. Finally, the conceptual groundwater flow model has been developed for the sustainable utilization of the groundwater resource in the future.

Keywords: Hydrogeophysics. Hydrochemistry. Water isotope. Volcanic aquifer. Groundwater flows conceptual model. Northwest Ethiopia.

ÖSSZEFOGLALÁS

Etiópia lakossági vízigényének kielégítése döntően a felszín alatti vízkészleteken alapul. Ugyanakkor a csapadék, az éghajlat, a topográfiai és hidrogeológiai tényezők együttes vizsgálata óriási kihívást jelent ezen létfontosságú erőforrás hatékony hasznosításához. A vizsgálati területemet képező, változatos morfológiájú, északnyugat-etiópiai Dangila városának térségét a kutak folyamatos meghibásodása és alacsony hozama jellemezte az elmúlt évtizedekben. A terciert és a negyedidőszakot felölelő korszakban lezajlott vulkánkitörések rendkívül összetett talajvíztároló jellegű eredményeztek. A tároló képződmény komplexitása, valamint a csapadék időszakossága a talajvíz előfordulásának, minőségének, mennyiségének és a víztartó réteg paramétereinek változásait okozza akár néhány száz méteres távolságon belül. Az Etióp-magasföld édesvíz készletét rejtő vulkanikus víztárolók számos kihívást jelentettek a fenntartható gazdálkodással kapcsolatban, ami a felszín alatti vizek kutatására ösztönzött.

Munkám során, a vulkanikus víztartó rétegek bonyolult természete komplex megközelítést igényelt, melyhez általam gyűjtött mérési adatokat és különböző forrású információkat használtam fel. Számos vizsgálati megközelítést alkalmaztam, beleértve a meglévő fúrások, kőzetfeltárások vizsgálatát; hidrokémiai-, stabilizotóp elemzéseket, felszínközeli geo-mágneses és vertikális elektromos szondázást, valamint szivattyúteszt elemzési technikákat. Emellett felmértem az új száloptikai technológiák alkalmazhatóságát a komplex geometriájú víztartó rendszerek megértésében. Ennek eredményeképpen megvizsgáltam a talajvíztartó réteg jellemzőit, a hidraulikai paramétereiket, a vízminőséget, valamint a talajvíz ivóvíz- és öntözési célú felhasználásra való alkalmasságát. Tanulmányoztam a talajvíz kémiai befolyásoló tényezőket, a talajvízben lévő ionok forrásait, a kőzet-víz kölcsönhatásokat és a talajvíz alakulását. Vizsgáltam továbbá az utánpótlódáshoz szükséges csapadékforrásokat, a talajvíz előfordulását és mozgását meghatározó jellemzőket, a beáramlási és kiáramlási területeket, valamint további kutak létesítésének lehetséges helyeit. Végül, a felszín alatti vízkészlet jövőbeni fenntartható hasznosítása érdekében, koncepcionális felszínalatti vízáramlási modellt dolgoztam ki.

Kulcsszavak: hidrogeofizika, hidrokémia, vízigény, vulkanikus víztartó réteg, felszín alatti vízfolyások koncepcionális modellje, északnyugat-Etiópia.

TABLE OF CONTENTS

PREFACE	III
ABSTRACT	V
LIST OF ABBREVIATIONS.....	XII
1. INTRODUCTION.....	1
1.1 Research Aim, Goals, and Objectives.....	5
1.2 General Description of the Study Area.....	7
1.2.1 Location and morphological setting.....	7
1.2.2 Climate and agriculture	2
1.2.3 Geological and hydrogeological setting.....	2
2. LITERATURE REVIEW AND THEORETICAL BACKGROUND OF APPLIED....	10
METHODS	10
3. MATERIALS AND METHODOLOGICAL PROCEDURES	17
3.1 Preliminary/Reconnaissance Study.....	18
3.2 Intermediate/Detail Investigation	19
a) Geological Data Set.....	19
b) Hydrogeological Data Set.....	19
c) Geophysical Data Set.....	23
3.3 Hydrogeological Model Development.....	27
4. RESULTS AND DISCUSSION	29
4.1 Properties of Volcanic Aquifer Reservoirs.....	29
4.1.1 Rock sample thin sections analysis.....	31
4.2. Hydrochemistry	34
4.2.1. Mechanisms controlling groundwater chemistry.....	39
4.2.2. Chemical weathering of rock-forming minerals	45
4.2.3. Water quality for irrigation	45
3.3 Water-stable Isotopes (¹⁸O and ²H).....	49
4.3.1 $\delta^{18}\text{O}$ versus d-excess	54
4.3.2 The spatial distribution of $\delta^{18}\text{O}$ and $\delta^2\text{H}$	55

4.4 Hydrogeophysical Properties.....	58
4.4.1 Geomagnetic survey results	58
4.4.2 Magnetic field profile plots.....	60
4.4.3 Vertical electrical sounding	62
4.4.4 Apparent resistivity graphs and two dimensional (2D) sections	63
4.4.5 One-dimension (1D) inverse modeling of VES data	68
4.4.6 The 2D Geoelectric sections	70
4.4.7 Three-dimensional (3D) visualization of 1D modeled VES results	72
4.4.8 The 3D sliced resistivity Plan maps and images.....	75
4.4.9 The possibilities of applying new/modern geophysical techniques.....	79
4.5. Aquifer Characteristics	81
4.5.1. Shallow aquifer system.....	81
4.5.2. Water level and groundwater flow.....	82
4.5.3. Deep aquifer.....	87
4.5.4. Pump Test and hydraulic parameter estimation.....	91
4.6 Hydrogeological Conceptual Model.....	94
4.6.1 Groundwater Flownets.....	95
4.7. Sustainable Groundwater Management of Dangila Town and its Surrounding Area	99
5. SUMMARY	100
ACKNOWLEDGMENT.....	106
REFERENCE	107
APPENDICES	120
Appendix 1: Hydrochemical and hydrophysical laboratory analysis data of volcanic aquifers.	120
Appendix 2: The calculated values of SAR, Na%, and RSC of groundwater samples.....	123
Appendix 3: The 32 VES Data point information.....	124
Appendix 4: 1D-model VES Curves	127

LIST OF FIGURES

Fig. 1 Systematic diagram of groundwater occurrences in fractured volcanic rocks	4
Fig. 2 Location map of the study area.	1
Fig. 3 Administration map of the study area with its kebele boundaries.	1
Fig. 4 Geological map of Lake Tana Basin.....	4
Fig. 5 Geological map of the study area.....	6
Fig. 6 Excavated fine-grained basalt from the quarry site along the Dangila to Chara Road.....	7
Fig. 7 Groundwater abstractions systems	9
Fig. 8 Current flow from a single surface electrode	14
Fig. 9 Schlumberger electrode configurations for VES survey.	14
Fig. 10 Optical fiber data transmission framework.....	16
Fig. 11 Stepwise/hierarchical methodological flow chart.	18
Fig. 12 Groundwater sample locations collected for hydrochemical analysis.	21
Fig. 13 Water-stable isotope sampling point locations with various water schemes.	23
Fig. 14 Photographs of resistivity equipment and field layout.	25
Fig. 15 GSM-19T proton precession magnetometer components.	26
Fig. 16 Location of VES and geomagnetic data points.....	28
Fig. 17 Photographs of topsoil, weathered rocks, and paleosoil	31
Fig. 18 Microscope images of thin sections from rock samples No1(a) and No2(b).	32
Fig. 19 Microscopic images of a thin section from rock sample No. 3.	33
Fig. 20 Piper diagram of hydrochemical data.	38
Fig. 21 Gibbs diagram of cations (a) and anions (b) of groundwater	40
Fig. 22 Na^+ Versus Cl^- graph (a) and HCO_3^- versus Ca^{+2} graph (b) of groundwater	42
Fig. 23 HCO_3^- versus $(\text{Ca}^{+2} + \text{Mg}^{+2})$ graph (a) and $(\text{Na}^+ + \text{K}^+) - \text{Cl}^-$ versus $(\text{Ca}^{+2} + \text{Mg}^{+2}) - (\text{HCO}_3^- + \text{SO}_4^{-2})$ graphs (b) of groundwater.	44

Fig. 24 Classification of groundwater using US regional laboratory staff salinity diagram.....	47
Fig. 25 Graph of $\delta^{18}\text{O}$ versus $\delta^2\text{H}$ values from different water schemes.	53
Fig. 26 Relationship between $\delta^{18}\text{O}$ versus d-excess in different water schemes.	55
Fig. 27 Contour map of $\delta^{18}\text{O}$ content overlaid on the digital elevation model with sample locations.	56
Fig. 28 Contour map of $\delta^2\text{H}$ content overlaid on the digital elevations model with sample locations.	57
Fig. 29 Total geomagnetic field maps with inferred structures.....	60
Fig. 30 Magnetic profiles from the total magnetic field data with the possible type of fault orientations.	61
Fig. 31 Three categories of VES curves on a Log-log graph.	66
Fig. 32 2D apparent resistivity pseudo-depth sections including selected VES points.	67
Fig. 33 Samples of 1D inverse modeled VES	69
Fig. 34 2D geoelectric section with its corresponding apparent resistivity pseudo-depth section.	71
Fig. 35 3D scatter plot of resistivity layers	73
Fig. 36 3D Box plot of uninterpolated resistivity layer data values	74
Fig. 37 3D volume representation of the grid layer resistivity data.	75
Fig. 38 3D sliced depth resistivity map in the XY plane.	76
Fig. 39 3D sliced oblique resistivity images with VES point locations.....	77
Fig. 40 3D sliced orthogonal resistivity images in the XY, XZ, and YZ planes	78
Fig. 41 Fiber optic cable coupling options in a borehole survey.	80
Fig. 42 Shallow groundwater level contour maps and flow direction overlain on the Digital elevation model map.	83
Fig. 43 Variations in groundwater and surface elevations; a long distance from A to B.	84
Fig. 44 Linear plot of groundwater elevations versus surface elevation face elevations from the grid data and SRTM surface elevations data B) along with profile AB of Fig. 43.....	85

Fig. 45 Regolith from the shallow hand-dug well (a), shallow hand-dug private well construction, top external part (b), internal part (c), and community-based hand-dug shallow well with a hand pump (d).	87
Fig. 46 Groundwater yield map of boreholes with a depth greater than 58 m.....	90
Fig. 47 Hydrogeological conceptual model of Dangila Town and its surrounding area aquifer system.....	95
Fig. 48 Simplified schematic of the groundwater flow of Dangila and its surrounding area	98

LIST OF TABLES

Table 1. Hydrochemical and physical summary of groundwater samples from boreholes	36
Table 2. Quality of groundwater samples from the study area for drinking purposes based on the WHO 2011 drinking water quality index (WHO, 2011).	37
Table 3. Different groundwater facies of the area.....	39
Table 4. Maximum, minimum, means, and standard deviation values of SAR, Na%, and RSC in the groundwater.....	46
Table 5. Classification of water for irrigation use based on SAR, Na%, and RSC values.	49
Table 6. Statistical summary for the water sample laboratory analysis results of $\delta^{2}\text{H}$, $\delta^{18}\text{O}$, and the calculated d-excess value in ‰.	51
Table 7. Summary of the minimum and maximum half current electrode AB/2 (m) and potential electrode MN/2 (m)	63
Table 8. Hydraulic conductivity, transmissivity, and storage coefficient values of four selected deep boreholes.....	93

LIST OF ABBREVIATIONS

1D: one dimension	SRTM: shuttle radar topographic mission
2D: two dimensions	TDS: total dissolved solids
3D: three dimensions	USGS: United States Geological Survey
AAS: atomic absorption spectrometry	VES: vertical electrical sounding
AI: artificial intelligence	VSMOW: Vienna Standard Mean Ocean Water
DC: direct current	WHO: World Health Organization.
DFOGSs: fiber optics geophysical sensors	
EC: electrical conductivity	
FBGs: fiber Bragg gratings	
GDP: gross domestic product	
GIS: geographic information systems	
GMWL: global meteoric water line	
GNIP: Global Network for Isotopes in Precipitation	
GNIP: Global Network of Isotope in Precipitation	
IAEA: International Atomic Energy Agency	
IC: ion chromatography	
IGRF: International Geomagnetic Reference Field	
LCD: liquid crystal display	
LMWL: local meteoric water lines	
Na%: sodium percentage	
NMA: National Meteorology Agency	
pH: potential hydrogen	
RSC: residual sodium carbonate	
SAR: sodium adsorption ratio	

1. INTRODUCTION

Groundwater supplies fresh drinking water for humanity. It provides freshwater to living things that help to sustain life on Earth. It accounts for >50% of the global population freshwater supply and 43% of all water used for irrigation (Poeter et al., 2020). The distinct attributes of groundwater being less susceptible to pollution, less affected by climate change, and abundance of supply irrespective of the rainfall amount make it preferable over surface water sources. Surface water is becoming increasingly unreliable due to climate change and anthropogenic pollution. Accordingly, understanding the groundwater system becomes essential.

Groundwater occurrence and its suitability as a freshwater resource have affected Ethiopian history and civilization. Groundwater has been used as the primary source of freshwater supply since the 1970s for cities, small towns, and rural communities in Ethiopia (Mengistu et al., 2019). Areas where groundwater is easily accessible to the community as springs have been centers of civilizations from ancient times (Kebede, 2013). The exponential growth of the population and agriculture led industrial development policies of Ethiopia are attracting greater attention from researchers in addition to the use of groundwater as a potentially cost-effective water supply source.

Conversely, surface water as a freshwater supply has been limited owing to high construction costs and inadequate water quality. The considerable dependency of urban and rural populations on groundwater as a primary drinking-water source and recent increases in its industrial and irrigation uses require a better understanding of the groundwater system. Ethiopia has implemented groundwater-based irrigation projects utilizing more than 9,000 boreholes, 28,000 monitoring wells, and 14,657 spring improvements and has achieved a 10% gross domestic product (GDP) growth during the last two decades (Mengistu et al., 2019). The nationwide pilot-scale irrigation practices will be expanded rapidly, and there are several small-scale irrigation schemes in the study area that require a thorough study of groundwater.

Volcanic rocks considered minor in areal coverage store volcanic aquifers that are vital and sometimes the only freshwater source in many regions. Volcanic rocks exposed on continents account for only 6.8%–8% of all the Earth's rock types (Blatt & Jones, 1975; Meybeck, 1987; Suchet et al., 2003). This rocks category includes both intrusive and extrusive rocks with basic and Rhyolitic magmas. The proportion of basaltic volcanic rocks is 4.1%–5.2% of the total extrusive rocks on

Earth (Meybeck, 1987; Suchet et al., 2003). The Earth's northern hemisphere from 0° to 30°N latitude comprises 36% of total extrusive or volcanic rocks, mainly contained in the Deccan Traps of India and Ethiopia (Suchet et al., 2003). Volcanic rocks cover <6% of sub-Saharan Africa's land area, mostly confined to East Africa. These rocks are good reservoirs of volcanic aquifers and supply fresh water for central and northwest Ethiopian plateau land dwellers (MacDonald et al., 2008). Ethiopia's groundwater, dominantly obtained from volcanic aquifers, supplies >90% of the freshwater demand for domestic and industrial uses (Kebede et al., 2018). These aquifers are the sources of various cross-boundary rivers, including the Blue Nile River, which is among the longest rivers in the world (Nile Basin Initiative, 2012).

Volcanic aquifers can be divided into islandic, which are found in volcanic islands, and continental, which are far from oceans. Although these aquifers possess volcanism, the main geological processes, i.e., rifting and jointing, essentially cause considerable structural variety, giving rise to much higher lateral and vertical variability in continental than islandic volcanic aquifers. However, it is possible to infer certain aquifer properties and to acquire a basic understanding of the hydrogeological functioning of continental volcanic aquifers from the study results of islandic volcanic aquifers. Numerous studies have been conducted to understand the chemical and physical properties of Islandic volcanic aquifers and to develop their conceptual hydrogeological models (Join et al., 2005; Lachassagne et al., 2014; Prada et al., 2005; Violette et al., 2014). The findings might be used as a benchmark to investigate continental volcanic aquifers that lack study results. Nevertheless, neither such results nor their conceptual models can be adapted to characterize continental volcanic aquifers that are highly affected by rifting and faulting.

The Ethiopian volcanic aquifers are among those less investigated volcanic aquifers. However, there have been minimal studies on Ethiopian continental volcanic aquifers that consider various aspects (Aberra, 1990; Ayenew et al., 2008; Vernier, 1993). Besides, some research has dealt with specific targets about the aquifer's specific parameters. The hydrochemical analysis has been employed to understand the movement and occurrence of groundwater (Ayenew et al., 2008) and to estimate the groundwater recharge and pollution sources (Demlie et al., 2008). The aquifer hydraulic property investigation based on borehole data (Sogreah & Geomatrix, 2013; Ayenew et al., 2008) and aquifer potential zone delineation and mapping using geophysical methods (Beshawered et al., 2010) have comprised the most prominent research. Moreover, water-stable isotope data have been analyzed for recharge area declination and amount estimation of volcanic aquifers (Demlie et al., 2007; Woldemariyam & Ayenew, 2016). Additionally, recharge estimation works

using water-level fluctuation (Walker et al., 2019a; Yenehun et al., 2020) are inadequate to understand the volcanic reservoir systems. Conversely, there has been a deficiency in studies that employ multiple instigation approaches to the study of aquifer systems.

The volcanic aquifers in northwest Ethiopia, surrounding the town of Dangila, have been the focus of numerous water-related sectors for the past decades. Multiple sectors have implemented numerous plans to alleviate the scarcity of drinking water over the past 47 y. Spring development, drilling shallow hand-dug wells (<25-m depth), and creating deep boreholes of 58–209 m in depth have been common groundwater abstraction mechanisms. The field observations—the Dangila Woreda water office’s status unpublished report (2020) and Amhara region waterworks design enterprise’s unpublished report (2017)—showed that there are more than 500 shallow hand-dug wells and more than 24 deep boreholes in the study area. However, a very limited number of springs, < 10, have been observed. The deep boreholes (depth > 100 m) are located mainly close to Dangila and are aimed primarily at supplying drinking water for the town. The groundwater yield from each spring and shallow well does not exceed 1 L/s, and except for four boreholes, the groundwater yield from deep boreholes does not exceed 4 L/s. Several springs become dry during dry seasons following the seasonal rainfall.

Several shallow and deep well failures were encountered despite various actions taken to alleviate the scarcity of fresh drinking water. For example, among more than 24 deep boreholes (depth > 58 m) found in the study area, only four have an initial groundwater yield of 18–30 L/s. Some reports showed that the groundwater yield of deep boreholes decreases with time after a few years of groundwater extraction. On the contrary, the demand for clean drinking water, small-scale irrigations, water bottling, and industrial applications increase with time. Moreover, the increase in population number over time, the yield reduction in several boreholes, the minimal amount of water available from shallow aquifers, and the increased demand by investors to establish water bolting companies have increased the strain on freshwater demand. Furthermore, the increased small-scale irrigation practice over time is one more foremost concern given the ever-increasing freshwater demand. However, the nature of the volcanic reservoir, as well as rainfall and morphological factors, negate the easy accessibility of the resource.

The natural geological environment plays a vital role in controlling the occurrence and circulation of groundwater and governs aquifer productivity. Its occurrence varies spatially owing to the complexities of regional and local geology and associated geological structures. The subsurface environment is highly heterogeneous, and non-linear coupled processes occur at multiple spatial and

temporal ranges (Linde et al., 2017). Groundwater in basaltic volcanic rocks occurs in vesicles, fractures, and joints formed during or after rock formation (Fig. 1). The porous rocks often show independent or connected fractures resulting from various geomechanical processes, including deformation, stress relaxation, and desiccation (Jougnot, 2020). The fracture systems of crystalline rocks formed when the rock is exposed to different stress are generally unpredictable in length, aperture opening, and pattern (Jane et al., 1996). The occurrence and hydraulic property of volcanic aquifers stored in the fractured and weathered volcanic rocks vary spatially due to the complexities of geology and associated geological structures.

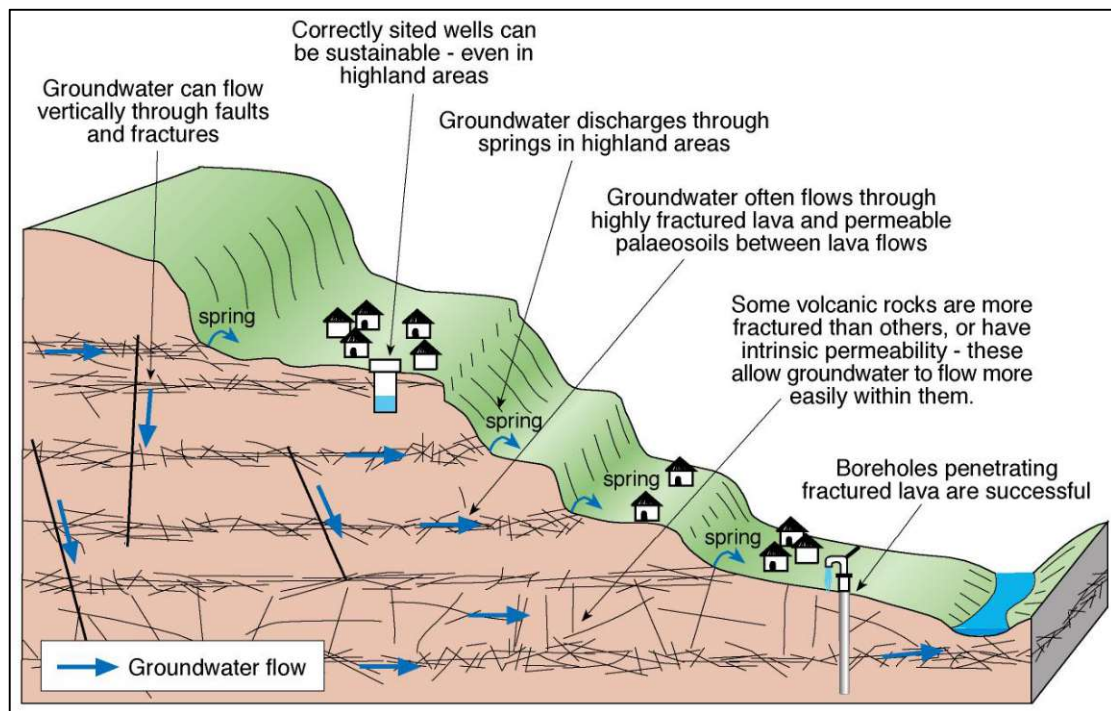


Fig. 1 Systematic diagram of groundwater occurrences in fractured volcanic rocks (Earthwise, 2021).

The hydrogeological frameworks of fractured rocks are essential as their presence facilitates access to groundwater storage, although they can impose a threat of leakage and passage of anthropogenic pollutants from surface and shallow aquifers to the deep aquifer systems. The fractures and volcanism cause volcanic aquifers to be highly complex, anisotropic, and heterogeneous, causing variation in the groundwater yield in space and time. Valuable information about subsurface structures and processes can be obtained from borehole measurements, outcrops, laboratory analysis of field samples, as well as geophysical and hydrogeological experiments; however, this information is

largely incomplete (Linde et al., 2017). Therefore, selecting appropriate explorations and aquifer characterizations techniques is essential to understanding the aquifer system and locating potential groundwater zones for drilling that help minimize well-drilling risks. The existence of numerous borehole failures and continuous freshwater demand in the area indicated that single investigation approaches aimed at understanding the hydrogeological system of the area and to explore the volcanic aquifers have not been efficient in the past couple of decades.

The approach of analyzing multiple datasets from a multidisciplinary investigation system is helpful to investigate the volcanic, geological setting, groundwater flow, hydrochemistry, and aquifer potential. Therefore, the aquifer characterization targets the research gaps about volcanic aquifer potential controlling factors, the water quality and sustainability for drinking, and irrigational use and estimation of aquifer hydraulic properties. The research aims to develop a conceptual groundwater flow model which can be helpful to manage the area's groundwater. Neither the large scale nor the islandic groundwater conceptual flow models can be adapted for such volcanic aquifers in the continental rifted context. These necessitate several investigational approaches involving geological, hydrogeological, geophysical, and available borehole and other open sources data. Therefore, this study mainly targets the research gap of volcanic aquifer characterization via field and laboratory data analysis.

1.1 Research Aim, Goals, and Objectives

Considering the growing global burden on groundwater resources with increasing anthropogenic effects, including climate change, an integrated multidisciplinary investigative approach is required to address the scientific and societal issues involving groundwater resources (Barbieri, 2019). The present research aims to characterize the hydrogeological system of the northwest Ethiopian volcanic aquifers using multidisciplinary data sets. This study attempts to describe the hydrogeological framework and the groundwater quality for drinking, irrigation, and industrial applications. Additionally, the controlling factors for groundwater flow and storage are identified, and the conceptual models are outlined for future sustainable groundwater management.

The present research mainly utilizes the various deep and shallow wells information, hydrochemistry, and stable water isotopic data, along with near-surface geophysical survey results, to characterize and infer valuable parameters of the complex geological settings of volcanic aquifers.

Subsequently, this study aims to comprehensively understand the volcanic aquifers systems, infer hydraulic parameters, and map the potential drilling sites for future groundwater abstraction. Therefore, within these frameworks, the following objectives are demarcated.

i) To assess the hydrogeological framework, map potential groundwater sites, and demarcate the groundwater storage and flow controlling factors. Research questions to be addressed are as follows:

What controls the groundwater flow system? Why have more than 15 deep wells drilled for groundwater abstraction become dry or unsuccessful? Why do few boreholes yield more than 18 L/s, whereas others yield less than 3.5 L/s, and their yield diminish with time and become dry after a few years of abstraction? Why does the yield of groundwater from shallow wells within less than 200-m distance from each other vary? At what depths are the main aquifers located, and in which geological unit and systems? Do the aquifer's characteristics vary with depth? Which places are better for future drilling of shallow and deep boreholes without excessive spending on both the drilling and construction costs?

ii) To evaluate the groundwater quality for drinking and irrigation and its hydrogeochemical evolution. Research questions to be addressed:

What controls the groundwater chemistry? Does the mineralogical composition of the reservoir rocks influence the hydrochemistry of aquifers? Does the groundwater chemistry change with depth and along flow paths? What affects the hydrogeochemical evolution of the groundwater? How is the rock–water interaction? Is there any mixing of water from different depth aquifers? Is the groundwater from various aquifers fresh, safe, of good quality for drinking, and applicable to industrial and small-scale irrigation?

iii) To determine groundwater's residence time, recharge sources, discharge areas, and surface water-groundwater interaction. Research questions to be addressed:

Which aquifer is young? What is the relationship between surface water and groundwater? Do they interact, and if so, which one recharges the other? What are the sources of recharge? Does the groundwater recharge the surface water or vice versa? Is there any mixing between aquifers? Do they recharge from regional or local aquifers or from both?

iv) To estimate the variations in hydraulic conductivity, total porosity, and transmissivity of the volcanic aquifers. Research questions to be addressed:

Why do some borehole aquifers have higher hydraulic conductivity than others? Why are the recharging and drawdown times fast in most deep boreholes? Are the transmissivity values of aquifers similar? Does the aquifer parameter vary laterally or horizontally? Are the aquifers anisotropic and homogeneous?

v) To assess the recent new geophysical technologies that can be applied in groundwater studies. Research questions to be addressed:

What are the recent possible technological advancements that can be applied in groundwater resources exploration? Are there any new technologies that can be used to understand the characteristics of volcanic aquifers? Can we apply proven techniques for oil and gas exploration to groundwater study?

vi) To develop a hydrogeological conceptual model from the combined results of multidisciplinary investigation approaches that will help to understand and manage the area's groundwater resources in the future. Research questions to be addressed:

How can the volcanic aquifer of the area be managed in the future? Where can either shallow or deep wells be drilled without adverse effects on the aquifer systems? Can overexploitation or groundwater depletion occur in the area? How to protect from overexploitation? How to manage the aquifer systems of the area in the future sustainably?

1.2 General Description of the Study Area

1.2.1 Location and morphological setting

The study area is situated in northwest Ethiopia, surrounding the town of Dangila, approximately 485 km from Addis Ababa, the capital city of Ethiopia and 80 km from Bahir Dar, the capital city of the Amhara regional state (Fig. 2). It is mainly located in the Dangila district, known in Ethiopia as a *woreda*, with partial components in the South Achefer *woreda* (Fig. 3). The area comprises more than 19 kebeles, the lowest administrative division in Ethiopia, with a total population of greater than 158,000, of which 131,000 are rural, and 27,000 reside within in urban parts (CSA, 2012).

The study area's upper Kilti and Branti river catchments cover approximately $\sim 450 \text{ km}^2$ with elevation values varying from 1949 to 2453 m above sea level. These rivers drain to the Gilgel Abay river catchment, which in turn is one of the four major river catchments of the Lake Tana Basin

(Fig. 2). The area is characterized mainly by gently flat topography and highland at the southwestern portion with a maximum elevation value of 2453 m. These rivers exhibit a radial draining system in the upper ridges and meandering system types at the lower floodplains.

The area's geomorphology is affected by various volcanic eruptions comparable to the vast volcanic land of Ethiopia. The volcanic cover of the Ethiopian landmass forms mostly highlands and rift basins that create complex relief patterns. The Ethiopian relief can be grouped into five distinct topographic regions: western highlands, western lowlands, eastern highlands and lowlands, and rift valleys (Ayenew et al., 2008). The Ethiopian highlands are a volcanic massif of flood and shield volcano basalts ranging from 0.5 to 3 km thick that form spectacular trap topography of 1,500 to 4,500 m altitude flanking the main Ethiopian Rift (Mohr, 1983). The research area is among the northwestern highlands within the Lake Tana Basin formed by a junction of three grabens (Chorowicz et al., 1998) later considered to be caldera (Prave et al., 2016). The 16,500 km² lake basin that contains Lake Tana, Ethiopia's largest lake with a diameter of 60–80 km, is the source of the world's longest river, the Blue Nile River.

The Oligocene-Miocene volcanism, followed by the later exogenic processes—weathering and erosion—played significant roles in the existing geomorphological features (Yenehun et al., 2020). Alluvial and colluvial processes play a substantial role in sedimentation in the gentle slopes and flat floodplain areas. A soil cover of more than 2.5-m thickness is observed along the Dangila-Chara weathered road close to the earlier and recent Quaternary volcanic flow boundaries. The weathering products of the earlier lava flow and pyroclastic falls are thicker than the recent Quaternary rock weathering products.

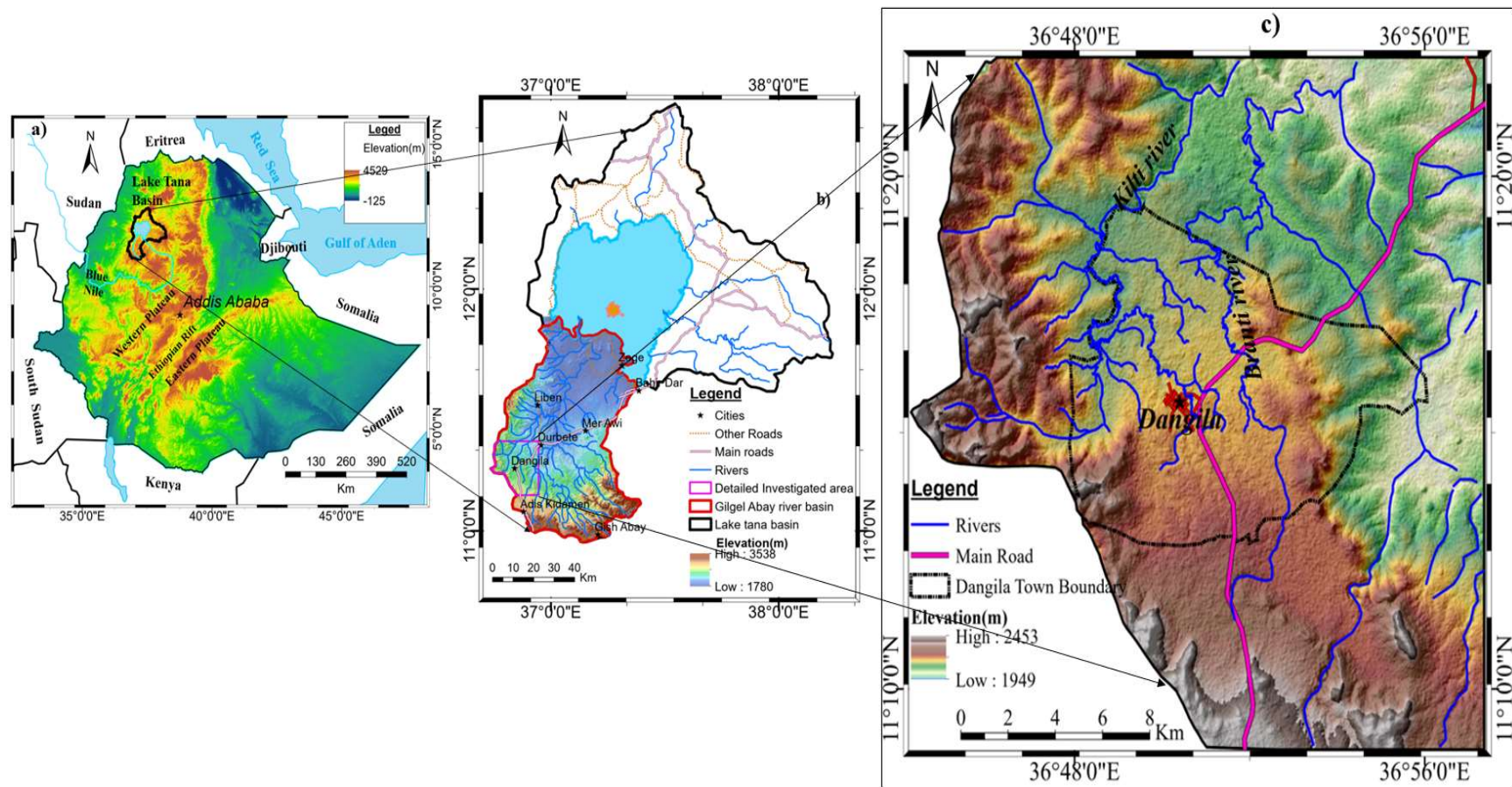


Fig. 2 Location map of the study area. **a)** Lake Tana Basin in Ethiopia. **b)** Gilgel Abay River catchment in Lake Tana Basin. **c)** Upper Kilti and Branti River catchments.

Moreover, the Ethiopian terrain is imprinted by volcanism, uplifting, and rifting, in which the uplifting accelerates erosional processes. The uplifted terrain of Ethiopia has been undergoing erosion at a rate of between 0.029 and 0.185 mm/y for nearly 30 million y (Pik et al., 2003). These processes over a long geological period produced highly rugged terrain, fragmented plateau, deep gorges, canyons, mountain peaks, and buttes. These prominent topographic features of Ethiopia, in turn, affect the precipitation pattern of groundwater occurrence and flow (Kebede, 2013).

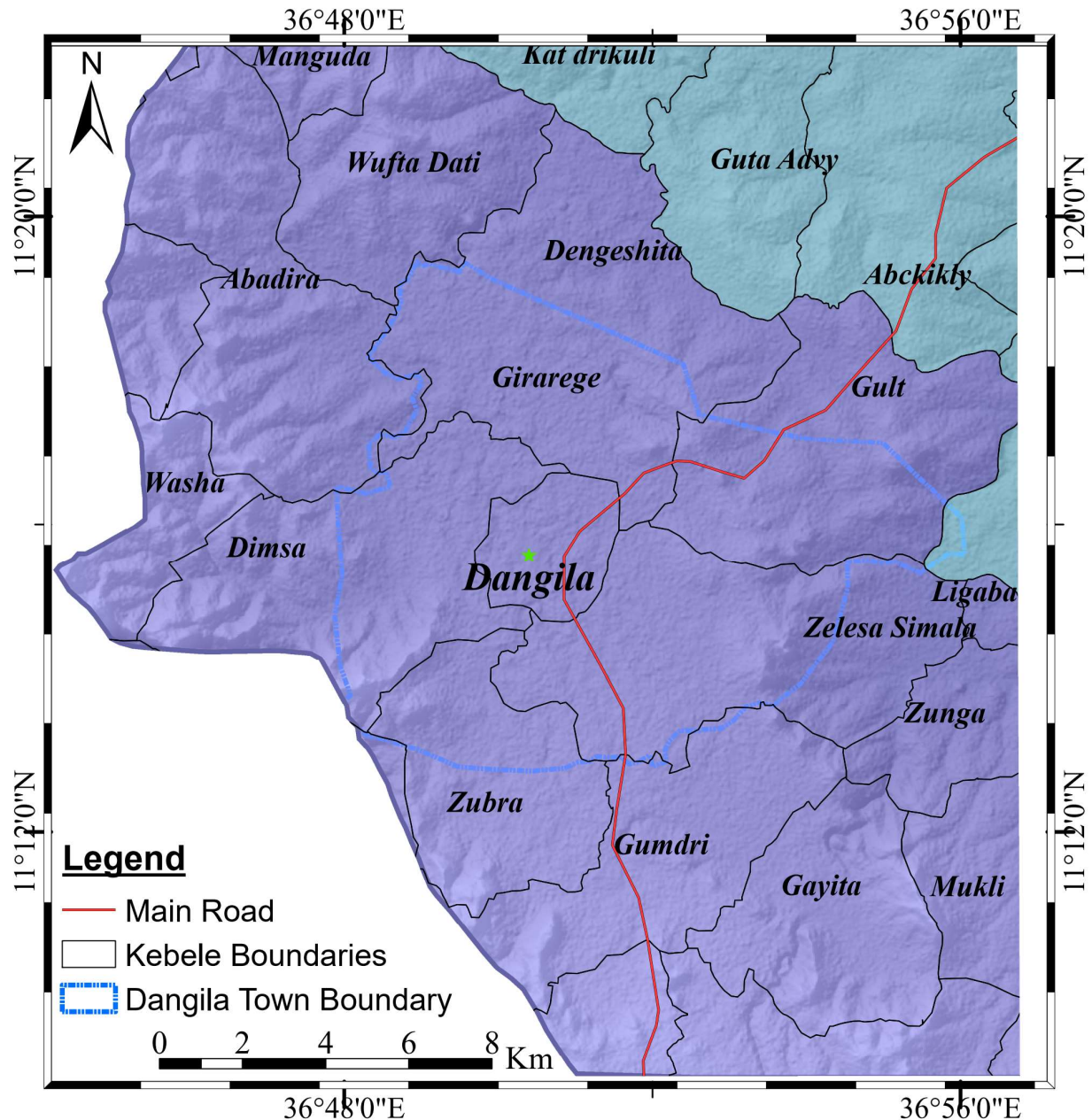


Fig. 3 Administration map of the study area with its kebele boundaries.

1.2.2 Climate and agriculture

The study area, Dangila town and its surroundings, has a mean annual rainfall of 1640 mm, as measured (since 1988) at the National Meteorology Agency (NMA) weather station at Dangila town, 91% of which falls from May to October (Walker et al., 2019a), with the main rainy season occurring from June to September. The average annual precipitation across the entire country of Ethiopia is 817 mm/y (Fazzini et al., 2015). The area's climate is moist subtropical (locally called *Woyna Dega*) with a median annual daily maximum temperature of 25°C and minimum of 9°C, as measured at the NMA weather station in Dangila town (Walker et al., 2016). The mean annual temperature of Ethiopia varies from over 25°C in the lowlands to less than 7°C–12°C in the high altitude plateaus (FAO, 2016).

The various physiography of the area with seasonally inundated large floodplains is used as pasture and rain-fed agriculture. There are small-scale backyard agricultural practices that have intensified recently. Crop–livestock mixed subsistence farming is the primary source of individual livelihood. Belay & Bewket (2013) approximated the irrigated cropland of Dangila woreda as 14%, which equates to 0.20 ha of irrigated land per household. Irrigated land is seen as a source of substantial cash income and household nutritional benefits. Irrigation is mainly through shared gravity diversions from seasonal and perennial rivers, as well as water lifting from shallow wells and boreholes. The increased tendency to use the groundwater resources for irrigation using boreholes at an individual level by the rural community notifies the necessity of legal documents. Legal documents concerning groundwater management will help future groundwater governance and avoid overexploitation.

1.2.3 Geological and hydrogeological setting

Geological setting of Ethiopia: An overview

The geology of Ethiopia is the result of a complex orogenic evolution that lasted from the Precambrian era to the recent Quaternary period. These long-term geological processes resulted in distinct topography and groundwater occurrence in Ethiopia. It started in the Precambrian era with terrain accretion and collision, followed by the Paleozoic peneplanation, glaciations, and Gondwana breakup. The Paleozoic geological processes are followed by the cyclic marine transgression and regression events that are principal to the accumulation of multilayered sedimentary rocks in the

Mesozoic era. The Cenozoic era featured vast continental flood basalt eruption and rift valley formation trailed by later sedimentation and deep incision of river valleys and pluvial-interpluvial sediment accumulation in the Quaternary period (Kebede, 2013). The Quaternary time experienced various extensional events with various tectonic activities resulting in the main Ethiopian Rift opening, the northeastward separations of Arabia from Africa, and the Red Sea spreading ridge. These geological processes, combined with the rifting coupled with the growth of the Red Sea and the East African-Ethiopian Rift Valley, have resulted in extensive fracturing (Kebede, 2013). The geological process from the Cenozoic era to recent Quaternary times resulted in volcanic rocks covering two-thirds of the Ethiopian landmass with a composite volcanic aquifer system.

Geological setting of the Lake Tana Basin: An overview

Lake Tana basin has various lithologic and tectonic features similar to the other Ethiopian landmass. Its formation has different explanations suggested as a junction of three grabens (Chorowicz et al., 1998) and as a caldera (Prave et al., 2016). The main geological aspects of the basin include subsidence and block fault formation, accumulation of Miocene organic-rich sedimentary rocks, Pleistocene basin volcanism, late Quaternary volcanic activity and recent lacustrine and alluvial deposition along the periphery of the lake (Kebede, 2013). Fault reactivation occurred in the Late Miocene–Quaternary, complemented locally by predominantly basaltic volcanism. The concentric and radial dike patterns and fault indicators feature the basin. Hautot et al. (2006) designated the incidence of consistent NW–SE trending sedimentary basin beneath the lava flow at southern and eastern parts of Lake Tana Basin from a magneto-telluric imaging survey. Kebede et al. (2005) hypothesized the presence of Mesozoic sediments beneath the volcanic cover from groundwater geochemistry and isotopic investigation. The landmass of the Lake Tana Basin is covered by two main types of volcanic rocks, the earlier called trap series and the recent Quaternary (Aden series) (Mohr, 1963) (Fig. 4). The trap series covers the area surrounding the lake, and the Aden series covers the area to the south of Lake Tana.

Numerous types of structures in the basin are described as (Sogreah & Geomatrix, 2013; Beshawered et al., 2010) gneissic foliation, schistosity, faults, fractures, folds, and micro shears, among other designations. The fault system of the basin has four distinct sets of linear features trending in NE–SW, NW–SE, N–S, and, rarely, E–W directions. Many subordinate joints and fractures are common in the basin. Beshawered et al. (2010) suggested three phases of deformation (D_1 , D_2 , and D_3) based on structural measurement analyses. The earliest deformation (D_1) is featured by NE–

SW trending tensional stress, resulting in strong regional foliation and schistosity. The second phase of deformation (D_2) is characterized by NE–SW-trending compressional stress-producing micro folds with a NW–SE trending axial trace. The youngest regional deformation event (D_3) is distinguished by its low-angle brittle fracture, representing right-lateral strike-slip fault.

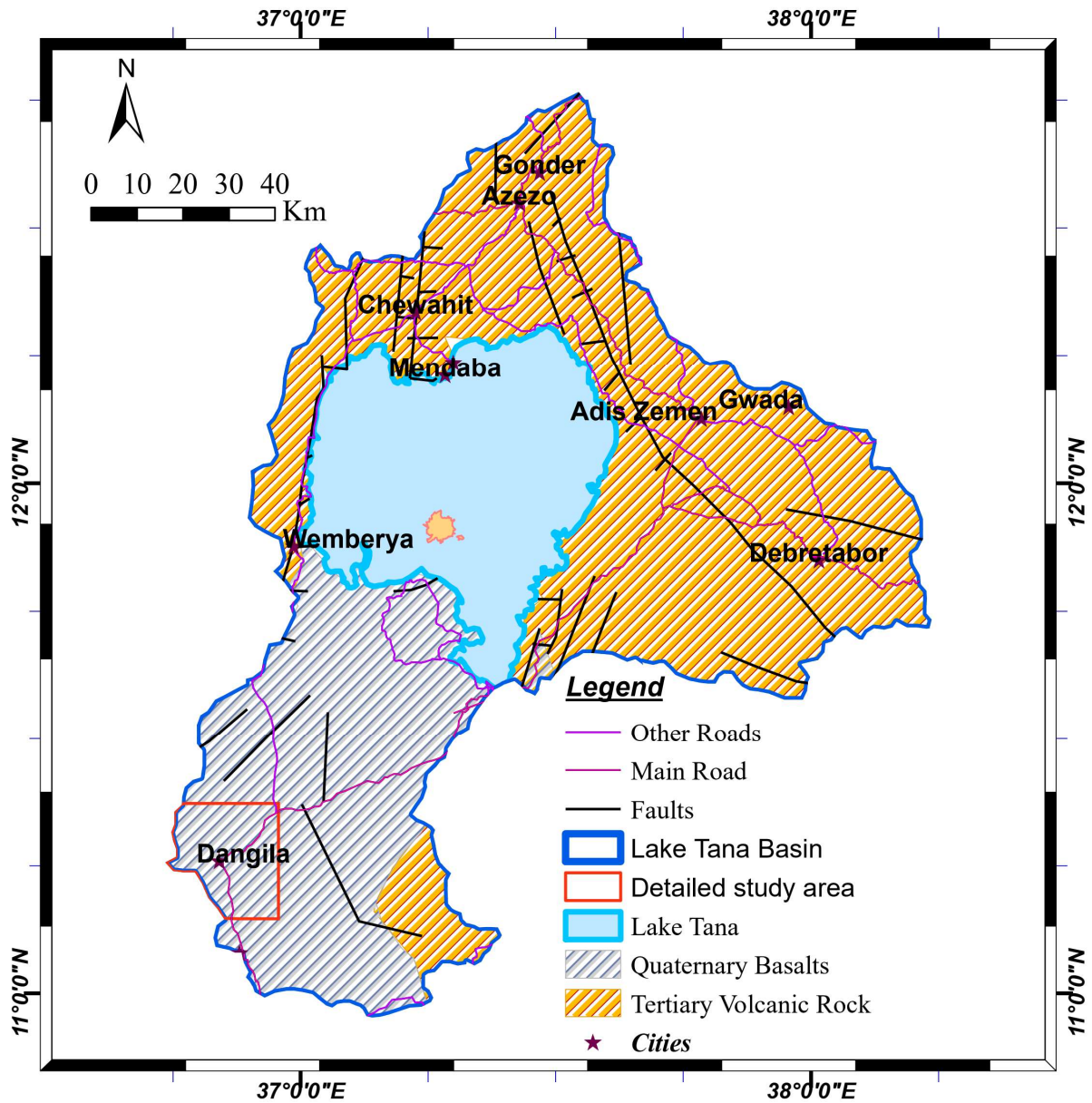


Fig. 4 Geological map of Lake Tana Basin.

Geological setting of the study area: An overview

The Quaternary basaltic lava flow is the main lithological unit covering the study area, although the trap series rock types are highly weathered and can be observed, notably in the eastern part of the area (Fig. 5a). The weathered trap series rocks have a thick cover on the surfaces observed in the southern and eastern parts of the area. Conversely, weathering produces soil and regolith that can extend up to 12-m thickness from the recent Quaternary basalts, scoriaceous basalt, and scoria falls. Information and various studies on basins near the Lake Tana Basin suggest that these volcanic rocks are underlain by Mesozoic sedimentary rocks and a Precambrian basement (Chorowicz et al., 1998; Hautot et al., 2006; Getaneh, 1991).

Quaternary basalts, alluvial sediments, clay soils, scoriaceous basalts, scoria falls, pyroclastic rocks, and ash, all with variable thicknesses and degrees of weathering and fracturing, were encountered at the study site during the drilling of water supply boreholes (Fig. 5b).

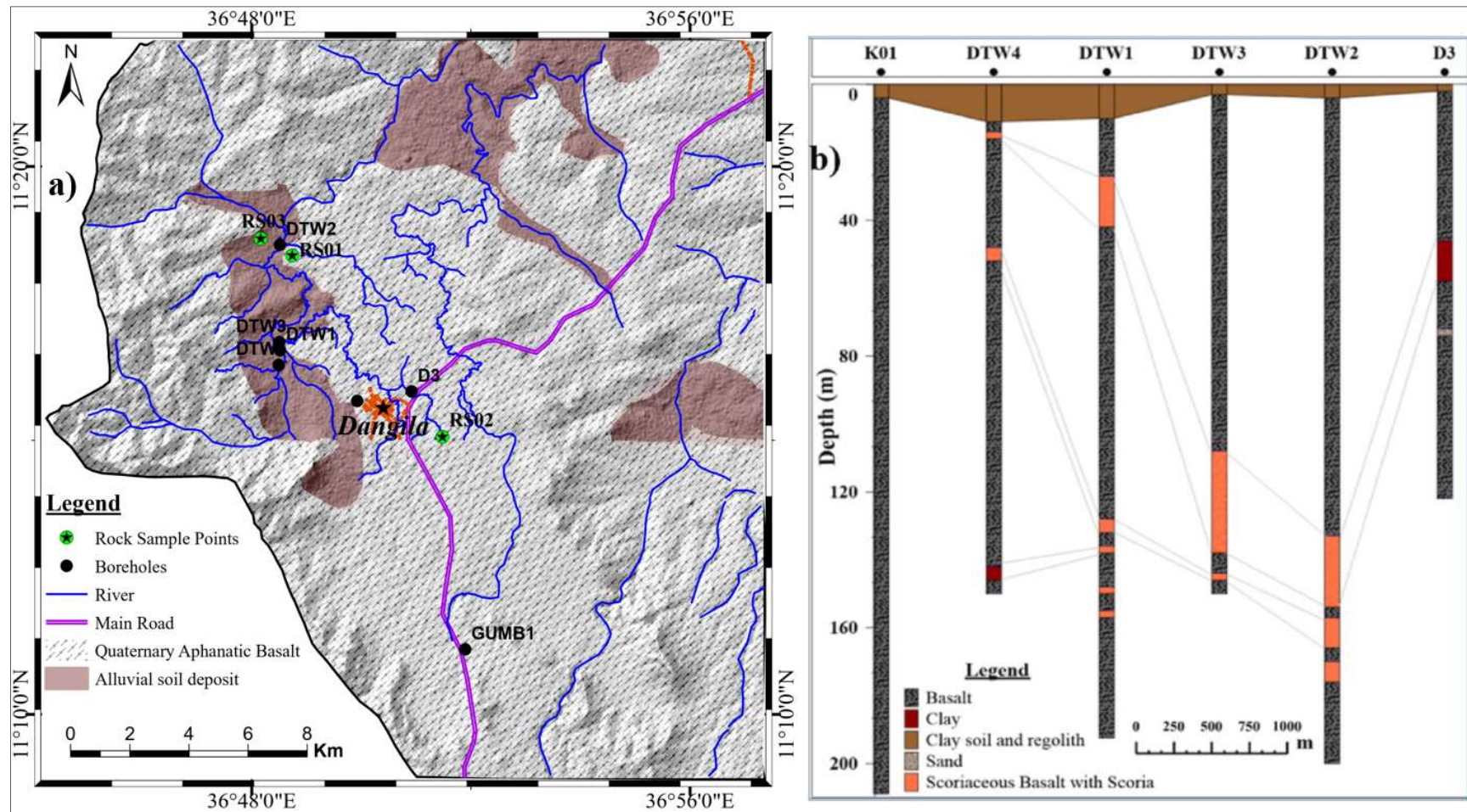


Fig. 5 Geological map of the study area (a) and simplified cross-section selected boreholes located in the map (b).

Quaternary basalts and alluvium deposits dominantly covered the study area with colluvial soils, and weathered tuff covers the subordinate locations. Basaltic rock is characterized as highly vesicular with rounded to elongated vesicles. Quaternary basaltic rocks exposed on the surface and excavated using hand digging at a shallow depth (<2 m) are commonly massive, resembling aphanitic and sometimes vesicular to amygdaloidal texture (Fig. 6). Massive aphanitic basalt is overlain by the weathered regolith, mainly of basaltic origin and clay loam soils. Aphanitic Quaternary basalt is dominantly observed at shallow-depth excavation for construction, whereas few localities exist that are covered with Quaternary vesicular basalts and occasionally amygdaloidal texture when vesicles are filled by calcite.



Fig. 6 Excavated fine-grained basalt from the quarry site along the Dangila to Chara Road (a and b); shallow depth (<2 m) excavated fresh Quaternary basalt in the floodplains (c and d).

Hydrogeological setting-hydrogeology of Ethiopia: An overview

The geological process that shapes the groundwater reservoir's nature determines Ethiopia's groundwater storage and occurrence. The Ethiopian different rock types possess groundwater in various proportions, being the most intricate and stores less water compared to aquifers in the rest of the world. Ethiopia possesses volcanic, sedimentary, metamorphic, and loose sediment aquifers, with volcanic aquifers being the most prominent in areal coverage (Kebede, 2013). However, the estimated aquifer sizes are higher in loose sediment than volcanic aquifers.

Though the geological setting causes challenges in accessibility, most Ethiopian volcanic aquifers are fresh for human utilization. However, there are fluoride effects particularly following the Ethiopian rift valley volcanic aquifers. Groundwater occurrence in the extensive Ethiopian volcanic plateau is in the phreatic form in the weathered zone above the hard rock. This occurrence is semiconfined to the fissures, fractures, joints, cooling cracks, lava flow junctions, and to the intertrapping beds between successive lava flows within the crystalline rocks.

Hydrogeology of Lake Tana Basin: An overview

The Lake Tana Basin geological structures and tectonic activities affect the groundwater systems of the basin. The basin's aquifer system is grouped into four classes: tertiary volcanic (upper basalt sequences and shield volcano) aquifer, Miocene sedimentary aquifer, Quaternary volcanic, and alluvia–lacustrine sedimentary aquifers. The alluvia–lacustrine sedimentary aquifers are located close to the lake; the Quaternary aquifers are found mainly to the south of Lake Tana; the upper basalt sequences and the shield volcano strata aquifers are found to the north and east of Lake Tana. The Quaternary volcanic aquifers are the most productive aquifer of the basin, and are recharged from rainfall, discharged to springs, wetlands, streams and directly to the southern part of Lake Tana (Kebede, 2013; Mengistu et al., 2019). The Quaternary basalt sequence forms a gently undulating morphology that obtains ample rainfall and has mild runoff resulting in a decent direct infiltration from rainfall to the upper aquifer layers.

The basin's location at the northwestern plateau of Ethiopia leads to gain an adequate rainfall than above the average rainfall in the entire Ethiopia. The basin margins receive a higher amount of rainfall and favors to develop a greater thickness of weathered rock and soil used as a shallow groundwater reserve and flow. The shallow aquifer sustains the rural people's freshwater supply accessed by shallow hand-dug wells and springs. SMEC (2008) stated that there is a convergence of groundwater flowing into the lake from all directions, with groundwater flowing from directions mostly consistent with the surface water flow.

Hydrogeological setting of the study area: An overview

The groundwater occurrence of volcanic rocks in the study area under the phreatic condition in the weathered zone above the hard rock and semiconfined to the confined condition at greater depths. The rural people extract groundwater mainly from the shallow aquifer. Three small rivers drain from the southwest of Dangila toward the northwest (Kilti, Amen, and Branti) catchment areas

have been the central area of groundwater extraction for decades. Springs that emerge from weathered and occasionally fractured parts of the Quaternary basalt have meager yields. The principal aquifer layers are several tens or hundreds of meters below the surface, making the abstracting of large quantities of water from hand-dug wells challenging. Groundwater is the primary source of freshwater supply in the area, so drilling boreholes are mandatory to extract a better freshwater yield than shallow wells and springs yield and supply it to densely populated towns. Spring developments, private hand-dug wells, community hand-dug wells, and deep boreholes of 58–209-m depth were the most common groundwater abstraction mechanism in the area (Fig. 7).

Nowadays, the rural community's demand to use groundwater for small-scale irrigation is increasing. However, shallow groundwater systems cannot sustain the demand for every household to have a freshwater supply for drinking and small-scale irrigation. Thus, drilling deep boreholes are becoming mandatory. There are boreholes with a groundwater yield > 30 L/s, although several dry boreholes exist. Generally, the groundwater yield for the existing boreholes varies from 0–30 L/s, depending on their location, depth, and the nature of the groundwater reservoir. Furthermore, the shallow hand-dug wells are exposed to anthropogenic pollution due to improper wellhead construction. Some of the shallow wells are located inside farmland, and anthropogenic pollution due to runoff from the farmland carrying the fertilizers and pesticides has been noted.



Fig. 7 Groundwater abstractions systems (a) typical household shallow hand-dug well, (b) hand pump installed shallow community well, and (c) deep borehole.

2. LITERATURE REVIEW AND THEORETICAL BACKGROUND OF APPLIED METHODS

The groundwater systems of volcanic aquifers have been investigated using various techniques to understand the aquifer characteristics. Geological, hydrogeological, and geophysical approaches have been among the most researched methods for groundwater investigations. The priority of the methods to be applied depends on the aim and objective of the research and the types of aquifer parameters that have to be inferred. Open-source satellite imagery data have been used in groundwater studies to produce digital elevation models, watershed delineation, and geological structure mapping applications (Abdunaser, 2015; Fetter, 2018; Chorowicz et al., 1998). The applications of geographic information systems (GIS) software enables ease of imagery data handling and management of the various data applied for groundwater investigations in a way helpful for making final decisions (Halbich & Vostrovský, 2011). Integrating the results of these methods enables us to better understand and characterize the aquifer system and to model the groundwater flow schemes (Oware, 2020; Francés, 2015).

2.1 Geological review

The geological reservoir is the main component of the aquifer that stores and transmits groundwater. Investigating the geology of a given area from diverse characteristics will help to understand the aquifer properties. Research has used geological information combined with hydrogeology and geophysics to understand the volcanic aquifer propriety (MacDonald et al., 2002; Lachassagne et al., 2014; Violette et al., 2014; Francés, 2015). The analysis of rock type and its mineralogical composition helps in understanding the hydrochemistry of aquifers (Aghazadeh et al., 2017). Detailed geological mapping, structural mapping, and analysis of thin sections of rock samples provide essential information about the geometry and hydrochemistry of the volcanic aquifers (Zhou et al., 2017). The subsurface geological setting is better understood, especially at greater depths, from drill boreholes where they exist. Drill boreholes provide plenty of information about the aquifer property and geology (MacDonald et al., 2002; Lachassagne et al., 2014; Babad et al., 2020). Boreholes information is used as a priori information during near-surface geophysical data modeling, which reduces uncertainty (Hubbard et al., 1997).

2.2 Hydrogeological review

Hydrogeological investigation techniques are decisive to understand the aquifer system (Fetter, 2001). Hydrogeological studies are helpful to estimate potential groundwater sites, aquifer geometry, hydraulic conductivity, porosity, transmissivity, etc. Winter et al. (1998) used water table maps of shallow unconfined aquifers to estimate the groundwater flow direction. In contrast, Charlier et al. (2011) use volcanic aquifer pump test data to determine the hydraulic property and transmissivity of aquifers located at different depths.

The hydrochemistry data enables groundwater suitability for drinking and irrigation uses (Li et al., 2014). Demlie et al. (2008) and Vivona et al. (2007) used hydrochemistry analysis of volcanic aquifers to determine the groundwater quality and its hydrochemical evolution. The hydrochemistry and hydrogen–oxygen water-stable isotopes data have been used widely to assess groundwater recharge sources and flow patterns (Ayenew et al., 2008). The results will generate scientific information for volcanic hydrogeology and support the sustainable management of the groundwater. Furthermore, groundwater stable and radiogenic isotopes have been used in hydrogeological investigations to estimate recharge and discharge areas, residence time, age, and intermixing of various aquifers from different sources (Xinyan et al., 2018; Hernández-Antonio et al., 2015; Kebede, 2004).

Constructing a conceptual model using pre-determined study results will help manage the aquifer systems better. A study by Teresita et al. (2012) described the various hydrogeological model types. Hydrogeological conceptual models have been used to conceptualize the groundwater flow and storage property of volcanic aquifers that can help to manage the groundwater system (Lachassagne et al., 2014; Violette et al., 2014; Join et al., 2005; Walker et al., 2019a; Izquierdo, 2014).

2.3 Hydrogeophysics review

Geophysical techniques have been applied to solve hydrogeological problems from a decade ago. They have been used to understand the groundwater reservoir type, geometry, depth, and thickness of the aquifer layers. Integration of various geophysical techniques has been applied to understand hydrogeological problems better. Hydrogeophysics uses geophysical methods to estimate complex subsurface hydrologic properties, to monitor hydrologic processes, groundwater flow, and transport processes, and to provide quantitative information over field-relevant spatial scales (Susan Hubbard & Linde, 2011). The flow and alteration of fluids in the shallow subsurface are governed by interactions between physical, biological, and geochemical processes occurring in

highly heterogeneous and often variably saturated soils, sediments, and bedrock compartments (Binley et al., 2015). Hydrogeophysics provides a suite of techniques that helps in understanding these complex interactions that are difficult to observe by quantifying the structure and functioning of the shallow subsurface. Saribudak & Hawkins (2019) used multi-geophysical methods to comprehend the character of fault, sinkhole, and karstic features on groundwater flow and the potential connection between the aquifers.

Conventional techniques for characterizing hydrogeological properties (including pumping, slug, and flowmeter tests) naturally depend on borehole access, and their spatial extent is limited to the vicinity near the wellbores. Applying such techniques can provide inferences of only limited information about subsurface flow and transport (Hubbard & Linde, 2011). However, the geophysical methods are less invasive than drilling or excavation (Jougnot, 2020) and cover a better spatial range than conventional techniques. Geophysical methods are used for groundwater explorations in diverse geological settings, and several aquifer parameters can be inferred (Binley et al., 2015; Binley et al., 2010; Hubbard & Linde, 2011). When hydrogeophysical data are closely examined, they enable us to infer the aquifer parameter and fluid state (Hubbard & Linde, 2011). Hydrogeophysical surveys, primarily obtained from the borehole and near-surface geophysical surveys, are helpful to determine the water quality and reservoir character of both fresh and saline water aquifers (Collier, 1993). The geophysical methods commonly used for shallow subsurface characterization and estimation or inversion modeling methods are used to integrate hydrological and geophysical measurements and quantify subsurface architecture that influence flow; delineate anomalous subsurface fluid bodies; monitor hydrological processes; and estimate hydrological properties and state variables (Hubbard & Linde, 2011). Geomagnetic and electrical resistivity techniques are among the geophysical methods that provide adequate information about groundwater.

2.3.1 Direct current (DC) resistivity

The direct current electrical resistivity method is a family of active geoelectrical techniques discovered by the Schlumberger brothers a century ago (Schlumberger, 1912). It has been widely used in groundwater exploration to map potential groundwater places, locate productive drilling sites, and to correlate between the electrical properties of the geological formations and their fluid content (Ogilvy, 1970; Zohdy et al., 1974; Slater, 2007; Oware, 2020). They are used to determine the geometry of the aquifer system (Robain et al., 1995) and to determine the subsurface geological structure in which the water exists, such as fracture, joint, etc.

The DC resistivity method that relies on Ohm's law is applied to a broad hydrogeological problem. The DC field experiment involves injecting a current into the ground, creating an electrical potential, which is measured using pairs of electrodes–receivers placed on the surface or in boreholes. The measurement of the resulting electrical potential differences enables the determination of the electrical resistivity or its reciprocal, the electrical conductivity of the medium. The electrical conductivity of a medium is strongly affected by the subsurface properties, including texture, structure, lithology, fluid saturation, and pore water chemical compositions (Journot, 2020).

The current density in any direction within a material is given by the negative partial derivative of the potential in that direction divided by the resistivity. Suppose we consider a single current electrode on the surface of a medium of uniform resistivity \mathbf{r} (Fig. 8a) and completed by a current sink at a considerable distance from the electrode. Current flows radially away from the electrode so that the current distribution is uniform over hemispherical shells centered on the source. The hemispherical shells in Fig. 8a mark surfaces of constant voltage and are termed equipotential surfaces. If the current sink is a finite distance from the source, the potential V_C at an internal electrode C is the sum of V_A and V_B 's potential contributions from the current source at A and the sink at B (Fig. 8b). Therefore, the potential difference between its two points is given by

$$\Delta V = V_C - V_D = \frac{\rho I}{2\pi} \left\{ \left(\frac{1}{r_A} - \frac{1}{r_B} \right) - \left(\frac{1}{R_A} - \frac{1}{R_B} \right) \right\} \quad (1)$$

The apparent resistivity (ρ_a) for the homogenous ground is given by

$$\rho_a = \frac{2\pi\Delta V}{I \left\{ \left(\frac{1}{r_A} - \frac{1}{r_B} \right) - \left(\frac{1}{R_A} - \frac{1}{R_B} \right) \right\}} \quad (2)$$

Equation (2) is the basic equation for calculating the apparent resistivity for any electrode configuration (Kearey et al., 2002).

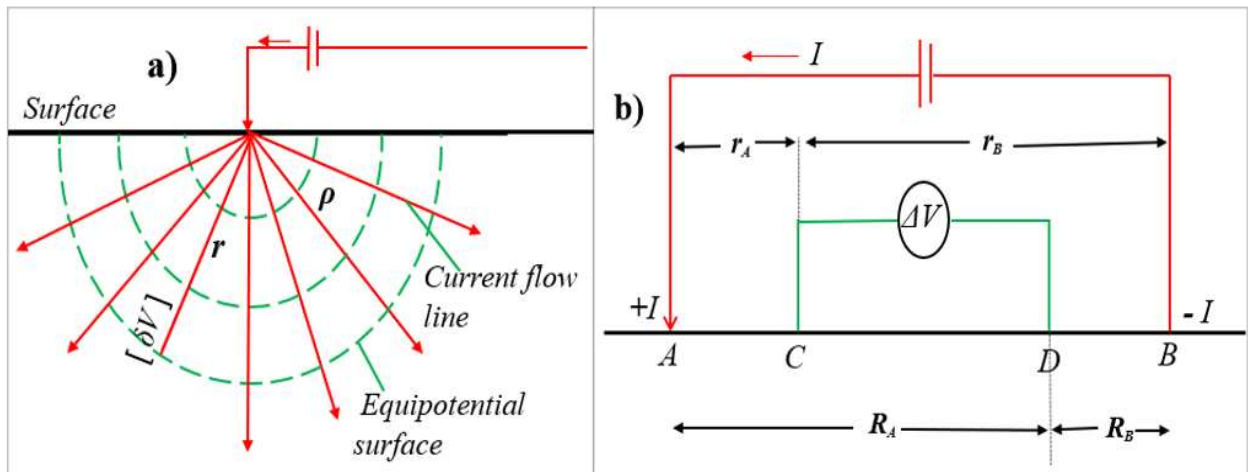


Fig. 8 Current flow from a single surface electrode (a) and the generalized form of the electrode configuration used in resistivity measurements (b). Modified from Kearey et al. (2002).

Vertical electrical sounding

Vertical electrical sounding (VES) is used primarily to study horizontal or near-horizontal interfaces with current, and potential electrodes maintained at the same relative spacing. The whole spread is progressively expanded about a fixed central point. Accordingly, readings are taken as the current reaches progressively greater depths, mainly employing the Schlumberger configuration. The Schlumberger configuration uses the inner potential electrodes and has a spacing of 2ℓ , which is small compared to the out current electrodes $2L$ (Fig. 9).

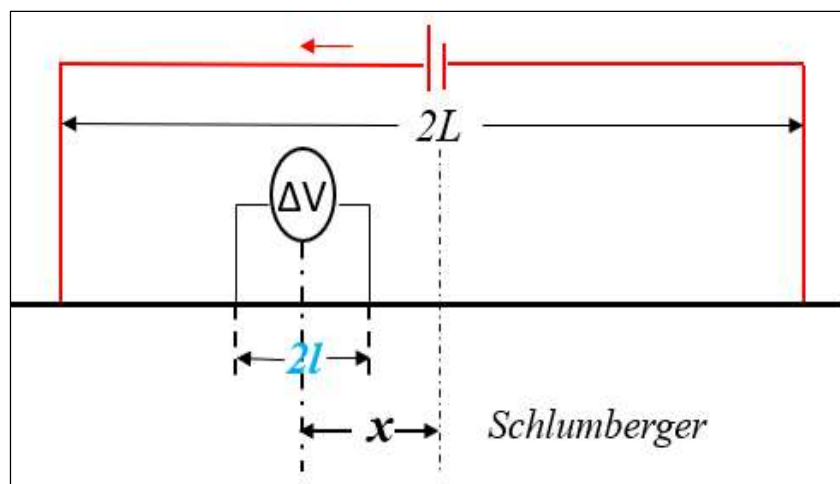


Fig. 9 Schlumberger electrode configurations for VES survey. Modified from Kearey et al. (2002).

During VES surveys, the potential electrodes remain fixed, and the current electrodes are expanded symmetrically about the center of the spread. In conjunction with substantial L's values, it may be necessary to increase ℓ to maintain a measurable potential. For such electrode spreads, the apparent resistivity is given by

$$\rho_a = \frac{\pi(L^2 - x^2)}{2\ell(L^2 + x^2)} \frac{\Delta V}{I} \quad (3)$$

where x is the separation of the mid-points of the potential and current electrodes. When used symmetrically, $x = 0$, so

$$\rho_a = \frac{\pi L^2}{2\ell} \frac{\Delta V}{I} \quad (4)$$

The apparent resistivity values will be changed into the true resistivity of layers, their depth, and their corresponding thicknesses using modeling techniques.

2.3.2 Geomagnetism

The geomagnetic technique obtains information related to the Earth's magnetic field's direction, gradient, or intensity. The intensity of the magnetic field at the Earth's surface is a function of the location of the observation point in the primary Earth magnetic field and of contributions from local or regional variations of magnetic material such as magnetite, the most common magnetic mineral. After correcting for the effects of the Earth's natural magnetic field, magnetic data can be used to understand hydrogeological problems. It helps locate lateral boundaries of volcanic aquifers or faults, fractures, and other weak volcanic geological settings.

The geomagnetic surveys are helpful to map the aquifer geometry, including faults, folds, and fractures that can be used as a conduit for groundwater flow and storage. In addition, it is widely applied to map the depth to bedrock, mostly found below the porous layer (Aboelkhair & Rabei, 2013). Moreover, when two or more geophysical techniques are combined, it helps to reduce uncertainty or the risk of pointing to a dry well selection site (Gbenga et al., 2015; Al-Garni, 2011).

2.3.3 Fiber optic and its basics

The use of fiber optic cables as a sensor in geophysical applications was heightened and experimented within the oil and gas industries. Fiber optic cables have been tested as distributed single-parameter detectors and multiparameter hybrid sensors for near-surface and borehole geophysical surveys. Its applications and capacity in geophysics and hydrogeophysics have not yet been fully

explored. The basic science, technology, working principle, and future opportunities in geophysics and hydrogeophysics are reviewed (Fenta et al., 2021).

The capacity of a fiber to be used as a sensor is its most convenient characteristic. When a fiber is used as a sensor, a light beam is converted into an electrical signal. The sensor measures the physical parameters of the light and translates the information into an output read by an instrument (Fig. 10a). The combination of the input and output circuitry, light sources, detector, and fiber optic cable enables data transmission over distances on the order of miles in light pulses through the optical fiber. A single thin optical fiber consists of three primary components: the core, the cladding, and the coating or buffer (Fig. 10b and c). Light propagates primarily along with the fiber core. The core-cladding arrangement creates an optical waveguide that confines the light in the core by total internal reflection at the core-cladding interface. The light traveling through the optical fiber carries information in the same manner as an electrical transmission copper conductor, and data transmission occurs at 99.7% of the speed of light in a vacuum (Rajpoot et al., 2017).

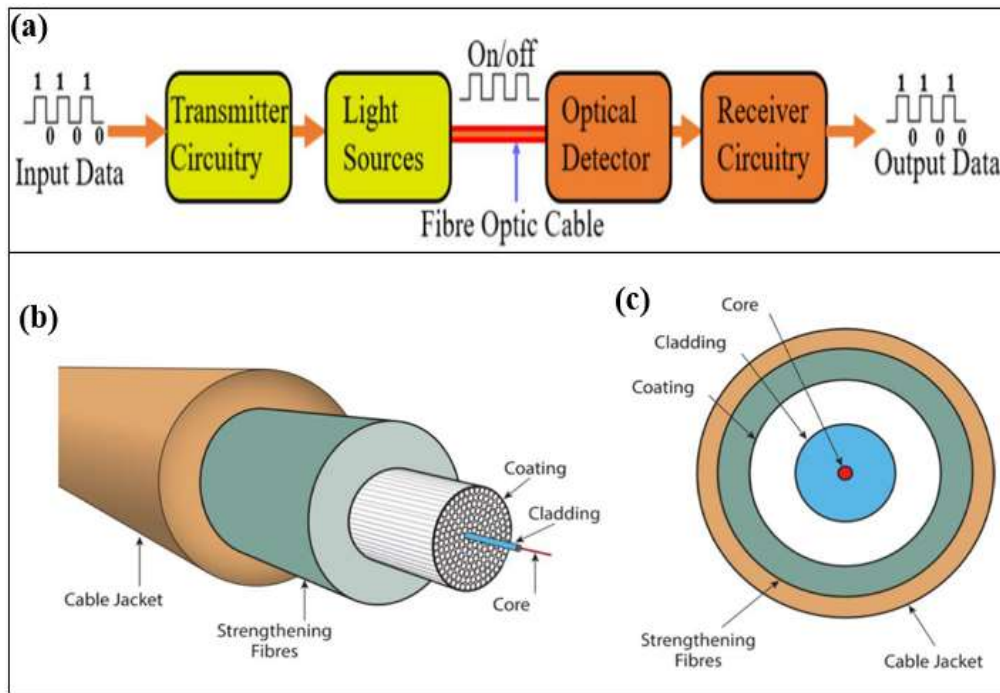


Fig. 10 Optical fiber data transmission framework(a), the basic structure of an optical fiber (b), and the internal structure of an optical fiber (c). Modified from (Elprocus, 2019; Fidanboylyu & Efendioglu, 2009; Media, 2019).

Fiber optic sensors are generally applied as point sensors or distributed sensors in geophysics. Fiber optic geophysical sensors, which are field-tested and show improvements in several aspects of

geophysical problems, are developed based on one of three types of back-scattering of light (Rayleigh scattering, Brillouin scattering, Raman scattering) or fiber Bragg gratings (FBGs). Back-scattering-based distributed fiber optics geophysical sensors (DFOGSs) measure physical parameters along the length of the fiber. DFOGSs can vary based on the scattered light type, the sensor's operating principles, the parameters to be measured, the spatial resolution, the time needed to acquire data, the light signal applied, and other factors.

The use of this technology enables the simultaneous detection of multiple physical parameters, providing various aquifer parameters in hydrogeological investigations. Its capability to integrate more than two fiber optic sensors to simultaneously detect two or more physical parameters (Karrenbach et al., 2019; Muanenda et al., 2016; Zhang et al., 2016) is a tremendous advantage. Therefore, fiber optic sensors will unquestionably be utilized in future groundwater resource exploration and management studies.

Moreover, computing and extensive data handling techniques will help interpret comprehensive data from long-distance fiber optic arrays. Among several big data handling techniques, artificial intelligence (AI) is a recent and helpful method to enhance the performance of future distributed fiber optic geophysical sensing systems through big data generation, artificial neural networks, and deep learning (Perol et al., 2018; Shiloh et al., 2018). Maximum sensitivity of fiber optic cables, an option to measure one or more physical parameters, a higher operating temperature, and enhanced coatings for both protection and sensitivity (Rehman & Mendez, 2012) are attractive capabilities in near-surface and borehole hydrogeophysical applications in the near future.

3. MATERIALS AND METHODOLOGICAL PROCEDURES

Multidisciplinary data sources and interpretation approaches are employed to achieve the desired goal and objectives and to characterize volcanic aquifers. The data are mainly gathered from the field surveys and laboratory analysis and limit causes from previously conducted projects and open data sources. The overall progress of the research followed a stepwise method to characterize the volcanic aquifer. The stepwise/hierarchical procedures used for data collection and interpretation of results can be summarized into three categories; preliminary/reconnaissance, intermediate/detailed investigations, and final/hydrogeological conceptual model development (Fig. 11). Each step, in turn, comprises various data sets that can be categorized as geological, hydrogeological, and geophysical, each with multiple data types. These procedures are followed to characterize the

volcanic aquifer system of the area, groundwater occurrence, groundwater potential, relative residence time, and quality and to infer aquifer parameters. Finally, the result is used to develop a conceptual hydrogeological model that can help to manage the volcanic aquifer of the area. The details of the stepwise procedures and the individual methodologies followed are:

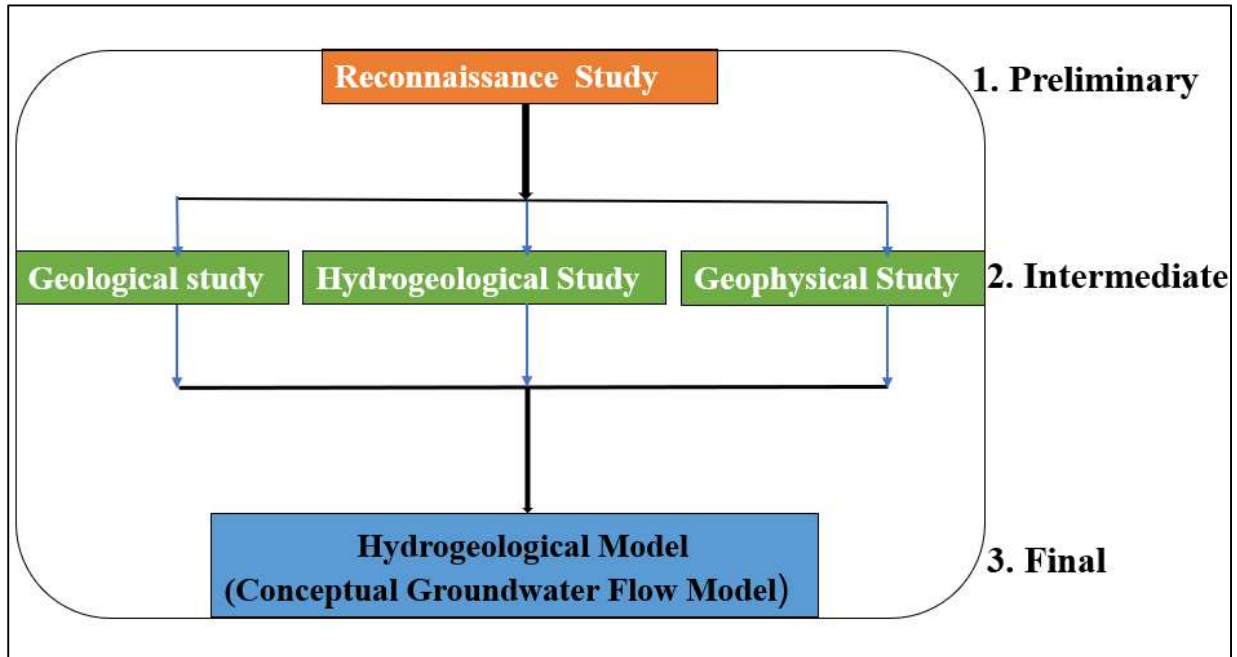


Fig. 11 Stepwise/hierarchical methodological flow chart.

3.1 Preliminary/Reconnaissance Study

The preliminary step consists of the reconnaissance study to define the study area boundary and waterpoints, to assess the existing boreholes, hand-dug wells, springs, and rivers, and to identify the geophysical survey lines. The previously conducted research has been reviewed, and information has been gathered. It contains both pre-field office work and short-duration field observations works. It is the basic step to frame the scope of the study and limit the required time resources for detailed investigations, and to plan what type and quantity of outputs are required to achieve the desired goal and objectives. The reconnaissance study is a common step in Earth resources explorations and characterization studies in hydrogeology (Hussain et al., 2020; MacDonald et al., 2002).

The Landsat-7 satellite images have been downloaded from the United States Geological Survey (USGS) explorer. The digital elevation model has been prepared, which helps to infer possible

surficial structures that emphasize near-surface geophysical survey design. The area's geomorphology and prevailing drainage pattern have been examined from three-dimensional (3D) global maps and satellite images in conjunction with a topographic map to define the study area. A preliminary field investigation was carried out to overview the area's geological, hydrogeological, and geomorphologic setup and to assure whether the existing features delineated in the office exist in the field.

3.2 Intermediate/Detail Investigation

The intermediate or detailed investigations step, comprising data collection from the field and analysis or delivery of samples to the laboratory works, as well as analysis of the results, have been conducted for various types of inquiries. The various data collection and analyses from different sources are geological, hydrogeological, and geophysical data sets.

a) Geological Data Set

The geological investigation comprises rock type identifications, outcrop sample collections, lithological log collections from previously drilled boreholes, thin sections preparations, and an ore microscope analysis. The area has more than 24 deep boreholes (58–210-m depth), and their lithological information has been collected. The information is vital to identify the possible groundwater reservoir rock types and their characteristics. During near-surface geophysical data modeling, the borehole lithological information has been used as a priori information. It has also been used to construct geological/ geoelectric sections and to support geological maps. Three rock outcrop samples have been analyzed at the University of Szeged Mineralogy, Geochemistry, and Petrology Laboratory for mineralogical composition and rock structure on a microscopic scale. Standard rock sample thin sections were prepared and analyzed using Ore and Raman microscopes. The thin section analysis result is used as information to understand the sources for variations in the hydrochemistry of the groundwater.

b) Hydrogeological Data Set

The hydrogeological data set comprises several data types: hydrochemistry (physical–chemical), water-stable isotope, boreholes pump test, groundwater yield, and piezometric water levels. The temperature, pressure, sunshine, the amount of recharge and discharge, and other valuable parameters are reviewed from previously conducted research.

Pump test

The constant rate pumping test data from four selected boreholes were analyzed using the Moench fracture flow model (Moench, 1984) to estimate the aquifer hydraulic parameters. It is not common practice to conduct pump tests following drilling work in shallow hand-dug wells in Ethiopia. The woreda water bureau estimated the yield of shallow hand-dug wells and springs using a constant yield container (water removal) system for a few hours. The hydraulic parameters of representative shallow wells are deduced from previous research.

Hydrochemical analysis

A total of 25 water samples from the deep and shallow aquifer (boreholes, shallow wells, and springs) were collected during the dry seasons (February to April) in 2016 and 2017. The water sampling was focused on the shallow and deep aquifer systems hydrochemical analysis. A two-liter water sample at each of the sampling points was collected; representative samples from 14 shallow wells, seven deep boreholes, and four springs were collected, which could represent the area close to the Dangila town in the upper Branti and Kilti river catchments (Fig. 12). The new plastic bottles were rinsed with the sample water, and groundwater samples were collected, stored in a cool place, and transported to the laboratory. The samples were taken after pouring water for a few minutes and were filtered with a 45-micron filter to remove the suspended particles before laboratory analysis. The samples were separately labeled with sample identification (ID) and water schemes.

The potential hydrogen (pH), electrical conductivity (EC), and total dissolved solids (TDS) were analyzed in the field using a pH/EC/TDS multiparameter measuring instrument (Hanna HI 991,301, USA). When conducting measurement of EC/TDS, the probe was placed in the sample water to be tested, and plastic beaker containers were used to minimize any electromagnetic interference. The values of EC, TDS, and temperature were taken after the temperature sensor reached thermal equilibrium. The meter was regularly calibrated for pH by immersing the probe in pure water with a neutral pH of 7.0 before pH measurements.

The samples were analyzed for physical and chemical parameters at Amhara Water Works Design and Supervision Enterprise Laboratory, Ethiopia. The physical parameters measured in the laboratory included pH, EC, and TDS. The chemical parameters analyzed in the laboratory comprised cations of calcium (Ca^{2+}), magnesium (Mg^{2+}), sodium (Na^+), potassium (K^+), iron (Fe), manganese

(Mn^{2+}), and anions of bicarbonate (HCO_3^-), sulfate (SO_4^{2-}), carbonate (CO_3^{2-}), chlorine (Cl^-), nitrate (NO_3^-), fluoride (F^-), and boron (B).

The atomic absorption spectrometry (AAS) (novAA 400P, Germany) integrated with ASPECT LS software was used to measure the concentration of cations, and the colorimetry instrument (Pal-intest photometer 7100, UK) was used to measure the concentration of anions. As an alternative, the concentration of carbonate and bicarbonate measurements were analyzed using titration too.

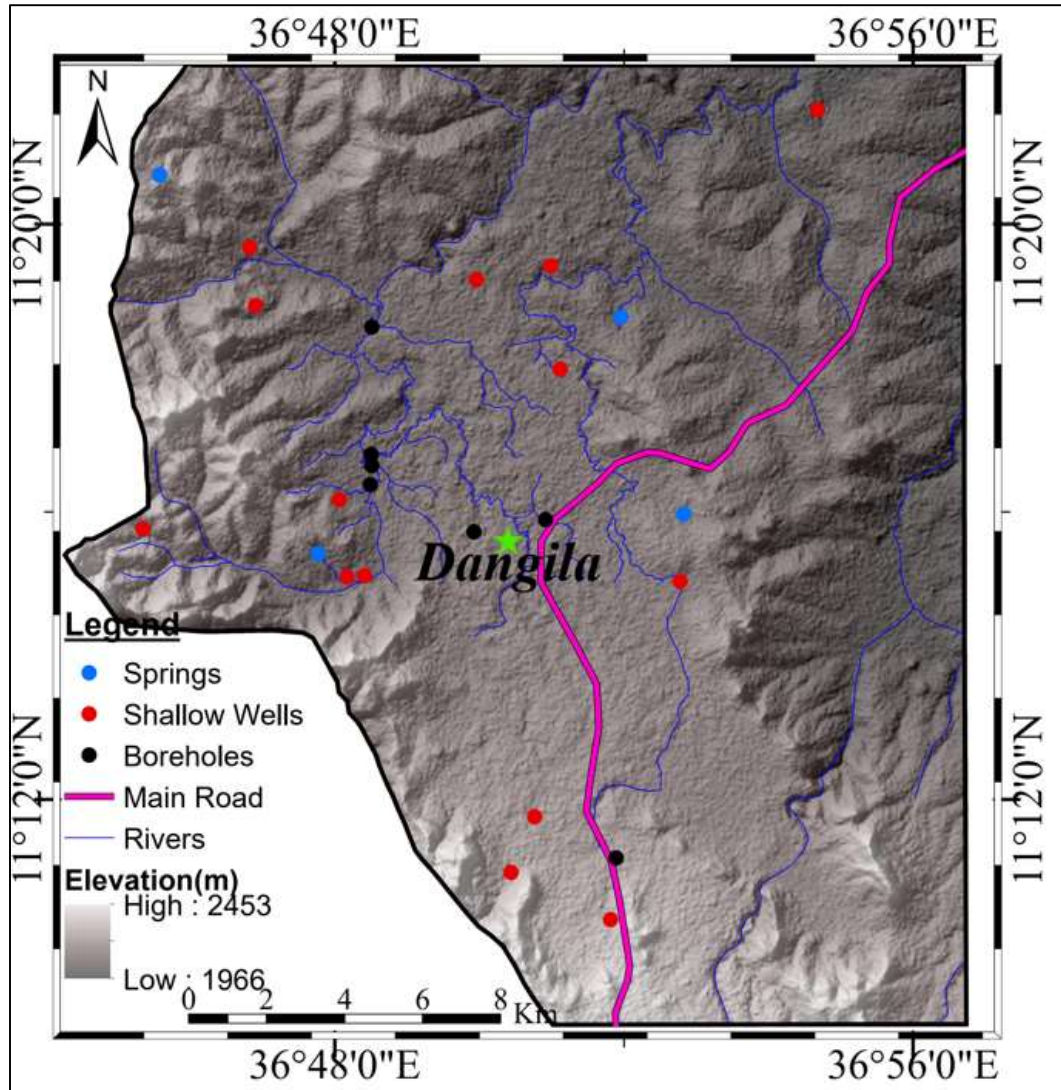


Fig. 12 Groundwater sample locations collected for hydrochemical analysis.

The laboratory analysis of water sample results was used to determine and examine variations in groundwater facies and in major cation and anion sources. Moreover, water sample data were used to assess the groundwater quality for human consumption. The calculated sodium adsorption ratio

(SAR), Na%, and the residual sodium carbonate (RSC) values were used to determine the overall groundwater quality for irrigational uses.

Water-stable isotope analysis

The seasonal water samples for water-stable isotope analysis were collected during autumn 2019 (September–October) and spring 2021 (March–April). The two sampling times were chosen to consider the heavy summer rain and the winter dry season, which enabled observation of the seasonal variations in the heavier water isotopes content.

The sampling was focused on the shallow and deep aquifers systems, surface water systems, and rain. Therefore, during the two-season water sample collections, 50 ml water samples with a centrifugal vial from each sampling point were collected and analyzed for water-stable isotopes (^2H & ^{18}O) at Debrecen Atomica Isotope Laboratory in Hungary. A total of 48 samples were collected within two seasons from shallow wells, boreholes, springs, rivers, and rain with new plastic centrifugal vials, 50 ml in size (Fig. 13). The new plastic vials were rinsed with the sample water, filled with water, stored in a cool place, then packed and transported to the Debrecen Atomica Isotope Laboratory. The samples were separately labeled with sample identification (ID) and water schemes, such as SP₁, to represent spring water sample no.1 in the field. The stable water isotope (^{18}O and ^2H) was analyzed in the laboratory using Thermo fisher, and the results were used to delineate the origins of recharge, perception, and discharge areas.

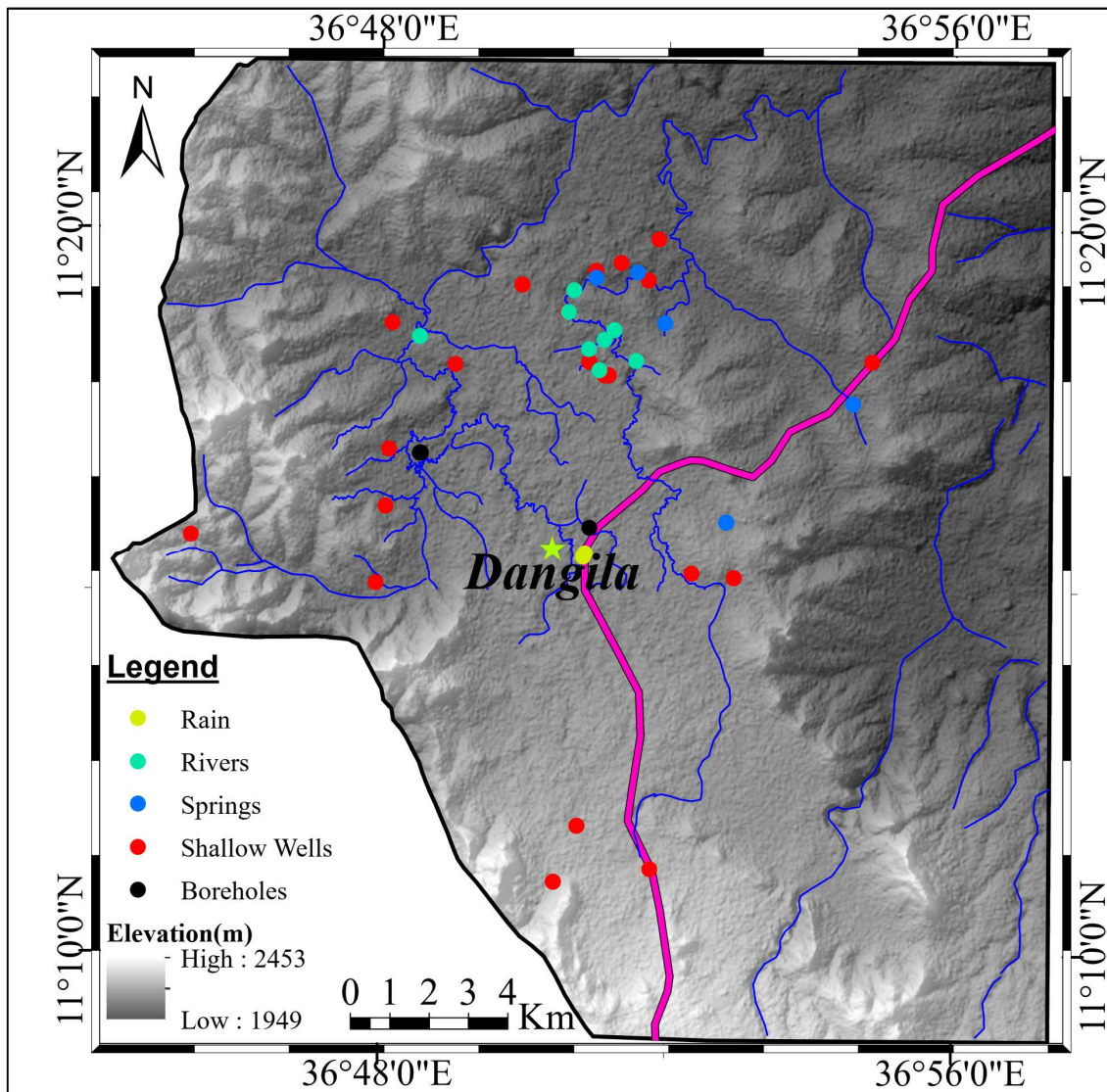


Fig. 13 Water-stable isotope sampling point locations with various water schemes.

c) Geophysical Data Set

The geophysical survey comprises of the VES and the near-surface geomagnetic surveys. The geophysical surveys were designed considering the study's objectives, geomorphologic setting, accessibility, time, the previously surveyed area, and the deep borehole field site locations.

Vertical electrical sounding survey

The VES techniques have been chosen because of their efficiency in surface electrical resistivity data acquisition. They require fewer corrections and involve easier filtering procedures than the potential geophysical methods (McDowell et al., 2002; Milsom, 2003; Reynolds, 1998; Telford et

al., 1990). The VES survey mainly covered the floodplain area close to the Dangila town and toward the northwest of the Denegeshita kebele. The additional 16 VES data collected by different survey companies around the Dangila town water supply deep borehole field were gathered from Amhara waterworks, Design and supervisions Bureau. In contrast, the primary 16 VES data were collected from February to April 2017 and in 2020. Therefore, a total of 32 of VES data were taken, using the Lud company product ABEM SAS 4000 terametre, along transects, traversals to streams, and expected structures.

The standard Schlumberger sounding cable set consists of $2\text{ m} \times 750\text{ m}$ current and $2\text{ m} \times 250\text{ m}$ potential long multicore high conductivity cables that have been used to connect the instrument to the current and potential measuring electrodes (Fig. 14). Additionally, two pairs of stainless steel electrodes (one pair as potential and one pair as current), $2\text{ m} \times 2\text{ m}$ connector cables and clips, hammers, tape meter, and handheld GPS for VES locations were used. The survey layout and the data location were designed, enabling the map of structures and groundwater potential areas.

ABEM SAS 4000 terametre's transmitter enables sending out well-defined and regulated signal currents, with strengths up to 1000 mA and voltages up to 400 V, limited by the output power of 100 W (ABEM, 2009). The current amplitude can vary from 1 to 1000 mA, depending on the field conditions. The SAS 400 terametre enables deep-penetration resistivity with an output sufficient for a current electrode separation of up to 2000 m. The receiver discriminates noise and measures voltages correlated with the transmitted signal current for resistivity surveying mode with a resistivity single reading resolution of 0.02 m Ω . The resistance values for each current and potential electrode spread are read out from the instrument, and their corresponding apparent resistivity values are calculated using the appropriate geometrical factor constants. The Schlumberger electrode spread extending AB/2(m) from 1.5 m (minimum) to 500–750 m (maximum) is used to investigate the groundwater potential extending from a maximum depth of 200–500 m.

The measurements at each survey point took 1–2 h, making it challenging to cover several data points. Resistivity surveys are usually restricted to relatively small-scale investigations because of the labor involved in physically planting the electrodes before each measurement. For this reason, resistivity methods are not commonly used in reconnaissance surveys (Kearey et al., 2002). The 32 VES points locations are concentrated around the flood plain, which has better potential groundwater at higher depths than the mountain fronts (Fig. 15).

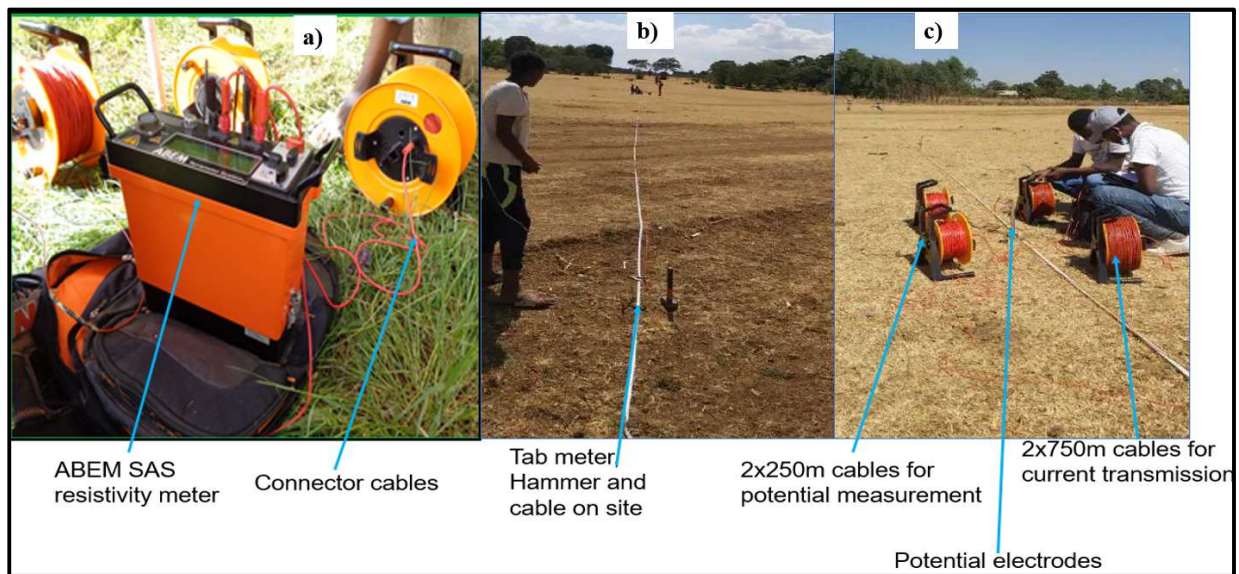


Fig. 14 Photographs of resistivity equipment and field layout. (a) ABEM SAS resistivity meter components and (b) and (c) VES survey layout during data collection.

The filtered 32 points VES data, each with 19 to 20 recordings, have been plotted on log-log paper to check the data adequacy, apply corrections, and smooth the data for further processing. The subsurface layer parameters (resistivity and thickness) were initially conducted using the manual interpretation technique matching the plotted field curves with two-layer master curves and the generalized Cagniard graphs (Koefoed, 1960; Orellana & Mooney, 1966). The results were used as an initial model to produce the final model using WINRESIT(Vander, 2004). Information from nearby boreholes has been used to minimize errors during modeling due to equivalence and superposition. The median depth terminology explained by Edwards (1977) and later experimentally supported by Barker (1989) has been used to determine the depth of investigation during 1D modeling. The results of 1D inverse modeling have been used to construct 2D sections, plain maps, sliced depth maps, three-dimension (3D) volumes, and 3D sliced depth and image maps. This enables visualizing and estimating the aquifer geometry and characterizing its variation, along with horizontal and vertical extent and 3D space.

Ground geomagnetic Survey

A magnetic survey has been undertaken to investigate subsurface geology based on anomalies in the Earth's magnetic field resulting from the magnetic properties of the underlying rocks. The survey results aim to map and model geological structures possibly used as a conduit for groundwater movement. It is a rapid and cost-effective technique, and it represents one of the most widely used

geophysical methods (Paterson & Reeves, 1985). The geomagnetic survey lines were planned based on the VES survey lines, borehole field, accessible roads, and previous information about the structural and georgical setting of the area. When geomagnetic data are collected, attention was paid to avoid the effect of manufactured ferrous objects that can equally generate magnetic anomalies.

The GSM-19T proton precession magnetometer, which is among the most commonly used for surface surveys and observatory geomagnetic field monitoring instruments, has been used for field data collection. The magnetometer setup includes a liquid-filled sensor, the coaxial sensor cable, a console with all electronic circuits, a sensor mounting stick, and power-input/output connectors (Fig. 15).

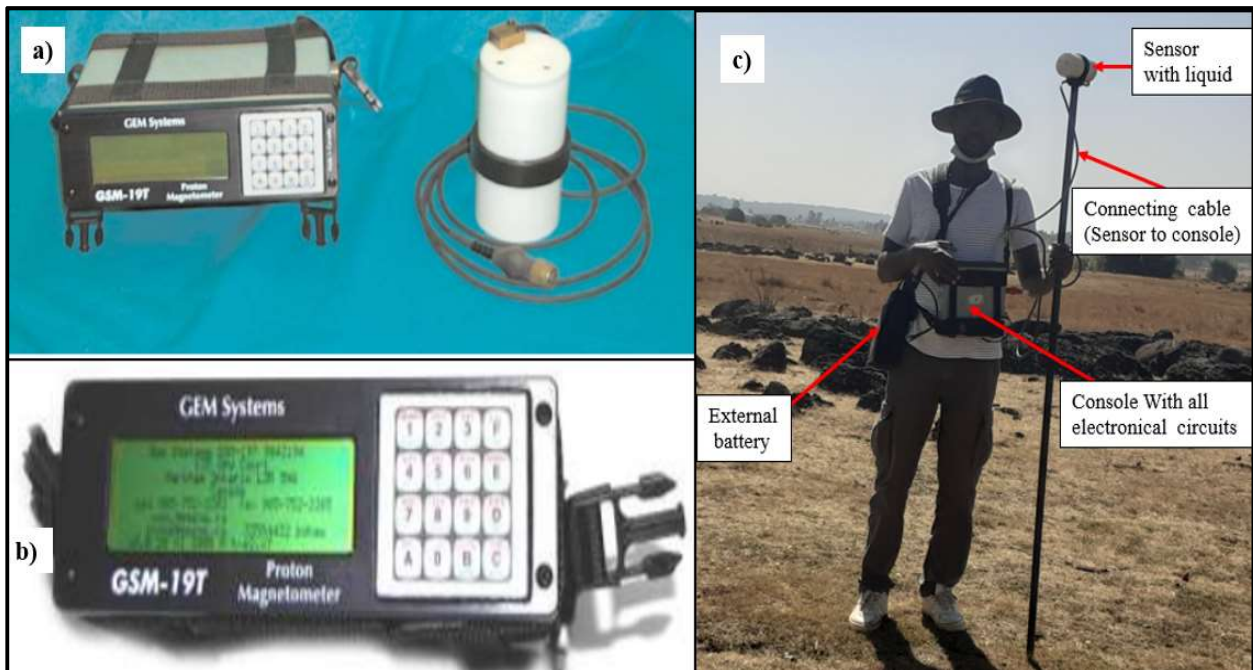


Fig. 15 GSM-19T proton precession magnetometer components. Sensor, console, radio frequency cable, shoulder harness, the display screen on the console circuitry (a and b) and the field setup (c).

The GSM-19T is a versatile and easy-to-use instrument for subsurface investigations and exploration. It is a multipurpose and accurate magnetometer for ground geophysical surveys to measure the Earth's magnetic field. The magnetometer has an absolute accuracy of ± 0.2 , a sensitivity of 0.15 nT, a resolution of 0.01 nT, a dynamic range of 20,000–120,000 nT and an operating temperature range of -40°C to $+50^{\circ}\text{C}$ (GEM, 2008).

Ground magnetic surveys were performed with station spacing of 50, 100, and occasionally 200 m, depending on the expected magnetic gradients and target structures. The total geomagnetic field

of the Earth was recorded at 718 discrete points along pre-selected traverses (Fig. 16). Readings were not taken in the vicinity of metallic objects such as cars, fencing, houses, etc., that might perturb the local magnetic field. Likewise, when GSP-19T magnetometer operations took place on the field, the operator removed any metallic objects, and base station readings were taken every 1–2 h to monitor diurnal variations. The sensor of the instrument was oriented north-south by keeping the orientations line of the sensor in a horizontal (east–west) position to keep the sensor axis approximately at right angles to the magnetic field to obtain the best signal. When large changes in the measured geomagnetic field were encountered between successive readings, a repeated reading was taken to get the accurate value at the measuring point. Even though the GSM-19T enables researchers to take the global position system(GPS) coordinates of each reading point, they were taken by handheld GPS, and the corresponding time is recorded separately.

Magnetic data is reduced to remove all magnetic variation causes from the observations other than those arising from the magnetic effects of the subsurface. Diurnal variations are recorded using the repeated readings on the base station. However, when the most erratic readings vary more than 1000 nT values on the same reading points, data recording is stopped until a storm is eliminated. After the diurnal and geomagnetic corrections have been applied, all remaining magnetic field variations are caused exclusively by spatial variations in the magnetic properties of the subsurface rocks called magnetic anomalies. The total geomagnetic field variations of the area were observed with 2D plan maps, and the types of structures were inferred from selected profile plots.

Search for new geophysical technologies

The new geophysical technologies and their possibilities for application to hydrogeological problems were reviewed from worldwide open sources data. Recent technology using fiber cables as a sensor and a data transmitter that employs light waves as a carrier is a modern technique that can detect both the static and dynamic characteristics of the aquifer. It is helpful for local and regional scale studies, and it has better accuracy than near-surface or borehole geophysical techniques. Like other geophysical techniques, it can be applied near the surface to detect physical parameters of the Earth materials or inside the borehole in various situations. Remarkably, its long-term measuring capacity is better than the time-lapse geophysical techniques.

3.3 Hydrogeological Model Development.

The information obtained from individual investigative approaches is used as an input for the conceptual hydrogeological model construction. The present-day existing conceptual hydrogeological

models of volcanic aquifers—the Hawaiian (McDonald et al., 1983), the Canary Islands (Custodio, 1989), and the Mayotte models (Lachassagne et al., 2014)—were used as benchmarks to construct the Dangila area’s hydrogeological conceptual model. However, these islandic volcanic aquifer hydrogeological conceptual models do not resemble the rifted or faulted continental aquifers systems. Therefore, a new model was developed that can consider the actual situation of the area using the field and laboratory data analysis results together with the information from boreholes, shallow hand-dug wells, and pumping test results.

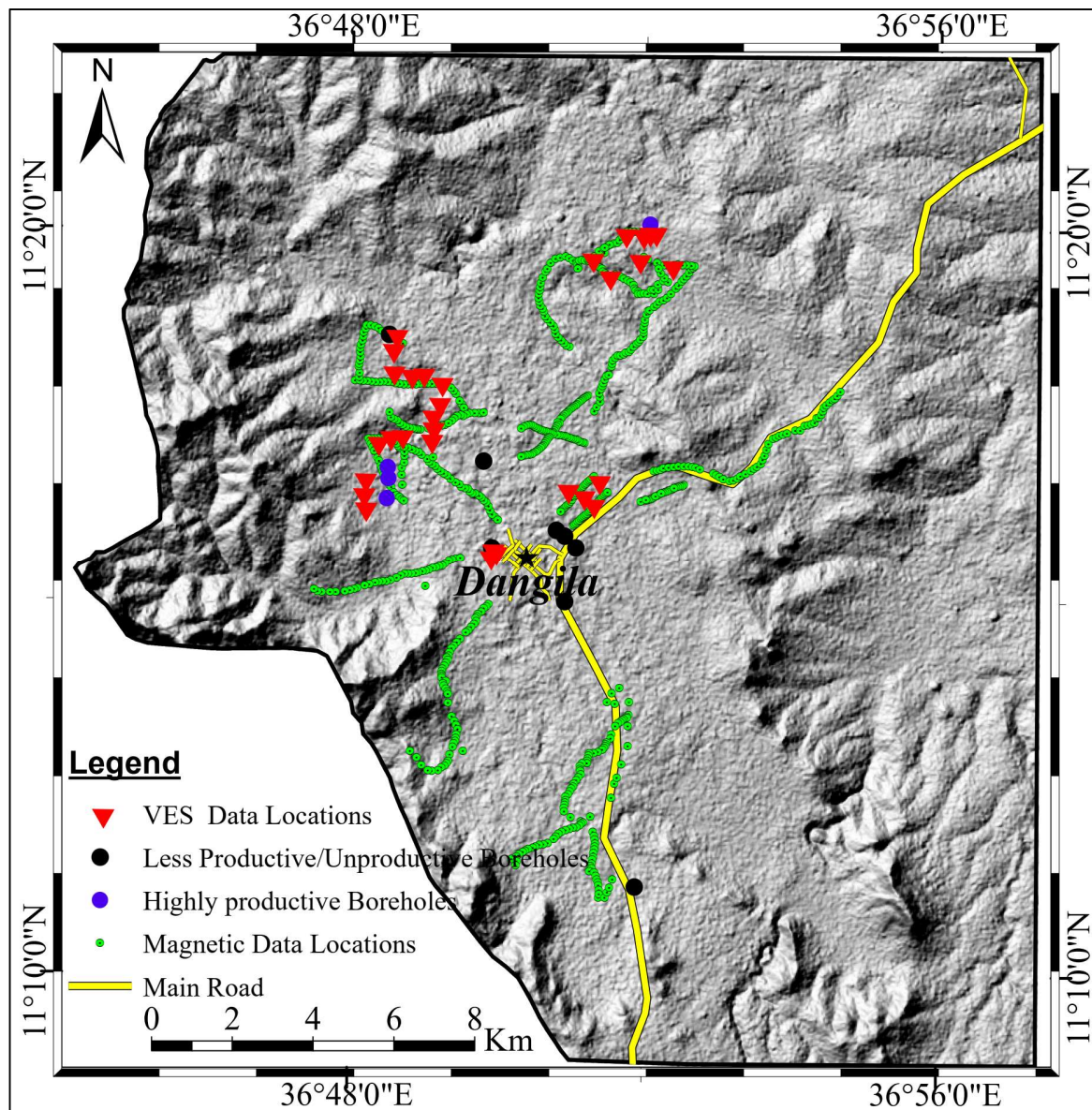


Fig. 16 Location of VES and geomagnetic data points.

Moreover, further analysis of the groundwater flow assumes a simplified groundwater flow enables to produce a flownet using Modflow. The flownet considers all the recharge and discharge areas, local, intermediate, and the possibility of a regional groundwater flow, by taking the surface topography from the area and using the Toth (1963) conceptual groundwater flow model in a small river catchment as a benchmark.

Conclusively, the research methodology followed used three sources of data or information: field-based data, laboratory-based data, and worldwide open sources of information. These data have been analyzed and modeled, and various parameters have been calculated to evaluate, characterize, and help in understanding the volcanic aquifer of the area.

4. RESULTS AND DISCUSSION

4.1 Properties of Volcanic Aquifer Reservoirs

The occurrence of groundwater and development of the groundwater resource primarily depends on the reservoir characteristics, the aquifer's current and historic properties, rainfall, and geomorphological factors. The reservoir determines the storage and flow properties of the aquifer, which are among the primary factors in understanding the aquifer systems. Volcanic aquifers stored in volcanic rock reservoirs have a complex geological setting resulting from the timing of volcanism. The boreholes and rock outcrops from Dangila and its surrounding area of northwest Ethiopia indicated that the volcanic rocks extending to 210 m are variable in type and groundwater storage. They comprise various basalts, scoria, scoriaceous basalt, pyroclasts, and tuff, along with weathering products such as soil and regolith.

The basalt locally varies laterally and with depth in age, mineralogical composition, degree of weathering, fracturing, the density of vesicles, and the amount of secondary minerals filling the vesicles. The thickness and depth of these layers vary considerably across the boreholes in the area. These variations showed that the area had experienced several eruptions from different sources and directions at various times. The upper layers interacted with the atmosphere and weathered before being overlain by younger basaltic lava flows, scoriaceous flows, and scoria falls.

The 12 boreholes with depths from 70–210 m, rock and soil samples collected at 2 m intervals and occasionally every meter whenever lithology changes were observed, comprise the following: 75.5% vesicular to aphanitic basalt lava flows, 7% scoriaceous basaltic lava flow, 6.5% scoria falls, 7.7% clay soil and regolith originating from both erosion and transport of volcanic rocks. The

alluvial sediment constitutes 1.6% ash with clay 7.7%, sand 0.15%, and pyroclastics 1.8% of the total collected and recorded samples. The bedrock below clay soil and regolith comprise basaltic lava flows followed by alternating rock layers. Generally, the scoria and scoriaceous basalt are weathered and altered to clay at some boreholes (D3 and DTW4).

The crystalline lava consists of hard, dense basalt of light to dark gray color. Basalt outcrops are either aphanitic, porphyritic, or vesicular in texture. In some cases, the vesicles are filled with secondary minerals, mainly calcite and occasional zeolite (Fig. 17). The secondary minerals that are expected to result from hydrothermal activities change the vascular basalt into an amygdaloidal texture. The calcite filling is highly weathered on surface outcrops but is easily observable in the subsurface where the soil has been excavated for road construction (Fig. 17c). However, in other places, the vesicular basalts and their secondary minerals filling the vesicles are observed up to 140 m depth in borehole lithologies (Fig. 17d).

Fractures occurring at the top and bottom of lava flows associated with paleosols and joints provide groundwater flow pathways. Weathered zones in rocks can be suitable aquifers unless they are dominated by secondary clay products (Hencher & McNicholl, 1995). Basalts are easily weathered compared to other crystalline silicate rocks (Suchet and Probst, 1993), though it depends on the cumulative effect of runoff and temperature (White & Blum, 1995).

The higher weathering fluxes associated with basalt due to its high intrinsic reactivity of basaltic mafic mineral assemblages increase the porosity in the basalt weathering zone (Desserta et al., 2003; Navarre-sitchler et al., 2015), which is observed in the upper soil and regolith layers. The basalt is aphanitic, though it can be porphyritic, consisting of olivine, pyroxene, and plagioclase porphyries. According to the Walker (1959) classification system based on petrology and texture of the rocks, the area's basalt can be classed into two different petrographic types: olivine basalt and porphyritic basalt. Similar basaltic volcanic rocks cover significant areas in the southern part of the Lake Tana Basin and the Ethiopian Rift. They are essential groundwater sources for several million people living in rural and urban areas. The highly vesicular and fractured permeable basalts are the most productive aquifers in the area.



Fig. 17 Photographs of topsoil, weathered rocks, and paleosol (a), weathered soil and regolith from a 7-m deep hand-dug well (b), a 0.5-m deep vesicular basalt (c), and drill cuttings from 140-m depth (d).

4.1.1 Rock sample thin sections analysis

The thin section analysis of rock samples from three different places in the study area showed that the rock samples 01 and 02 are more similar to each other than sample 03. The close examination of the two rock samples (samples 01 and 02) showed the rocks are aphanitic, microcrystalline, medium-grained, inequigranular, and holocrystalline oriented. The sample has porphyritic, intersepta, and amygdaloidal textures. The felsic component is plagioclase (~50%), between 250–750 μm in size, and appears in the matrix. It has a lath shape and is oriented spectacularly around the porphyries. The olivine (20%) appears in two types as in the matrix and porphyries. The olivines in the matrix are small (~100–250 μm in size), whereas the porphyries are 400–1000 μm in size and are idiomorphic. The olivine crystals often have an iddingsite alteration rim. The clinopyroxene

(20%) is frequent in the matrix (~300–500 μm in size), rarely apparent as porphyry, with a size of 600–3000 μm in both cases and with a columnar shape. The amount of glass is ~10%, and the opaque minerals are usually idiomorphic, with ~150 μm crystal size. The amygdales are filled with multigenerational carbonate, as fine-grained and coarse-grained calcite phases (Fig. 18).

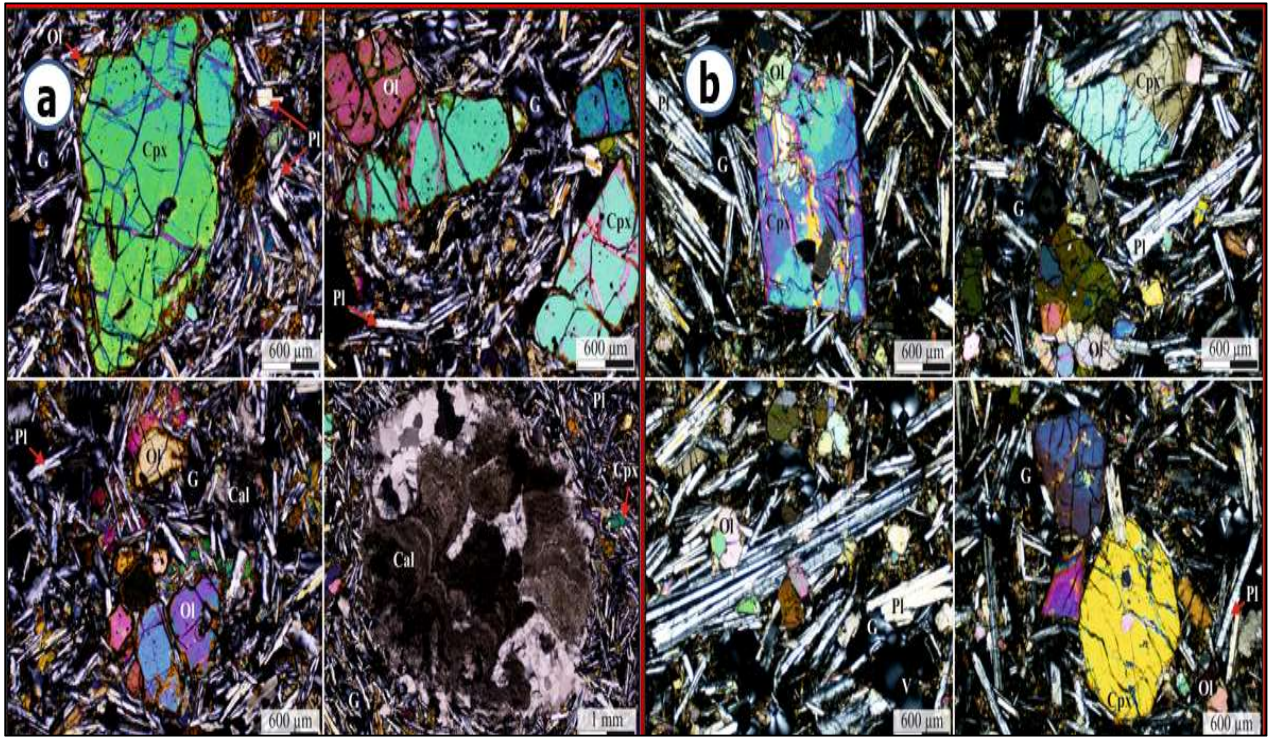


Fig. 18 Microscope images of thin sections from rock samples No1(a) and No2(b). Ol-olivine, Cpx-Clinopyroxene, Pl-plagioclase, Cal-calcite, G-glass, and V-vesicular.

The rock sample no.03 thin section microscopic observations showed that the rock has a different mineralogical assemblage than the other two samples (Fig. 19). It is aphanitic, microcrystalline, fine-grained, inequigranular, holocrystalline and disoriented. The sample has porphyritic, intergranular and amygdaloidal textures. The felsic component is plagioclase (~60%), which appears in the matrix. It has a maximum size of ~100 μm and has a lath shape. The olivine (20%) appears in the matrix at approximately 30 μm and as porphyries from 50–100 μm in size. The olivine crystals often have iddingsite alterations similar to the first two rock samples. The clinopyroxene appears in the matrix (~30 μm) and as porphyries (~70–250 μm) and is usually idiomorphic. The porphyries sometimes are skeletal crystals or contain undifferentiated inclusions. The amount of opaque minerals is ~10%, but the sizes are small, approximately between 10–20 μm .

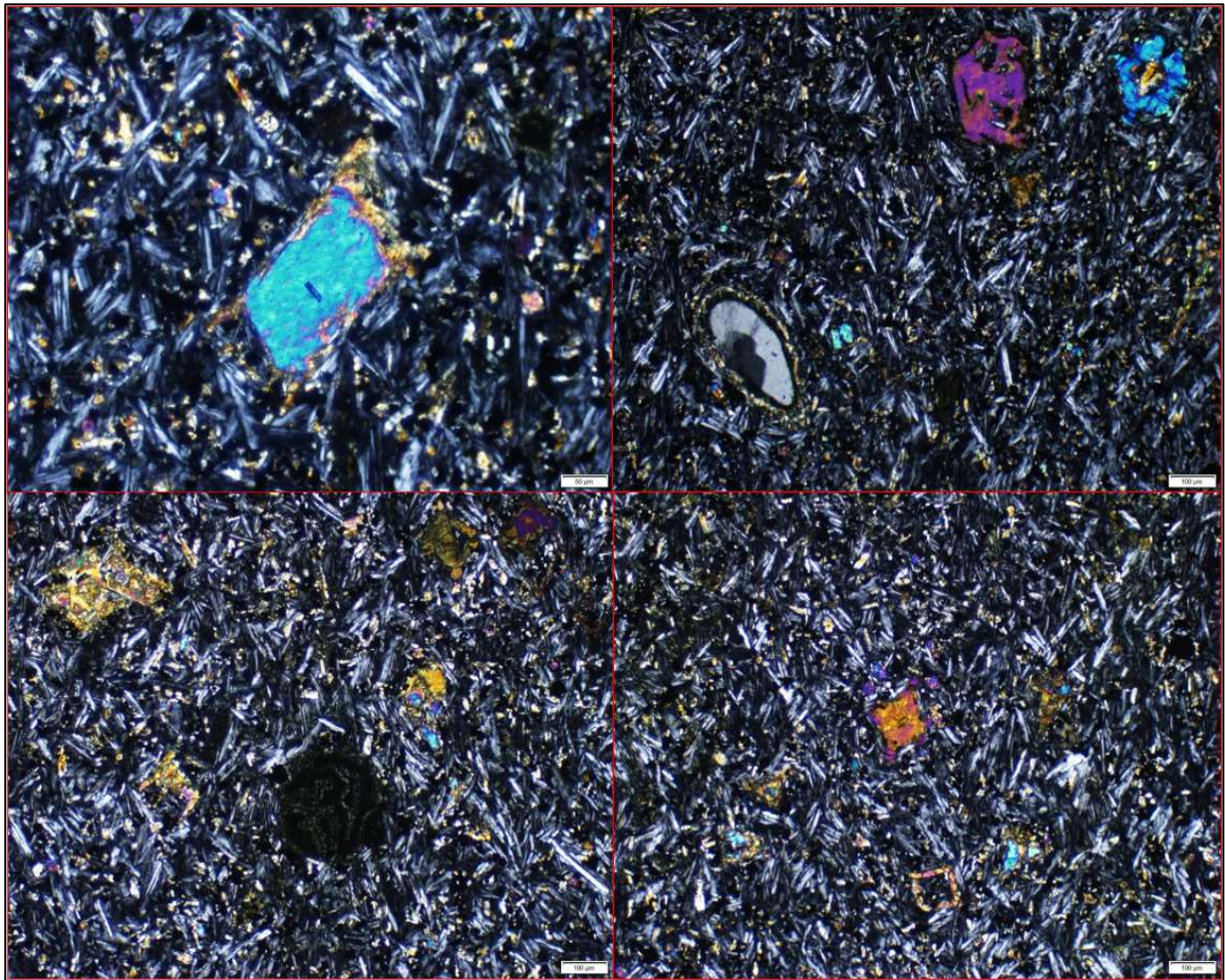


Fig. 19 Microscopic images of a thin section from rock sample No. 3.

It has thin fractures that might have fluid alterations which change the color to pale yellow. The small size vesicles are filled with carbonates that change the texture to amygdaloidal. Thin section laboratory analysis of the three rock samples showed that vesicles are not interconnected at the microscopic scale and, in some instances, were filled by calcite, which reduces the porosity and permeability of the rock.

The dominant minerals in the rocks obtained by Thermo DXR Raman spectroscopy include forsterite (Mg_2SiO_4) from olivine, augite and diopside from pyroxene, and albite ($\text{NaAlSi}_3\text{O}_8$) and anorthite ($\text{Ca}(\text{Al}_2\text{Si}_2\text{O}_8)$) from plagioclase groups. The augite and diopside minerals comprise (Ca, Mg, and Fe) and rarely aluminum. The opaque minerals comprise magnetite (Fe_3O_4), ilmenite (FeTiO_3), and hematite (Fe_2O_3). Hematite (Fe_2O_3) is the most resistant mineral to weathering and might cause the reddish color of soil and regolith in the area.

The rock mineralogical and textural differences between the rock samples might be associated with the magma fractionation. Even though no rock age determination works in the area, the first two samples (Sample No1 and No2) are more recent in the Quaternary. In contrast, the third sample is close to the tertiary basaltic lava. The petrological thin section analyses agree with previous works by Wolde (1996) on olivine alkaline basalts.

Abate et al. (1998) explained that the more recent Dek-Island and earlier Gimjabet-Kosober alkali basalts are liable to have resulted from fractional crystallization of the same basaltic magma source. The eruption of basaltic magmas creates several well-preserved eruption points visible to the south of Lake Tana. Hofmann et al. (1997) and Abate et al. (1998) related the origin of Lake Tana Basin basaltic magma to the Afar plume and the main Ethiopian Rift. These Quaternary basalt flows are characteristically alkaline and represent the final pulse of basaltic volcanism on the Ethiopian Plateau. The Quaternary basalt dated by Prave et al. (2016) from the Blue Nile River outlet of Lake Tana Basin has a plateau age of 33,000 y.

4.2. Hydrochemistry

Groundwater geochemical properties depend on chemical constituents of rainfall and various geochemical processes as water moves from recharge to discharge areas (Freeze & Cherry, 1979; Matthes, 1982). The Ethiopian volcanic aquifer hydrochemistry variations result from various controlling mechanisms (Ayenew et al., 2008; Demlie et al., 2007; Kebede et al., 2005; Woldemariyam & Ayenew, 2016).

Hydrochemical laboratory analysis of representative groundwater samples from boreholes, shallow wells, and springs provided the groundwater physio-chemical parameters. The pH values of water samples from boreholes vary from 6.83 to 8.81, with a mean value of 8.07 ± 0.73 (Table 1). These values suggest that deep aquifers have a neutral to a weakly alkaline character. The pH values of shallow wells and spring water samples representing the shallow aquifer system vary from 5.37 to 6.88, with a mean value of 5.62 ± 0.29 (Tables 1 & 2). These values suggest that the shallow aquifer system has a character close to neutral in a few shallow wells and is weakly acidic in the remaining shallow wells and springs. The pH values in the shallow aquifer system indicate that the upper unconfined aquifer is recharged from rain locally and did not travel long distances before discharge to the surface. The increased pH value of deep aquifers is due to rock–water interaction during groundwater flow or storage in the volcanic reservoirs.

The area's groundwater has very low salinity, with TDS values varying from 24 to 312 mg/L. The EC values vary from 40 to 480 $\mu\text{S}/\text{cm}$, with the smallest values in springs and the highest in shallow wells and boreholes. The lowest EC values in the springs and some shallow wells are related to the recently recharged young groundwater. The higher EC values of boreholes and a few shallow wells imply older groundwater. The high EC value of the upper unconfined aquifer means that it either stayed a long time in the reservoir or traveled from the nearby highland recharge area to the shallow wells through fractures.

The physical parameters of the groundwater (pH, TDS and EC) indicated that the lowest values are from springs, and the highest values are from shallow wells and boreholes. The high values are due to increases in the dissolution of ions in the aquifers with time and depth, whereas low values in shallow aquifers imply young groundwater with low residence time.

The concentration of cations and anions varies from shallow to deep aquifer systems. The dominant cations in the borehole groundwater samples are in the order of $\text{Na}^+ > \text{Ca}^{2+} > \text{Mg}^{2+} > \text{K}^+$ whereas in the shallow wells and springs they are $\text{Ca}^{2+} > \text{Mg}^{2+} > \text{Na}^+ > \text{K}^+$. The dominant anions in both shallow and deep aquifer systems are in the order of $\text{HCO}_3^- > \text{Cl}^- > \text{SO}_4^{2-}$. Therefore, the most abundant cation in the deep aquifer system is Na^+ , whereas, in shallow aquifers, it is Ca^{2+} . The groundwater system of the area, both shallow and deep aquifers, are mainly dominated by HCO_3^- from among all other anions. The fluoride concentration is less than 0.82 mg/l, unlike the groundwater of Ethiopian Rift volcanic rocks that cause health problems (Ashley & Burley, 1994). Though the concentration of sulfate and nitrate is low in both aquifers systems, a tendency to increase in the shallow aquifer system is observed. The low concentration of sulfate and nitrate indicates little human impact on the groundwater. However, consideration of fertilizers used for agriculture should be taken in the future that may affect the shallow aquifer system. Except for one shallow well with 12.5 mg/L of Cl and a few shallow and deep wells pH and Fe concentrations values, all physical and chemical water parameters are within the drinking water limits of the World Health Organization (WHO, 2011) (Table 2). This makes the groundwater suitable for human consumption without consideration of microbial water quality. The high value of Cl^- in the single shallow well is attributed to anthropogenic effects related to well-being, as it is located close to a village and is poorly constructed.

Table 1. Hydrochemical and physical summary of groundwater samples from boreholes, shallow wells, and springs. Total dissolved solids (TDS), cations, and anions are given in (mg/L), whereas the EC is in ($\mu\text{S}/\text{cm}$). The summary presented includes the minimum (Min), maximum (Max), mean, and standard deviation (SD) values of 16 groundwater parameters from the three water schemes. The detailed physico-chemical data of water samples are presented in Annex 1.

Water scheme		pH	EC	TDS	Ca ²⁺	Mg ²⁺	Na ⁺	K ⁺	Mn ²⁺	Fe ²⁺	Cl ⁻	SO ₄ ²⁺	HCO ₃ ⁻	CO ₃ ²⁻	NO ₃ ⁻	F ⁻	B ⁻
Bore- holes (total 7)	Min	6.83	204	124	0.97	1.95	13.60	0.90	0	0	0	0.5	90	0	0.13	0	0
	Max	8.81	335	214	36.00	6.92	39.00	15.10	0.02	0.08	2.5	8	175	15	4.8	1.1	0.06
	Mean	8.07	277.71	177.54	20.06	4.64	26.15	5.73	0.01	0.013	1.47	2.14	130.03	4.2	1.44	0.42	0.02
	SD	0.73							0.01	0.023	0.93	2.62	36.51	7.18	1.60	0.40	0.03
			44.21	33.56	14.20	1.75	9.32	5.43									
Shal- low well (total 14)	Min	5.37	70	45.50	6.09	1.89	0.08	0.15	0.00	0	0.5	0.5	15	0	1	0.21	0
	Max	6.88	480	312.00	27.10	3.44	7.45	9.06	0.03	4.3	12.5	6.2	125.4	0	15	0.66	0.06
	Mean	5.99	213.04	120.64	19.34	2.58	2.18	2.73	0.01	0.49	3.04	1.43	75.03	0	4.32	0.37	0.02
	SD											1.41		0			
		0.40	108.99	67.88	5.74	0.54	2.13	2.42	0.01	1.19	3.19		26.69		3.92	0.13	0.03
Springs (total 4)	Min	5.31	40	24	3.58	1.80	0.08	1.24	0.00	0.00	0.80	0.80	15.50	0	0.80	0.37	0.00
	Max	6.00	189.60	97	23.30	3.87	2.09	5.13	0.01	0.01	1.70	5.00	91.20	0	6.82	0.82	0.30
	Mean	5.62	88.32	48.94	14.88	2.52	1.16	2.54	0.00	0.01	1.13	2.33	51.73	0	3.12	0.66	0.09
	SD	0.29	69.14	33.95	8.42	0.94	0.90	1.79	0.01	0.00	0.43	1.91	30.96	0	2.59	0.21	0.14

Table 2. Quality of groundwater samples from the study area for drinking purposes based on the WHO 2011 drinking water quality index (WHO, 2011). The values of TDS, cations, and anions are given in (mg/L), whereas the EC is in ($\mu\text{S}/\text{cm}$).

Water quality parameter	Measured ranges of samples			WHO (2011) maximum allowable limit	Samples above allowable limit
	Boreholes	Shallow wells	Springs		
pH	6.83–8.81	5.37–6.88	5.31–6.00	6.5–8.5	3 borehole samples
EC	204–335	70–480	40–189.60	1000 $\mu\text{S}/\text{cm}$	Nil
TDS	124–214	45.50–312	24–97	500 mg/L	Nil
Ca^{+2}	0.97–36	6.09–27.1	3.58–23.3	75 mg/L	Nil
Mg^{+2}	1.95–6.92	1.89–3.44	1.80–3.87	50 mg/L	Nil
Na^{+}	13.60–39	0.08–7.45	0.08–2.09	200 mg/L	Nil
Fe	BDL–0.08	BDL–4.3	BDL–0.01	0.4 mg/L	2 shallow well samples
HCO_3^{-}	90–175	15–125.4	15.50–91.20	120 mg/L	4 borehole & 1 shallow well samples
SO_4^{-2}	0.5–8	0.5–6.2	0.80–5	250 mg/L	Nil
Cl^{-}	0–2.5	0.5–12.5	0.80–1.70	250 mg/L	Nil
NO_3^{-}	0.13–4.8	1–15	0.80–6.82	50 mg/L	Nil
F^{-}	0–1.1	0.21–0.66	0.37–0.82	1.5 mg/L	Nil

BDL* represents below detectable limit for iron using flame AAS instrument with 0.005 mg/L value (PerkinElmer, 2018).

Groundwater flows are accompanied by rock–water interaction in the aquifer. Rock–water interaction changes the hydrochemistry of the groundwater and leads to trends that provide essential information about the hydrogeochemical processes and evolution (Li et al., 2014). The Piper diagram (Piper, 1944) is often used to determine groundwater's main composition and hydrochemical facies. The Piper diagram (Fig. 20) depicts five main water facies Ca-HCO_3 and Ca-Mg-HCO_3 in shallow aquifers, and Na-Ca-HCO_3 , Ca-Na-HCO_3 and Na-HCO_3 in the deep aquifer system. The influence of anthropogenic pollution on the shallow aquifer leads to having $\text{Ca-HCO}_3\text{-Cl}$ and $\text{Ca-Mg-HCO}_3\text{-Cl}$ water facies in two shallow well water samples. Ca^{+2} , Mg^{+2} and Na^{+} concentrations are significant in a few borehole water samples, leading to Ca-Na-Mg-HCO_3 water facies. This type of water facies might be due to intermixing shallow and deep aquifers where fractures connect them. The dominant water type in the shallow aquifer system is Ca-HCO_3 , a typical water facies in shallow young groundwater.

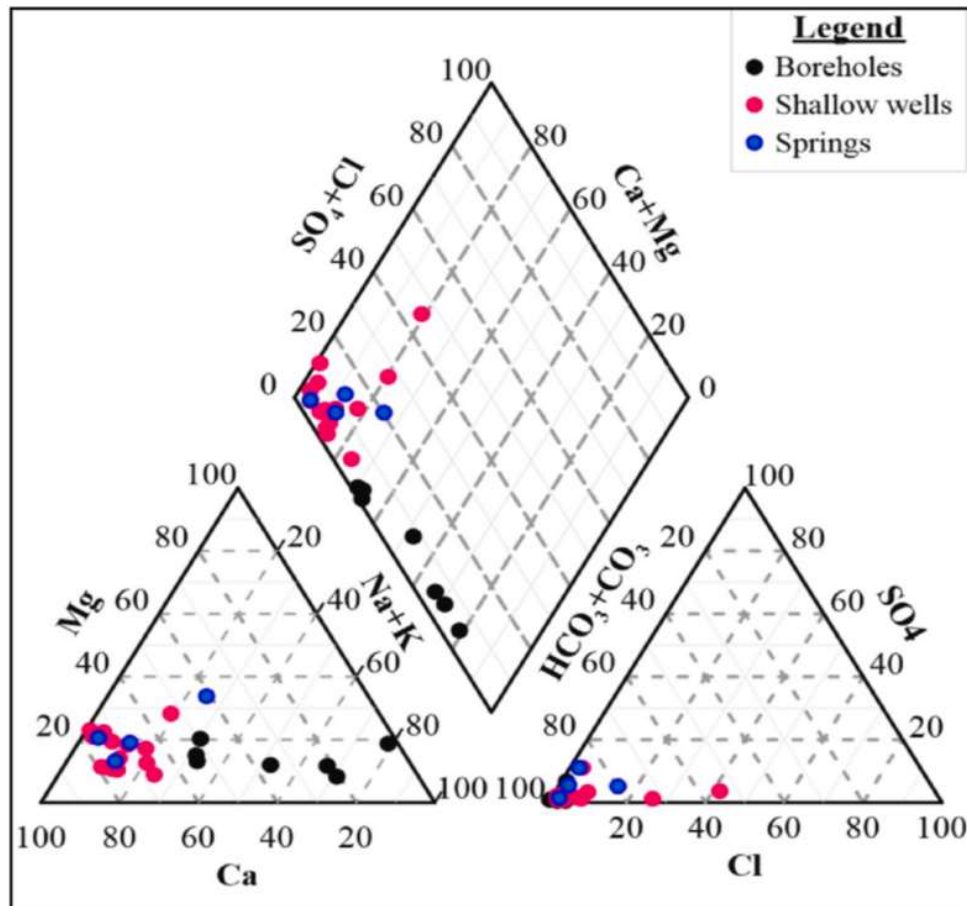


Fig. 20 Piper diagram of hydrochemical data.

The dominant water facies in a relatively deep aquifer (borehole) is Na–Ca–HCO₃ and Na–HCO₃ types though Ca–Na–HCO₃ water facies have been obtained (Table 3). The results of the hydrochemical analysis and groundwater facies are in agreement with the study by Abiye & Kebede (2011) on the upper Blue Nile basin, a broader region that includes the study area. Abiye & Kebede (2011) discussed most springs having a character of Ca–HCO₃ hydrochemical composition and a low TDS value. However, the mineralized springs have a character of Na–HCO₃ water facies.

Table 3. Different groundwater facies of the area.

No.	Water scheme	Sample quantity	Water facies type
1	SP	1	Ca–HCO ₃
2	SW	7	Ca–HCO ₃
3	SP	3	Ca–Mg–HCO ₃
4	SW	5	Ca–Mg–HCO ₃
5	BH	2	Ca–Na–HCO ₃
6	BH	3	Na–Ca–HCO ₃
7	BH	1	Ca–Na–Mg–HCO ₃
8	BH	1	Na–HCO ₃
9	SW	1	Ca–Mg–HCO ₃ –Cl
10	SW	1	Ca–HCO ₃ –Cl

4.2.1. Mechanisms controlling groundwater chemistry

The chemistry of groundwater is affected by several factors, including the original composition of recharge water or precipitation, the reservoir rock mineralogical composition, residence time in the reservoir rock, and other affecting factors during its flow (Redwan & Moneim, 2015). The groundwater composition controlling mechanism is assessed using the Gibbs diagram (Gibbs, 1970) that relates water composition to its dominant sources. The three distinct zones—precipitation dominance, evaporation dominance, and rock weathering dominance—have been defined and labeled in the Gibbs diagram (Fig. 21).

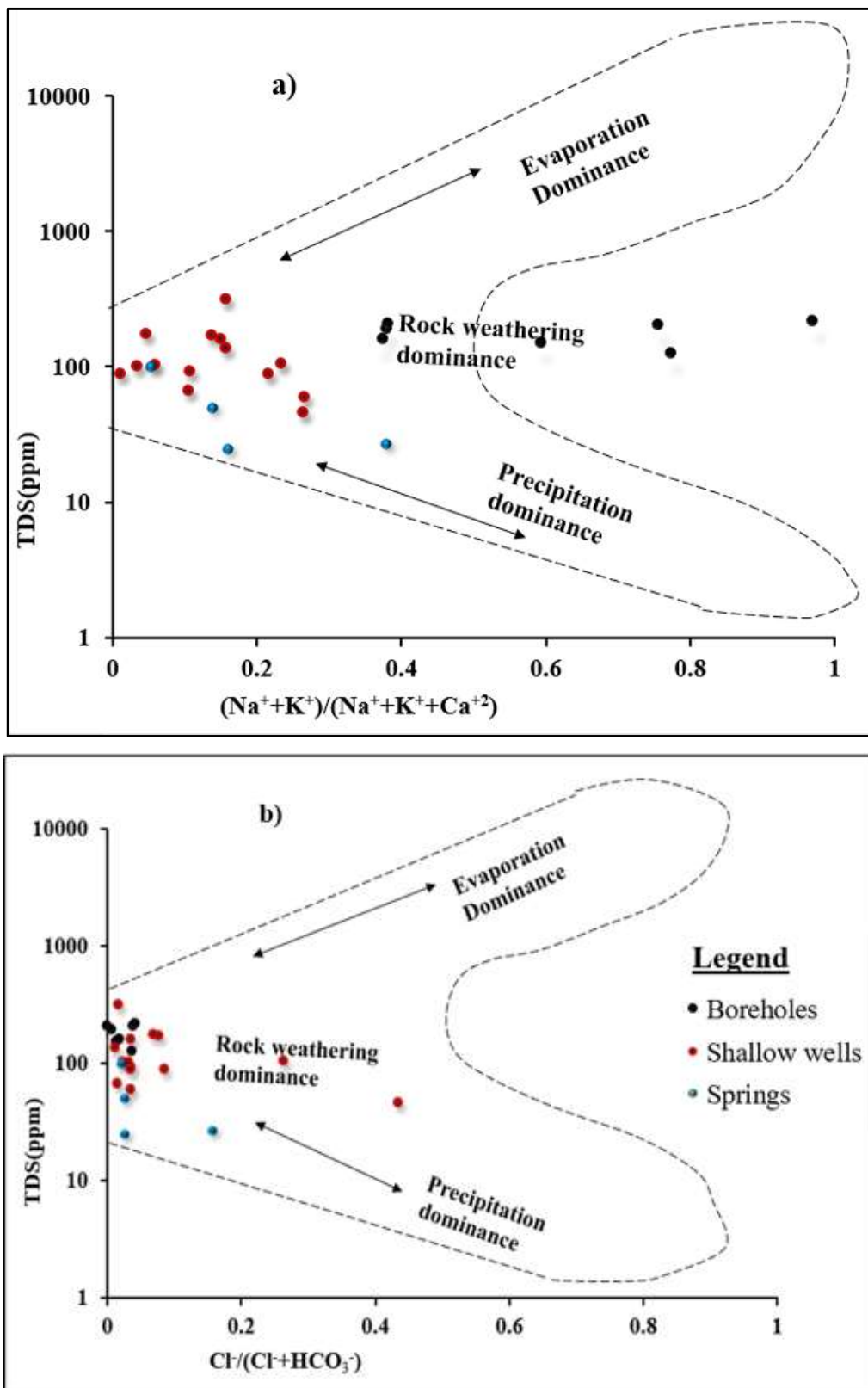


Fig. 21 Gibbs diagram of cations (a) and anions (b) of Dangila Town and its surrounding area groundwater sources.

The weight ratio of major cations $\text{Na}^+ / (\text{Na}^+ + \text{Ca}^{+2})$ is drawn on the x-axis and the variation in total salinity on the y-axis. Similarly, the weight ratio of major anions $\text{Cl}^- / (\text{Cl}^- + \text{HCO}_3^-)$ versus total dissolved salts is drawn for anions. The cation and anion diagrams indicated that rock weathering dominates as the controlling factor for groundwater chemistry. The diagram depicted both rock weathering and precipitation dominance in some shallow wells and springs. The Gibbs diagram plot showed that the influence of evaporation on groundwater chemistry is minimal.

The relation between major cations and anions could help to identify the change in the groundwater chemical compositions, the origin of ions, and hydrochemical processes involved in the evolution of groundwater (Wang et al., 2013). The relationship between Na^+ to Cl^- and Ca^{+2} to HCO_3^- is presented in Fig. 22 along the halite and calcite dissolution lines. The majority of shallow wells and spring samples, and all borehole samples, are plotted below and to the right of the halite dissolution line (Fig. 22a). It indicated that halite dissolution is not the source of either sodium or chlorine. Instead, the weathering of rock-forming silicate minerals and cation exchange possibly increased the concentration of Na^+ from the shallow to the deep aquifer system. The low concentration of Na^+ in some shallow aquifer samples located above and left of the halite dissolution line may originate from the combined effect of recharge water and limited weathering of surface or unsaturated zone rocks. A similar characteristic is observed in a relationship between Ca^{+2} and HCO_3^- values of groundwater with respect to the calcite dissolution line (Fig. 22b). The groundwater concentrations for these ions are situated below and to the right of the calcite dissolution line that indicates the source of HCO_3^- is not CO_3^{-2} that results from calcite dissolution.

The plot of HCO_3^- versus the sum effect of Ca^{+2} and Mg^{+2} ($\text{Ca}^{+2} + \text{Mg}^{+2}$) showed a similar increase in bicarbonate values from the shallow aquifer to the deep aquifer system (Fig. 23a). The continuous increase of bicarbonate concentrations in the aquifer with residence times and depth suggests that the primary source of bicarbonate in volcanic aquifers can be attributed to soil carbon dioxide interacting with water to form carbonic acid (Freeze & Cherry, 1979; Kebede et al., 2005).

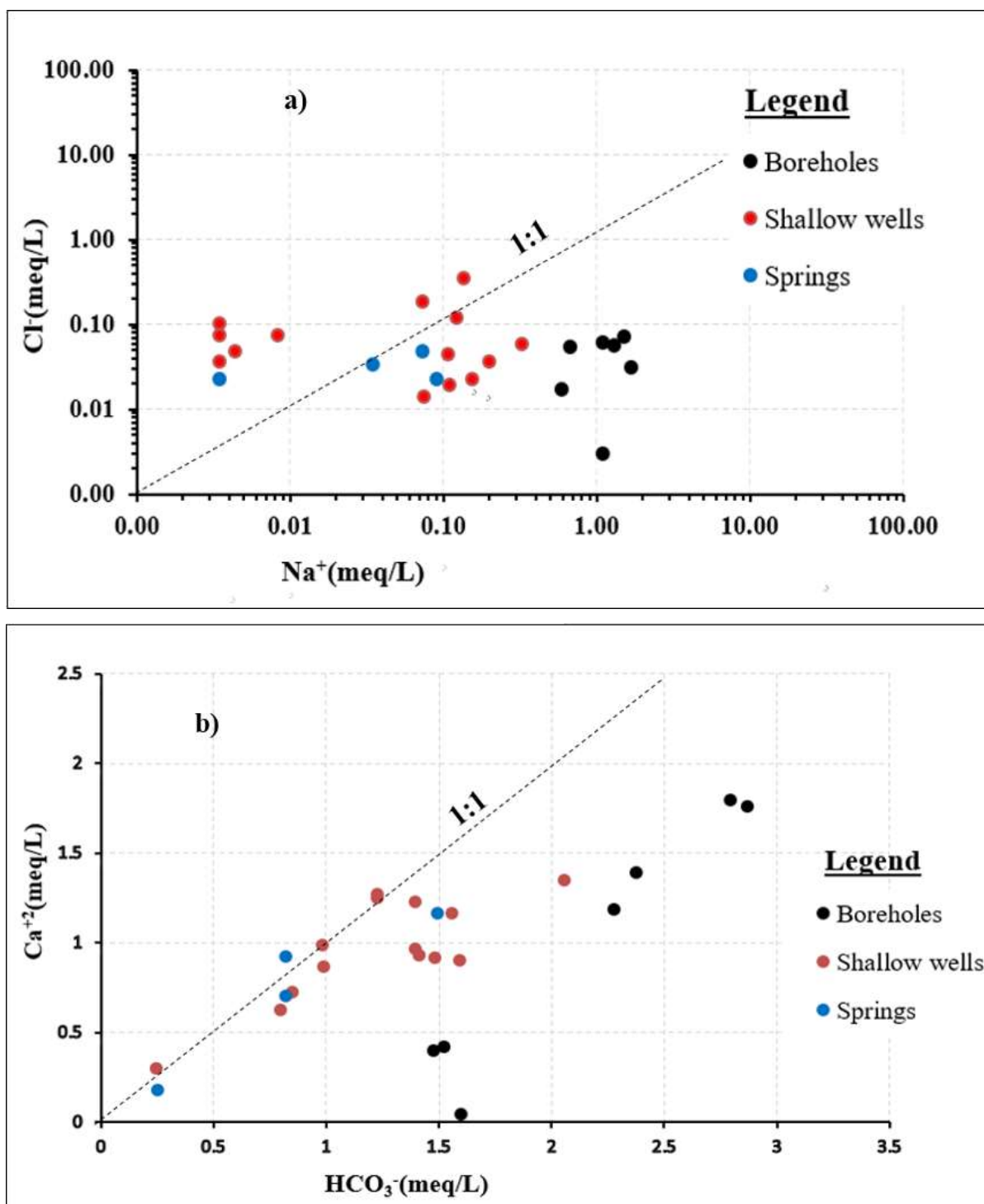


Fig. 22 Na^{+} Versus Cl^{-} graph (a) and HCO_3^{-} versus Ca^{+2} graph (b) of groundwater along the halite and calcite dissolution lines.

The low amount of Na^{+} and relatively higher Ca^{+2} and Mg^{+2} in shallow aquifers are attributed to recharge water chemistry and limited rock–water interaction. The increasing amount of Na^{+} but

decreasing values of Ca^{+2} with depth is due to cation exchange (exchange of Ca^{+2} and Mg^{+2} by Na^{+}) and dissolution of Na^{+} containing silicate minerals. The increase in Na^{+} content and decreasing Ca^{+2} content along the flow path and with depth indicated cation exchange, where Ca^{+2} was absorbed into clay minerals, and Na^{+} was released. This release of Na^{+} into the groundwater changed the chemical compositions of groundwater in deep aquifers to Na^{+} dominant. This result is supported by the relation of HCO_3^{-} versus $(\text{Ca}^{+2} + \text{Mg}^{+2})$ and $((\text{Na}^{+} + \text{K}^{+}) - \text{Cl}^{-})$ versus $((\text{Ca}^{+2} + \text{Mg}^{+2}) - (\text{HCO}_3^{-} + \text{SO}_4^{-2}))$ graphs (Fig. 23a and b). The plot $((\text{Na}^{+} + \text{K}^{+}) - \text{Cl}^{-})$ versus $((\text{Ca}^{+2} + \text{Mg}^{+2}) - (\text{HCO}_3^{-} + \text{SO}_4^{-2}))$ graphs which are often used to study cation exchange in groundwater (Ahmed et al., 2013), have a negative relationship. The negative correlation or slope of groundwater sample values is neither precisely on the line 1:1 with slope -1 nor very close to it, which would show complete cation exchange had occurred (Fisher & Mullican, 1997). This suggests that even though there is a cation exchange of major cations, Ca^{+2} and Mg^{+2} by Na^{+} , the higher amount of Na^{+} was released into the aquifer from weathering of Na^{+} containing silicate minerals.

The results revealed that calcium and magnesium ions change from dominant to subordinate in relation to total cations, with increasing depth and as groundwater flows away from recharge sources. Generally, groundwater associated with a recharge in the shallow aquifers is represented by water dominant in calcium, magnesium, and bicarbonates, with lesser amounts of sodium; as groundwater flows away from the source of recharge, the interaction between water and rock increases. Sodic lithologic units are encountered as the groundwater moves along a flow path, and calcium and magnesium ions are exchanged for sodium ions attached to aquifer solids. Moreover, the sodium-containing silicates' weathering increases with depth and along flow paths, so that both processes' reactions result in a decrease in calcium and magnesium and a corresponding increase in sodium and bicarbonate as groundwater flows away from the source of recharge. This results in water that evolves to sodium-bicarbonate and sodium- calcium-bicarbonate types between recharge and discharge areas. It is possible to propose two distinct hydrochemical systems: 1) A shallow, localized, perched system with little interaction with the deeper aquifer that is hydrodynamic with the atmosphere and generally less than 25 m deep in the shallow geochemical zone. 2) An underlying deeper, intermediate, probably regional, and relatively chemically static system along the fault and fracture lines in the deep hydrochemical zone.

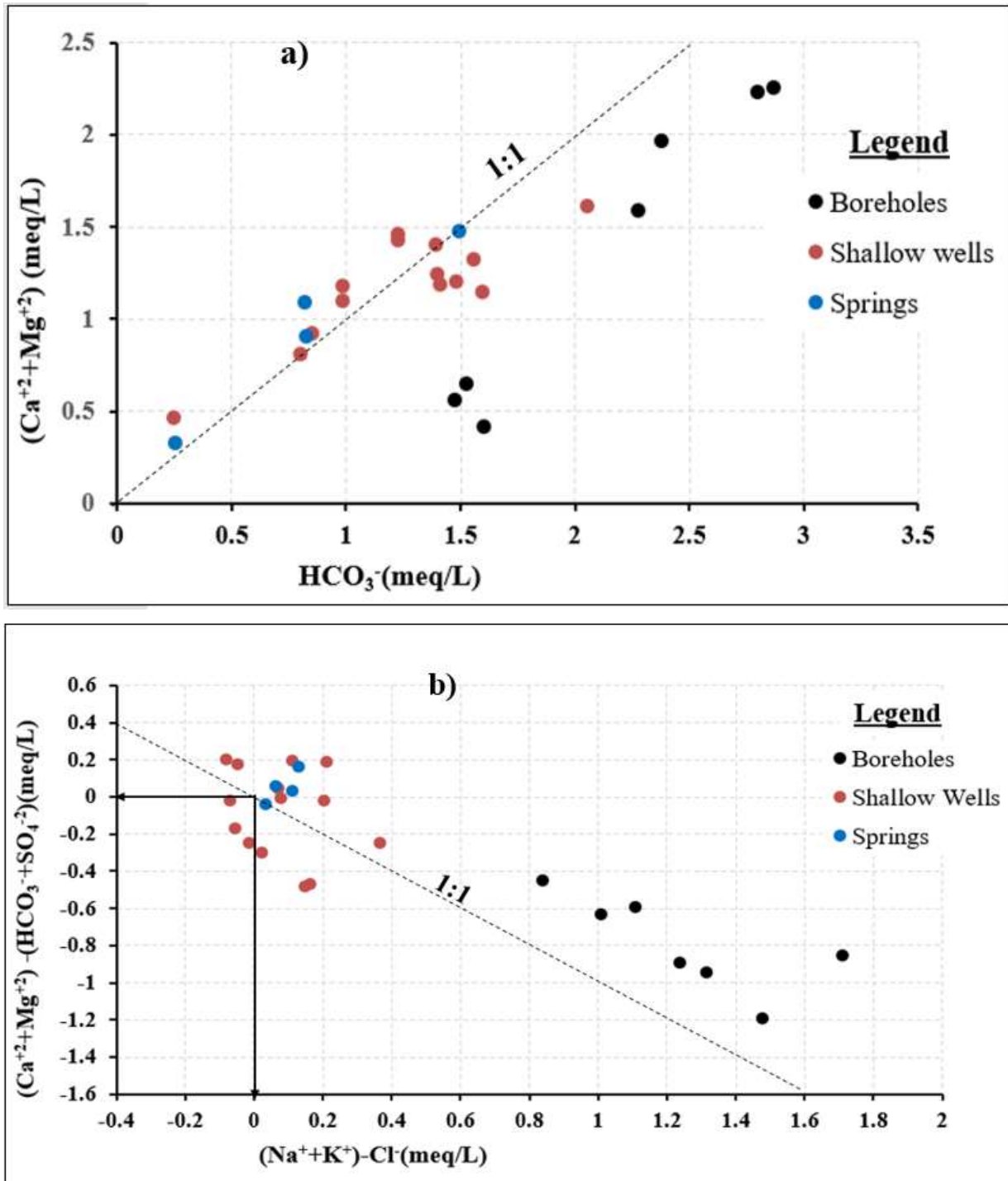


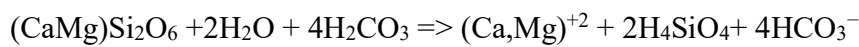
Fig. 23 HCO_3^- versus $(Ca^{+2} + Mg^{+2})$ graph (a) and $(Na^+ + K^+) - Cl^-$ versus $(Ca^{+2} + Mg^{+2}) - (HCO_3^- + SO_4^{2-})$ graphs (b) of groundwater.

4.2.2. Chemical weathering of rock-forming minerals

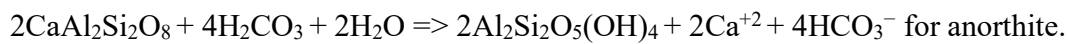
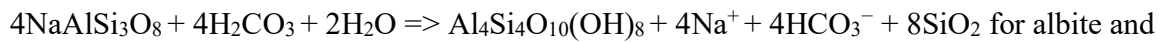
The silicate rock-forming mineral weathering is the main factor for the prevalence of cations Ca^{+2} , Mg^{+2} , Na^{+} , and K^{+} with a significant amount in groundwater (Srinivasamoorthy et al., 2014). Forsterite, identified by laboratory analysis from rock outcrop samples, dissolves with the presence of carbonic acid. The dissolution results in magnesium ion, silicic acid, and dissolved bicarbonate as follows:



Pyroxene minerals, diopside ($\text{CaMgSi}_2\text{O}_6$) and augite ($((\text{CaMgFe})(\text{MgFe})\text{Si}_2\text{O}_6)$), dissolve to produce Ca, Mg, Fe, bicarbonate ion, and silicic acid. Diopside dissolution is given by



Plagioclase feldspar minerals, albite ($\text{NaAlSi}_3\text{O}_8$) and anorthite ($\text{CaAl}_2\text{Si}_2\text{O}_8$), undergo hydrolysis during reaction with water to give cations, clay mineral (kaolinite), silica, and hydroxide as follows:



The minor opaque mineral hematite can further react with water as $\text{Fe}_2\text{O}_3 + \text{H}_2\text{O} \Rightarrow 2\text{FeO}(\text{OH})$ (goethite). However, hematite and goethite are very insoluble in water, and they remain as residual minerals of iron oxides that give many soils their reddish color. Chemical weathering of silicate minerals produces insoluble clay minerals, positively charged metal ions (Ca^{2+} , Mg^{2+} , Na^{+}), negatively charged ions (OH^{-} , HCO_3^{-}), and some soluble silica. The presence of these ions in soil and water causes variations in groundwater chemistry.

4.2.3. Water quality for irrigation

The tendency to use groundwater for small-scale irrigation on small backyard agricultural land is expanding because of its simplicity and ease of management. The suitability of groundwater for agricultural use depends mainly on the mineralogical contents of the water in soil and plants. Salts in groundwater can change soil structure, permeability, and aerations, which in turn affect plant development. The sodium adsorption ratio (SAR), sodium percentage ($\text{Na}\%$), and residual sodium carbonate (RSC) are the commonly employed parameters to assess the suitability of water for irrigation. SAR is the benchmark measure of probable sodium hazard for irrigation water set by the United States Salinity Laboratory Staff (1954).

The relative concentration ratio of Na^+ ions to Ca^{+2} and Mg^{+2} ions in irrigation water is used to estimate the potential accumulation of Na^+ in soil due to the regular use of sodic water for irrigation. The relationship between SAR in irrigation water and the extent to which the soils adsorb sodium helps decide the suitability of water for irrigation. When high sodium and low calcium water is used for irrigation, the cation exchange development may become saturated with sodium, damaging the soil structure due to the distribution of clay particles (Singh, 2002). It will reduce water movement and aeration in soils, affect plants' growth, and reduce crop yield. The deficiency of Ca^{+2} and Mg^{+2} may arise due to the high accumulation of Na^+ , which necessitates the evaluation of sodic water hazards. SAR is determined using the equation given below (Suarez et al., 2006).

$$\text{SAR} = \frac{\text{Na}^+}{\sqrt{\frac{(\text{Ca}^{2+} + \text{Mg}^{2+})}{2}}} \quad (5)$$

Where Na^+ , Ca^{+2} and Mg^{+2} are in meq/l. SAR values ranged from 0.004 to 3.28, with a mean varying from the value of 0.087 ± 0.079 to 1.69 ± 1.00 respective to the three groundwater schemes in the study area (Table 4).

Table 4. Maximum, minimum, means, and standard deviation values of SAR, Na%, and RSC in the groundwater. The detail of each item of data is presented in Annex 2.

Water scheme	Total no.	Water quality indicator	Min	Max	Mean	SD
Boreholes	7	SAR	0.60	3.28	1.69	1.00
		Na%	20.35	76.26	46.47	22.30
		RSC	0.61	1.18	0.89	0.20
Shallow wells	14	SAR	0.004	0.398	0.124	0.116
		Na%	0.27	18.54	6.90	5.97
		RSC	-0.229	0.451	0.052	0.242
Springs	4	SAR	0.005	0.180	0.087	0.079
		Na%	0.335	16.642	6.639	7.29
		RSC	-0.27	0.014	-0.102	0.120

The plot of EC ($\mu\text{S}/\text{cm}$) versus SAR on the United States Salinity Laboratory Staff (1954) illustrates that most of the groundwater samples of boreholes belong to the categories C2S1, which is medium salinity and low sodium (Fig. 24). The shallow well samples belong to C2S1 and C1S1 (low salinity and low sodium), whereas the samples from springs belong to the C1S1 categories. All samples from the three groundwater schemes fall in the low sodium class (S1) with SAR values <10 , which shows that no alkali hazard to crops is anticipated. Shrinking and swelling of clay soil

particles can occur if the amount of SAR in the irrigation water is greater than 6–9 (Saleh et al., 1999). The C2S1 and C1S1 categories of water with low to medium salinity and low sodium water imply that groundwater can be used for irrigation on all soil types without any danger of exchangeable sodium.

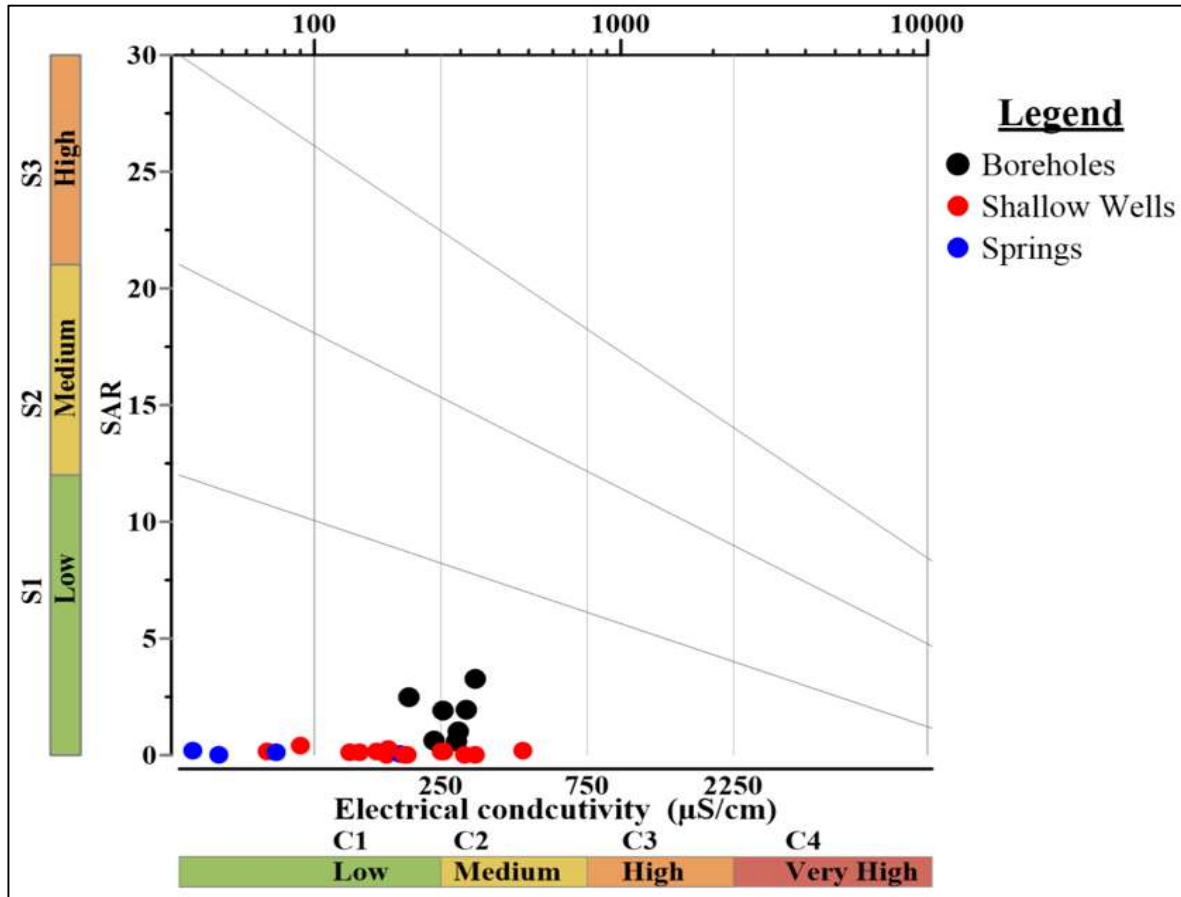


Fig. 24 Classification of groundwater using US regional laboratory staff (1954) salinity diagram.

Na% is considered a parameter for determining water suitability for irrigation (Wilcox, 1948). The reaction of Na^+ with a weak acid (CO_3^{2-}) results in alkaline soil, whereas Na^+ reacts with strong acids (Cl^-), results in saline soils. The use of both alkaline and saline soils retard plant growth (D. Todd, 1980) because a high concentration of Na^+ in irrigation water will remove Ca^{+2} and Mg^{+2} ions through a base-exchange reaction in clay soil particles. The exchange of Ca^{+2} and Mg^{+2} by Na^+ will reduce water and air movement, and the soils become hard during the dry season (Saleh et al., 1999). Na% is calculated using the formula,

$$\text{Na \%} = \left[\frac{\text{Na}^+}{(\text{Ca}^{2+} + \text{Mg}^{2+} + \text{Na}^+ + \text{K}^+)} \right] \times 100 \quad (6)$$

Where Na^+ , Ca^{+2} , Mg^{+2} , and K^+ are in meq/l. The Na% of groundwater samples from boreholes ranged from 20.35 to 76.26 with a mean of 46.47 ± 22.30 . The Na% value in shallow wells samples ranged from 0.27 to 18.54 with a mean of 6.90 ± 5.97 , and from springs samples ranged from 0.335 to 16.642 with a mean of 6.639 ± 7.29 (Table 4). Irrigation water is classified based on Na% as excellent (<20%), good (20%–40%), permissible (40%–60%), doubtful (60%–80%) and unsuitable (>80%). The Na% values indicate that the groundwater from springs and shallow wells are excellent, whereas boreholes range from good to doubtful categories. Therefore, using groundwater from boreholes that can yield a high amount of water for irrigation without any adjustment may result in a high concentration of Na^+ that reduces permeability and internal drainage of the soil.

Excess amounts of RSC, which results from the sum of carbonate and bicarbonate, also affects the suitability of groundwater for irrigation use. RSC is calculated based on the United States Salinity Laboratory Staff (1954).

$$\text{RSC} = (\text{HCO}_3^- + \text{CO}_3^{2-}) - (\text{Ca}^{2+} + \text{Mg}^{2+}) \quad (7)$$

Where HCO_3^- , CO_3^{2-} , Ca^{+2} , and Mg^{+2} are in meq/l.

The RSC values in water samples from boreholes range from 0.61 to 1.18 with a mean of 0.89 ± 0.20 . The SRC values in shallow well samples range from -0.229 to 0.451 with a mean of 0.052 ± 0.242 and from spring samples from -0.27 to 0.014 with a mean of -0.102 ± 0.120 (Table 4).

The United States Salinity Laboratory Staff (1954) classified irrigation waters into three categories based on the RSC values: RSC values < 1.5 (probably safe), 1.5 to 2.5 (marginal) and > 2.5 (not suitable) for irrigation use. The RSC values of all the samples from the three groundwater schemes have less than 1.25 and are considered suitable for irrigation. Based on the calculated values, all water samples have low SAR values (<10), categorizing all samples as excellent for irrigational use. The Na% values of shallow wells and spring samples are <20, classifying the shallow groundwater as excellent for irrigational purposes. The Na% values of boreholes vary from 20 to 40 (3 boreholes), 40–60 (2 boreholes), and 60–80 (2 boreholes), which classifies the different deep aquifers as good, permissible, and doubtful, respectively, for irrigational use.

Moreover, the RSC values in boreholes denote that Na^+ existence in the soils is possible. In contrast, the negative values in shallow wells and spring samples denote that the concentration of Ca^{2+} and Mg^{2+} is in excess. The different categories of water for irrigation use based on the three water quality indicators is summarized in Table 5. The area's groundwater is of good quality but can be vulnerable to contamination. The distribution of the shallow wells in farmlands increases their exposure to anthropogenic contamination.

Table 5. Classification of water for irrigation use based on SAR, Na%, and RSC values.

Parameter	Range	Water class	Water scheme		
			Boreholes	Shallow wells	Springs
SAR	<10	Excellent	7	14	4
	10–18	Good	Nil	Nil	Nil
	18–26	Doubtful	Nil	Nil	Nil
	>26	Unsuitable	Nil	Nil	Nil
Na%	<20	Excellent	Nil	14	4
	20–40	Good	3	Nil	Nil
	40–60	Permissible	2	Nil	Nil
	60–80	Doubtful	2	Nil	Nil
	>80	Unsuitable	Nil	Nil	Nil
RSC	<1.25	Good	7	14	4
	1.25–2.5	Doubtful	Nil	Nil	Nil
	>2.5	Unsuitable	Nil	Nil	Nil

3.3 Water-stable Isotopes (^{18}O and ^2H)

The sciences of isotope hydrogeology that evolved in physics in the 1950s helped to solve Earth and environmental science problems (Barbieri, 2019). The stable water isotopes of hydrogen (^1H , ^2H) and oxygen (^{16}O , ^{18}O) that naturally occur within the water molecule itself undergo fractionation during evaporation/condensation. The fractionation of the water isotopes in most hydrological processes enhances heavier isotopes preferentially in liquid and solid phases while enhancing lighter isotopes in gaseous phases. The heavier isotopes of ^2H and ^{18}O decreased faster than lighter isotopes of ^1H and ^{16}O during the movement of a moist air mass which is saturated with water from the ocean to land. Accordingly, the heavier isotopes are continuously distilled from the air mass

with precipitation. The ratio of heavy to light isotopes in precipitation decreases with time, distance from the sources, and precipitation.

The isotope composition ratio of $^2\text{H}/^1\text{H}$ and $^{18}\text{O}/^{16}\text{O}$ in the water samples are expressed as per mil (‰) deviation relative to the standard mean ocean water (Dansgaard, 1964), which is later modified as Vienna Standard Mean Ocean Water (VSMOW).

$$\delta (\text{‰}) = \frac{R_{\text{Sample}} - R_{\text{VSMOW}}}{R_{\text{VSMOW}}} \times 1000 \quad \text{or} \quad \delta (\text{‰}) = \left(\frac{R_{\text{sample}}}{R_{\text{VSMOW}}} - 1 \right) \times 1000 \quad (8)$$

where $R = ^2\text{H}/^1\text{H}$ or $^{18}\text{O}/^{16}\text{O}$ in the sample and in the standard. Therefore, the $\delta(\text{‰})$ value of a sample identical to the standard will be 0‰, and positive values indicate a greater proportion than the standard, while negative values indicate a lower proportion of the heavier isotope than in the VSMOW. The relative abundance of heavier isotopes to the standard solution help to identify the origins of recharge water relative to the groundwater system and the relationship between surface water and groundwater (Horita & Wesolowski, 1994).

Forty-eight representative samples from rain, surface water, and groundwater were collected during two seasons and analyzed for $\delta^2\text{H}$ and $\delta^{18}\text{O}$ contents. The rainy season samples were collected during September–October 2019 and the dry season from March–April 2021. A statistical summary of the laboratory analysis results of water samples from rain, shallow wells, deep boreholes, springs, and rivers is given in Table 6. The total analytical accuracies are estimated at 0.12‰ for $\delta^{18}\text{O}$ and 0.65‰ for $\delta^2\text{H}$, and the deuterium excess (d-excess) values are calculated using Dansgaard's (1964) equation as

$$\text{d-excess} = \delta^2\text{H} - 8\delta^{18}\text{O} \quad (9)$$

The water samples from different water schemes of the study area showed a wide range of variations with less abundant isotopes enrichment in dry seasons from rain. The $\delta^2\text{H}$ values of the rainfall varied from -1.99‰ to $+55.50\text{‰}$ with a mean value of 23.37‰ , and $\delta^{18}\text{O}$ values ranged from -2.80‰ to $+6.84\text{‰}$ with a mean value of 1.46‰ . The d-excess values of the rain samples vary from 0.77‰ to 20.38‰ with mean and SD values of 11.67‰ and 8.35‰ , respectively (Table 6). Stable water isotopes of the deep aquifers (boreholes) have minimum, maximum, and mean values of -7.99‰ , 0.93‰ , and -2.57‰ respectively for $\delta^2\text{H}$, and -3.98‰ , -1.02‰ , and -2.40‰ respectively for $\delta^{18}\text{O}$. The deep aquifer systems have d-excess values ranging from 6.55‰ to 30.21‰ with mean and SD values of 16.65‰ and 9.89‰ , respectively.

Similarly, the $\delta^2\text{H}$ values of the shallow aquifers varied from -5.04‰ to $+6.01\text{‰}$, with a mean value of 0.69‰ , and $\delta^{18}\text{O}$ values ranged from -2.86‰ to $+11.39\text{‰}$, with a mean value of 1.30‰ . The shallow aquifer has d-excess values that range from -90.4‰ to 17.87‰ , with mean and SD

values of -9.73‰ and 36.16‰ , respectively. The boreholes and rain samples are among the highest d-excess values with a maximum of 30.21‰ and 20.38‰ , respectively. Conversely, the least d-excess values are in the shallow wells followed by the rivers with minimum values of -90.40‰ and -86.25‰ , respectively.

Generally, the stable isotope values of the different water schemes showed variation in deuterium ($\delta^2\text{H}$) values ranging from -7.99‰ to 55.50‰ , the maximum deuterium values from rain samples collected during the dry season and the minimum values in boreholes. Similarly, the heavier oxygen isotope ($\delta^{18}\text{O}$) showed the highest values of 11.39‰ and 10.98‰ in shallow wells and river samples, respectively. The lowest values, -3.98‰ of $\delta^{18}\text{O}$, are obtained from borehole water samples.

Table 6. Statistical summary for the water sample laboratory analysis results of $\delta^2\text{H}$, $\delta^{18}\text{O}$, and the calculated d-excess value in ‰ .

Water scheme	Total no.	Stable isotope	Min. (‰)	Max. (‰)	Mean (‰)	SD
Boreholes	4	$\delta^{18}\text{O}$	-3.98	-1.02	-2.40	1.27
		$\delta^2\text{H}$	-7.99	0.93	-2.57	3.81
		d-excess	6.55	30.21	16.65	9.89
Shallow wells	28	$\delta^{18}\text{O}$	-2.86	11.39	1.30	4.50
		$\delta^2\text{H}$	-5.04	6.01	0.69	2.37
		d-excess	-90.40	17.87	-9.73	36.16
Springs	7	$\delta^{18}\text{O}$	-1.97	5.39	1.23	2.78
		$\delta^2\text{H}$	-1.45	3.98	0.36	1.73
		d-excess	-42.78	14.33	-9.52	22.31
Rain	4	$\delta^{18}\text{O}$	-2.80	6.84	1.46	4.14
		$\delta^2\text{H}$	-1.99	55.50	23.37	24.80
		d-excess	0.77	20.38	11.67	8.35
River	5	$\delta^{18}\text{O}$	-1.88	10.98	4.24	5.260
		$\delta^2\text{H}$	1.16	20.80	7.98	9.242
		d-excess	-86.25	16.52	-25.97	46.37

The depleted heavier isotope and high d-excess values in the deep aquifer indicate the aquifer system is recharged from precipitation less affected by evaporation but performs moisture recycling in the atmosphere. The moisture recycling depletes the heavier isotopes and results in a higher d-excess. The precipitation was in a cold season with high moisture content. The previous research on the stable isotopes of northwest Ethiopian precipitation (Kebede & Travi, 2012) related the sources of the precipitation to the Atlantic Ocean, Congo forests transpiration, and possibly to local recycled moisture. The global rainwater's annual mean d-excess values were above 10‰ of the

ocean moisture (Dansgaard, 1964), which is the primary rainfall source. Brubaker et al. (1993) explained transpired moisture can be an important moisture source for many terrestrial regions, and Wirmvem et al. (2017) designated high d-excess values ($>10\text{‰}$) suggest a further source of moisture, such as moisture recycling.

As a comparison, a long-term (1965–2016) stable water isotope analyzed from monthly precipitation data has been retrieved from the Global Network of Isotope in Precipitation (GNIP) stations situated at Addis Ababa (IAEA/WMO, 2021). The GNIP station value of $\delta^{18}\text{O}$ varies from -7.97‰ to 8.38‰ , and $\delta^2\text{H}$ varies from -55.1‰ to 49.58‰ .

The seasonal variations in $\delta^{18}\text{O}$ and $\delta^2\text{H}$ values are noticeable mainly in the rain samples suggesting atmospheric evaporation before precipitation. The groundwater evaporation and surface evaporation before recharge might be the leading cause of heavier stable isotopes enrichment of shallow groundwater systems and floodplain rivers. The stable water isotopes from borehole samples taken during rainy and dry seasons are depleted in heavier isotopes. This suggests that the deep aquifer system was recharged with depleted heavier isotopes in distant mountains during the rainy season. The relationship between $\delta^2\text{H}$ and $\delta^{18}\text{O}$, elucidated by Dansgaard (1964), called “global meteoric water line” (GMWL), is the basis for interpreting the stable water isotopes related to hydrological processes. The laboratory analysis result values plots of $\delta^{18}\text{O}$ versus $\delta^2\text{H}$, together with GMWL, as presented in Fig. 25. The Addis Ababa GNIP station is considered the nearest GNIP station, 25-year value of $\delta^{18}\text{O}$ and $\delta^2\text{H}$ is used as a local meteoric water line (LMWL). The GMWL is calculated based on the equation $\delta^2\text{H} = 8\delta^{18}\text{O} + 10\text{‰}$ derived by Craig (1961), whereas the Addis Ababa LMWL is represented by the equation $\delta^2\text{H} = 7.0\delta^{18}\text{O} + 11.56\text{‰}$. The Addis Ababa LMWL equations have an approximately similar slope to GMWL’s, showing the dynamic fractionation during precipitation formation. The higher intercept indicates the moisture recycling before rainfall as the moisture travels from the sources to the high elevation topography of Addis Ababa.

The stable isotope data from the rain samples are closer to LMWL than the GMWL. The seasonal variations are observed in the rain’s samples with a proportional increase in heavier isotopes during the dry season. A similar characteristic is observed in some rivers, shallow wells, and springs samples, with enrichment of heavier isotopes during the dry season and depleted heavier isotopes during the rainy season. The higher proportional enrichment of stable isotopes is detected in rain and river samples during dry seasons. The dry season rains possess atmospheric evaporation that enriches heavier isotopes in precipitation samples more than the rainy season precipitation. The atmospheric temperature effect is observed in the dry season precipitation and direct evaporation in

the rivers during the dry season. The higher $\delta^{18}\text{O}$ values than $\delta^2\text{H}$ in the shallow aquifer system (shallow well and spring samples) are related to the groundwater evaporation in the vadose zone or when the groundwater flows to the discharge zones such as springs. The atmospheric evaporation results in a proportional and synchronized increase of $\delta^2\text{H}$ and $\delta^{18}\text{O}$ content in precipitation, whereas the surface evaporations enrich $\delta^{18}\text{O}$ to a greater extent than $\delta^2\text{H}$ content. The global atmospheric precipitation has a synchronized $\delta^2\text{H}$ and $\delta^{18}\text{O}$ content, the average $\delta^2\text{H}$ value being eight times higher than $\delta^{18}\text{O}$ values, triggered mainly by the dynamic fractionation during evaporation (Li et al., 2020). Therefore, the deviation of the data values from GMWL is controlled by climatic and geographic variables (Dansgaard, 1964). However, the Ethiopian mounts in the plateau land orographically enhance rainfall while creating a variable climate and a variable isotope composition than the sources (Kebede & Travi, 2012).

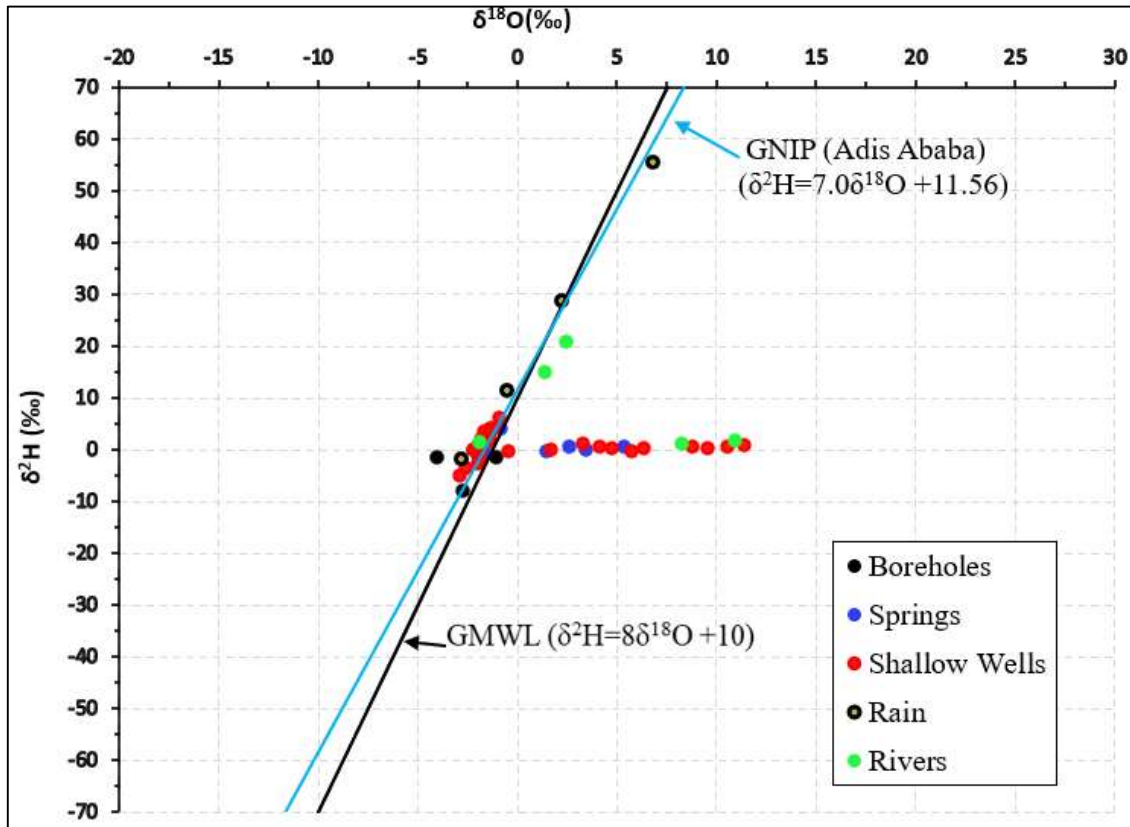


Fig. 25 Graph of $\delta^{18}\text{O}$ versus $\delta^2\text{H}$ values from different water schemes. The GMWL and LMWL of GNIP stations in Addis Ababa are used as a comparison.

4.3.1 $\delta^{18}\text{O}$ versus d-excess

The prominent character of the different water schemes stable isotope analysis data is the relationship between the $\delta^{18}\text{O}$ and *d*-excess (Fig. 26). The rain samples are positioned with *d*-excess between 0‰ to 10‰ with the dry season samples below 10‰. The three samples from boreholes located above 10‰ and a few spring, river, and shallow wells samples have *d*-excess values close to 10‰. The values above 10‰ suggest atmospheric moisture recycling, whereas below 10‰ suggest atmospheric evaporation before precipitation. Kebede et al. (2009) related the Ethiopian Plateau land deep volcanic aquifers characterized by depleted heavier isotopes to the late Holocene humid phase based on the ^{14}C data.

There are water samples from rivers, shallow wells, and a few springs with a low *d*-excess value but enriched in $\delta^{18}\text{O}$ content. This suggests that the groundwater samples are affected by evaporation in different ways. The shallow aquifer is recharged from the river exposed to the surface's evaporation at places where the geology favors that. The reverse scenario is possible depending on the geology, as the shallow groundwater might be affected by evaporation at the vadose zone or when the flows close to the surface emerge as a spring. The springs recharge the rivers, and again the river is exposed for further evaporation, particularly during the high sunshine dry season. There are seasons of stagnant waters in the floodplains due to the clay soil reducing the recharge. The water can be affected by the evaporation while recharging the shallow groundwater system at a slow rate because of the minor permeability nature of clay soils.

The variations in the $\delta^{18}\text{O}$ and *d*-excess in the groundwater system indicate that the groundwater is recharged at different places from different sources. The precipitation, being the main recharging source, recharges the boreholes, rivers' upstreams, Highland Springs and shallow wells. The rivers recharge the shallow aquifer at favorable places along its channels, and the shallow well also recharges the rivers, depending on the geology and morphology. The stagnate water in the wetlands recharges the groundwater, and the reverse is also true—that the groundwater from the mountain fronts recharges the wetlands.

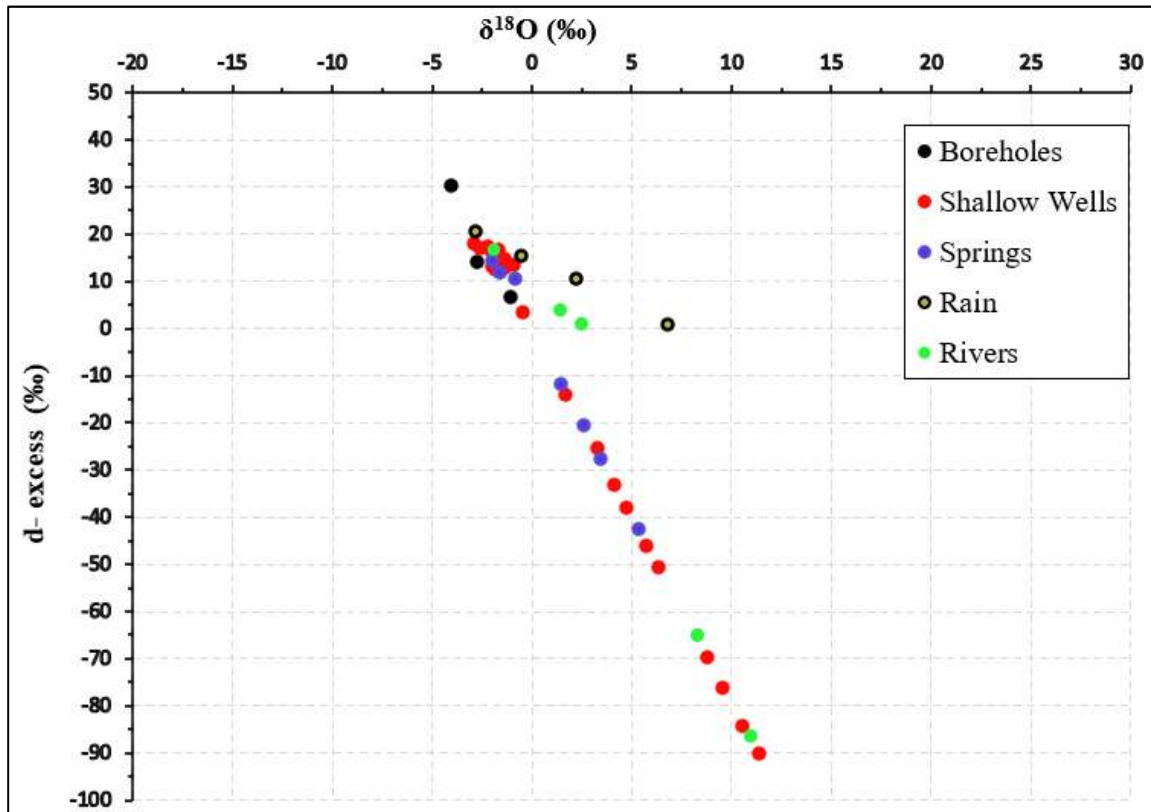


Fig. 26 Relationship between $\delta^{18}\text{O}$ versus d-excess in different water schemes.

4.3.2 The spatial distribution of $\delta^{18}\text{O}$ and $\delta^2\text{H}$

The precipitation amount has a minor effect on the stable water isotope of northwest Ethiopian precipitation, and the latitude variations are minimal too, with $\delta^{18}\text{O}$ being 0.1‰/100 m (Kebede & Travi, 2012). However, there has not been a spatial distribution of isotopes in small watershed scales that enables observation, including watching of local effects. The spatial distributions of the content of $\delta^{18}\text{O}$ and $\delta^2\text{H}$ are presented in contour maps (Figs. 27 and 28).

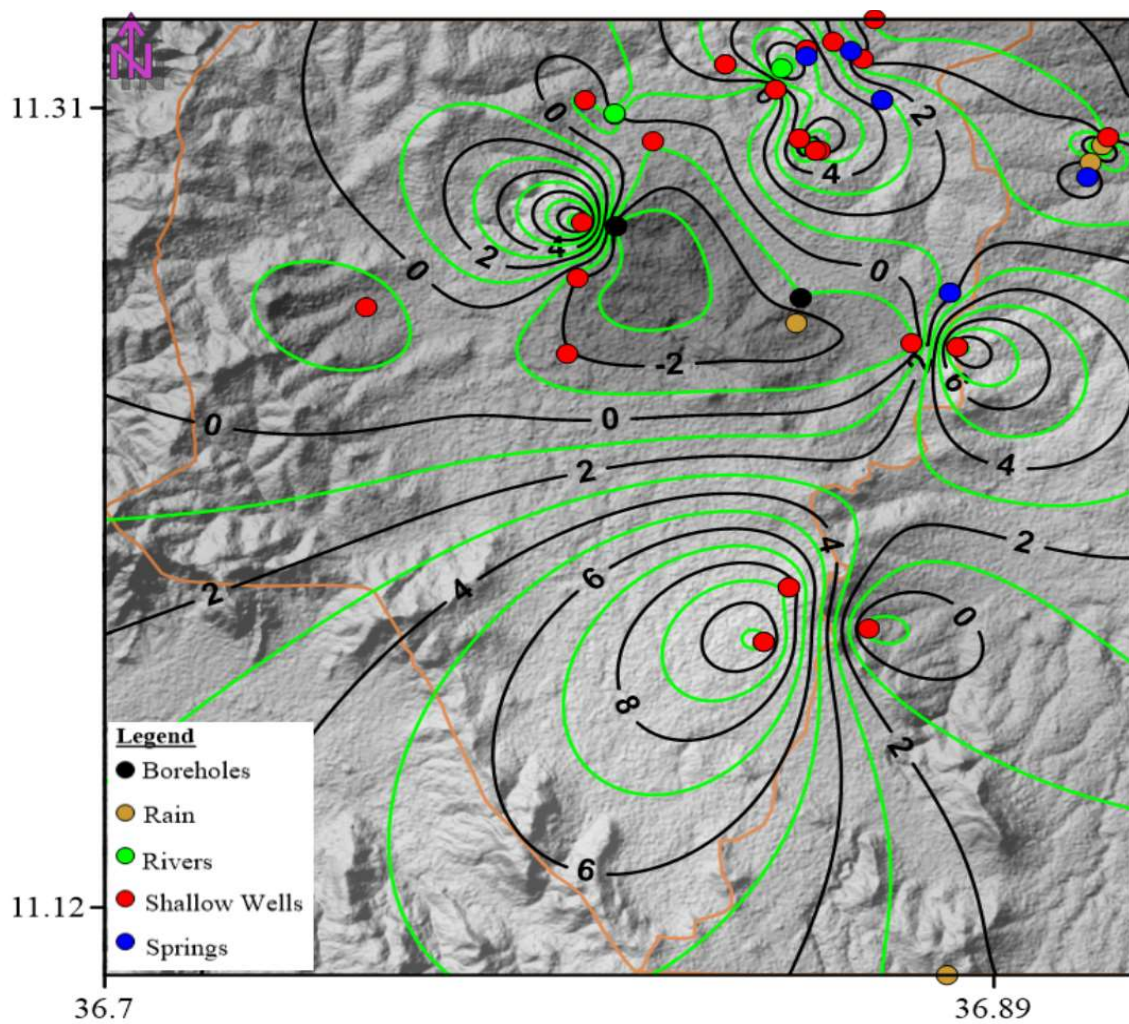


Fig. 27 Contour map of $\delta^{18}\text{O}$ content overlaid on the digital elevation model with sample locations.

The relationship between the elevations used as a proxy for surface water flow and enrichment of heavier isotopes is noticeable for the shallow aquifer system. The direct increase with topography or decrease with the direction of surface water flow is more recognizable for deuterium than for $\delta^{18}\text{O}$. However, the $\delta^{18}\text{O}$ distributions also indicate an increase in the surface water flow. This suggests that the deuterium content is more affected in atmospheric phenomena, including moisture recycling than in surface and groundwater evaporation. However, the content of $\delta^{18}\text{O}$ is affected by both factors, being more influenced by surface evaporation. Conversely, there has not been any relationship observed between the rain and boreholes samples' stable isotope concentrations and surface water flow directions or topography.

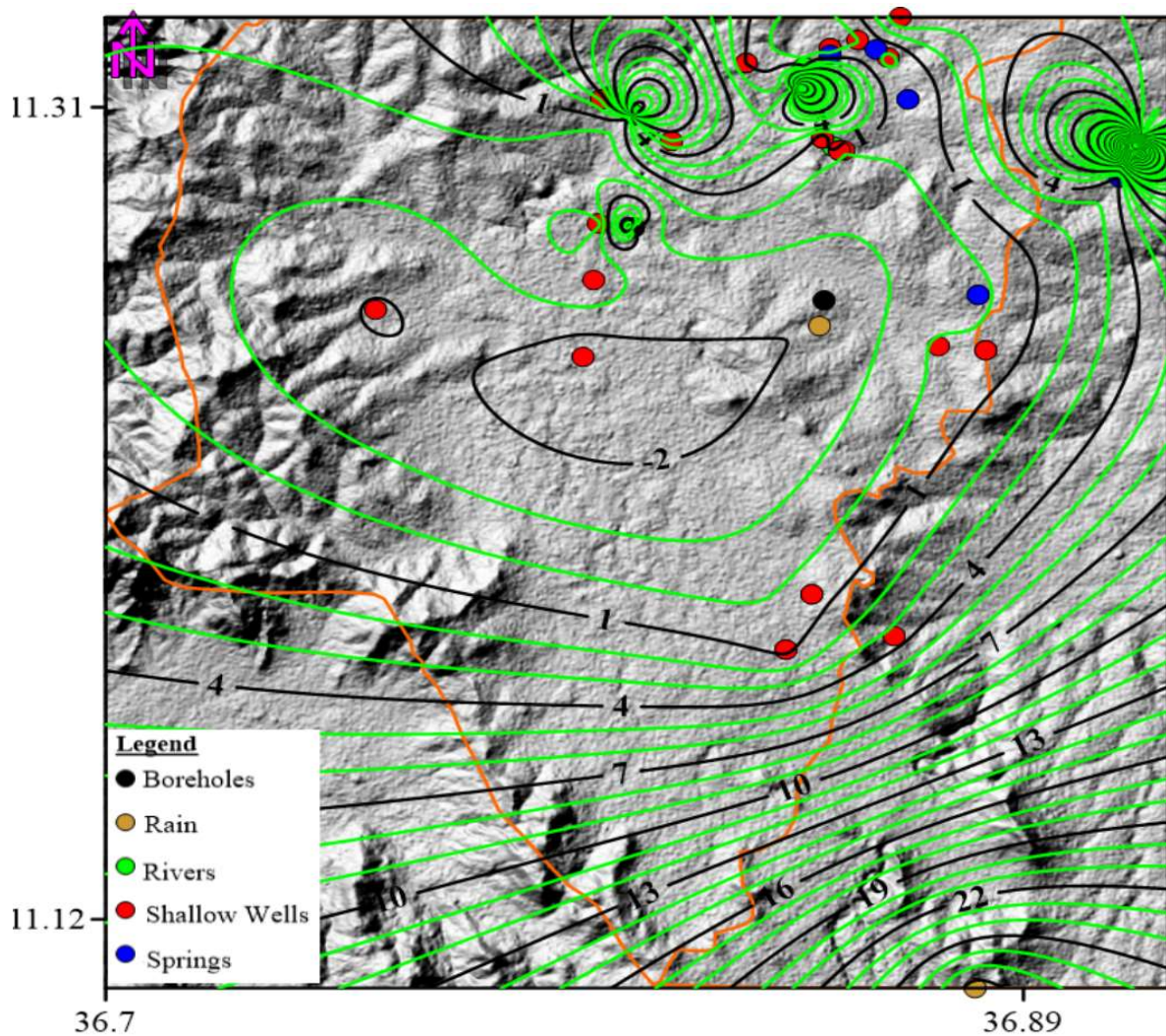


Fig. 28 Contour map of $\delta^2\text{H}$ content overlaid on the digital elevations model with sample locations.

Generally; based on the stable water isotope data analysis, the recharge systems of the groundwater can be observed in three forms:

1) direct, preferential, and rapid recharge favored by faults, thick soil, and regolith, and by abundant rainfall in uplands. This recharge system recharged the highland area shallow aquifer system and discharged as springs and streams. It possesses an intermediate groundwater flow through the fault and recharges the deep aquifer system. This results in depleted heavier isotopes groundwater being recharged mainly during the cold rainy season.

2) direct and rapid recharge to the shallow aquifer system through the thick soil and regolith. The system discharges locally to the upper part of the river using springs near the foot of mountains.

However, this type of recharge is not connected to the fault. It is favored by local shallow groundwater to flow with local discharge at close distances from the recharge.

3) diffuse recharge in the floodplains from the rain and stagnant water in the wetlands. This recharges the shallow groundwater system in relative lowlands with an enriched heavier oxygen isotope. The system includes a recharge from the return of water from small-scale irrigation using the river water and the shallow groundwater to groundwater with enriched heavier isotopes content. The small-scale irrigation at the floodplains with diverted river canals and shallow hand-dug wells produces a return flow.

4.4 Hydrogeophysical Properties

4.4.1 Geomagnetic survey results

The near-surface geomagnetic data, at 718 locations excluding repeated readings, were gathered during February 2018 and March 2021. A quiet day was chosen for the survey, and data were collected at a far distance from power lines that occasionally produce strong and local anomalies. These data have been corrected for diurnal and cultural effects that possibly affect the survey results. The corrected data are grided with kriging statistics (Shi, 2014) using the minimum and maximum limits based on the survey data. The gridding procedure uses grid node values based on the known data points from the neighboring node, with each data point weighted by its own distance from the node. The points that are located further from the node have less weight in the estimations of the node. The extrapolation effect has been limited by considering the part of the study area, close to points where the magnetic data was gathered, during the total magnetic field map production.

The processed total magnetic field data values vary from 34,000 nT to 65,000nT. The theoretical geomagnetic field value of a place located in the area has approximately 36,274nT based on the International Geomagnetic Reference Field (IGRF) model-13. Conversely, the Earth's total magnetic field vector varies in strength from approximately 24,5000 to 67,000 nT, with the largest field intensities occurring in Siberia, Australia and the Antarctic, and the lowest in South America (Alken et al., 2021).

The common cause of magnetic anomalies in volcanic terrains are massive basaltic intrusive rocks, the underlaying metamorphic basement below the Mesozoic sediments, dikes, faults, folded sills, basaltic lava flows, and magnetite ore bodies. The magnetite mineral (Fe_3O_4) that causes the most common geomagnetic field anomaly has a Curie temperature of 578°C. The Mesozoic sediments

below the basaltic lava flow have lower influences on the surface geomagnetic survey data unless they possess iron-containing bodies. Therefore, the high magnetic field values observed at specific and localized places are related to the basic igneous rocks with high magnetite contents. The effect of magnetite on the magnetic field data decreases with increasing acidity in igneous rocks (Kearey et al., 2002). The basic igneous rocks, basalts, are found close to the surfaces; therefore, the main magnetic field signals that cause high magnetic field anomalies are related to the shallow depth of basic igneous rocks and their structures.

The overlapping nature of magnetic susceptibility values of most rocks results in an overlapping magnetic anomaly in measured geomagnetic field data. This creates difficulty in precisely identifying the anomalies by basic igneous rocks and lower metamorphic basement rocks. However, the influence of sedimentary rocks on the near-surface geomagnetic field measurements is insignificant, as most sedimentary rocks are nonmagnetic or have a small susceptibility value. Exceptional cases can occur if the sedimentary rock contains significant magnetite as a fraction of heavy minerals.

The magnetic survey is aimed at mapping the fractures and other structures in the hard rock up to a certain depth of the crust, mainly caused by the upper basaltic lava flow and the lower and lower metamorphic basement. It suits shallow structural mapping and geological study such as a Curie isotherm for common ferrimagnetic minerals that lie at or above a depth of approximately 20 km. Accordingly, the sources of major anomalies are consequently restricted to the upper part of the continental crust (Kearey et al., 2002).

The total magnetic field maps show the presence of several structures which are buried and not observed on the ground or on the geological map (Fig. 29). However, these structures have the same orientation as the Lake Tana Basin regional structures identified by Beshawered et al. (2010). They have orientations of N–S, NW–SE, NE–SW, and E–W with different vertical and lateral extents. The majority of these fractures are not visible on the surfaces due to the weathered rock and soil cover. The N–S oriented structures have greater influences on the near-surface geomagnetic data, and they are situated at greater depths relative to other structures. The NW–SE, NE–SW, and E–W oriented structures have lower influences on the total magnetic field data due to their relatively shallow depths.

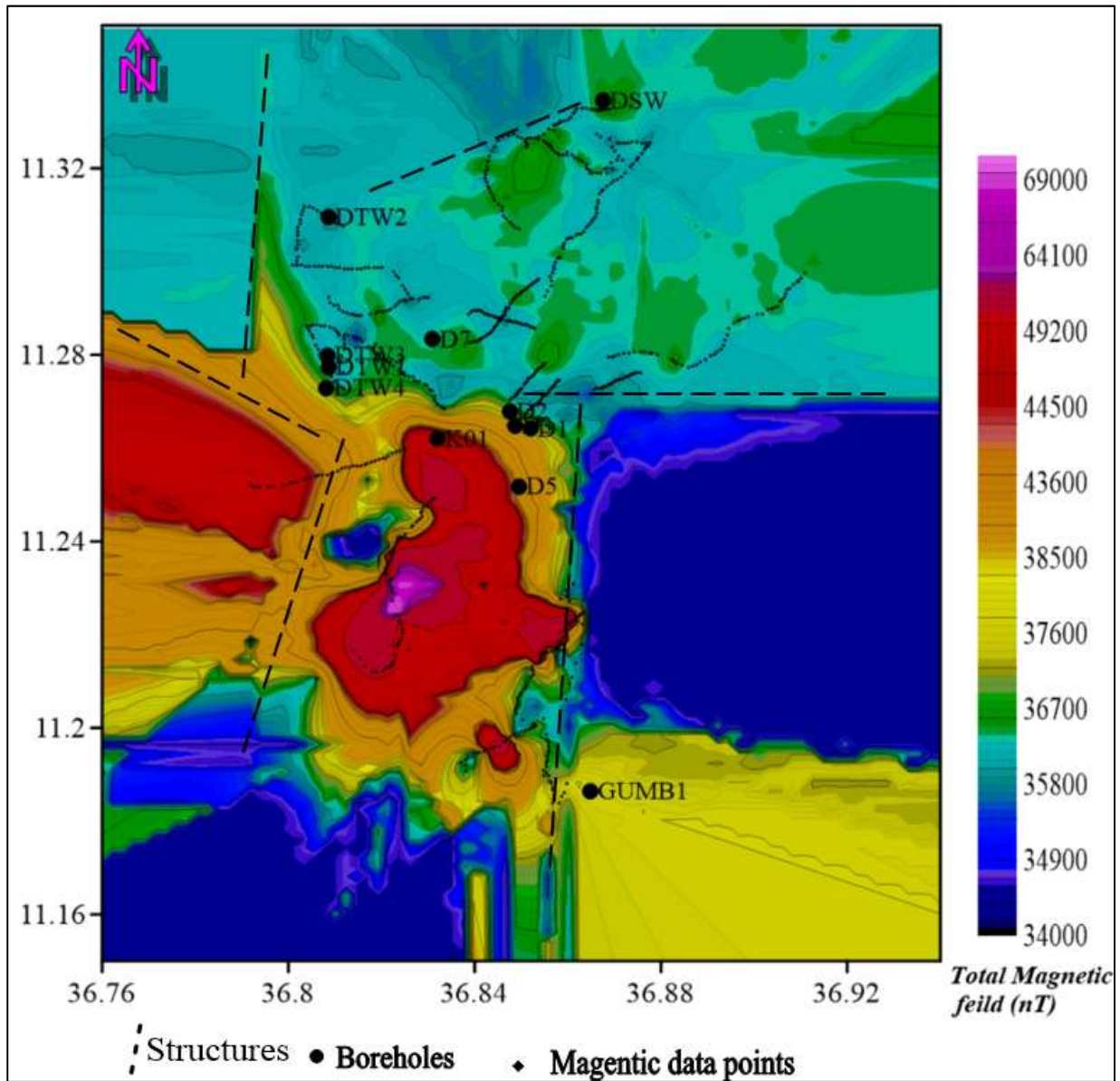


Fig. 29 Total geomagnetic field maps with inferred structures.

4.4.2 Magnetic field profile plots

The total magnetic field profile plots and the borehole lithology at the structural lines indicate that these inferred structures are mainly faults and fractures (Fig. 30). Several faults form a horst and graben structure used as a groundwater conduit and storage, depending on their recharge locations. The two magnetic profile plots of the total magnetic field data, profile AB approximately oriented NW–SE and profile CD approximately oriented E–W, enables the inference of normal and reverse faults, respectively (Fig. 30). The most productive boreholes that supply fresh groundwater to the town of Dangila

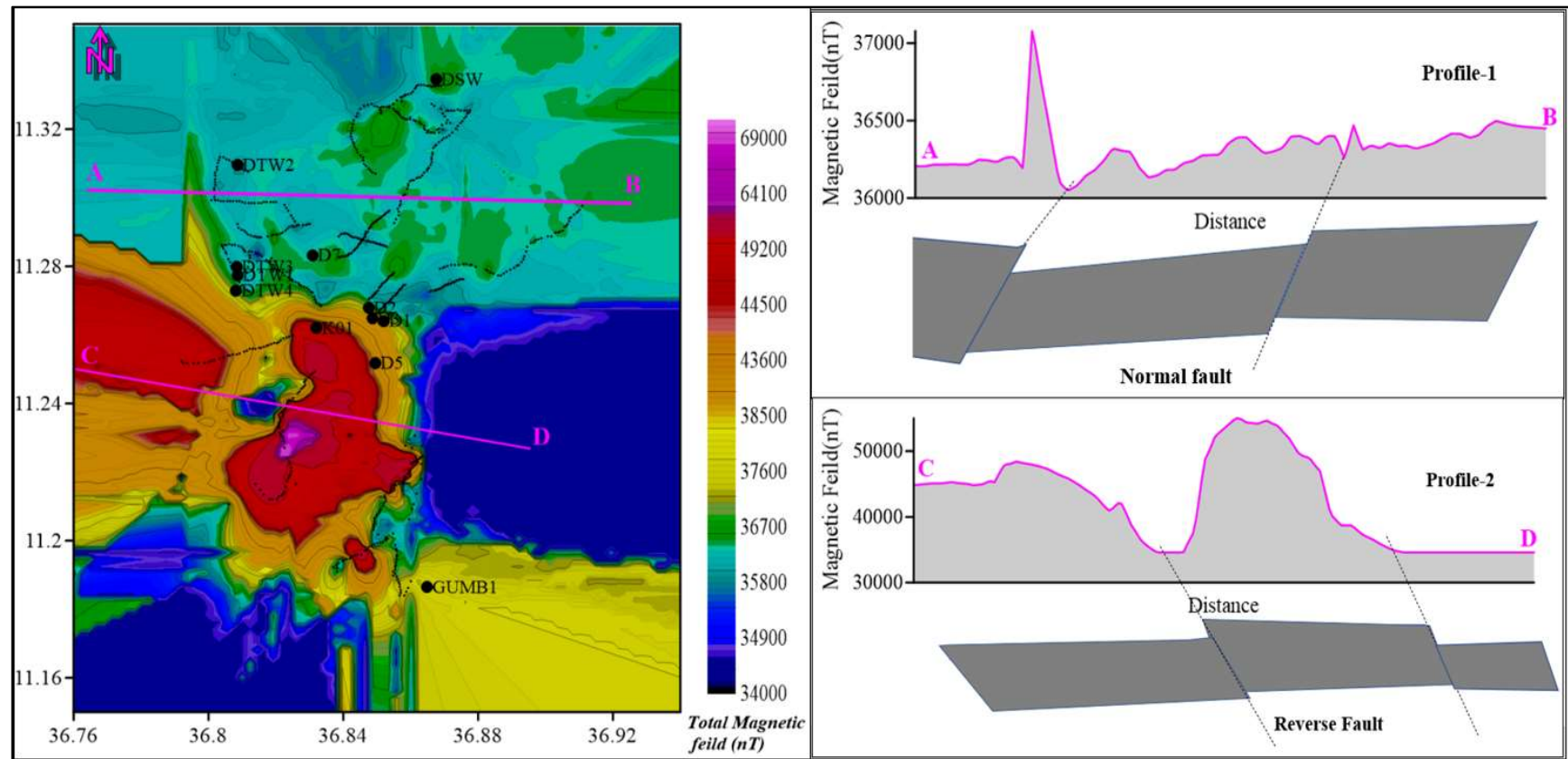


Fig. 30 Magnetic profiles from the total magnetic field data with the possible type of fault orientations.

(DTW1, DTW3, and DTW4) are located along the NW–SE fracture. Similarly, the recently drilled Denegeshita kebele borehole that supplies >30 L/s fresh groundwater is situated along the NE–SW fracture. These indicate that the deep aquifer systems use these structures as groundwater conduits and storage. Therefore, a detailed investigation of these shallow structures might be helpful when selecting the production well site in the future.

There are no boreholes in the area that penetrate and supply groundwater from the E–W oriented structures, so their influence on groundwater movement and storage are not yet recognized. The fractures, joints, or termination points are the most promising places for groundwater storage. The higher depth boreholes might be valuable for groundwater abstraction if they penetrate this N–S oriented deep fractures. These structures have a tendency to affect the lower Mesozoic sediments and the basement rock of the region. The fractures are possible groundwater conduits for regional groundwater flows. Therefore, a deeper borehole greater than 200 m in depth might be more important than the already existing boreholes for abstraction of groundwater from the Mesozoic and fractured basement rocks, along with the N–S fractures.

4.4.3 Vertical electrical sounding

VES geophysical techniques offer hydrogeologists unprecedented access to understanding potential groundwater zones, geological structures, aquifer parameters, and hydrogeological processes. VES data were gathered at 32 points, with 19 to 24 readings at each point, employing the Schlumberger electrode arrangement (Table 7). A total of 129 readings from 32 points were collected, with two main types of potential and current electrode distance arrangements from the central point. Five readings were recorded in a single log cycle, and repeated readings were taken at each point where the potential electrode distance from the central point changes. The change in potential electrode distance was considered to avoid the minimum value of potential readings due to a varying distance of the current electrodes from the VES point. Minimum half current electrode spreads of 1.5, and 1 m and maximum half current electrode spread of 300, 330, 400, 500 and 750 were used, depending on the target depth of penetration and the suitability of the landscape.

Table 7. Summary of the minimum and maximum half current electrode AB/2 (m) and potential electrode MN/2 (m) spread; the number of readings taken at each VES point, with the total number of VES. Detailed information about each VES is presented in Appendix 1.

No.	Min.	Max.	Min.	Max.	No. of reading		Total
	AB/2 (m)	AB/2 (m)	MN/2 (m)	MN/2 (m)	Single VES	Total	VES
1	1.5	330	0.5	45	19	39	2
2	1.5	500	0.5	45	20	200	10
3	1.5	750	0.5	45	21	84	4
4	3	400	1	50	23	253	11
5	3	300	1	50	22	88	4
6	3	500	1	50	24	24	1
Total						688	32

4.4.4 Apparent resistivity graphs and two dimensional (2D) sections

The corrected and smoothed apparent resistivity data values vary from $6.9\Omega\text{m}$ to $460\Omega\text{m}$. Even though the cumulative value of the nearby layers results in the reading, the lower resistivity values are obtained due to low resistivity layers situated at various depths. The majority of soil and rock-forming minerals are inherently non-conductive. Conversely, metallic ore minerals are uncommon relative to other crustal materials. However, even in small quantities, their presence can significantly affect the bulk resistivity. Therefore, electric current below the surface flows entirely through water, occupying pore spaces and fractures. The variation of the resistivity of soil and rocks is used to identify water-bearing horizons and can be modeled to infer each layer's resistivity, depth, and thickness. The apparent resistivity is affected by materials at increasingly greater depth as the electrode spacing is increased; as a result, a plot of apparent resistivity against electrode spacing is used to indicate vertical variations in resistivity.

The VES data is displayed in log-log graphs to qualitatively estimate the minimum number of resistivity layers and the characteristics of VES curves (Fig. 31). Using a simplified classification system based on qualitative remarks, the 32 VES curves were divided into three categories. Category A containing H and HK type curves vary from 3 to 4 layers, and category B with K, KH, and KHK curves varies from 3 to 5 layers. Category C of 5 VES with HK type curves are profoundly

influenced by fractures and faults. In general, Categories A, B, and C account for 59.4 %, 28%, and 15.6% of all VES, respectively.

The qualitative observations of the VES data were performed using the distance between VES points in the horizontal axis, and the half current electrode spread served as a proxy for depth in the vertical axis. The 2D pseudo-depth sections along VES data points depicted variations in apparent resistivity with depth due to variation in subsurface layers. The two selected 2D pseudo-depth maps are presented (Fig. 32), which are helpful for observing the variations in apparent resistivity with pseudo-depth and for identifying groundwater-bearing layers.

The 2D pseudo-depth map made from the apparent resistivity value of four VES points (V26, V27, V31, V28) shows that the apparent resistivity value continues as low beneath V31 and V28. The apparent resistivity values continue being $<35 \Omega\text{m}$ with depth and later change to $<15 \Omega\text{m}$. The fracture beneath these two VES points is saturated with groundwater, influencing the apparent resistivity values to drop to less than $15 \Omega\text{m}$. A borehole drilling at V31 with an 8-in diameter and maximum depth of 160 m, depending on the geophysical survey results of this thesis, resulted in a confined, artesian well with a yield of $>30 \text{ L/s}$. The borehole information indicated that the intermediate depth with a very low resistivity value is a confining aquifer layer that results in an artesian borehole.

The magnetic data map of the area demonstrated that the borehole is located at the terminating point of the fracture with NE–SW orientation. The different timing of volcanic eruption after the formation of fracture results in a basaltic lava flow on the top of the fracture and acts as a confining layer. Perversely, a dry borehole with 80-m depth is located approximately 1km from the artesian and productive boreholes, suggesting that the groundwater system is primarily fracture controlled. The 2D pseudo-depth map made from the apparent resistivity value of four VES points (V26, V27, V31, V28) showed that the apparent resistivity value continues as low beneath V31 and V28. The apparent resistivity values continue being $< 35\Omega\text{m}$ with depth and later change to $< 15 \Omega\text{m}$. The fracture beneath these two VES points is saturated with groundwater, influencing the apparent resistivity values to less than $15 \Omega\text{m}$. A borehole drilling at V31 with a diameter of 8 in and a maximum depth of 160 m, depending on the geophysical survey result of this thesis, resulted in a confined, artesian well with a yield $> 30 \text{ L/s}$. The borehole information indicated that at the intermediate depth with a very low resistivity value is a confining aquifer layer that results in an artesian borehole. The magnetic data maps of the area depicted that the borehole is located at the terminating point of the fracture with NE–SW orientation. The different timing of volcanic eruption after the

formation of fracture results in a basaltic lava flow on the top of the fracture and acts as a confining layer. Perversely, a dry borehole with 80-m depth is located approximately 1km from the artesian and productive boreholes, suggesting that the groundwater system is primarily fracture controlled. Similarly, the 2D pseudo-depth maps comprised of seven VES points (V8, V9, V10, V11, V21, V22, V23) showed low apparent resistivity values beneath VES points V8, V9, and V10. The value increases with depth, indicating that the water-bearing layers decrease with depth beneath these three VES points. The apparent resistivity indicates the existence of faults close to these three VES points, which would have been used as a conduit and groundwater storage. The water-bearing fractured layers are at a greater depth than the confined aquifer layers located at V31. The three boreholes drilling close to the three VES points yield 18.5, 24, and 30 L/s. These boreholes serve as the main sources of fresh water for the town of Dangila.

However, the isotope and hydrochemistry data indicated that direct recharge from the surface is minimal. The deep aquifers from these boreholes are depleted ^2H and ^{18}O values, unlike the floodplains' shallow aquifer system. Moreover, the deep aquifers of these boreholes have Na-HCO_3 type water, which is a characteristic of deep and long residence time groundwater, unlike the shallow aquifers systems, which have Ca-CHO_3 water types.

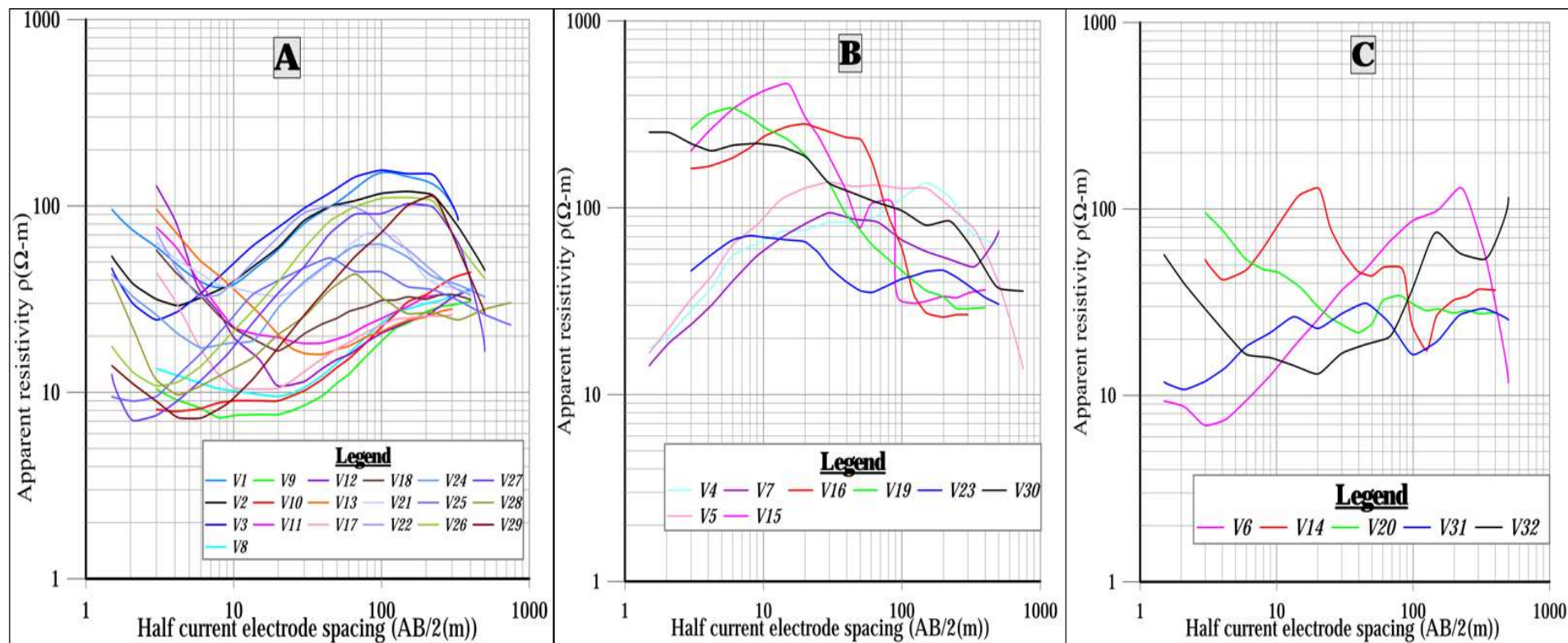


Fig. 31 Three categories of VES curves on a Log-log graph.

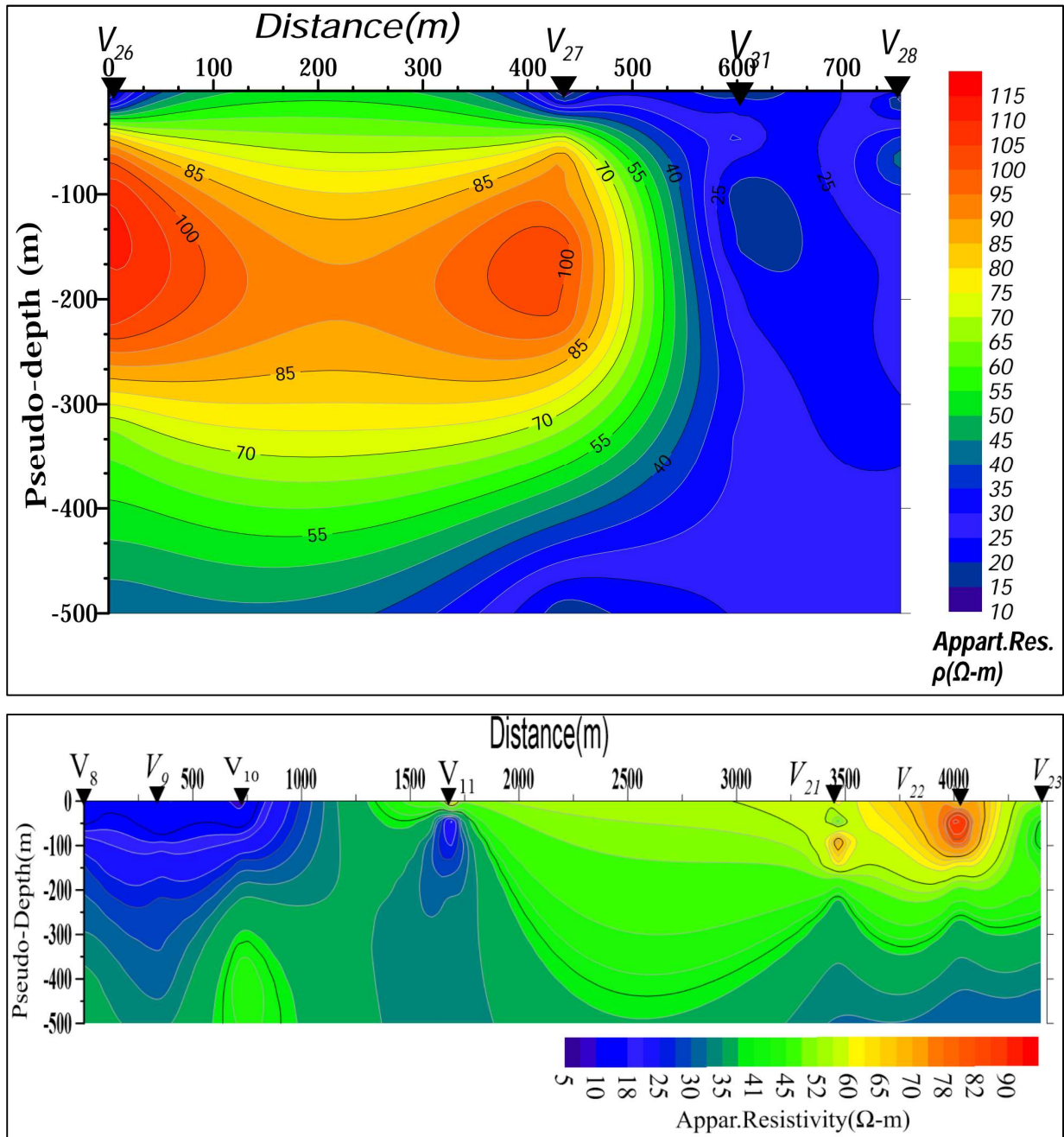


Fig. 32 2D apparent resistivity pseudo-depth sections including selected VES points.

Moreover, a fault is observed from the same 2D section between V11 and V21, though those VES points are found at far distances approximately 1780 m apart. Contrarily, the apparent resistivity beneath these two VES points did not imply the presence of an aquifer with a higher yield. There are stratified layers beneath V21, V22, and V23 with a low gradient decrease in apparent resistivity values with depth. A borehole drilled close to V23 results in 3 L/s groundwater yield, mainly from the weathered scoria and scoriaceous aquifer layers situated at a relatively greater depth. The low

yield of the boreholes is due to the absence of major fractures connected to recharge that can hold and transmit groundwater. The 3 L/s yield in the boreholes could be due to low hydraulic conductivity scoria. Scoriaceous aquifer and the upper unconfined aquifer add volumes of water through the boreholes' surrounding openings and gravel packs arranged during borehole construction.

4.4.5 One-dimension (1D) inverse modeling of VES data

The apparent resistivity map and 2D sections enables qualitative observation of the VES survey result. However, a detailed quantitative interpretation of the field data is crucial to characterize the aquifer system of the area. Therefore, after the qualitative examination of the VES curves, matching of the field data curve with the master curves, followed by a 1D inverse modeling of each VES point data item, have been conducted. The results of qualitative and curve matching techniques are used as an initial model for 1D inverse modeling. The borehole information is used to avoid non-uniqueness and the effects of thin layers. Besides, the penetration depth (Z) that depends on the current electrode spreads (AB) has been carefully chosen for meaningful and reasonable depths. Kearey et al. (2002) stated that when the current electrode spread is $(AB) = \text{depth } (Z)$, approximately 30% of the current flows below Z , and when $AB = 2Z$, approximately 50% of the current flows below Z , as 1 km is the limit of the depth of penetration for standard field equipment. The depth determination methodology called median depth (Edwards, 1977; Barker, 1989), which accounts for >50% current flow above the target penetration depth, has been considered during 1D inverse modeling.

The 1D inverse modeling of VES data allows inferring the causative five to eight geological layers. Samples of the 1D inverse model VES curves are given in Fig. 33, while the remaining are presented in Annex 3. These layers differ in rock type, depth of burial, and degree of weathering and fracturing. The resistivity of these layers varies from 1 to 15171 $\Omega\text{-m}$, associated with weathered scoria, scoriaceous, altered clay, and water-bearing layers to the fresh aphanitic basalt without pores and fractures. The scoria layers situated at higher depths are highly weathered and changed into clay soil, resulting in much lower resistivity than the water-bearing fractured basalts.

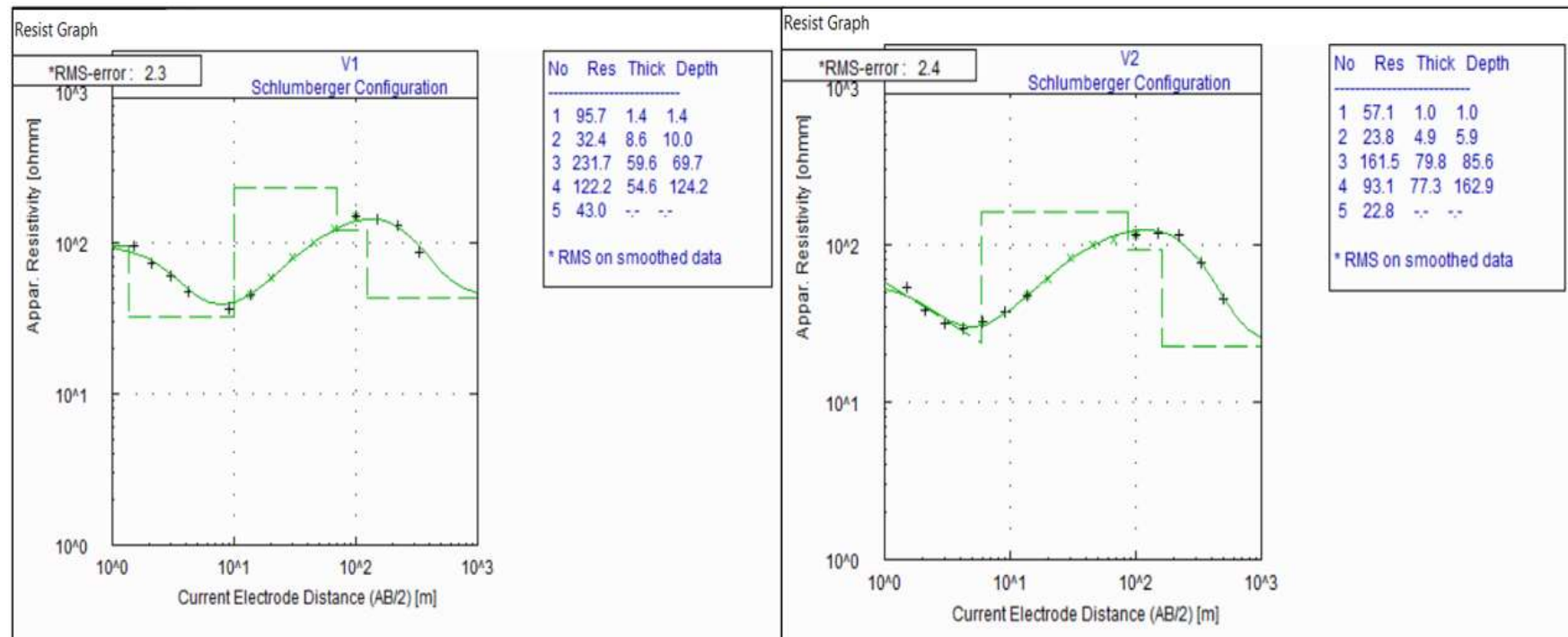


Fig. 33 Samples of 1D inverse modeled VES with corresponding resistivity, thickness, and depth.

4.4.6 The 2D Geoelectric sections

The model resistivity values of VES data and their corresponding pseudo-depth sections are used to construct 2D geoelectric sections. The geoelectric sections comprising selected VES 1D inverse modeling data make up seven different resistivity layers (Fig. 34). The two faults passing close to these VES points are inferred with their corresponding orientations in 2D vertical sections. The nearby borehole data are used to correlate the rock types that depicted the different layer resistivity values. The different layers from top to bottom include clay soil or dry soils, highly weathered basalt with scoria, weathered vesicular with scoriaceous basalt, highly weathered basalts, massive basalts, and weathered and fractured basalt layers. These layers' resistivity values differ depending on the presence or absence of water, the degree of weathering and fracturing, and the rock type constituting each layer. However, the presence or absence of water within the layers depends on the degree of weathering and fracturing and connections to the fractured layers and the recharge area. The total depth of these layers in the inferred geoelectric sections extends from 0–160 m.

The resistivity variation in each of these layers include: clay soil (6–8.2 Ω -m), highly weathered basalt with scoria (18–26 Ω -m), highly weathered basalt (67–99 Ω -m), massive basalt (122–184 Ω -m), weathered and fractured basalt (16–33 Ω -m), and weathered scoriaceous basalt (18–43 Ω -m).

Except for massive basalt, these different resistivity layers are water-bearing at different depths. The groundwater yields of boreholes fully or partially penetrating these aquifers differ depending on their location in relation to fractures and recharge. The most prominent aquifer layer is the highly weathered and fractured basalt situated below 130 m.

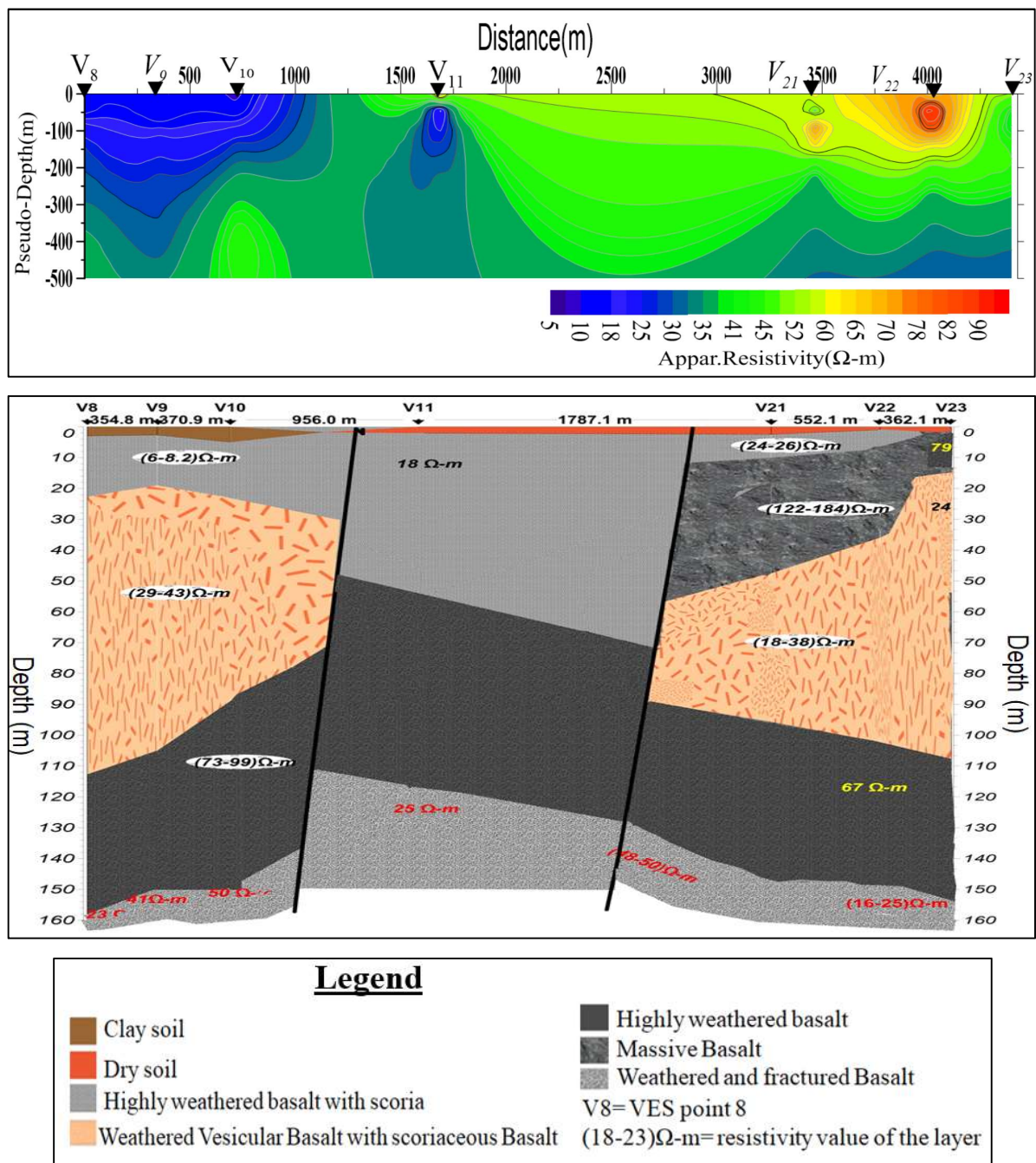


Fig. 34 2D geoelectric section with its corresponding apparent resistivity pseudo-depth section.

4.4.7 Three-dimensional (3D) visualization of 1D modeled VES results

The 1D modeling results of the VES data are used to visualize the variations in the resistivity values beneath each VES point in 3D. Suppose the resistivity of each layer is represented by point resistivity at the medium thickness of each resistivity layer. In that case, the variation in resistivity is visualized in 3D space volume using 3D scatter plots (Fig. 35). Another alternative is using the backlash for the layers represented by a single resistivity beneath each VES point and visualizing the variation beneath the VES points. It is shown that the resistivity values at each VES point at different depths is variable, indicating the presence of heterogeneous resistivities that corresponds to the heterogeneous aquifer. The resistivity value varies vertically and laterally in space, mainly showing low resistivities at greater depths. The northwest part of the area, encompassing the flood-plains, has a better groundwater potential, whereas the southeast parts have less groundwater potential, including the greater depths. Generally, the heights' resistivity values are at shallow and intermediate depths and lost resistivity layers are at depths > 130 m. The 3D scatter indicates that the occurrence of water beneath the ground is very complex and heterogeneous, as there are no uniform, homogenous aquifers at a given depth. The heterogeneity occurs at shallow depths, resulting from the upper shallow unconfined aquifer system being a perched aquifer system.

The 3D visualization is further represented by the 3D boxplots filling the spaces between the resistivity values with uniform pixels from the nearest data resistivity value (Fig. 36), which enables visualization of the resistivity in different directions.

The 3D boxplot represents interpolated cubes of an input matrix using one unit in each of the X, Y, and Z directions in which different colors represent each component value. The resistivity values vary from place to place and in different directions. The high resistivity is found at a shallow depth due to the massive basaltic layers resulting from the mafic lava flow. The lowest resistivity values at greater depths are either due to the fractured basalt that stores groundwater representing good groundwater potential or the presence of highly weathered scoria and scoriaceous layers, occasionally altered into clay, at greater depths.

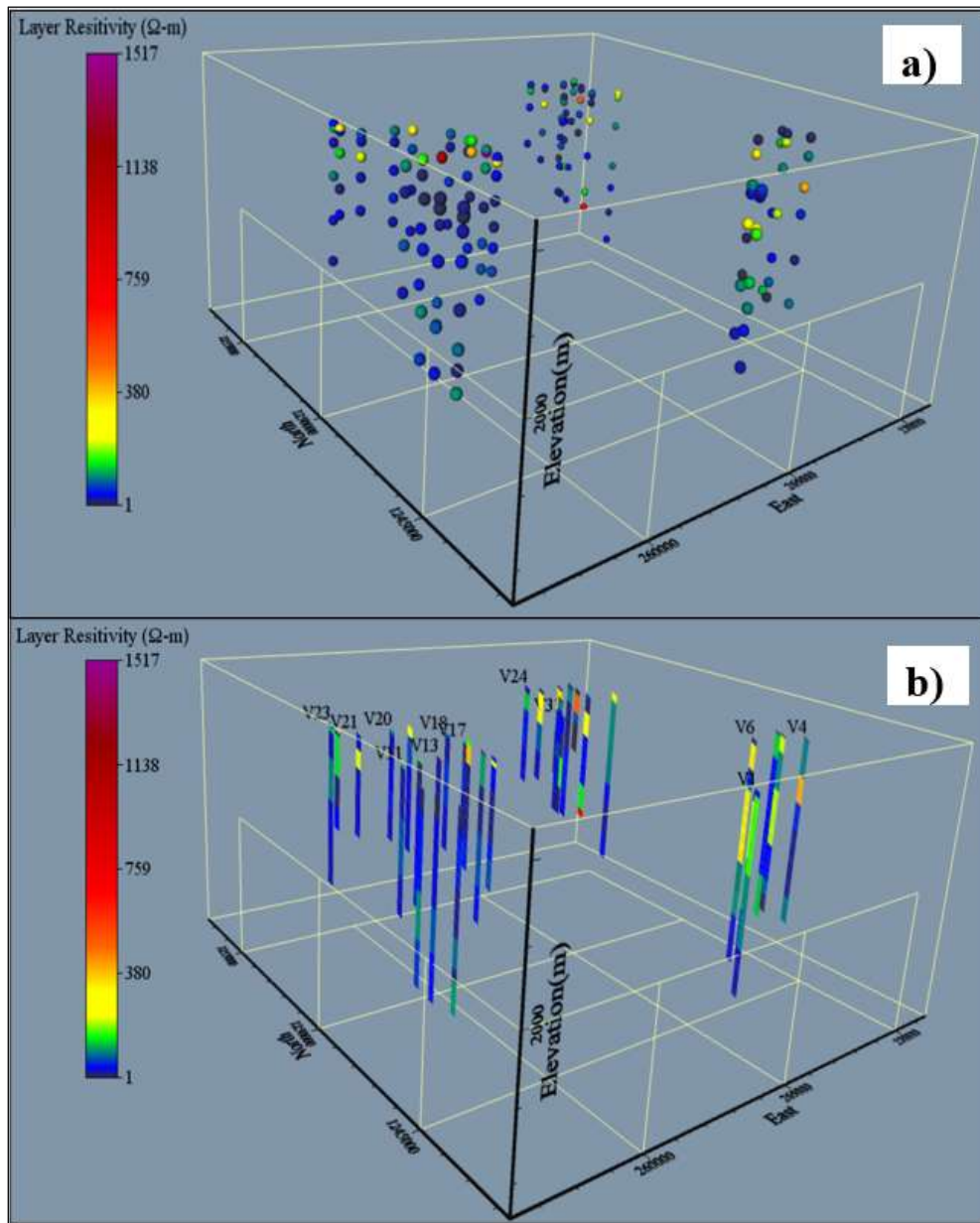


Fig. 35 3D scatter plot of resistivity layers represented using the layer values at the middle of the layer thickness (a) and using a uniform color-shed of the layers having similar resistivity values (b). XYZ axes are exaggerated for better visualization.

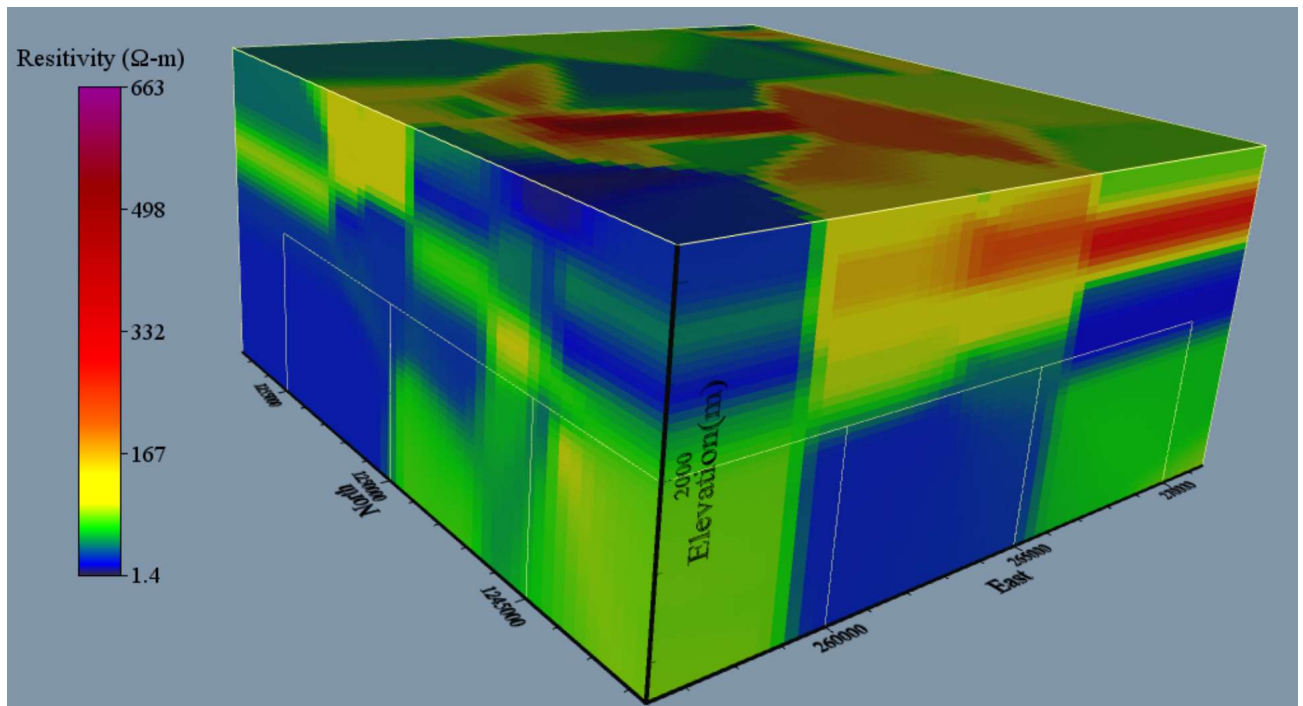


Fig. 36 3D Box plot of uninterpolated resistivity layer data values along X, Y, and Z directions.

Further processing and gridding of the uniform boxplot resistivity values enable observation of the various values in relation to different directions (Fig. 37). A gridding algorithm called “inverse distance to the power” is applied to grid the layer resistivities in 3D volume (Lu & Wong, 2008). The gridding techniques assume that the attribute value of an unsampled point is the weighted average of known values within the neighborhood. The weights are inversely related to the distances between the predictions and the sampled locations (Lu & Wong, 2008). A smoothing interpolation technique does not extrapolate the grid data values beyond their range, and the anisotropy factor is considered during interpolation. The grid volume data representation helps in visualizing the resistivity variation in space and along different directions. The 3D resistivity values for grid volume plots showed that the low resistive layers, which are potential groundwater reservoirs, do not continue to lateral and vertical extents. The fracture dominant deep aquifer system has an anisotropic nature. The principal aquifers are discretized along different directions. The aquifer layers of productive boreholes are not found at similar depths. The aquifer geometry complexity is the result of volcanic eruption producing an intricate geological system that is later affected by weathering and other geological processes. Generally, the aquifer and geometrical setting systems are heterogeneous and anisotropic, mainly due to the nature of the volcanism.

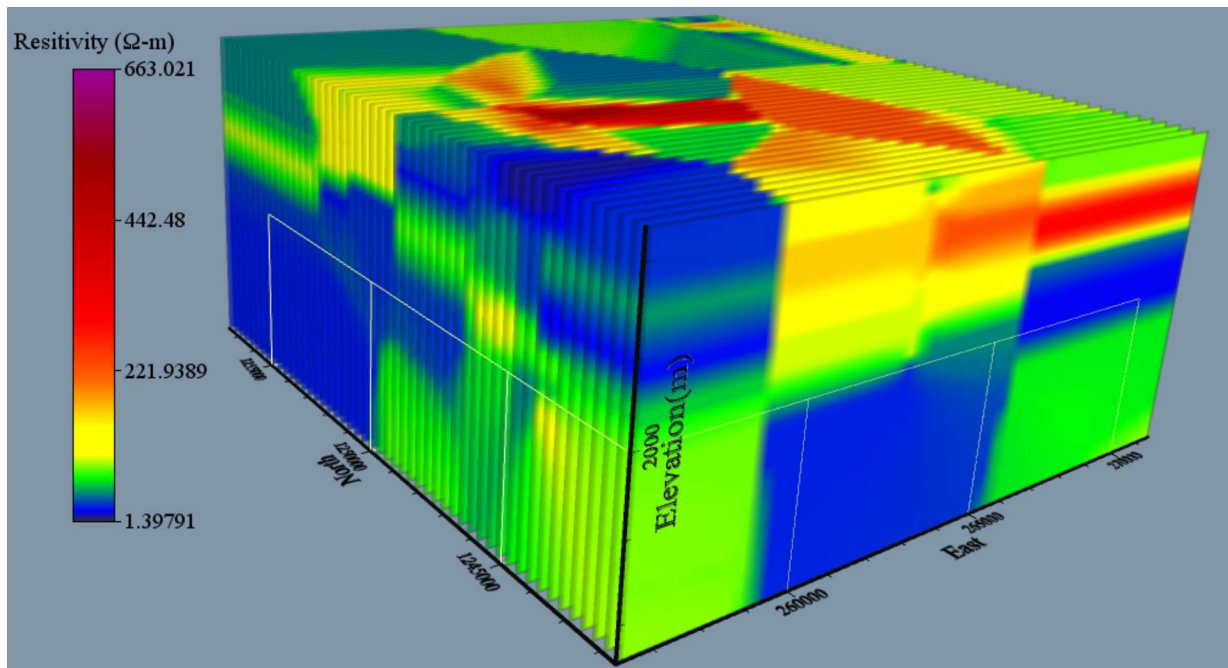


Fig. 37 3D volume representation of the grid layer resistivity data.

4.4.8 The 3D sliced resistivity Plan maps and images

The 3D volume of grid resistivity layers is sliced at specified depths to observe the lateral resistivity variations at those depths. The sliced maps are prepared at six selected depths from shallow 4 m to deep 180 m (Fig. 38). The low resistivity places at 4-m depth do not continue at higher depths; instead, it changed to high resistivity. The orientation of fractures' effects on the water-bearing layers and their resistivity values are observable at shallow depths. The effect is more negligible at shallow depths than at increased depths, as the resistivity and the water-bearing layers are dispersed in a wide area at a 4-m depth. However, as depth increases (15, 45, and 100 m), the effects of fractures and faults controlling the storage and flow of the groundwater increase, changing the resistivity of aquitard as high relative to that of aquifers layers. The fractures that store groundwater at greater depths are mainly oriented in a NE–SW direction, and the water-bearing characteristics vary with depth. The aquifer system is concentrated around a circular geometry at 145 m along these fracture lines; however, the lower aquifer at 180-m depth becomes aligned to the fracture lines similar to the upper 45- and 100-m depth aquifers. The presence of these fractures leads to have a heterogeneous and anisotropic aquifer. Therefore, the NE and SW parts of the area are not suitable to drill productive boreholes for groundwater abstraction from deep aquifers.

The influence of the fracture on the aquifer system is detectable from 45-m depth, so that borehole drilling plans in the area should consider the fracture orientation. Moreover, the tendency to strike the deep aquifers below 45-m depth is less without proper investigation. Therefore, the future groundwater management plan for the area should include at least the lower aquifer system found around 145 m, as it is well concentrated and expected to have a better yield than the other depth aquifers.

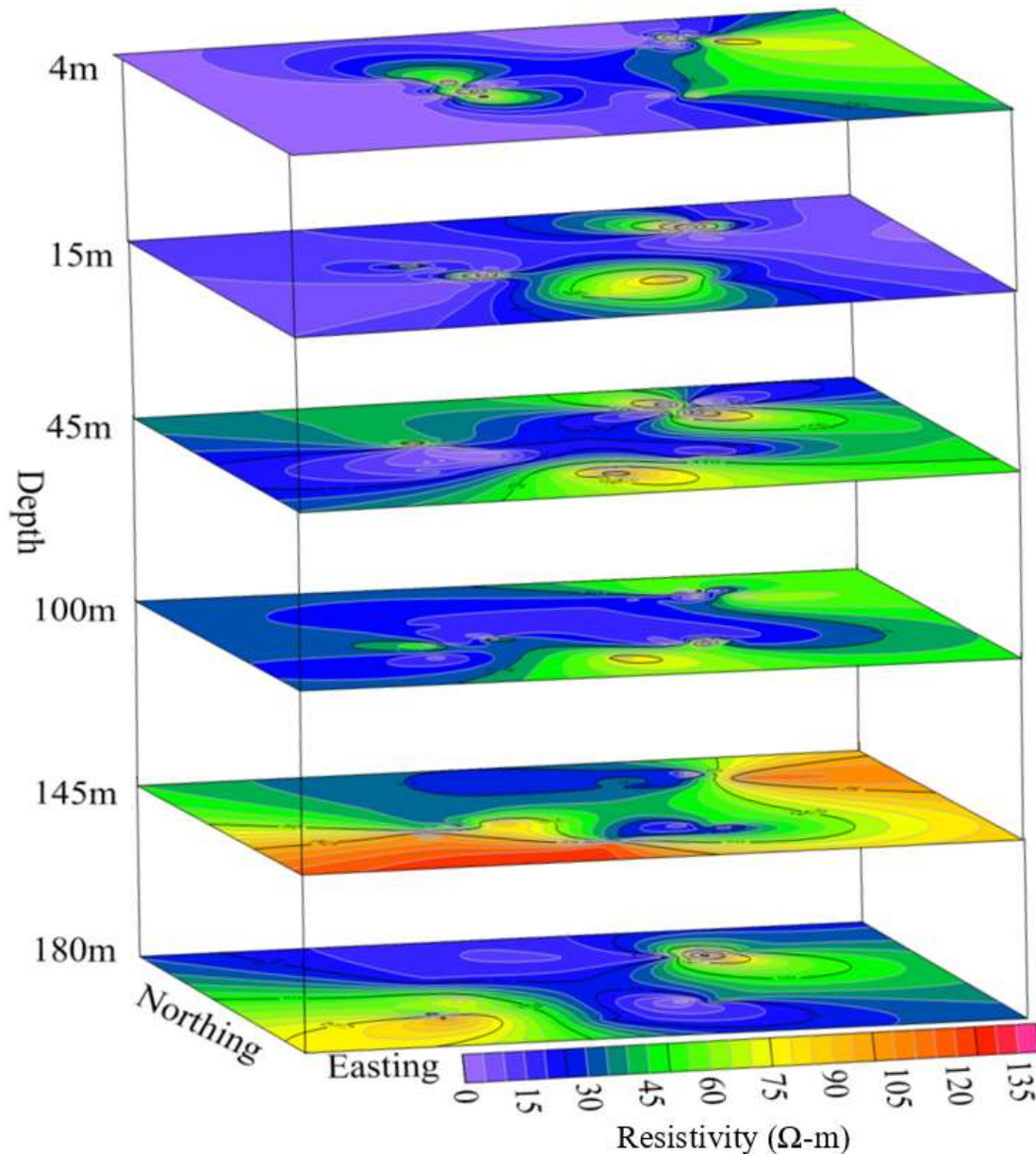


Fig. 38 3D sliced depth resistivity map in the XY plane. The plane maps are at six specific depths of 4, 15, 45, 100, 145, and 180 m.

The oblique images from the 3D grid volume of resistivity values (Fig. 39) show that reactivity varies along with vertical and oblique plans, suggesting the aquifer system's anisotropic nature. Therefore, the aquifer system varies more according to the geological setting of the area than in relation to the recharge and rainfall. Furthermore, the localized and specified areas potential aquifers were observed as discrete aquifer systems in the 3D resistivity volume maps. The localized and directional aquifer system in the plan sliced resistivity depth maps indicates the heterogeneous nature of the aquifer System. The oblique resistivity image extends from the different corners of the 3D volume map to horizontal and vertical planes.

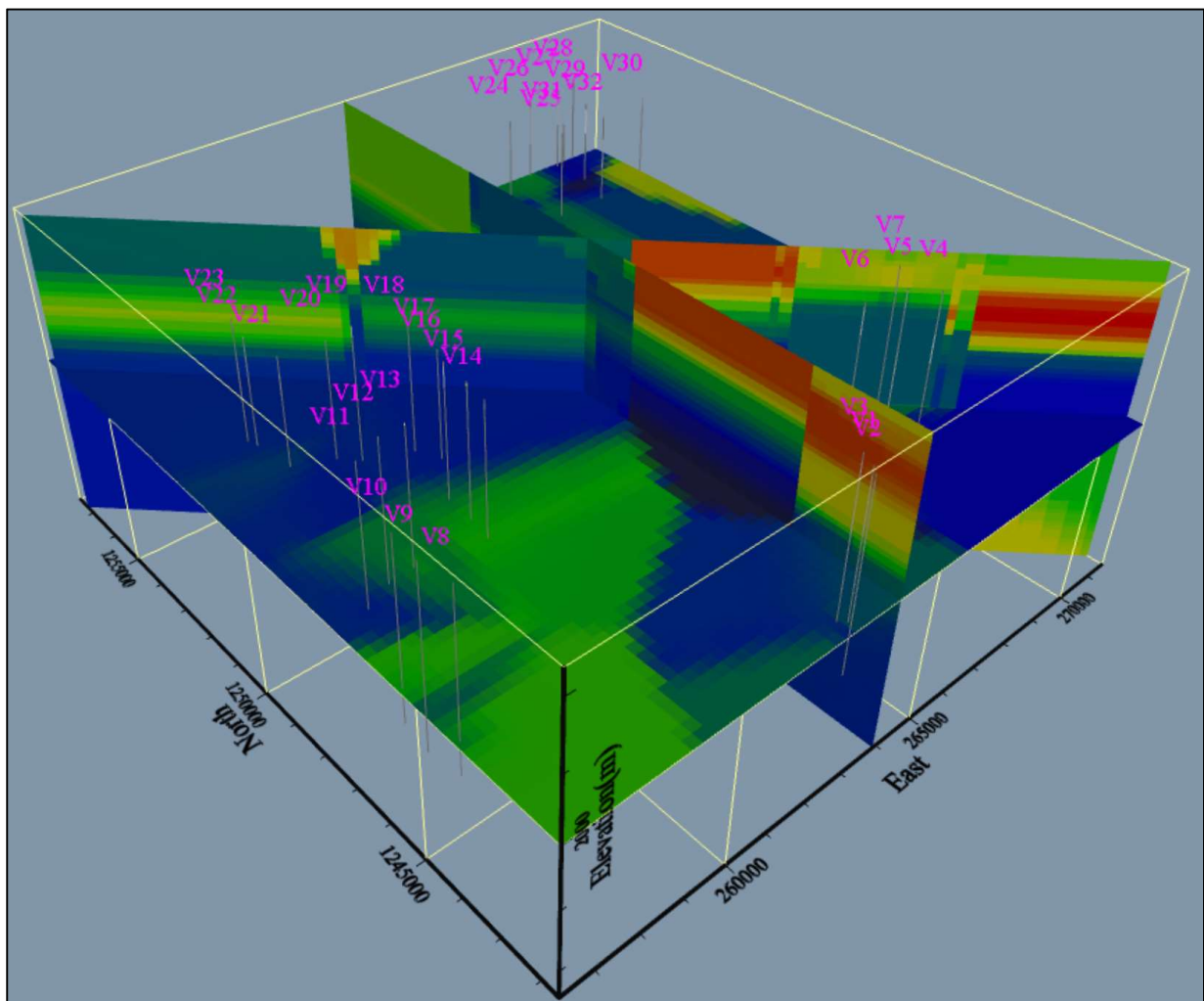


Fig. 39 3D sliced oblique resistivity images with VES point locations.

The orthogonal resistivity image maps taken from the grid 3D resistivity volume allow one to observe the resistivity layer variations along the different XY, XZ, and YZ perpendicular planes (Fig. 40). The northeast parts of the area are shown to have good groundwater potential at increased depths. The southern part of the maps is not a potential groundwater area with shallow depths. They are places that can be good groundwater potential at greater depths. Their yield from such an aquifer is not yet known. In most product borehole locations, the aquifers do not continue with increased depth; instead, they have a limited lateral extent that indicates the aquifers system possibly possesses an intermediate flow system recharged from the southern highlands. The fractures having NW–SE and NE–SW orientations are used as conduits and storage of an aquifer, as noted, at different depths in the sliced depth maps, resulting in more productive aquifers at alternative depths. The deep aquifer system might be a regional aquifer system recharged from the southern highlands, west highlands, or nearby basins. However, drilling and detailed investigations are required to recommend an intense >210 m depth in productive boreholes drilling.

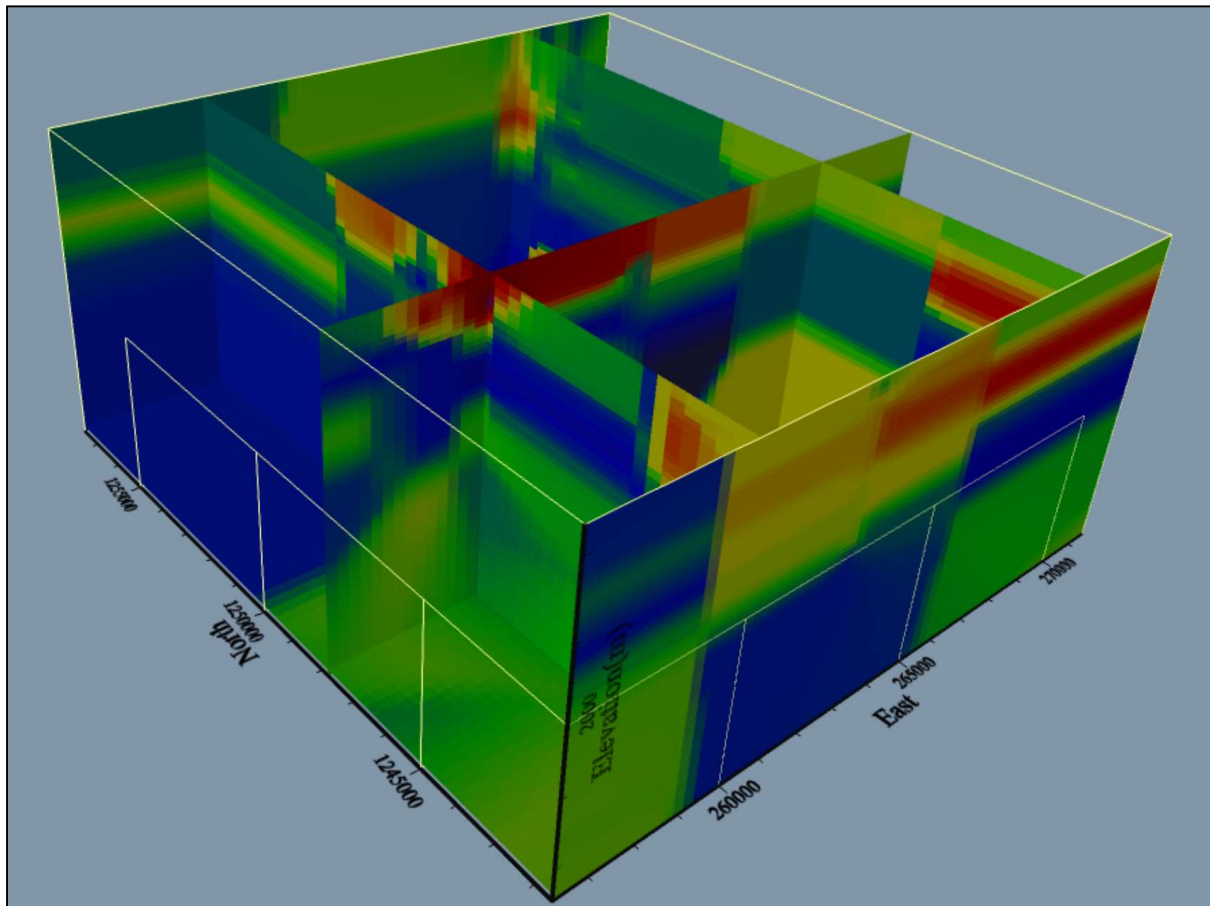


Fig. 40 3D sliced orthogonal resistivity images in the XY, XZ, and YZ planes parallel to the X, Y, and Z axes.

Generally, the area with low resistivity layers at increased depths have better groundwater potential and can obtain >30 L/s groundwater. The borehole drilling with >10-in production casing diameter and drilling to 200 m depths can be a suitable well design. The low resistivity layer at (<50 m) depth is caused mainly by the scoriaceous and scoria layers that can hold water but with a limited yield. The borehole drilling with these layers as an aquifer but without the main fracture stat connect the recharge, and these reservoirs can obtain from 2–3.5 L/s groundwater yield. Therefore, in the fracture dominant low resistivity aquifers found at greater depths, borehole drilling is recommended at a minimum of 150–180 m depth penetration. The depth will enable the strike of the main aquifers found at 135–155 m depths that facilitates obtaining a groundwater yield of >18 L/s. Moreover, the resistivity surveys are the most widely employed techniques in hydrogeology investigations and provide important information on the geological structure, lithologies, and subsurface water resources without the high cost of extensive drilling programs (Kearey et al., 2002). However, similar to other geophysical techniques, interpretation imposes an ambiguity problem (Binley et al., 2015). Therefore, independent geophysical and geological controls are necessary to discriminate between valid and alternative interpretations of the resistivity data (Kearey et al., 2002).

4.4.9 The possibilities of applying new/modern geophysical techniques

The worldwide field and laboratory experimental research results review enable observation of the possibility of applying the new fiber optic sensor technology in the complex geometry aquifer characterization and management. The new fiber optic sensor prospecting has great potential for hydrogeophysical applications. Techniques for measuring temperature, pressure, acoustic, and strain in distributed systems that detect single or multi-parameters are currently being developed. There are numerous opportunities to apply the developed sensors to improve multiparameter, low-cost sensors with increased spatial resolution and reduced loss. The new prospects can measure dynamic and static responses via active/passive methods using fiber optical sensors (Jousset et al., 2018; Marra et al., 2018; Pevzner et al., 2017). Fiber optic sensors will unquestionably be utilized in water resource management. The new sensors can detect the salinity of well fluid and the variability of viscosity, clogging merle, clay, salt, and silica in wells. This technology can be applied to detect the accumulation of silica, calcite, algae, and silt or fine materials in a well through screen openings for cased wells. Moreover, the technology core for high-temperature geothermal wells in detecting mineral dissolution changes in inflow from reservoir rocks to the well and changes in borehole liquid density during drilling and production.

The maximum sensitivity of fiber optic cables, the option to measure one or more physical parameters, the higher operating temperature, and the enhanced coatings for both protection and sensitivity (Rehman & Mendez, 2012) are attractive for near-surface and borehole geophysical surveys. Unlike other geophysical sensors, the fiber cables are deployed below the ground with 0.8–1-m depth for near-surface surveys.

However, the technology has various options for the borehole survey instruments: cementing on the outside of the casing, as well as clamping on the production casing and inside the tubing (Correa et al., 2019; Li et al., 2015; Mateeva et al., 2014) are among field-tested coupling options (Fig. 41). Cementing the fiber optic cable to the borehole wall provides the optimal coupling technique regarding data quality (Li et al., 2015). The field test experiment by Munn et al. (2017) proposed a coupling technique analogous to a fully cemented deployment in that the cable was continuously coupled directly to the formation with the use of a flexible borehole linearly inflated using hydrostatic pressure. Even though the coupling technique cannot be used for deep boreholes due to its depth limitations of up to 425 m, it is beneficial in hydrogeological problems as most productive boreholes are less than 425 m in depth.

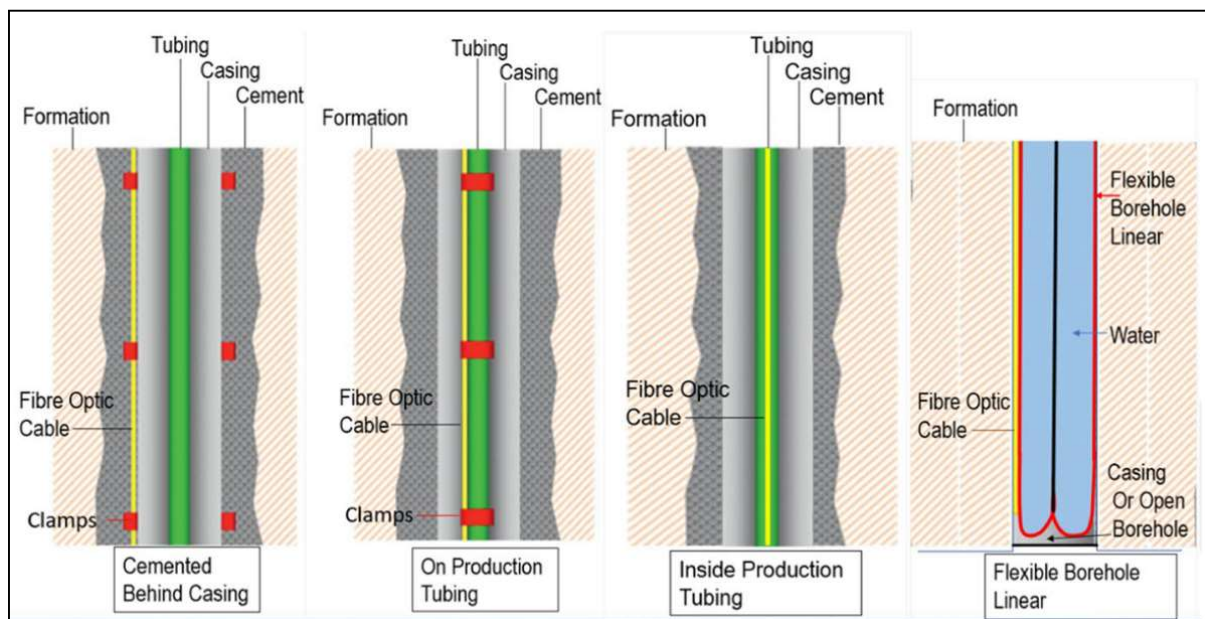


Fig. 41 Fiber optic cable coupling options in a borehole survey. Modified from Munn et al. (2017) and Naldrett et al. (2020).

Moreover, the development of computing and extensive data handling techniques will help one to interpret comprehensive data from long-distance fiber optic arrays. Among several big data handling techniques, artificial intelligence (AI) is a recent and helpful method to enhance the performance of future distributed fiber optic geophysical sensing systems through big data generation, artificial neural networks, and deep learning (Gharbi & Denolle, 2018; Shiloh et al., 2018). Therefore, the applications of the new technology in hydrogeological problems will help to understand various complex aquifers systems which have not been recognized using conventional geophysical techniques.

4.5. Aquifer Characteristics

4.5.1. Shallow aquifer system

The terminology '*shallow aquifer*' in this thesis represents the unconfined aquifer in the soil, weathered rock, or regolith. In addition, it incorporates the top weathered and fractured part of the basalt layer found beneath the regolith that can store and transmit groundwater. The aquifer is primarily unconfined and highly interacts with surface water and rainfall. However, the shallow aquifer is not continuous; instead, it has been intercepted by impermeable basaltic flow, pyroclastic deposits, and clay soil that led to the formation of a perched unconfined aquifer. The top clay soil can have a considerable thickness in the floodplains and reduces the vertical hydraulic conductivity acting as a semiconfining layer.

The clay soil and regolith, being at high altitudes, are always under the influence of rainfall, temperature variation, and erosion. The rock fragments in the upper weathered soil and regolith, consisting of well-rounded vesicular basalt, usually highly weathered, are both resting on the soil surface and partly embedded in the top layer. The thickness of the topsoil cover and regolith varies to 7- and 19-m depth at different parts of the study area. The weathered rock /regolith thickness is high to the southern mountains, including localities of Dimsa kebele and in the eastern highlands. The topsoil can be sandy soil, clay soil in flood plains, and clay loamy soil varieties with high thickness at the flood plains.

Generally, shallow wells are more productive where fractured rocks underlie the soil and regolith. Precipitation recharges the upper-perched aquifer directly through the vadose zone or following the shallow fractures. Walker et al. (2019b) estimated recharge of this shallow aquifer at 280–430

mm/y, or 17%–26% of mean annual precipitation, from nine different recharge estimation techniques. Comparably, Yenehun et al. (2020) estimated the average groundwater recharge value from 429 mm to 477 mm/y based on four different recharge estimation techniques and 28% of total evapotranspiration. The mean annual recharge value of these techniques was 477 mm/y. The previous work and the water-stable isotope data analysis indicate that the recharge has a substantial spatial variability and significant temporal variation. Nearly all recharge takes place during the principal rainy summer season. In conformity to the water-stable isotope results, Yenehun et al. (2020) and Walker et al. (2018) noticed with water table fluctuation recharge estimation techniques that recharge is highest in the mountainous area and lowest in the alluvial and floodplain areas.

4.5.2. Water level and groundwater flow

Groundwater researchers usually use a water-level contour map to denote groundwater flow directions and examine the continuum attempt. Assuming the steady-state condition for the aquifer system, the groundwater flow lines lie perpendicular to the water table contours (Todd, 1959). The shallow groundwater level contour maps prepared from the groundwater level data collected after the primary rainy season and piezometer level of deep boreholes showed the flow is highly local topography dependent (Fig. 42). A further assumption is that the perched aquifer is considered a continuous unconfined aquifer. The shallow groundwater level is situated at relatively shallow depths at the south and northwest area highlands, increasing following the decrease in topography toward the north. The groundwater flows parallel to the rivers at some localities and toward the river where the groundwater recharges the rivers. The flow is toward the rivers in most parts of the area. However, there are places in the flood plains where the river recharges the groundwater. The groundwater flows away from the river, especially at the north part of the study area at the localities of Dengeshita and Wufta Daty kebeles, where the Kilti river recharges the shallow groundwater system.

A different characteristic is observed for the Branti river. The river recharges the groundwater system to the eastern side of the river, and the groundwater recharges the river on the western side of the river. The flow system might have changed at various locations during the dry seasons. Yenehun et al. (2020) remarked that the Kilti river recharges the groundwater during the dry season and the reverse during the rainy season in the floodplain. The upper unconfined aquifer has high interaction with rainfall and rivers. A time series of rainfall and river stage measurements by Walker et al. (2019a) at Dengeshita kebele showed that the rivers are very flashy, with sharp peaks

in the river stage quickly following rainfall events. A similar pattern of seasonal variation and fluctuations in groundwater levels in the shallow wells is reflected.

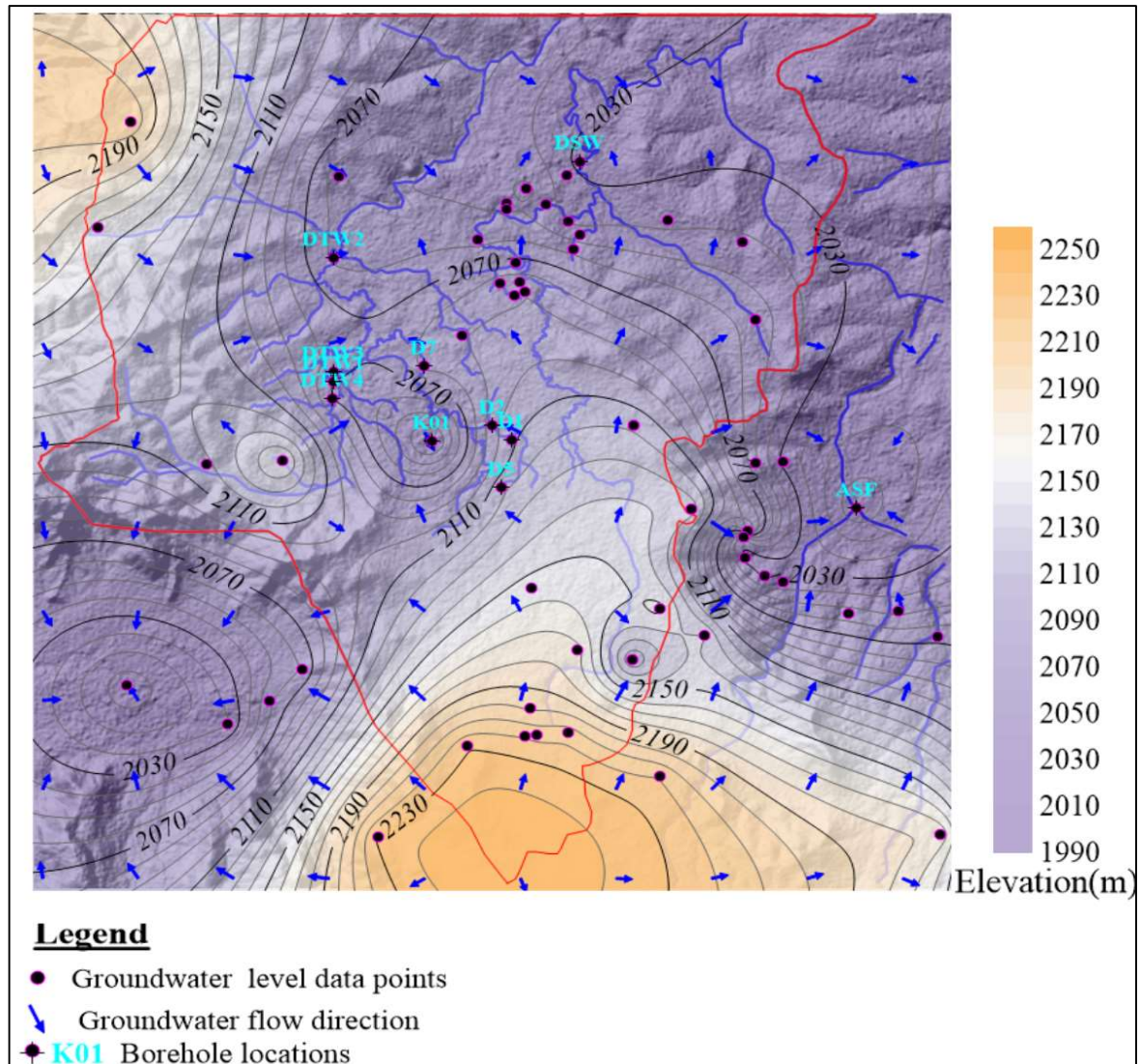


Fig. 42 Shallow groundwater level contour maps and flow direction overlain on the Digital elevation model map. The red polygon represents the upper catchment parts of the Kilti and Branti Rivers.

The fractured zone below the soil and regolith profoundly affects the hydraulic properties of shallow-depth aquifers. Lack of fractured zones causes a gradual decline of groundwater levels during the dry season; their presence rapidly increases the amount of water in the shallow aquifer during the rainy season. Walker (2016) calculated the shallow aquifer's mean hydraulic conductivity based on the five shallow wells data with the values of 2.3 m/d in the dry season and 9.7 m/d in the wet season. The hydraulic conductivity of the shallow aquifer was relatively high during the rainy season when the saturated thickness was greater and more transmissive layers were intercepted. The

field observations on the yield and recovery of shallow wells that abstract water from the shallow aquifers indicated that recovery from the shallow aquifers is slow, implying the hydraulic conductivity of the shallow aquifer is low. The characteristic recharge by the river and the shallow aquifer is notable in the water-stable isotopes too. The sample from spring, shallow wells, and rivers showed similar enrichment and depletions for heavier isotopic compositions of water samples depending on the sample's locations.

4.5.2. 1 The correlation between groundwater level and local topography

The linear plot of groundwater level versus elevation taken from the SRTM data of the area along a profile (Fig. 43) and (Fig. 44) indicated > 99.6% correlation with the local topography. The variable and rugged topography in volcanic trains, along with the interactions of the aquifer with the massive basaltic lava flow to the surfaces, and the presence of clay soil at the top at some localities, cause the shallow aquifer system to be a local flow following the local topography. The hydrochemistry of the shallow aquifer indicated that most of the shallow wells and spring samples have Ca-HO₃ type water, which is a typical groundwater type of shallow aquifer with low residence time. The groundwater is recharged and discharged locally so that several localities are used as local recharge and discharge areas.

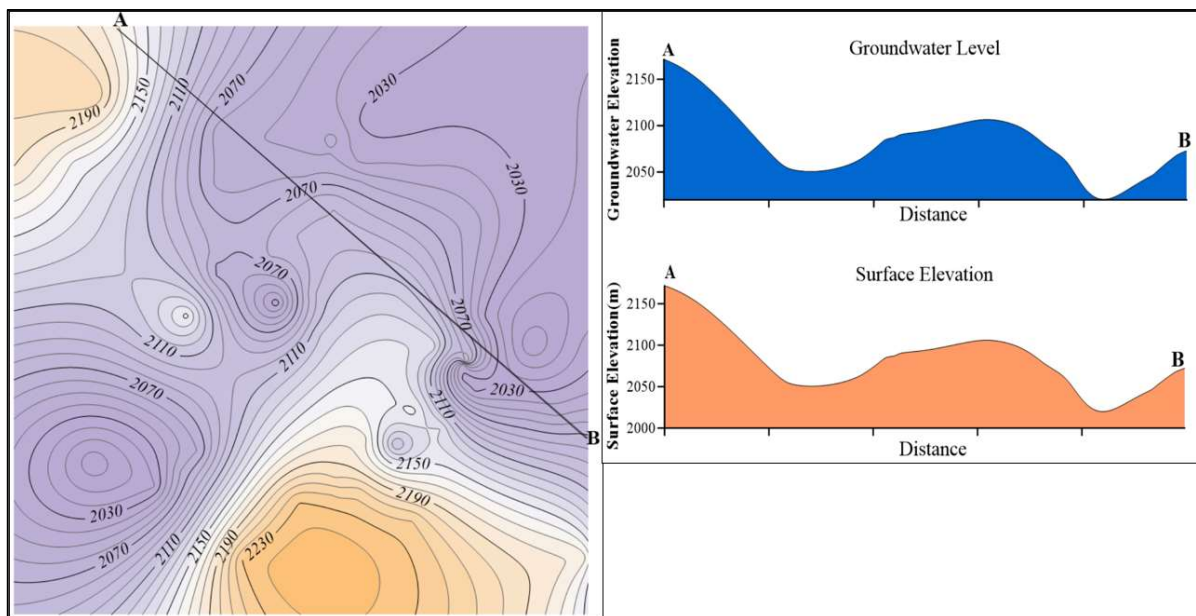


Fig. 43 Variations in groundwater and surface elevations; a long distance from A to B.

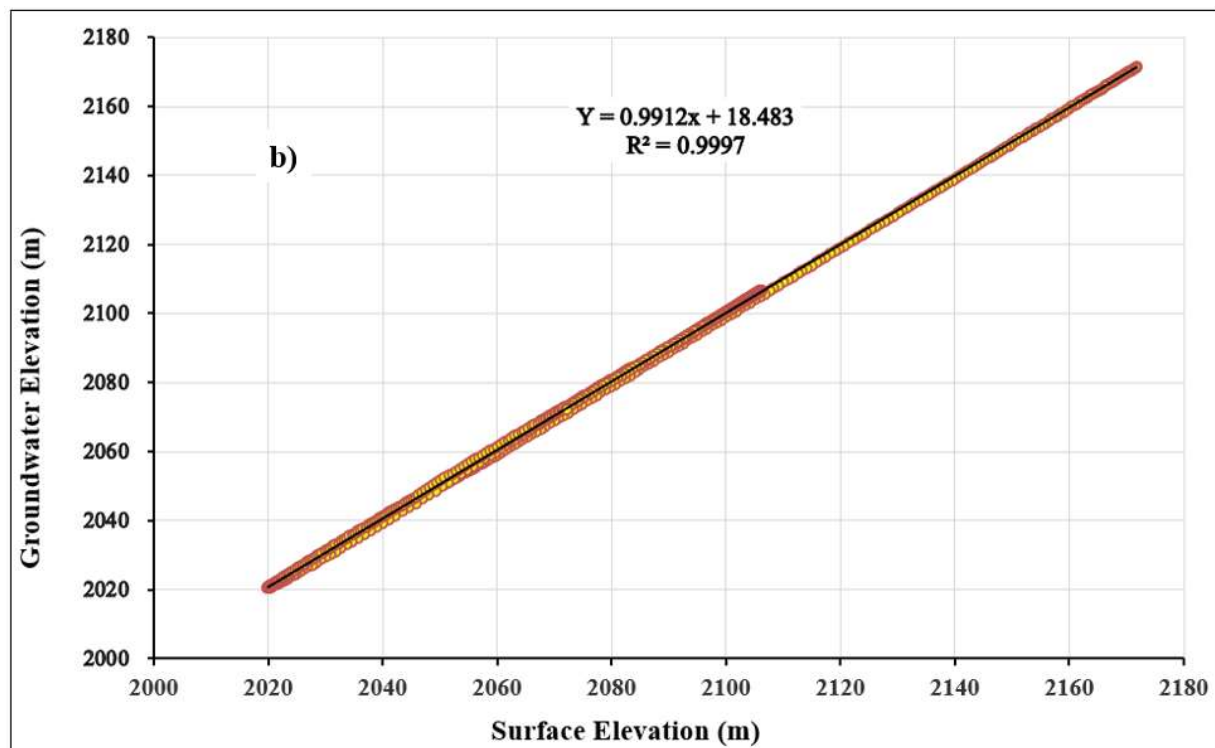
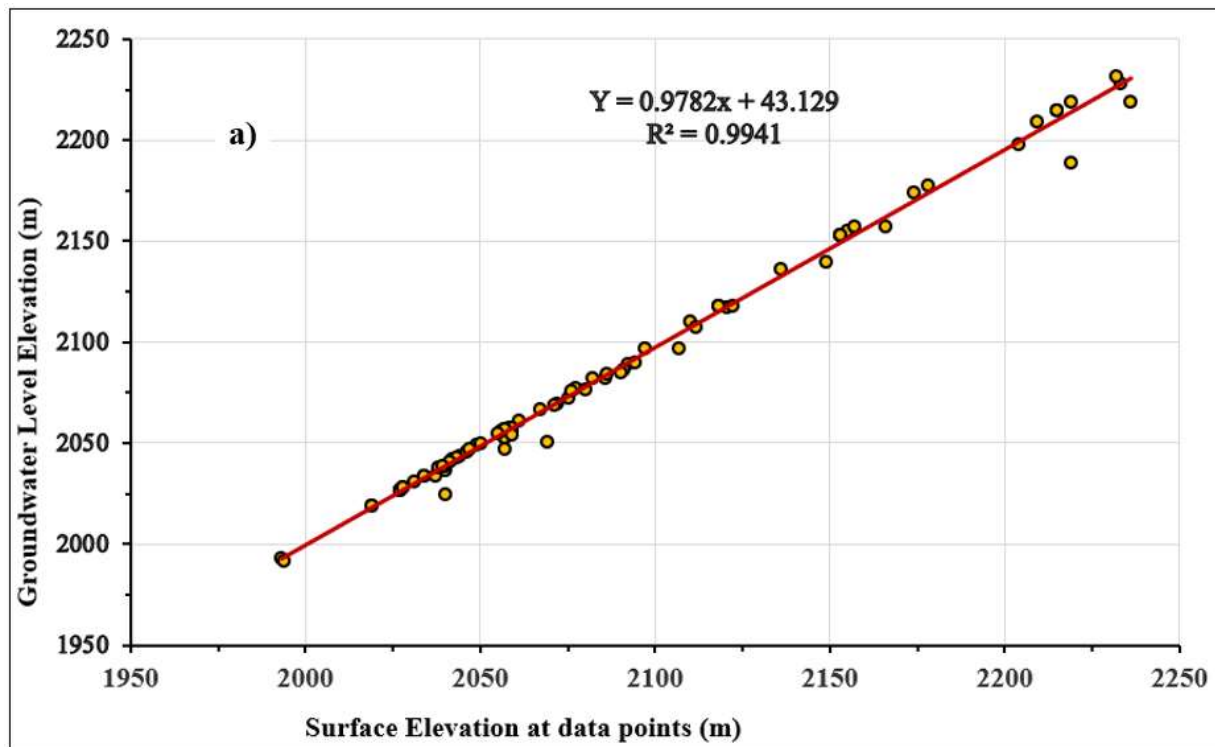


Fig. 44 Linear plot of groundwater elevations versus surface elevation of data points A) and groundwater elevations to surface elevations from the grid data and SRTM surface elevations data B) along with profile AB of Fig. 43.

The shallow aquifer is the important aquifer that supplies fresh water for the rural community that lacks a fresh water supply from boreholes. It is abstracted through three different mechanisms: 1) natural springs or developed springs, 2) private hand-dug wells, and 3) community dug wells (Fig. 45). The construction of private and community wells are different. Usually, the community wells are screen stalled and surrounded by boulders and gravel to protect the falling of soil into the well. Hand pumps are installed in the well, and the top part is closed by cementing to preserve the surface pollution of the groundwater. The private wells are not well constructed and are mostly exposed to pollution. The wells are mainly exposed to surface contamination due to erosion and farming practices as they are located close to farmlands or toilets. The water chemistry of a few shallow wells samples resulted in $\text{Ca-CHO}_3\text{-Cl}$ and $\text{Ca-Mg-CHO}_3\text{-Cl}$ water types that indicate the presence of anthropogenic effects in the shallow aquifer system.

The springs, hand-dug wells, and community shallow well, all abstract groundwater from the shallow aquifer, have <1 L/s. The yield varies from place to place and with seasons. Most of the mountain front springs become dry during dry seasons when the level decreases following the rainy season. However, the springs in the flood plains that emerge from the fractured surfaces sustain their yields for the whole season, and they are the main freshwater supply system for the rural people when the yield of the shallow well decreases during the dry season. Despite the minimal groundwater yield, the shallow wells supply fresh water and sustain the drinking water demand of the rural population. Furthermore, the wells have been used as a source of water for small-scale backyard vegetable farming too.

Generally, the increase in plantations of eucalyptus trees, the reduced wetland at times, as they are dependent on the seasonality of the shallow aquifers system from shallow wells, as well as dryness of some shallow wells and springs during the long dry seasons are the basic challenges for the management and supply of fresh groundwater from the shallow aquifer system. Besides, the complex geology requires an a priori knowledge or detailed investigations similar to the approach to the deep boreholes.

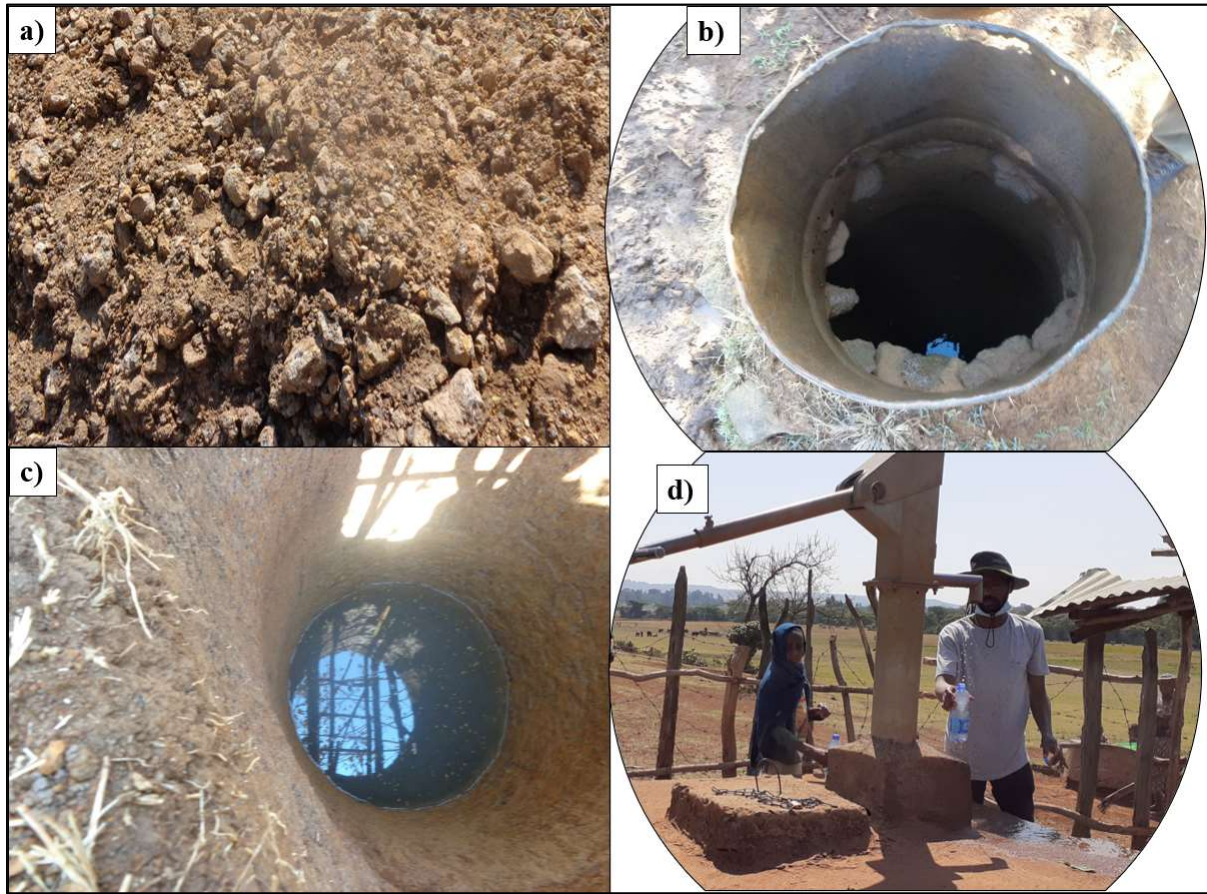


Fig. 45 Regolith from the shallow hand-dug well (a), shallow hand-dug private well construction, top external part (b), internal part (c), and community-based hand-dug shallow well with a hand pump (d).

4.5.3. Deep aquifer

The “*deep aquifer*” in this thesis represents all the aquifer layers found below the upper unconfined aquifer up to 210-m depth. The deep aquifer is a multi-layer aquifer system with alternating confined and semiconfined layers in the weathered and fractured basalt, scoriaceous basalt, scoria fall, and pyroclastic materials. The scoria falls, and pyroclastic materials are highly weathered and altered into clay layers at depths greater than 100 m. They reduce the aquifer interaction and vertical hydraulic conductivity by forming a semiconfining layer. The weathered scoriaceous basalt layers found at alternate depths to the massive and fractured basaltic layers are mostly weathered and serve as an aquifer. The basaltic layers found at different depths occasionally will be weathered,

fractured, or massive layers. The weathered and fractured layers are usually suitable for groundwater storage and are the most promising groundwater sites when they have connections to the recharge.

Depending on the nature and their influences on groundwater, the fractures/faults of the area can be categorized into two, namely, the minor and major fractures/faults.

a) Minor fractures/faults: These types of fractures are observed in the weathered and fractured basalts and scoriaceous basalts at several depths. They form a horizontal aquifer later bounded from above and below by an aquifuge of massive basalt or aquitard layers of scoria fall or clay. All drilled boreholes of the area possess these types of fracture layers; however, due to lack of vertical connections with each other or to the recharge area, the total groundwater yield from these sets of aquifers is usually <3.5 L/s. For example, among the deep boreholes that lack the major fracture but have alternate aquifer layers due to weathered layers and minor fracture set layered aquifers are K01 and DTW2 boreholes. The bordellos (K01) with various horizontal fracture layers but lacking the major fracture that connects to each aquifer layer, along with the recharge, have a groundwater yield of 3.5 L/s. A similar case is observed for borehole DTW2, which has a 200-m depth and a groundwater yield of 3.5 L/s. Several other boreholes that present the same characteristics have groundwater yields of <3 L/s, and they are mostly either dry or currently abandoned.

b) Major fractures/faults: These fractures/faults have a different lateral and vertical extent. In both cases, they connect the other minor fractured, weathered basaltic and scorious aquifer layers to the recharge. These fractures are also used as groundwater conduits and for storage. The nature of groundwater stores is high when they are intercepted by massive basalt or have a wider fracture/fault aperture. The geophysical survey results indicated that not all major fractures and faults are water-bearing; instead, only those connected to the recharge or upper aquifer have high groundwater potential. Even though they are very useful fractures to connect the nearly horizontal layers of minor fractured and weathered reservoirs, they also act as barriers for groundwater flow, making a discretized and disconnected, or compartmentalized aquifer system.

Depending on the morphology, gravitation force, and hydrostatic force of the aquifer layers, these fractures can be used by the groundwater to move an intermediate distance, performing an intermediate flow. Most productive boreholes of the area infuse these sets of fractures with the recharge areas. The three product boreholes that supply fresh water to the Dangila town are located at the

floodplains of Berayita kebele and have these major fractures at a relative shallower depth than the other recently drilled productive boreholes at Dengeshita kebele. The Berayita kebele boreholes, DTW1, DTW3 and DTW4, have depths of 192.5, 150, 150 m and groundwater yield of 24.7, 30, 18.2 L/s, respectively. The yield variation depends on the boreholes' location relative to the fracture/ fault.

On the other hand, the Dengeshita borehole with a depth of 160 m has a groundwater yield of >30 L/s. The resistivity survey results show that an increase in the depth of the Berayita borehole would not increase yield as the aquifer is at a relatively shallow depth. In contrast, there is the possibility of increasing the yield by increasing the depth of the Dengeshita borehole. The Dengeshita boreholes' aquifer layers are found at greater depths, and the top part of the fracture is covered by basaltic lava flow, acting as a confining impermeable layer. Alternatively, in the Berayita boreholes sites, the major fracture is close to the main recharge (western high land areas). It may have a minimum direct recharge from the wetland and upper unconfined aquifer. In contrast, the Dengeshita borehole fracture is far from the main recharge (mountains), and is blocked by an impermeable massive basaltic layer on the top upper part. Therefore, in such cases, recharged is expected at a far distance and flows down, flowing the elevations difference from high lands to lowlands through fractures. Therefore, the groundwater potential of the areas and boreholes yield varies depending on the nature of the fracture and its connection to the recharge and the depth of the borehole (Fig. 46).

Given the information and survey results on the shallow wells and deep borehole, along with the near-surface geophysics survey results, the principal aquifer bearing layers of the area can be grouped into the following depth classes: The aquifers start from shallow depths of 3–15 m and extend at alternative depth ranges of 35–65, 130–155, and 180–210 m. However, a depth might vary depending on the fractured nature and the area's morphology. The first depth range, 3–15 m, belongs to the shallow unconfined aquifers within the soil and regolith, and the maximum yield by drilling shallow wells will always be less than 1 L/s.

The depth range of 36–65 m layers can be found in different thicknesses and variable depth intervals. The layers are dominated mainly by weathered pyroclastic and scoria falls that occasionally have been altered into clay. Drilling a borehole up to 70-m depth can yield a maximum of <2.5 L/s. However, this yield depends on the connection to the upper unconfined aquifer and the borehole site location relative to the major fracture and recharge area that might increase the yield to 4 L/s. In contrast, the boreholes have a higher tendency to become dry after a few years of abstractions.

For example, more than six boreholes with depths ranging 60–72 m at Gundri, Dengeshita, and Kuandisha localities are abandoned due to their low yield of <0.5 L/s.

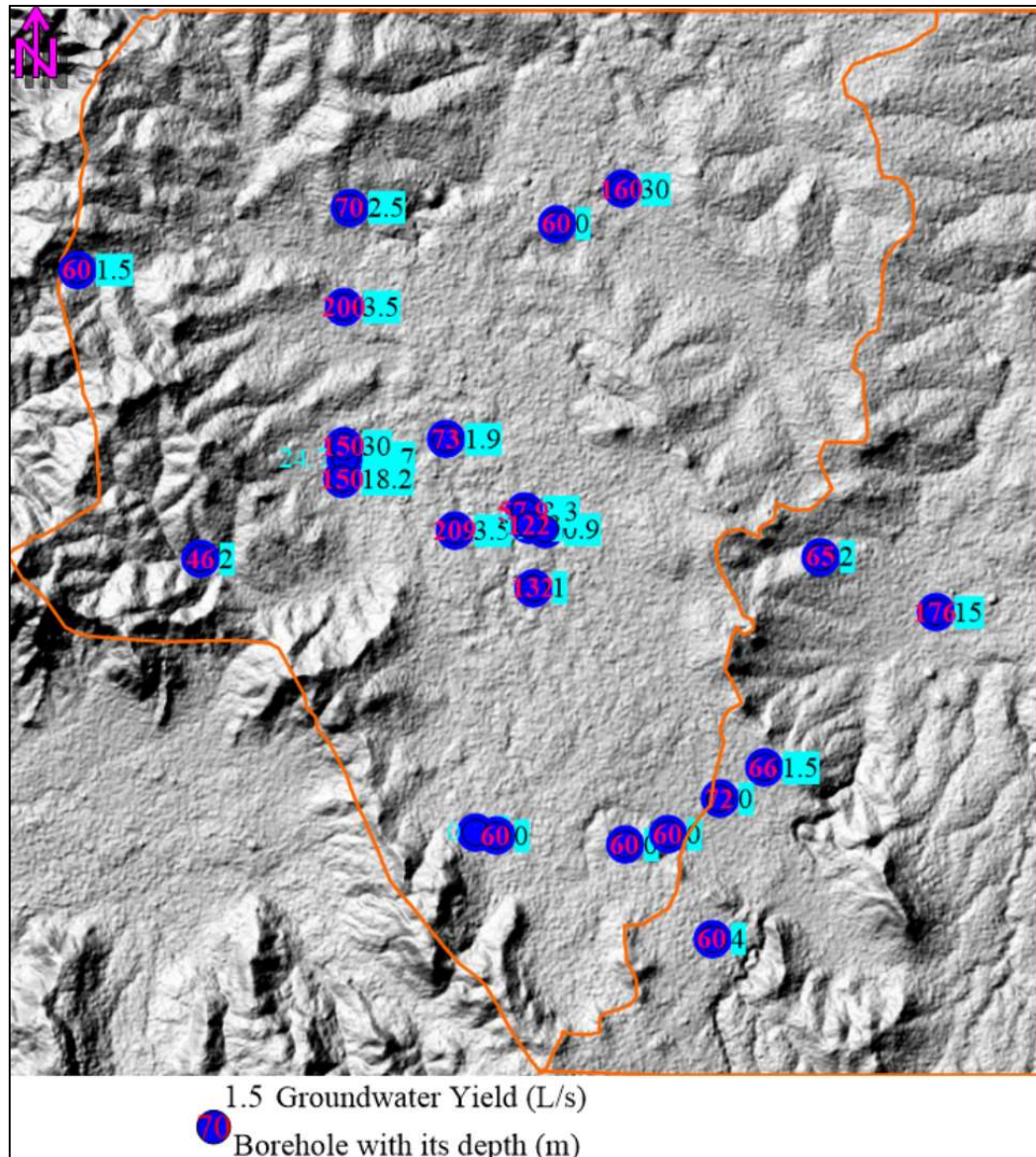


Fig. 46 Groundwater yield map of boreholes with a depth greater than 58 m.

The productive aquifer layers of the study area are primarily found at 130–155 m and can yield better groundwater depending on the borehole locations relative to the fracture and recharge. As an aquifer, these layers have different degrees of weathered and fractured basaltic layers, and they yield >15 L/s if well connected to the recharge by the major fractures, or <3.5 L/s at places with no connections to major fractures or recharge. On the contrary, these layers have been found to

form at 100-m depth in the Dengeshita borehole, which is relatively shallower than the other productive borehole. For example, the boreholes K01 and DTW2, with depths of 210 and 200 m, respectively, struck the above three ranges of aquifers but did not locate along the major fracture and did not connect with the main recharge area; they each have a groundwater yield of 3.5 L/s.

The other deep aquifer layers of the study area are situated at depths of 180 - 210 m. This aquifer layer has a characteristics of an increased water storage capacity due to increased thickness and decreased weathered scoria or pyroclastic materials. However, the penetration of these layers does not increase their yield if their locations are not on the major fracture lines connected to the recharge. Therefore, the primary factor in exploiting high groundwater yield > 15 L/s from deep aquifers extending up to 210-m depth is tracing the major fracture lines and inspecting their connection to the recharge. Generally, the Dangila and surrounding deep aquifer groundwater flow are both morphologically and structurally controlled. The gravitation flow follows the morphology, whereas the structure dissects the aquifer system, forming compartmentalized aquifer systems that execute reduced interaction.

4.5.4. Pump Test and hydraulic parameter estimation

The reality and use of aquifer depend on the three properties called recharge, storage, and flow (Mejías & Plata, 2007). The aquifer requires a recharge that replenishes water, a void space to store the water, and the water should flow through the rock. Various aquifer parameters can describe these three properties that determine the existence of an aquifer. A pump test is among other mechanisms to determine parameters that can characterize the aquifer. The recorded water level, draw-down and time, the quantity of water removed from the borehole, and recovery with time data can be found depending on the type of test. The data can be analyzed to infer aquifer parameters. The three main parameters that describe the aquifer, called hydraulic conductivity (K), transmissivity (T), and storativity (S_y) or the storage coefficient, have been calculated based on selected borehole constant yield pump test data. These parameters describe the simplicity of water to flow through the aquifer and the capacity of water to be extracted from the aquifer.

The hydraulic conductivity (K) expresses the ease of fluid flow through the solid using the void spaces, and the transmissivity considers the aquifer techniques. The hydraulic conductivity is the amount of water that will flow through a unit that is a cross-sectional area of the aquifer (confined

or unconfined) under a unit gradient of the hydraulic head at a determined temperature. The hydraulic conductivity is derived mainly from Darcy's law (Darcy, 1856) which is expressed mathematically as

$$Q = -k \frac{(h_2 - h_1)}{\Delta L} A \quad (10)$$

Where k (hydraulic conductivity) accounts for restriction to flow imposed by the solid medium and for the density and viscosity of the fluid flowing through the porous medium, it depends on the aquifer's properties (type of pores) and the fluid's (viscosity and specific weight) properties.

Conversely, transmissivity (T) is the product of the average hydraulic conductivity (K) and the saturated thickness of the aquifer Δz as $T = k\Delta z$. It is the factor that best expresses aquifer flow potential representing the flow rate under a unit hydraulic gradient through a cross-section of unit width over the whole saturated thickness of the aquifer. Besides, the storativity or storage coefficient (S_y) of a confined aquifer (or aquitard) is defined as the volume of water released from storage per unit of surface area of the aquifer per unit decline in hydraulic head. It is a dimensionless quantity expressed in percentage and provides information about the amount of water to be obtained from the aquifer.

Interpretation of the hydraulic tests showed several improvements after applying the work of Darcy's law (Darcy, 1856). Several analytical solutions involving different aquifer geometries have been derived, and their corresponding computer algorithms have been developed. For example, the work by Dupuit (1863) on an unconfined and confined aquifers and by Dupuit (1863) on the an unsteady-state groundwater flow systems are among the earlier works. Theis (1935) explanation about interpretation of pump test data the base for the recent techniques used to interpret hydraulic test of confined, infinite, homogeneous and isotropic aquifers, with a fully penetrating and with a negligible radius borehole. Moreover, the effects of the large-diameter borehole on the pump test data (Papadopoulos & Cooper, 1967), and a fracture network continuum within a porous matrix, introduce the concept of double porosity by Gringarten et al. (1974), among other concepts. The algorithms developed based on analytical solutions have been used to interpret pumping test data by fitting the results obtained with the already developed models. The most commonly used asymptotic pump test interpretation technique is Theis' solution, which is applied to extended periods (Cooper & Jacob, 1946) and the dual porosity of inclining fractures (Moench, 1984).

The test results drawdown as a function of time that can be represented in semi-logarithmic or logarithmic plots. Depending on the test and interpretation model selected, these representations

can be extrapolated to a straight line. The slope is used to calculate the hydraulic conductivity. Once the fit has been obtained from the drawdown and the initial time, the hydraulic parameters (hydraulic conductivity, transmissivity, and storage coefficient) are calculated. The hydraulic conductivity, transmissivity, and the storage coefficient of the deep aquifer are estimated using data gathered during borehole pumping tests. The calculated K, T and S_y values from the four selected deep boreholes were calculated using the Moench fracture flow model (Moench, 1984), and the values are given in (Table 8).

The hydraulic conductivity of the boreholes dominated by fractures is higher, and during pumping tests, the recovery of these boreholes was fast. The boreholes (DTW3 and DTW1), which have more fracture dominant aquifer layers, have a higher hydraulic conductivity values. As an example, the most productive borehole aquifer 's of the area (in borehole DTW3) has a hydraulic conductivity value of 3.6×10^{-1} (m/d) and transmissivity values of 5.20×10^1 (m²/d). The dominant fracture aquifer of all these boreholes is mainly found in the borehole (DTW1) with the high hydraulic conductivity values of 3.63×10^{-1} (m/d) and highest storage coefficient values of 9.17×10^{-2} . The aquifer hydraulic parameter values imply that the major fractures create an easy flow for the water, and a higher amount of water stored in the aquifer can be extracted.

Table 8. Hydraulic conductivity, transmissivity, and storage coefficient values of four selected deep boreholes.

No.	Borehole ID	Hydraulic conductivity (m/d)	Transitivity (m ² /d)	Storage coefficient	Aquifer character
1	DTW1	3.63×10^{-1}	6.53×10^1	9.17×10^{-2}	Fracture dominant
2	DTW2	5.7×10^{-2}	8.5×10^0	6.02×10^{-2}	Both fracture and weather dominant
3	DTW3	3.6×10^{-1}	5.20×10^1	6.25×10^{-2}	More Fracture, less weathered dominant
4	DTW4	9.76×10^{-3}	1.37×10^0	5.00×10^{-2}	More fracture, less weathered dominant

The three boreholes aquifer Parmenter values are within the maximum values ranges of fracture igneous rocks (Freeze & Cherry, 1979). The transmissivity values of the tertiary basalt aquifer of the Lake Tana Basin vary from 0.1 to 32 m²/day (SMEC, 2008) and have average productivity with a yield in the order of 0.7–17 L/s (Kebede, 2013). Therefore, the Quaternary basalt aquifers of the basin are the most productive aquifers characterized by plenty of vesicles, as well as highly weathering and fracturing nature.

4.6 Hydrogeological Conceptual Model

The hydrogeological modeling consists of either conceptual, numerical, or both, valuable for water resources management. Even though both modeling techniques have their own pros and cons, creating a conceptual model before the numerical model might be helpful for the numerical model or might be sufficient for water management. Based on the multi-investigation approaches results, a conceptual model with its corresponding groundwater flownet is built to imply the groundwater flow. The findings of this study showed that neither of the available islandic volcanic aquifer conceptual models nor the previous large-scale conceptual groundwater flow model of Ethiopian volcanic aquifers could be adapted without modification for the study area. Therefore, the conceptual hydrogeological model called the Dangila model is constructed that can fulfil the specific study area aquifer characteristics.

Since there is no continuous basal aquifer, the two most commonly retained hydrogeological conceptual models for volcanic aquifers of basaltic islands—the Hawaiian model (McDonald et al., 1983), having a low-lying basal aquifer linked to inland dike-impounded and perched aquifers, and the Canary Islands model (Custodio, 1989) having a continuous basal aquifer—cannot be employed. The perched aquifer of the Hawaiian model has some similarities to the upper-perched aquifer of the new Dangila model. The upper unconfined perched aquifer in the soil, regolith, and occasionally in the upper fractured basalt resembles the Mayotte model (Lachassagne et al., 2014). The Mayotte hydrogeological conceptual model for complex multiphase partly eroded and subsided basaltic islands describes the main hydrogeological structures as superimposed paleovalleys filled with various types of volcanic products. Its discontinuous and perched aquifer lacking a continuous basal aquifer, resembles the Dangila area model (Fig. 47). Though there are similarities, the Mayotte model cannot be adapted because: 1) The Mayotte model has several discontinuous perched aquifers with depth, but the Dangila model has a single upper unsaturated soil and regolith aquifer. 2) In the Mayotte model, groundwater flows through low permeability volcanic rocks and discharges as springs when the perched aquifer intersects the surface.

In the Dangila model, flow is highly controlled by fractures/faults, and the deeper aquifers found at depths extending up to 210 m below the surface are recharged from the upper unconfined aquifer through fractures. The permeability of the lower aquifers is not low due to weathered and fractured Quaternary basalt, scoriaceous rocks, and scoria. However, their interconnection depends on the nature and density of fracture lines. The layers may have fractures to store and transmit groundwater but need another high aperture fracture to be connected to other shallower or deeper weathered

and fractured layers. The Dangila model does not resemble the groundwater flow model of the Tana basin (Fenta et al., 2016) due to its fracture dissected flow systems. The conceptual model is in agreement with the shallow aquifer conceptual model of the area by Walker et al. (2019a), who also noted the lack of interaction between shallow and deep groundwater. The model will have a considerable advantage in exploring and managing groundwater from volcanic aquifers of complex geological settings affected by the fault, fracture, or rifting. It can be transferred to an area with a similar geological setting for groundwater exploration with great emphasis on fracture networks.

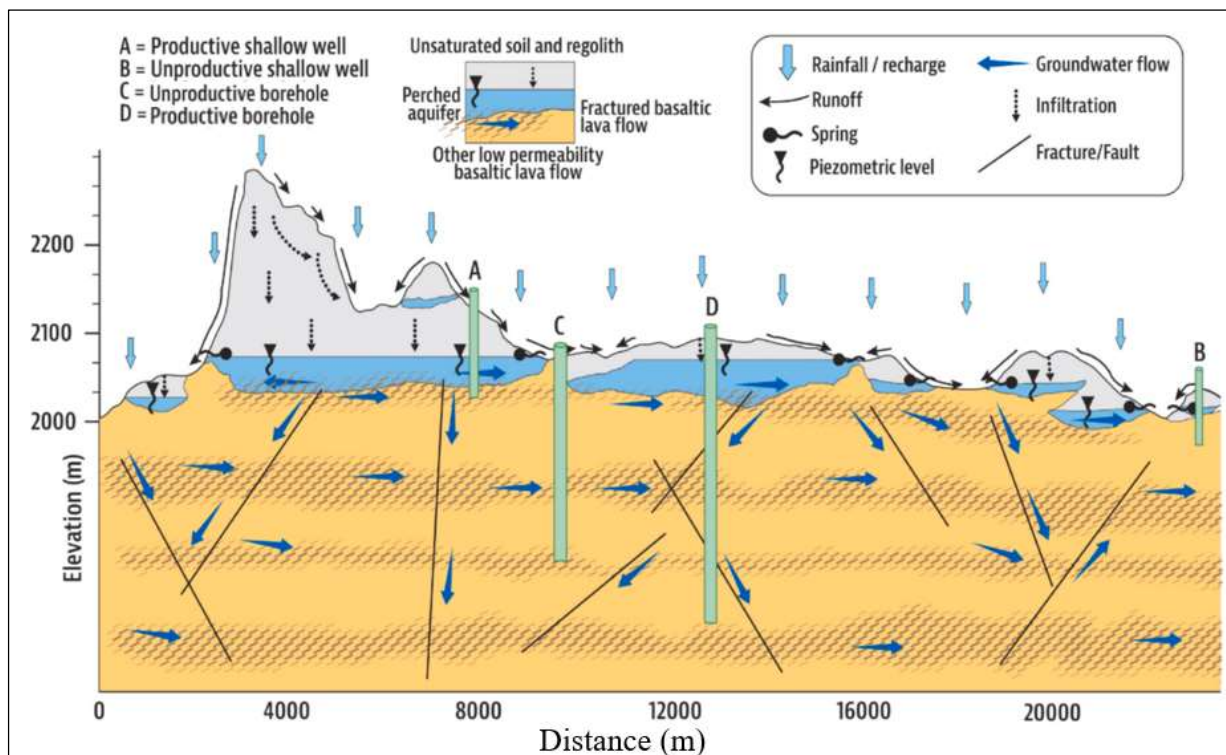


Fig. 47 Hydrogeological conceptual model of Dangila Town and its surrounding area aquifer system.

4.6.1 Groundwater Flownets

The groundwater movement through the surface is not visible; however, it is possible to visualize the flow paths in 2D and 3D space. The visualization of groundwater flow using flow nets uses various assumptions and flow boundaries. Flow nets indicate the recharge, discharge, area, and flow types (local, intermediate, and regional) and help one to understand the groundwater flow's driving forces.

The groundwater flow system can be categorized as topographic controlled flow using gravitation as a driving force for the upper unconfined aquifer and graviton and hydrostatic for the deep aquifer system. The shallow groundwater flow system, which depends on the local topography or is gravity-driven, can be represented as a local groundwater flow system. It is recharged at various localities and discharged after traveling a short distance locally. Therefore, the shallow aquifer system local flow comprises several local recharge and discharge areas. Conversely, the deep multi-layer aquifers system consists of various permeable and impermeable layers with different degrees of weathering and fracturing. The impermeable layers and mass above the aquifer create a considerable hydrostatic pressure that can drive the water to the surface when the upper lying mass is removed by drilling. The presence of an artesian borehole with a total depth of 160 m at Dengeshita kebele and the shallow-depth piezometer water levels in other boreholes varying from 2.5–15 m indicates the presence of hydrostatically upward driven movement in the lower multilayered aquifers. However, except for the borehole data, there has been no evidence indicating the discharge of deeper multi-layer aquifers to springs and rivers. The stable water isotope investigation showed that the deep aquifer system is mainly recharged from the mountains or highlands and flows through the main fracture lines to the reservoir. Therefore, the deep aquifer flow system can be represented by an intermediate flow recharged at topographically high lands and possibly discharged at lowlands to the river, or it might follow deeper to recharge the regional groundwater.

The fracture control flow systems are not uniform as fractures are not homogeneously distributed in the rock mass. The permeability of the fracture system is very sensitive to the fracture aperture and degree of fracture connectivity (Banks & Robins, 2002). However, assuming a continuous steady-state flow and considering the information gathered from the multidisciplinary hydrogeological investigations, the groundwater flownet has been represented by a modified Toth's (Toth, 1963) groundwater flow model. The Toth (1963) theoretical analysis of groundwater flow in a small river basin considers a local, intermediate, and regional groundwater flow system. The local flow systems are highly dynamic and shallow; they have the most astonishing exchange with surface water and discharge much water to the surface. The Dangila and its surrounding area groundwater flownet showed that the shallow aquifer is recharged from rainfall, and later it recharges the deep aquifers systems (Fig. 48). Apart from Toth's (1963) model that describes the presence of a regional groundwater flow in a small river basin, there is no confirmation of the presence of regional groundwater flow in the area. According to Toth's (1963) model, groundwater flow systems

occur not only in aquifers (unconfined and confined) but also in aquitards. The confining aquifers are recharged at outcrop sites or by downward water leakage from overlying aquifers, and may discharge in the form of upward leakage of water into overlying aquifers at downgradient areas.

The local system flow paths are relatively short, whereas the intermediate flow systems originate in recharge areas and discharge downgradient following topography and fracture network. Intermediate flow systems encompass at least one local flow system; regional flow systems originate at regional recharge areas and flow to distant discharge locations, with relatively long flow paths. The regional system often surrounds one or more local and intermediate flow systems.

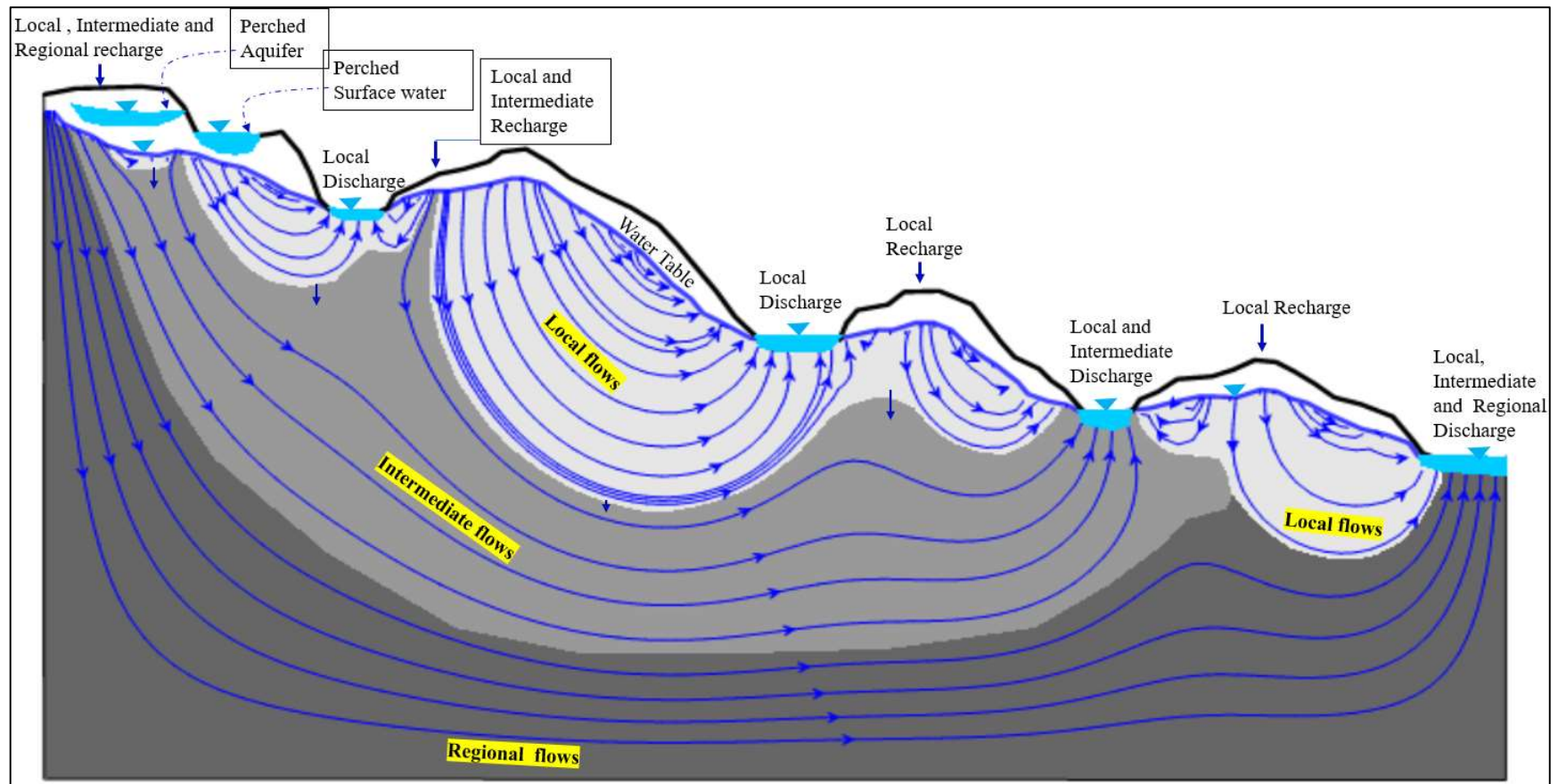


Fig. 48 Simplified schematic of the groundwater flow of Dangila and its surrounding area based on Toth (1963).

4.7. Sustainable Groundwater Management of Dangila Town and its Surrounding Area

The limited resource requires a wise management program that satisfies the demand. Population growth followed by the establishment of new settlements and agricultural expansion increase the freshwater demand. Besides, there are interests among the private sector to establish water bottling companies to add to the present two companies. However, the yield of boreholes reduces with years of abstraction as the abstraction is more than the replacement rate or recharge. Furthermore, fertilizer and pesticides, locations of shallow wells in the farmlands, inadequate and shallow well construction expose the aquifer for anthropogenic pollution. The Ethiopian government is currently implementing countrywide irrigation projects using groundwater to achieve the country's development goals (Mengistu et al., 2019).

The sustainable management for rural development is dependent on research results to enable wise utilization of the diverse geological setting of volcanic aquifers. The common utilization of groundwater in the study area and throughout Ethiopia has traditionally been through the use of hand-dug shallow wells and springs. Drilling deep wells require a considerable budget, and insufficient study will cause many budgets to be spent ineffectively. The deep drilling and pumping technology in the country since the 1970s has enabled groundwater exploitation and human settlement to be extended in response to the increasing population. However, the sanitation risk of the shallow groundwater still raises questions. Conversely, irrigation water from springs and shallow wells is appropriate when it comes to quality. However, the yield is meager and cannot be used for more than small-scale backyard agriculture.

Moreover, the study results showed that the groundwater of Dangila town and its surrounding area is good quality for drinking and industrial use while needing a few adjustments of the deep groundwater for irrigation due to Na% that will lead to sodic soil. The above-stated pressing concerns should be addressed for better monitoring and sustainable management of groundwater to support sustainable development. Therefore, the results of this study will assist the water sector in sustainably managing groundwater as the only available freshwater source.

The methodology employed resulted in two successful deep boreholes during the PhD thesis research project life span. The first of these boreholes, with a groundwater yield of 3.5 L/s, is currently used for water bottling purposes by '*Kefilta wuha*' private company at Dangila town. The second set of a borehole, with a groundwater yield of >30 L/s, are used for small-scale irrigation and freshwater drinking supply for rural populations at Dengeshita kebele of Dangila woreda. These boreholes help to minimize the scarcity of the freshwater supply for drinking, irrigation and industrial applications.

The future management of groundwater for sustainable development should focus on modeling fracture and fault-based groundwater flow and handling of anthropogenic pollution. Traditional practices to manage groundwater based on observation and previous data alone will lead to a loss of time and budget. There is also evidence of overexploitation of groundwater, which emends further assessment and may lead to re-injection of aquifer technology. Besides, preserving the natural ecosystems and protecting the overgrazing eucalyptus tree plantations, along with other activities that deteriorate the aquifer systems, should be averted. Furthermore, the development of a digital well recoding database, which consists of borehole history and web links, is helpful to develop a better groundwater management system.

5. SUMMARY

The quest to meet the clean water demand in Ethiopia will be accomplished with the sustainable use of its groundwater resources. The distinct attributes of groundwater, being less susceptible to anthropogenic pollution and climate change, and its accessibility in most rural parts of the country encourage the various sectors to focus on groundwater resources. It has the capacity to alleviate the scarcity of fresh water for drinking and small-scale irrigation use. However, the groundwater reservoir's nature and rainfall have caused variations in groundwater occurrence, quality, quantity, and aquifer parameters within hundreds of meters of spatial separation. It causes challenges to managing the resources of the area without conducting intensive investigations efficiently.

The varying physiographic area surrounding Dangila town of northwest Ethiopia has been affected by continual borehole failure and low yield for the past number of decades. Volcanic rocks mainly cover the northwest Ethiopian Plateau land, and their volcanic aquifers are the primary source of fresh water. Unlike the Icelandic volcanic aquifers that have been the focus of research, there has been minimal research conducted on the continental volcanic aquifers affected by rifting and faulting. These imposed sustainable exploration and management contests that prompted groundwater research.

Volcanic aquifers demand multi-investigation approaches using field surveys, laboratory analysis, and open-source information gathering to understand the nature of the aquifer system. Multi-investigation approaches employing existing boreholes, rock outcrops, hydrochemistry, water-stable isotope analysis, near-surface geomagnetic and VES surveys, and pump test analysis techniques have been used. Moreover, open sources databases, satellite images, and published research works have provided essential information.

The findings of the study showed that the volcanic aquifer systems of the area comprise a multi-aquifer system with alternating groundwater-bearing layers. It has an unconfined perched aquifer at a shallow depth and semiconfined and confined aquifers at greater depths. The perched unconfined aquifer in the upper soils and regolith overlies the confined and semiconfined aquifers in the weathered and fractured rocks consisting of mainly vesicular to aphanitic basalt lava flows, scoriaceous basaltic lava flow, and scoria falls.

The outcrop basaltic rocks have either aphanitic, porphyritic or vesicular texture with olivine, pyroxene, and plagioclase rock-forming minerals that are porphyries. The vesicles are filled occasionally with multigenerational carbonates that change the texture to amygdaloidal. The highly vesicular and fractured permeable basalts are the most productive aquifer of the regions. The recent basalts of the Lake Tana Basin that include the study area result from fractional crystallization of the same basaltic magma source with the most recent known age of 33,000y. A total of 25 groundwater samples from springs, shallow wells, and boreholes representing the shallow and deep aquifers systems have been analyzed for major cation and ion constituents of the groundwater system. The hydrochemistry laboratory results comprising 13 hydrochemical and three hydrophysical parameters have been examined for the dominant ion sources in the aquifer, groundwater facies, and water quality for drinking and irrigation uses. The results of the hydrochemical analysis indicated that the physical water parameters (pH, TDS, and EC) are lowest in the shallow aquifer system and highest in the deep aquifer system. The highest values are due to increases in the dissolution of ions in the aquifers with time and depth, whereas low values in shallow aquifers imply young groundwater with low residence time. The dominant cations in the deep aquifer system are in the order of $\text{Na}^+ > \text{Ca}^{2+} > \text{Mg}^{2+} > \text{K}^+$ whereas in the shallow aquifer system they are $\text{Ca}^{2+} > \text{Mg}^{2+} > \text{Na}^+ > \text{K}^+$. The dominant anions in both aquifer systems are in $\text{HCO}_3^- > \text{Cl}^- > \text{SO}_4^{2-}$. Therefore, the most abundant cation in the deep aquifer system is Na^+ , whereas in shallow aquifers it is Ca^{2+} while HCO_3^- is the dominant anion in both aquifer systems.

The volcanic aquifers of the area have five groundwater facies: Ca-HCO_3 , Ca-Mg-HCO_3 , Ca-Na-HCO_3 , Na-Ca-HCO_3 and Na-HCO_3 . The Ca-HCO_3 groundwater types dominate the shallow, unconfined aquifer system, and mainly Na-HCO_3 types dominate deep aquifer systems. The presence of a significant amount of chloride in a few shallow wells due to anthropogenic pollution results in $\text{Ca-HCO}_3\text{-Cl}$ and $\text{Ca-Mg-HCO}_3\text{-Cl}$ water types. The shallow wells are mainly exposed to surface contamination due to erosion and farming due to inadequate well construction. In addition, the presence of Ca-Na-Mg-HCO_3 type of water facies might be caused by the intermixing of shallow and deep groundwater systems through fractures.

Unlike the groundwater of Ethiopian Rift volcanic rocks that cause health problems, the fluoride concentration of both aquifer systems is less than 0.82 mg/l, and sulfate and nitrate concentrations are low. Therefore, except for Cl, pH, and Fe being high concentration values of a few shallow and deep aquifer locations, all physical and chemical water parameters are within the drinkable water limits of WHO standards. This suggests that water from both aquifer systems are potable without considering the microbial water quality. Moreover, the appraisal of the aquifer system suitability for irrigation use based on the three commonly used factors, SAR, Na%, and RSC, showed that SAR and RSC values from all groundwater schemes are of excellent quality and can be used for irrigation without any challenge. However, high Na% in the aquifer system restricts the deep groundwater suitability for irrigation without adjustment and can result in sodic soils, which later result in low crop yield.

The groundwater composition controlling mechanism evaluation with its dominant sources indicates that the rock weathering dominates the groundwater chemistry, as opposed to evaporation and precipitation. Further analysis of the relationship between cations and anions constituents of the aquifer reveals that more sodic lithologic units are encountered as the groundwater moves along a flow path. Besides, calcium and magnesium ions are exchanged for sodium ions attached to aquifer solids. The sodium-containing silicates weathering increases with depth and along flow paths. These processes result in a decrease in calcium and magnesium and a corresponding increase in sodium.

Conversely, the continuous increase of bicarbonate concentrations in the aquifer with residence times and depth implies that the primary source of bicarbonate in volcanic aquifers is attributed to soil carbon dioxide interacting with water to form carbonic acid. These result in water that evolves to a sodium-bicarbonate type and sodium-calcium-bicarbonate types when water travels from recharge to deeper storage or discharge areas. Generally, the rock–water interactions involving silicate weathering, cation exchange, and carbonation are the main hydrogeochemical processes that control the composition of groundwater chemistry in the processes of groundwater evolution.

The 48 seasonal rain, surface and groundwater samples were collected after the main rainy and dry seasons. The laboratory analysis of these samples for their deuterium and ^{18}O content indicated that deuterium values range from -7.99‰ to 55.50‰ , with maximum values from rain samples collected during the dry season and the minimum values from boreholes representing the deep aquifer system. Similarly, the heavier oxygen isotope ($\delta^{18}\text{O}$) showed the highest values of 11.39‰ and 10.98‰ in shallow wells and river samples, respectively. The lowest value,

–3.98‰ of $\delta^{18}\text{O}$, was obtained from borehole water samples. The seasonal variations are observed in the rain samples with a proportional increase in heavier isotopes during the dry season.

The higher $\delta^{18}\text{O}$ values than $\delta^2\text{H}$ in the shallow aquifer system are related to surface evaporation before recharge and groundwater evaporation in the vadose zone. This suggests that the deuterium content is more affected in atmospheric phenomena, including moisture recycling than in surface and groundwater evaporation. However, the content of $\delta^{18}\text{O}$ is affected by both factors being more influenced by surface evaporation. The depleted heavier isotope and high d-excess values in the deep aquifer indicate that the aquifer system is recharged from precipitation that retains moisture recycling in the atmosphere and less affected by evaporation. The sources of northwest Ethiopian precipitation are related to the Atlantic Ocean, Congo forests transpiration, and possibly from local recycled moisture. Simultaneously, deep aquifer recharge time is related to the late Holocene humid phase.

Precipitation recharges the upper-perched aquifer directly through the vadose zone or following the shallow fractures, while the deep aquifer is recharged through the major fractures. The recharge estimation values of the shallow aquifer range from 280–477 mm/y or 17%–26% of mean annual precipitation, with 28% of total evapotranspiration. The upper unconfined aquifer has high interaction with rainfall and rivers with the sharp peaks in the rivers' stage and the shallow aquifer water level following rainfall events. The groundwater level data analysis collected after the main rainy season showed that the shallow aquifer mainly recharges the Kilti river on the mountain fronts and highlands part of the river catchment. Conversely, the river recharges the groundwater at relative lowlands. However, a different characteristic is observed for the Branti river in that the river recharges the groundwater in most parts of the area following the rainy season.

A near-surface geomagnetic survey aimed at mapping the possible structures that control the groundwater movement and storage was conducted and data were collected at 718 locations. The ground total magnetic data was processed to avoid various possible effects on the survey. The result has been used to prepare a total magnetic intensity map to infer faults and fractures used as a groundwater conduit and for storage. The magnetic anomalies in a volcanic terrain underlain by Mesozoic sediments and metamorphic basement rocks are mainly attributed to the shallow depth of basic igneous rock due to their high magnetite content.

The inferred fracture and faults based on the surface geomagnetic field data have the same orientation as the Lake Tana Basin regional structures, with four main structural orientations: N–S, NW–SE, NE–SW, and E–W. The N–S oriented structures have more significant influences on the near-surface geomagnetic data, and they are situated at greater depths than other

structures. The NW–SE, NE–SW, and E–W oriented structures have lower influences on the total magnetic field data due to their relatively shallow depths. The most productive boreholes of the area that supply fresh groundwater to the Dangila town and the recently drilled Dengeshita kebele borehole are situated at NW–SE and NE–SW fractures, respectively.

The VES data were gathered at 32 points, with 19 to 24 readings at each point employing the Schlumberger electrode arrangement. A total of 129 readings were recorded, processed and interpreted qualitatively and quantitatively to map the various aquifers' potential groundwater area, depth, and geometry. The qualitative and quantitative interpretations have been conducted using graphs, pseudo-depth sections, geoelectric sections, curve matching techniques, 1D inverse modeling, 2D resistivity sections, 3D volume representations and resistivity images.

The resistivity of the layers varies from 1 to 15171 Ω -m and is associated with the weathered scoria, scoriaceous, altered clay, water-bearing layers to the fresh aphanitic basalt without pores and fractures. The resistivity of layers that store water in the pore spaces is generally < 15 Ω -m with a highly variable aquifer system mainly controlled by the major fractures. However, the minor fracture in the basalts and scoriaceous basalts have meager aquifers with <3.5 L/s yield for a borehole drilling up to 210 m in depth. The fractures used as a conduit and for storage of groundwater flow forms a discontinued aquifer system that interacts minimally with the shallow unconfined aquifer.

The principal aquifer bearing layers of the area can be grouped into the following depth classes: 3–15, 35–65, 130–155, and 180–210 m. However, a depth might vary depending on the fracture's nature, the area's morphology, and the season. The first depth (3–15 m) represents the shallow unconfined aquifers within the soil and regolith, with a maximum yield of <1 L/s. Furthermore, it is used as a water source for small-scale backyard farming in addition to drinking and household use. Drilling a borehole up to 70-m deep can yield from 0–4 L/s depending on the fracture and recharge conditions, with a higher tendency to become dry after a few years of abstraction. The most productive aquifer layers are mainly situated in a 130–155 m depth range with a possible groundwater yield of >15 L/s per borehole. On the contrary, it might yield 0–3.5 L/s if the layers are not connected to the major fracture and the recharge areas. Generally, the aquifer potential and geometrical setting system are heterogeneous, anisotropic and dissected aquifer systems, mainly resulting from the nature of the volcanism.

Moreover, the reviews of the new technology of the geophysical fiber optic sensors show that it represents the future for groundwater exploration and management situated in complex geological settings. It is more capable than current geophysical techniques of sensing performance

comprising sensing range, spatial resolution, and measurement parameters. It can be said that fiber optic technology is a revolutionary technological departure from traditional copper wires. As we move forward in the Information Technology age, the movement of extremely high amounts of data can potentially fall on the shoulders of this new technology. The application of this technology in hydrogeophysics will result in a new paradigm.

The hydraulic conductivity of the deep aquifer in the dominant fractures layers is higher than dominated by weathered layers, and during pumping tests, the recovery was fast. The most productive borehole has a 3.6×10^{-1} (m/d) hydraulic conductivity and 5.20×10^1 (m²/d) transmissivity value. The dominant fracture aquifer has the maximum storage coefficient values of 9.17×10^2 . Conversely, the shallow aquifer's mean hydraulic conductivity value varies from 2.3 m/d to 9.7 m/d during dry and rainy seasons, respectively. The higher transmissivity values during the rainy season are related to the increase in thickness saturated and to transmissive layers.

The results of the multi-investigation approach have been used to generate a groundwater conceptual flow model with its corresponding groundwater flownet. The findings of this study showed that neither the available islandic volcanic aquifer conceptual model nor the previous large-scale conceptual groundwater flow model of Ethiopian volcanic aquifers could be adapted. Therefore, the conceptual hydrogeological model of the area called the Dangila model that can fulfill the specific study area of aquifer characteristics has been constructed. The model will be helpful for future sustainable groundwater management of the area.

Persuasively, the volcanic aquifer investigation of northwest Ethiopia plateau land is twofold: In the first cases, the investigation minimizes the problems surrounding the water supply for drinking, irrigation, and industrial applications in the area due to the recommendation of two productive boreholes drilling. Secondly, it contributes detailed scientific knowledge to the understanding of the complex volcanic aquifer nature of the area for future groundwater management that has faced many borehole failures during past decades.

ACKNOWLEDGMENT

Most Notably, I would like to thank the Tempus public foundation for providing a stipendium hungaricum scholarship for my PhD study. I would like to express my extraordinary gratitude and thanks to my supervisor, professor János Szanyi. He devoted his unreserved time guiding all aspects of my study and research at the University of Szeged. He was not only encouraging my research but also supporting and sharing solutions, as well as a colleague to solve even non-academic issues. I would like to thank Professor Toth Tivadar for his unreserved support and for sharing ideas during my study and research times. His inspiration for geology started from my first field trip with him at Mecsek Mountains fault zone(Mecsekalja Zone).

I thank Professor Palcsu László, Institute for Nuclear Research, Debrecen Laboratory of Climatology and Environmental Physics section head, who helped me with groundwater sample laboratory analyses. Furthermore, I am grateful to Mr Atilla Bencsik, an academic staff of the Department of Mineralogy, Geochemistry and Petrology, who helped me prepare thin sections of rock samples and Mr Adrian, who helped me analyse the thin sections using Ore and Raman microscopes at the same Department. It was a pleasure to work with a friendly team in such a friendly and enjoyable atmosphere as in the Mineralogy, Geochemistry, and Petrology Department of the University of Szeged.

This thesis was only possible with the help of Bahir Dar University and the Earth Sciences staff, who assisted me and provided field logistics during my fieldwork in Ethiopia. I want to thank the Dangila woreda water Bureau of Ethiopia for their information about the status of hand-dug, spring data, and assistance in collecting geomagnetic data around Dangila town. I thank the Abay River basin office of Bahir Dar Branch for supporting the field car, multimeter and technician to collect a water sample from the Gilgel Abay river catchment. I am also grateful to the Amhara water works design and supervision enterprise for providing boreholes and some VES data.

Moreover, I would like to thank all of my colleagues and friends at the University of Szeged who make my stay at the university magnificent. Finally, I am grateful to my family and friends and those who were always there for me.

REFERENCE

- Abate, B., Koeberl, C., & Korner, W. (1998). Petrography and geochemistry of basaltic and rhyolitic rocks from Lake Tana and the Gimjabet-Kosober areas (North Central Ethiopia). *Journal of African Earth Sciences.*, 26(1), 119–134. [https://doi.org/10.1016/S0899-5362\(97\)00140-1](https://doi.org/10.1016/S0899-5362(97)00140-1)
- Abdunaser, K. (2015). Satellite Imagery for Structural Geological Interpretation in Western Sirt Basin, Libya : Implication for Petroleum Exploration. *Geosciences*, 5(1), 8–25. <https://doi.org/10.5923/j.geo.20150501.02>
- ABEM (2009). ABEM SAS 4000/SAS 1000 Instrument Instruction Manual. Sweden.
- Aberra, T. (1990). The hydrogeology and water resources of the Ansokia Highlands springs. In *Memoires of the 22nd Congress of IAH (Vol. XXII)*. Lausanne.
- Abiye, T., & Kebede, S. (2011). The role of geodiversity on the groundwater resource potential in the upper Blue Nile River Basin, Ethiopia. *Environmental Earth Sciences*, 64(5), 1283–1291. <https://doi.org/10.1007/s12665-011-0946-7>
- Aboelkhair, H., & Rabei, M. (2013). Delineation of the subsurface structures and basement surface of the Abu-Rodaym area, Southwestern Sinai, using ground magnetic data. *Earth Planets Space*, 65, 749–757. <https://doi.org/10.5047/eps.2012.12.006>
- Aghazadeh, N., Chitsazan, M., & Golestan, Y. (2017). Hydrochemistry and quality assessment of groundwater in the Ardabil area, Iran. *Applied Water Science*, 7(7), 3599–3616. <https://doi.org/10.1007/s13201-016-0498-9>
- Ahmed, M., Samie, S., & Badawy, H. (2013). Factors controlling mechanisms of groundwater salinization and hydrogeochemical processes in the Quaternary aquifer of the Eastern Nile Delta, Egypt. *Environmental Earth Sciences*, 68, 369–394.
- Al-garni, M. (2011). Magnetic and DC resistivity investigation for groundwater in a complex subsurface terrain. *Arab Journal Geoscience*, 4, 385–400. <https://doi.org/10.1007/s12517-009-0071-z>
- Alken, P., Thébault, E., Beggan, C., Amit, H., Aubert, J., Baerenzung, J., ... Zhou, B. (2021). International Geomagnetic Reference Field: the thirteenth generation. *Earth, Planets and Space*, 73(1). <https://doi.org/10.1186/s40623-020-01288-x>
- Ashley, R., & Burley, M. (1994). Controls on the occurrence of fluoride in groundwater in the Rift Valley of Ethiopia. In Nash, G., and McCall, H. (Ed.) *Groundwater Quality*. London.: Chapman & Hall.

- Ayenew, T., Demlie, M., & Wohnlich, S. (2008). Hydrogeological framework and occurrence of groundwater in the Ethiopian aquifers. *Journal of African Earth Sciences*, 52, 97–113. <https://doi.org/10.1016/j.jafrearsci.2008.06.006>
- Ayenew, T., Kebede, S., & Alemyahu, T. (2008). Environmental isotopes and hydrochemical study applied to surface water and groundwater interaction in the Awash. *Hydrological Processes*, 1563, 1548–1563. <https://doi.org/10.1002/hyp.6716>
- Babad, A., Burg, A., & Adar, E. (2019). Conceptual hydrological approach to a geologically complex basin with scarce data: the Hula Valley, Middle East. *Hydrogeology Journal*, 28(2), 703–722. <https://doi.org/10.1007/s10040-019-02031-x>
- Banks, D., & Robins, N. (2002). An introduction to Groundwater in Crystalline Bedrock. Norges geologiske undersøkelse. Retrieved from [http://www.ngu.no/filea archive /91 /In tro_to_groundwater.pdf](http://www.ngu.no/filea%20archive%2091/In%20tro%20to%20groundwater.pdf)
- Barbieri, M. (2019). Isotopes in Hydrology and Hydrogeology. <https://doi.org/10.3390/w11020291>
- Barker, R. (1989). Depth of investigation of collinear symmetrical four-electrode arrays. *Geophysics*, 54(8), 1031–1037. <https://doi.org/10.1190/1.1442728>
- Belay, M., & Bewket, W. (2013). Traditional irrigation and water management practices in highland Ethiopia: Case study in Dangila woreda. *Irrigation and Drainage*, 62(4), 435–448.
- Beshawered, E., Ashenafi, S., Edris, M., Burusa, G., Zewede, T., Tesfaye, Y., ... Wendant, M. (2010). *Geology, Geochemistry and Gravity Survey of Bahir-Dar Area*. Addis Ababa, Ethiopia
- Binley, A., Cassiani, G., & Deiana, R. (2010). Hydrogeophysics - Opportunities and Challenges. *Bollettino Di Geofisica Teorica Ed Applicata*, 51(4).
- Binley, A., Hubbard, S., Huisman, J., Revil, A., Robinson, D., Singha, K., & Slater, L. (2015). The emergence of hydrogeophysics for improved understanding of subsurface processes over multiple scales. *Water Resources Research*, 51, 1–30. <https://doi.org/10.1002/2015WR017016>
- Blatt, H., & Jones, R. (1975). Proportions of Exposed Igneous, Metamorphic, and Sedimentary Rocks. *Geological Society of America Bulletin*, 86(8), 1085–1088. [https://doi.org/10.1130/B0016-7606\(1975\)86<1085:POEIMA>2.0.CO;2](https://doi.org/10.1130/B0016-7606(1975)86<1085:POEIMA>2.0.CO;2)
- Brubaker, K., Entekhabi, D., & Eagleson, P. (1993). Estimation of continental precipitation recycling. *Journal of Climate*, 6, 1077–1089. [https://doi.org/10.1175/1520-0442\(1993\)006<1077:EOC PR>2.0.CO;2](https://doi.org/10.1175/1520-0442(1993)006<1077:EOC PR>2.0.CO;2)

- Charlier, J., Lachassagne, P., Ladouche, B., Cattani, P., Moussa, R., & Voltz, M. (2011). Structure and hydrogeological functioning of an insular tropical humid andesitic volcanic watershed : A multi-disciplinary experimental approach. *Journal of Hydrology*, 398, 155–170. <https://doi.org/10.1016/j.jhydrol.2010.10.006>
- Chorowicz, J., Collet, B., Bonavia, F., Mohr, P., Parrot, J., & Korme, T. (1998). The Tana basin, Ethiopia : intra-plateau uplift, rifting and subsidence. *Tectonophysics*, 295, 351–367. [https://doi.org/10.1016/S0040-1951\(98\)00128-0](https://doi.org/10.1016/S0040-1951(98)00128-0).
- Collier, H. (1993). Borehole Geophysical Techniques for Determining the Water Quality and reservoir Parameters of Fresh and Salt Water Aquifers in Texas. Retrieved from http://www.twdb.texas.gov/publications/reports/numbered_reports/doc/r343/r343vol1_1.pdf
- Cooper, H., & Jacob, C. (1946). A generalized graphical method for evaluating formation constants and summarizing well-field history. *Transactions American Geophysical Union*, 27, 526-534.
- Correa, J., Pevzner, R., Bona, A., Tertyshnikov, K., Freifeld, B., Robertson, M., & Daley, T. (2019). 3D vertical seismic profile acquired with distributed acoustic sensing on tubing installation : A case study from the CO2CRC Otway Project. *Interpretation, SEG Special Section.*, 7(1). <https://doi.org/10.1190/INT-2018-0086.1>
- Craig, H. (1961). Isotopic variations in meteoric waters. *Science (New York, NY)* 133:1702–1703. *Science*, 133, 1702-1703. <https://doi.org/10.1126/science.133.3465.1702>
- CSA. (2012). Summary and Statistical Report of the 2012 Population and Housing Census- Population Size by Age and Sex. Addis Ababa, Ethiopia.
- Custodio, E. (1989). Groundwater Characteristics and Problems in Volcanic Rock Terrains. Isotopic Techniques in the Study of the Hydrology of Fractures and Fissured Rocks. In *Panel Proceedings Series - (pp. 87–137)*. Vienna: International Atomic Energy Agency.
- Dansgaard, W. (1964). Stable isotopes in precipitation. *Tellus*, 16, 436–468. <https://doi.org/10.1134/1.1261687>
- Darcy, H. (1856). *Les Fontaines Publiques de la Ville de Dijon*. Paris, France: Victor Dalmont.
- Demlie, M., Wohnlich, S., & Ayenew, T. (2008). Major ion hydrochemistry and environmental isotope signatures as a tool in assessing groundwater occurrence and its dynamics in a fractured volcanic aquifer system located within a heavily urbanized catchment, central Ethiopia. *Journal of Hydrology*, (352), 175–188.
- Demlie, M., Molla, W., Wohnlich, S., Wisotzky, F., & Gizaw, B. (2007). Groundwater recharge, flow and hydrogeochemical evolution in a complex volcanic aquifer system, central Ethiopia. *Hydrogeology Journal*, (15), 1169–1181. <https://doi.org/10.1007/s10040-007-0163-3>.

- Desserta, C., Bernard, D., Jerome, G., Louis M., & Claude J., A. (2003). Basalt weathering laws and the impact of basalt weathering on the global carbon cycle. *Chemical Geology*, 202, 257–273. <https://doi.org/10.1016/j.chemgeo.2002.10.001>
- Dupuit, J. (1863). *Etudes theoriques et pratiques sur le mouvement des eaux dans les canaux decouverts et a travers les terrains permeables*. Dunod, Paris.
- Earthwise, B. (2021). Volcanic Aquifers. Retrieved from http://earthwise.bgs.ac.uk/images/1/1e/Volcanic_aquifers.png
- Edwards, L.(1977). A modified pseudo section for resistivity and induced polarization. *Geophysics* 42(5):1020-1036, 42(5), 1020–1036. <https://doi.org/10.1190/1.1440762>.
- FAO. (2016). Climate of Ethiopia, food and agricultural organization of the united nation. Retrieved from http://www.fao.org/nr/water/aquastat/countries_regions/ETH/. Cited on 12 March 2019
- Fazzini, M., Bisci, C., & Billi, P.(2015). The Climate of Ethiopia. In P. Billi (Ed.), *Landscapes and Landforms of Ethiopia*, World Geomorphological Landscapes. pp. 65–87. Springer. https://doi.org/10.1007/978-94-017-8026-1_3.
- Fenta, M., Potter, D. & Szanyi, J. (2021). Fibre Optic Methods of Prospecting : A Comprehensive and Modern Branch of Geophysics. *Surveys in Geophysics*, 42, 551–584. <https://doi.org/10.1007/s10712-021-09634-8>
- Fenta, N., Camp, M., Kebede, S., & Walraevens, K. (2016). Journal of African Earth Sciences Hydrologic interconnection between the volcanic aquifer and springs, Lake Tana basin on the Upper Blue Nile. *Journal of African Earth Sciences*, 121, 154–167. <https://doi.org/10.1016/j.jafrearsci.2016.05.015>
- Fetter, C. (2001). *Applied Hydrogeology* (4th edition). Prentice-Hall, Inc. Upper Saddle River, New Jersey.
- Fetter, C.(2018). *Applied Hydrogeology* (4th edition). Waveland Press, Inc.
- Fisher, R., & Mullican, W. (1997). Hydrochemical evolution of sodium-sulfate and sodium-chloride groundwater beneath the Northern Chihuahuan Desert, Trans-Pecos, Texas,US A. *Hydrogeology Journal*, 5, 4–16.
- Francés, A.(2015). Integration of hydrogeophysics and remote sensing with coupled hydrological models. University of Twente. <https://doi.org/10.3990//1.9789036539166>
- Freeze, Q., & Cherry, J. (1979). *Groundwater*. Prentice-Hall, Inc.
- Gbenga, M., Olayanju, A., Adelusi, & Kola, A. (2015). Combined Use of Ground Magnetic and Electrical Resistivity Methods in Bedrock Mapping : Case Study of NTA Premises , Oba Ile Area, South-Western Nigeria. *EJGE*, 6591–6606.
- GEM (2008). GSM-19: Instruction users Manual.

- Getaneh, A. (1991). Lithostratigraphy and environment of deposition of Late Triassic to Early Cretaceous sequences of the central part of Northwestern Plateau. Ethiopia. N. Jb. Geol. Palaont. Abb., 182, 255–284.
- Gibbs, R. (1970). Mechanisms Controlling World Water Chemistry. *Science*, 170, 1088–1090. <https://doi.org/DOI: 10.1126/science.170.3962.1088>
- Gringarten, A., Ramey, H. , & Raghavan, R. (1974). Unsteady-state pressure distributions are created by a single infinite conductivity vertical fracture. *Society of Petroleum Engineers Journal*, 14(4), 347.
- Halbich, Č., & Vostrovský, V. (2011). GIS as spatial decision support system. *Agris On-Line Papers in Economics and Informatics*, III(2), 67–74.
- Hamilton, P. (2005). Groundwater and surface water: A single resource. *Water Environment and Technology* (Vol. 17). Denver, Colorado.
- Hautot, S., Whaler, K., Gebru, W., & Desissa, M. (2006). The structure of a Mesozoic basin beneath the Lake Tana area, Ethiopia, revealed by magnetotelluric imaging. *Journal of African Earth Sciences*, 44, 331–338. <https://doi.org/10.1016/j.jafrearsci.2005.11.027>
- Hencher, S., & McNicholl, D. (1995). Engineering in weathered rock. *Quarterly Journal of Engineering Geology and Hydrogeology*, 28(3), 253–266. <http://doi.org/10.1144/GSL.QJEGH.1995.028.P3.04>
- Hernández-Antonio, A., Mahlkecht, J., Tamez-Meléndez, C., Ramos-Leal, J., Ramírez-Orozco, A., Parra, R., ... Eastoe, C. (2015). Groundwater flow processes and mixing in active volcanic systems : the case of Guadalajara (Mexico). *Hydrol. Earth Syst. Sci.*, 19, 3937–3950. <https://doi.org/10.5194/hess-19-3937-2015>
- Hofmann, C., Courtillot, V., Feraud, G., Rochette, P., Yirgu, G., Ketefo, E., & Pik, R. (1997). Timing of the Ethiopian flood basalt event and implications for plume birth and global change. *Nature*, 389, 838–841. <https://doi.org/https://doi.org/ 10.1038/39853>.
- Horita, J., & Wesolowski, D. (1994). Liquid-vapour fractionation of oxygen and hydrogen isotopes of water from the freezing to the critical temperature. *Geochimica et Cosmochimica Acta*, 58(16), 1–13. Retrieved from <papers2://publication/uuid/ F9BCD32F-8569-4ACF-81AF-08518BF40A32>
- Hubbard, S., Peterson, J., Majer, E., Zawislanski, P., Williams, K., Roberts, J., & Wobber, F. (1997). Estimation of permeable pathways and water content using tomographic radar data. *Leading Edge*, 16(11), 1623–1630.
- Hubbard, S., & Linde, N. (2011). *Hydrogeophysics* (pp.1–107).

- Hussain, Y., Uagoda, R., Borges, W., Nunes, J., Hamza, O., Condori, C., ... Cárdenas-Soto, M. (2020). The potential use of geophysical methods to identify cavities, sinkholes and pathways for water infiltration. *Water*, 12. <https://doi.org/10.3390/w12082289>
- IAEA/WMO. (2021). Global Network of Isotopes in Precipitation. The GNIP Database. Retrieved December 1, 2021, from <https://nucleus.iaea.org/wiser>
- Izquierdo, T. (2014). Conceptual hydrogeological model and aquifer system classification of a small volcanic island (La Gomera ; Canary Islands). *Catena*, 114, 119–128. <https://doi.org/10.1016/j.catena.2013.11.006>
- Jane CS, L. et al. (1996). Physical Characteristics of Fractures and Fracture Patterns. In *Rock Fractures and Fluid Flow. Contemporary Understanding and Applications* (pp. 29–102). Washington, D.C.: The National Academies Press.
- Join, J., Folio, J., & Robineau, B. (2005). Aquifers and groundwater within active shield volcanoes. Evolution of conceptual models in the Piton de la Fournaise volcano. *Journal of Volcanology and Geothermal Research*, 147, 187–201. <https://doi.org/10.1016/j.jvolgeores.2005.03.013>
- Jougnot, D. (2020). Developing hydrogeophysics for critical zone studies, importance of heterogeneities and processes at the mesoscopic scale. Sorbonne Université, Paris.
- Jousset, P., Reinsch, T., Ryberg, T., Blanck, H., Clarke, A., Aghayev, R., ... Krawczyk, C. M. (2018). Dynamic strain determination using fibre-optic cables allows imaging of seismological and structural features. *Nature Communications*, 9(1). <https://doi.org/10.1038/s41467-018-04860-y>
- Karrenbach, M., Cole, S., Ridge, A., Boone, K., Kahn, D., Rich, J., ... Langton, D. (2019). Fiber-optic distributed acoustic sensing of microseismicity, strain and temperature during hydraulic fracturing. *Geophysics*, 84(1), D11–D23. <https://doi.org/10.1190/geo2017-0396.1>
- Kearey, P., Brooks, M., & Hill, I. (2002). *An Introduction to Geophysical Exploration* (3rd edition). Blackwell Science Ltd.
- Kebede, S. (2004). Environmental isotopes and geochemistry in investigating groundwater and lake hydrology: cases from the Blue Nile basin & the Ethiopian Rift (Ethiopia).
- Kebede, S, Hailu, A., Crane, E., Dochartaigh, B., & Bellwood-Howard, I. (2018). *Africa Groundwater Atlas. Hydrogeology of Ethiopia*. British Geological Survey.
- Kebede, S. (2013). *Groundwater in Ethiopia. Features, Numbers and Opportunities*. Springer-Verlag Berlin Heidelberg.

- Kebede, S., & Travi, Y. (2012). Origin of the $\delta^{18}\text{O}$ and $\delta^2\text{H}$ composition of meteoric waters in Ethiopia. *Quaternary International*, 257, 4–12. <https://doi.org/10.1016/j.quaint.2011.09.032>
- Kebede, S., Travi, Y., Alemayehu, T., & Ayenew, T. (2005). Groundwater recharge, circulation and geochemical evolution in the source region of the Blue Nile River, Ethiopia. *Applied Geochemistry*, 20, 1658–1676. <https://doi.org/10.1016/j.apgeochem.2005.04.016>
- Kebede, S., Travi, Y., & Rozanski, K. (2009). The $\delta^{18}\text{O}$ and $\delta^2\text{H}$ enrichment of Ethiopian lakes. *Journal of Hydrology*, 365(3–4), 173–182. <https://doi.org/10.1016/j.jhydrol.2008.11.027>
- Koefoed, O. (1960). A generalized cagniard graph for interpretation of geoelectrical sounding data. *Geophysics Prospecting*, 8(3), 459–469. <https://doi.org/10.1111/j.1365-2478.1960.tb01728.x>
- Lachassagne, P., Aunay, B., Frissant, N., Guilbert, M., & Malard, A. (2014). High-resolution conceptual hydrogeological model of complex basaltic volcanic islands : a Mayotte , Comoros , case study. *Terra Nova*, 26(4), 307–321. <https://doi.org/10.1111/ter.12102>
- Li, J., Wang, W., Wang, D., Li, J., & Dong, J. (2020). Hydrochemical and Stable Isotope Characteristics of Lake Water and Groundwater in the Beiluhe Basin, Qinghai – Tibet Plateau. *Water*, 12(2269), 1–19. <https://doi.org/10.3390/w12082269>
- Li, M., Wang, H., & Tao, G. (2015). Current and Future Applications of Distributed Acoustic Sensing as a New Reservoir Geophysics Tool. *The Open Petroleum Engineering Journal*, 8(1), 272–281. <https://doi.org/10.2174/1874834120150625E008>
- Li, P., Wu, J., & Qian, H. (2014). Hydrogeochemistry and quality assessment of shallow groundwater in the southern part of the yellow river alluvial plain (Zhongwei section), Northwest China. *Earth Sciences Research Journal*, 18(1), 27–38. <https://doi.org/10.15446/esrj.v18n1.34048>
- Linde, N., Ginsbourger, D., Irving, J., Nobile, F., & Doucet, A. (2017). On uncertainty quantification in hydrogeology and hydrogeophysics. *Advances in Water Resources*, 110, 166–181. <https://doi.org/10.1016/j.advwatres.2017.10.014>
- Lu, G., & Wong, D. (2008). An adaptive inverse-distance weighting spatial interpolation technique. *Computers and Geosciences*, 34(9), 1044–1055. <https://doi.org/10.1016/j.cageo.2007.07.010>
- MacDonald, A., Davies, J., & Calow, R. (2008). “African hydrogeology and rural water supply”, *Applied Groundwater Studies in Africa*. In S. Adelana & A. MacDonald (Eds.), *IAH Selected Papers in Hydrogeology* (pp. 127–148). Taylor and Francis Group.

<https://doi.org/https://doi.org/10.1201/9780203889497>.

- MacDonald, A., Davies, J., & Dochartaigh, B. (2002). Simple methods for assessing groundwater resources in low permeability areas of Africa. Nottingham.
- Marra, G., Clivati, C., Luckett, R., Tampellini, A., Kronjäger, J., Wright, L., ... Calónico, D. (2018). Ultrastable laser interferometry for earthquake detection with terrestrial and submarine cables. *Science*, 361(6401), 486–490. <https://doi.org/10.1126/science.aat4458>
- Mateeva, A., Lopez, J., & Potters, H. (2014). Distributed acoustic sensing for reservoir monitoring with vertical seismic profiling. *Geophysical Prospecting*, 62, 679–692.
- Matthess, G. (1982). The properties of groundwater. Wiley and Sons, New York, 406 p. New York: Wiley and Sons.
- McDonald, G., Abbott, A., & Peterson, F. (1983). *Volcanoes in the Sea, the Geology of Hawaii*. , Honolulu. p 517. Honolulu: University of Hawaii Press.
- McDowell, P., Barker, R., Butcher, A., Culshaw, M., Jackson, P., McCann, D., ... Arthur, J. (2002). *Engineering Geophysics in investigations*. 2002.
- Mejías, M., & Plata, J. (2007). General concepts in hydrogeology and geophysics related to MRS. *Boletín Geológico y Minero*, 118(3), 423–440.
- Mengistu, H., Demlie, M., & Abiye, T.(2019). Review: Groundwater resource potential and status of groundwater resource development in Ethiopia. *Hydrogeology Journal*, 27(3), 1051–1065. <https://doi.org/10.1007/s10040-019-01928-x>
- Meybeck, M. (1987). Global Chemical Weathering of Surficial Rocks Estimated from River Dissolved Loads. *American Journal of Science*, 287, 401–428. <https://doi.org/10.2475/ajs.287.5.401>.
- Milsom, J. (2003). *Field Geophysics* (3rd Edition). London.
- Moench, A. (1984). Double-Porosity Models for a Fissured Groundwater Reservoir With Fracture Skin. *Water Resources Research*, 20(7), 831–846. <https://doi.org/10.1029/WR020i007p00831>
- Mohr, P. (1963). *Geological map of Horn of Africa*, scale 1:2,000,000. London, Philip, and Tacey.
- Mohr, P. (1983). Ethiopian flood basalt province. *Nature*, 303, 577–584. <https://doi.org/10.1038/303577a0>
- Muanenda, Y., Oton, C., Faralli, S., Nannipieri, T., Signorini, A., & Pasquale, F. (2016). Hybrid distributed acoustic and temperature sensor using a commercial off-the-shelf DFB laser and direct detection. *Optics Letters*, 41(3), 587–590. <https://doi.org/10.1364/OL.41.000587>

- Munn, J., Coleman, T., Parker, B., Mondanos, M., & Chalari, A. (2017). Novel cable coupling technique for improved shallow distributed acoustic sensor VSPs. *Journal of Applied Geophysics*, 138, 72–79. <https://doi.org/10.1016/j.jappgeo.2017.01.007>
- Navarre-sitchler, A., Brantley, S., & Rother, G. (2015). How Porosity Increases During Incipient Weathering of Crystalline Silicate Rocks. *Reviews in Mineralogy & Geochemistry*, 80(Tugrul 2004), 331–354. <https://doi.org/10.2138/rmg.2015.80.10>.
- Nile Basin, I. (2012). The Water Resources of the Nile Basin. In *The State of the River Nile Basin* (pp. 25–56).
- Ogilvy, A. (1970). Geophysical prospecting for groundwater in the Soviet Union.
- Orellana, E., & Mooney, H. (1966). Master table and curves for vertical electrical sounding data. *Geophysics Prospecting*, 8(3), 1966. Retrieved from <https://lib.ugent.be/catalog/rug01:001374284>.
- Oware, E. (2020). The use of hydrogeological process constraint for high-resolution proxy-modelling in hydrogeophysics. In *SEG international expositions and 90th Annual Meeting* (pp. 3582–3586). <https://doi.org/10.1190/segam2020-3428367.1>
- Papadopoulos, I., & Cooper, H. (1967). Drawdown in a well of large diameter. *Water Resour. Res.*, 3(1), 241–244.
- Paterson, N., & Reeves, C. (1985). Applications of gravity and magnetic surveys - The state of the art in 1985. *Geophysics*, 50, 2558–2594.
- PerkinElmer. (2018). *Atomic Spectroscopy: A Guide to Selecting the Appropriate Technique and System*. Waltham, USA.
- Perol, T., Gharbi, M., & Denolle, M. (2018). Convolutional neural network for earthquake detection and location. *Science Advances*, 4(2), 1–24. <https://doi.org/10.1126/sciadv.1700578>
- Pevzner, R., Urosevic, M., Popik, D., Shulakova, V., Glubokovskikh, S., Ziramov, S., ... Freifeld, B. (2017). 4D surface seismic tracks small supercritical CO₂ injection into the subsurface : CO₂CRC Otway Project. *International Journal of Greenhouse Gas Control*, 63(March), 150–157. <https://doi.org/10.1016/j.ijggc.2017.05.008>
- Pik, R., Marty, B., Carignan, J., & Lave, J. (2003). Stability of Upper Nile drainage network (Ethiopia) deduces from (U–Th)/He thermochronometry: implication of uplift and erosion of the Afar plume dome. *Earth Planet. Sci. Lett.*, 215, 73–88. [https://doi.org/10.1016/S0012-821X\(03\)00457-6](https://doi.org/10.1016/S0012-821X(03)00457-6)
- Piper, A. (1944). A graphic procedure in the chemical interpretation of water analysis. *American Geophysical Union Transactions*, 25, 914–928. <https://doi.org/10.1029/T R025i006p00914>

- Poeter, E., Fan, Y., Cherry, J., Wood, W., & Mackay, D. (2020). Groundwater in our water cycle – getting to know Earth’s most important freshwater source. The Groundwater Project, Guelph, Ontario, Canada.
- Prada, S., Silva, M., & Cruz, J. (2005). Groundwater behaviour in Madeira, volcanic island (Portugal). *Hydrogeology Journal*, 13(5), 800–812. <https://doi.org/10.1007/s10040-005-0448-3>
- Prave, A., Bates, C., Donaldson, C., Toland, H., Condon, D., Mark, D., & Raub, T. (2016). Geology and geochronology of the Tana Basin, Ethiopia : LIP volcanism, super-eruptions and Eocene -Oligocene environmental change. *Earth and Planetary Science Letters*, 443, 1–8. <https://doi.org/10.1016/j.epsl.2016.03.009>
- Pryet, A., D’Ozouville, N., Violette, S., Deffontaines, B., & Auken, E. (2012). Hydrogeological settings of a volcanic island (San Crist ´ Galapagos) from joint interpretation of airborne electromagnetics and geomorphological observations. *Hydrology and Earth System Sciences*, 16, 4571–4579. <https://doi.org/10.5194/hess-16-4571-2012>
- Rajpoot, S., Singh, P., Solanki, S. and, & Yasin, S. (2017). Future Trends in Fiber Optics Communication. *International Journal on Cybernetics & Informatics (IJCI)*, 6(1/2), 23–28. <https://doi.org/10.5121/ijci.2017.6203>
- Redwan, M., & Moneim, A. (2015). Factors controlling groundwater hydrogeochemistry in the area west of Tahta, Sohag, Upper Egypt. *Journal of African Earth Sciences*, 118, 328–338. <https://doi.org/10.1016/j.jafrearsci.2015.10.002>
- Rehman, S., & Mendez, A. (2012). Optical fibres present opportunities and challenges for geophysical applications. *Offshore Magazine*, 72(3), 1–5. <https://doi.org/10.1021/ja012023z>
- Reynolds, J. (1998). *An Introduction to Applied and Environmental Geophysics*.
- Robain, H., Braun, J., Albouy, Y., & Ndam, J. (1995). An electrical monitoring of an Elementary watershed in the rain forest of Cameroon. In *Proceedings of 1st Environmental and Engineering Geophysics Meeting* (pp. 411–414). Torino, Italy.
- Saleh, A., Al-Ruwaih, F., & Shehata, M. (1999). Hydrogeochemical processes operating within the main aquifers of Kuwait. *Journal of Arid Environments*, 42, 195–209. <https://doi.org/10.1006/jare.1999.0511>
- Saribudak, M., & Hawkins, A. (2019). Hydrogeophysical characterization of the baby Crossing fault, San Antonio, Texas, USA. *Journal of Applied Geophysics*, 162, 164–173. <https://doi.org/10.1016/j.jappgeo.2019.01.009>
- Schlumberger, C. (1912). *Premières expériences. Carte des courbes équipotentiellles, tracées au courant continu Val-Richer (Calvados). Calvados*.

- Shi, G. (2014). Kriging. In *Data Mining and Knowledge Discovery for Geoscientists* (pp. 238–274). Elsevier Inc. <https://doi.org/10.1016/B978-0-12-410437-2.00008-4>
- Shiloh, L., Eyal, A., & Giryas, R. (2018). *Deep Learning Approach for Processing Fiber Optic DAS Seismic Data*. OSA Publishing.
- Singh, A. (2002). Quality assessment of surface and sub-surface water of Damodar river basin, India. *Journal of Environmental Health*, 44, 41–49.
- Slater, L. (2007). Near Surface Electrical Characterization of Hydraulic Conductivity : From Petrophysical Properties to Aquifer Geometries — A Review. *Surveys in Geophys*, 169–197. <https://doi.org/10.1007/s10712-007-9022-y>
- SMEC. (2008). *Hydrological Study of The Tana-Beles Sub-Basins*.
- Sogreah, C., & Geomatrix. (2013). *Consulting Service for Detailed Groundwater Investigation & Monitoring in Tana and Beles Sub-Basins. (Vol. II)*.
- Srinivasamoorthy, K., Gopinath, M., Chidambaram, S., Vasanthavigar, M., & Sarma, V. . (2014). Hydrochemical characterization and quality appraisal of groundwater from Pungar subbasin, Tamilnadu, India. *Journal of King Saud University - Science*, 26(1), 37–52. <https://doi.org/10.1016/j.jksus.2013.08.001>
- Suarez, D., Wood, J., & Lesch, S.(2006). Effect of SAR on water infiltration under a sequential rain – irrigation management system. *Agricultural Water Management*, 86, 150–164. <https://doi.org/10.1016/j.agwat.2006.07.010>
- Suchet, A., Probst, J., & Ludwig, W. (2003). Worldwide distribution of continental rock lithology : Implications for the atmospheric /soil CO₂ uptake by continental weathering and alkalinity river transport to the oceans. *Global Biogeochemical Cycles*, 17(2), 1–14. <https://doi.org/10.1029/2002GB001891>
- Telford, W., Geldart, L., & Sheriff, R.(1990). *Applied Geophysics* (2nd edition). Cambridge University Press.
- Teresita, B., Carlos, A., & John, F. (2012). Conceptual Models in Hydrogeology, Methodology, and Results. In Gholam A. Kazemi (Ed.), *Hydrogeology - A Global Perspective* (pp. 203–222). IntechOpen.
- Theis, C. (1935). The relation between the lowering of the piezometric surface and the rate and duration of discharge of well-using groundwater storage. *Transaction American Geophysical Union*, 16, 519–524.
- Todd, D. (1980). *Groundwater hydrology*. (2nd edition). New York: Wiley.
- Todd, D. (1959). *Groundwater hydrology*. New York. John Wily & Sons, Inc., New.
- Toth, J. (1963). A Theoretical Analysis of Groundwater Flow in Small Drainage Basins. *Journal of Geophysical Research*, 68(16), 4795–4812.

- United States Salinity Laboratory Staff, U. (1954). *Diagnosis and Improvement of Saline and Alkali Soils (Agriculture)*. Washington D.C: United States Department of Agriculture.
- Vander, V. (2004). WinRESIST version 1.0. Electrical resistivity inversion program. ITC, Netherlands.
- Vernier, A. (1993). Aspects of Ethiopian Hydrogeology. From Geology and mineral resources of Somalia and surrounding regions, 1st Agron. Oltremare, Firenze, Relaze Monogr, 113, 687-698.
- Violette, S., Ozouville, N., Pryet, A., Deffontaines, B., Fortin, J., & Adelinet, M. (2014). Hydrogeology of the Galápagos Archipelago : An Integrated and Comparative Approach Between Islands. American Geophysical Union, 167–183.
- Vivona, R., Preziosi, E., Madé, B., & Giuliano, G. (2007). Occurrence of minor toxic elements in volcanic-sedimentary aquifers : a case study in central Italy. *Hydrogeology Journal*, 15, 1183–1196. <https://doi.org/10.1007/s10040-007-0169-x>
- Walker, D. (2016). Properties of shallow thin regolith aquifers in sub-Saharan Africa : a case study from northwest Ethiopia. In S. RWSN, St Gallen (Ed.), 7th RWSN Forum ““Water for Everyone.”” Retrieved from https://rwsnforum7.files.wordpress.com/2016/12/full_paper_0061_submitter_0166_walker_david-rev1.pdf. Cited on 14 March 2017.
- Walker, D., Forsythe, N., Parkin, G., & Gowing, J. (2016). Filling the observational void : Scientific value and quantitative validation of hydrometeorological data from a community-based monitoring programme. *Journal of Hydrology*, 538, 713–725. <https://doi.org/10.1016/j.jhydrol.2016.04.062>
- Walker, D., Parkin, G., Gowing, J., & Haile, A. (2019). Development of a Hydrogeological Conceptual Model for Shallow Aquifers in the Data Scarce Upper Blue Nile Basin. *Hydrology*, 6(43), 1–24. <https://doi.org/doi:10.3390/hydrology6020043>
- Walker, D., Parkin, G., Schmitter, P., Gowing, J., Tilahun, S., Haile, A., & Yimam, A. (2019). Insights From a Multi-Method Recharge Estimation Comparison Study. *Groundwater*, (57), 245–258. <https://doi.org/10.1111/gwat.12801>
- Walker, G. (1959). Geology of the reyoarforour area, Eastern Iceland. Geological Society of London. *Quarterly Journal*, 114, 367–393.
- Wang, P., Yu, J., Zhang, Y., & Liu, C. (2013). Groundwater recharge and hydrogeochemical evolution in the Ejina Basin, northwest China. *Journal of Hydrology*, 476, 72–86. <https://doi.org/10.1016/j.jhydrol.2012.10.049>
- White, A., & Blum, A. (1995). Effects of climate on chemical weathering in watersheds. *Geochimica et Cosmochimica Acta*, 59(9), 1729–1747. [https://doi.org/10.1016/0016-7037\(95\)00078-E](https://doi.org/10.1016/0016-7037(95)00078-E)

- WHO. (2011). Guidelines for Drinking-water Quality. Geneva, Switzerland.
- Wilcox, L. (1948). The Quality of Water for Irrigation Use. Washington D.C. US Department of Agriculture, Technical Bulletin No. 962.
- Wirmvem, M., Ohba, T., Kamtchueng, B., Taylor, E., Fantong, W., & Ako, A. (2017). Variation in stable isotope ratios of monthly rainfall in the Douala and Yaounde cities, Cameroon: local meteoric lines and relationship to regional precipitation cycle. *Applied Water Science*, 7(5), 2343–2356. <https://doi.org/10.1007/s13201-016-0413-4>
- Wolde, B. (1996). Spatial and temporal variations in the compositions of Upper Miocene to Recent basic lavas in the northern main Ethiopian rift : implications for the causes of Cenozoic magmatism in Ethiopia. *Geologische Rundschau*, 85(2), 380–389. <https://doi.org/10.1007/bf02422243>
- Woldemariyam, F., & Ayenew, T. (2016). Application of hydrochemical and isotopic techniques to understand groundwater recharge and flow systems in the Dawa River basin, southern Ethiopia. *Environmental Earth Sciences*, 75(1002), 1–17. <https://doi.org/10.1007/s12665-016-5777-0>
- Xinyan, L., Hao, W., Hui, Q., & Yanyan, G. (2018). Groundwater Chemistry Regulated by Hydrochemical Processes and Geological Structures. *Water*, 10(338), 1–16. <https://doi.org/10.3390/w10030338>
- Yenehun, A., Nigate, F., Belay, A., Desta, M., Camp, M., & Walraevens, K. (2020). Ground water recharge and water table response to changing conditions for aquifers at different physiography : The case of a semi-humid river catchment, northwestern highlands of Ethiopia. *The Science of the Total Environment*, 748, 142243. <https://doi.org/10.1016/j.scitotenv.2020.142243>
- Zhang, J., Zhu, T., Zhou, H., Huang, S., Liu, M., & Huang, W. (2016). High spatial resolution distributed fibre system for multi-parameter sensing based on modulated pulses. *Optics Express*, 24(24), 27482–27493. <https://doi.org/10.1364/OE.24.027481>
- Zhou, P., Li, M., & Lu, Y. (2017). Hydrochemistry and Isotope Hydrology for Groundwater Sustainability of the Coastal Multilayered Aquifer System (Zhanjiang, China). *Geofluids*. <https://doi.org/10.1155/2017/7080346>
- Zohdy, A., Eaton, G., & Mabey, D. (1974). Application of surface geophysics to groundwater investigation. (Book 2). USGS. Techniques of Water-Resource Investigation.

APPENDICES

Appendix 1: Hydrochemical and hydrophysical laboratory analysis data of volcanic aquifers.

Hydrochemical and physical data of volcanic aquifers sampled from boreholes. The values of TDS, cations, and anions are given in (mg/L), whereas the EC is ($\mu\text{S/cm}$).

Borehole ID	pH	EC	TDS	Ca²⁺	Mg²⁺	Na⁺	K⁺	Mn²⁺	Fe	Cl⁻	SO₄²⁺	HCO₃⁻	CO₃²⁻	NO₃⁻	F⁻	B
BH1	6.83	245	159.25	35.34	6.03	15.54	15.1	0.022	0.08	1.9	1	175	0	1	0.63	0.057
BH2	7.84	262	150	23.8	4.9	39	1.7	0.022	BDL *	1.08	8	139	0	0.13	0.25	0
BH3	8.67	290	188.5	27.94	6.921	13.6	10.32	0.005	BDL	0.6	1.8	145	15	1.5	0.34	0.06
BH4	8.4	295	204	36	5.35	25	0.9	BDL	BDL	0	1.6	170.6	14.4	4.8	0	0
BH5	8.51	204	124	8	1.95	30	2.6	BDL	BDL	2	1.3	90	0	0	1.1	0
BH6	7.44	313	203	8.4	2.8	25.4	7.63	BDL	BDL	2.2	0.8	93	0	1.23	0	0
BH7	8.81	335	214	0.97	4.51	34.5	1.86	BDL	0.01	2.5	0.5	97.6	0	1.44	0.64	0
Min	6.83	204	124	0.97	1.95	13.60	0.90	0	0	0	0.5	90	0	0.13	0	0
Max	8.81	335	214	36.00	6.92	39.00	15.10	0.02	0.08	2.5	8	175	15	4.8	1.1	0.06
Mean	8.07	277.71	177.54	20.06	4.64	26.15	5.73	0.01	0.013	1.47	2.14	130.03	4.2	1.44	0.42	0.02
SD	0.73	44.21	33.56	14.20	1.75	9.32	5.43	0.01	0.023	0.93	2.62	36.51	7.18	1.60	0.40	0.03

BDL* represents below detectable limit for manganese and iron using flame AAS instrument with 0.0015mg/L and 0.005mg/L values respectively. These low detection limits of flame AAS instrument values are based on PerkinElmer's work that determined elemental standards in dilute aqueous solution with a 98% confidence level(PerkinElmer, 2018).

Hydrochemical and physical data of volcanic aquifers sampled from shallow wells. The values of TDS, cations, and anions are given in (mg/L), whereas the EC is ($\mu\text{S}/\text{cm}$).

Shallow well ID	pH	EC	TDS	Ca ²⁺	Mg ²⁺	Na ⁺	K ⁺	Mn ²⁺	Fe	Cl ⁻	SO ₄ ²⁺	HCO ₃ ⁻	CO ₃ ²⁻	NO ₃ ⁻	F ⁻	B
SW1	6.12	260	169	24.62	2.116	2.78	2.94	0.016	0.01	4.2	0.8	85	0	3	0.66	0.06
SW2	6.07	480	312	25.1	2.14	3.56	3.12	0.006	BDL	0.8	0.5	75	0	11	0.35	0.06
SW3	5.62	70	45.5	6.09	1.98	1.69	1.39	0.029	BDL	6.7	0.8	15	0	1	0.34	0.05
SW4	5.37	90	58.5	23.41	1.89	7.45	3.92	0.029	BDL	2.1	0.8	95	0	3	0.48	0.04
SW5	6.14	160	104	19.81	2.288	3.14	6.52	0.02	BDL	12.5	0.7	60	0	3	0.4	0.05
SW6	6.4	140	91	25.55	2.23	2.45	1.9	0.005	BDL	1.6	1.5	75	0	15	0.44	0.06
SW7	5.53	171.9	87	12.5	2.28	0.08	0.15	BDL	0.01	2.7	1.5	48.8	0	4.85	0.21	0
SW8	6.31	264.4	135	18.07	2.94	2.54	2.29	BDL	1.65	0.7	1.6	97.3	0	1.22	0.56	0
SW9	6.17	174	88	17.4	2.81	4.6	1.54	BDL	BDL	1.3	6.2	60.2	0	1.48	0.4	0
SW10	5.83	130.7	66	14.6	2.37	1.73	0.42	BDL	0.2	0.5	1.1	52	0	4.37	0.22	0
SW11	6.88	334.9	172	19.4	3.4	0.08	1.74	BDL	0.01	3.7	1.1	85.2	0	2.9	0.31	0
SW12	5.76	200.4	102	18.4	3.44	0.08	2.13	BDL	0.01	1.3	0.84	90.4	0	3.2	0.32	0
SW13	5.69	196.8	100	18.7	3.12	0.1	1.14	BDL	4.3	1.7	1.4	86.1	0	2.37	0.28	0

SW14	5.99	309.4	159	27.1	3.18	0.19	9.06	BDL	0.7	2.7	1.2	125.4	0	4.12	0.25	0
Min	5.37	70	45.50	6.09	1.89	0.08	0.15	0.00	0	0.5	0.5	15	0	1	0.21	0
Max	6.88	480	312.00	27.10	3.44	7.45	9.06	0.03	4.3	12.5	6.2	125.4	0	15	0.66	0.06
Mean	5.99	213.04	120.64	19.34	2.58	2.18	2.73	0.01	0.49	3.04	1.43	75.03	0	4.32	0.37	0.02
SD	0.40	108.99	67.88	5.74	0.54	2.13	2.42	0.01	1.19	3.19	1.41	26.69	0	3.92	0.13	0.03

BDL* represents below detectable limit for manganese and iron using flame AAS instrument with 0.0015mg/L and 0.005mg/L values respectively(PerkinElmer, 2018).

Hydrochemical and physical data of volcanic aquifers sampled from Springs. The values of TDS, cations, and anions are given in (mg/L), whereas the EC is (μ S/cm).

Springs ID	pH	EC	TDS	Ca²⁺	Mg²⁺	Na⁺	K⁺	Mn²⁺	Fe	Cl⁻	SO₄²⁺	HCO₃⁻	CO₃²⁻	NO₃⁻	F⁻	B
SP1	5.64	75	48.75	18.55	1.99	2.09	2.35	0.002	BDL	0.8	5	50	0	6.82	0.65	0.06
SP2	5.53	40	26	3.58	1.8	1.67	1.45	0.012	BDL	1.7	0.8	15.5	0	0.8	0.82	0.3
SP3	6	189.6	97	23.3	3.87	0.8	1.24	BDL	0.01	1.2	1.1	91.2	0	2.5	0.37	0
SP4	5.31	48.67	24	14.1	2.42	0.08	5.13	BDL	0.01	0.8	2.4	50.2	0	2.34	0.8	0
Min	5.31	40	24	3.58	1.80	0.08	1.24	0.00	0.00	0.80	0.80	15.50	0	0.80	0.37	0.00
Max	6.00	189.60	97	23.30	3.87	2.09	5.13	0.01	0.01	1.70	5.00	91.20	0	6.82	0.82	0.30
Mean	5.62	88.32	48.94	14.88	2.52	1.16	2.54	0.00	0.01	1.13	2.33	51.73	0	3.12	0.66	0.09
SD	0.29	69.14	33.95	8.42	0.94	0.90	1.79	0.01	0.00	0.43	1.91	30.96	0	2.59	0.21	0.14

BDL* represents below detectable limit for manganese and iron using flame AAS instrument with 0.0015mg/L and 0.005mg/L values respectively(PerkinElmer, 2018).

Appendix 2: The calculated values of SAR, Na%, and RSC of groundwater samples

The calculated values of SAR, Na%, and RSC of groundwater samples from boreholes, shallow hand-dug wells, and springs.

Water scheme and Sample ID		Water quality indicator calculated values			Water scheme and Sample ID		Water quality indicator calculated values		
Water scheme	Sample ID	SAR	Na%	RSC	Water scheme	Sample ID	SAR	Na%	RSC
Boreholes	BH1	0.636	20.35	0.608	Shallow wells	SW1	0.144	7.563	-0.010
	BH2	1.902	50.93	0.687		SW2	0.183	9.310	-0.199
	BH3	0.597	20.98	0.913		SW3	0.152	12.764	-0.221
	BH4	1.028	32.49	1.039		SW4	0.398	18.538	0.233
	BH5	2.467	67.57	0.915		SW5	0.178	9.227	-0.193
	BH6	1.939	56.67	0.875		SW6	0.125	6.604	-0.229
	BH7	3.277	76.26	1.180		SW7	0.005	0.425	-0.012
	Min	0.60	20.35	0.61		SW8	0.146	8.416	0.451
	Max	3.28	76.26	1.18		SW9	0.270	14.943	-0.113
	Mean	1.69	46.47	0.89		SW10	0.111	7.454	-0.071

Springs	<i>SD</i>	1.00	22.30	0.20	SW11	0.004	0.269	0.148
	SP1	0.123	7.329	-0.270	SW12	0.004	0.276	0.280
	SP2	0.180	16.642	-0.073	SW13	0.006	0.356	0.221
	SP3	0.040	2.248	0.014	SW14	0.009	0.446	0.441
	SP4	0.005	0.335	-0.080	<i>Min</i>	0.004	0.27	-0.229
	<i>Min</i>	0.005	0.335	-0.27	<i>Max</i>	0.398	18.54	0.451
	<i>Max</i>	0.180	16.642	0.014	<i>Mean</i>	0.124	6.90	0.052
	<i>Mean</i>	0.087	6.639	-0.102	<i>SD</i>	0.116	5.97	0.242
	<i>SD</i>	0.079	7.29	0.120				

Appendix 3: The 32 VES Data point information.

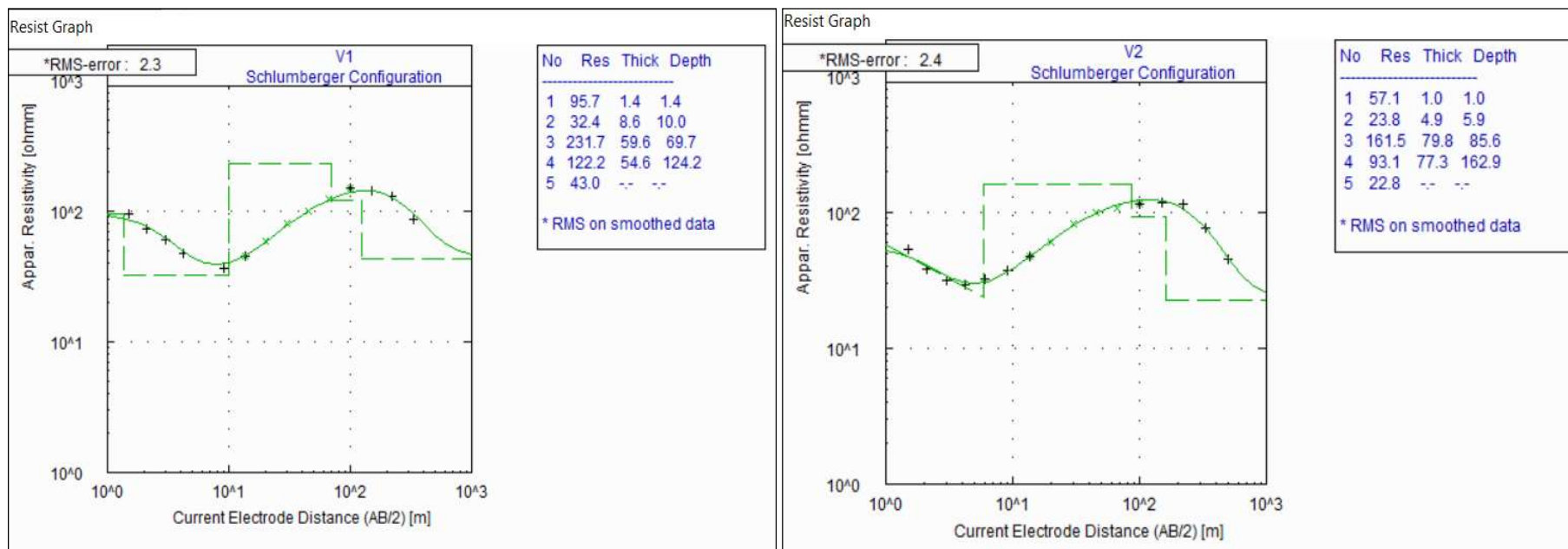
The VES point coordinates, the minimum, and maximum half current and potential electrode spread (AB/2(m), and (MN/2(m)), and the number of readings taken at each VES point.

VES No.	Easting(m)	Northing(m)	Elevation(m)	AB/2 Min (m)	AB/2 max(m)	MN/2 Min(m)	MN/2 max (m)	No. of readings
V1	263364	1245725	2100	1.5	330	0.5	45	19
V2	263230	1245605	2106	1.5	500	0.5	45	20
V3	263295	1245790	2112	1.5	330	0.5	45	19
V4	265783	1246894	2106	1.5	500	0.5	45	20
V5	265543	1247105	2108	1.5	750	0.5	45	21

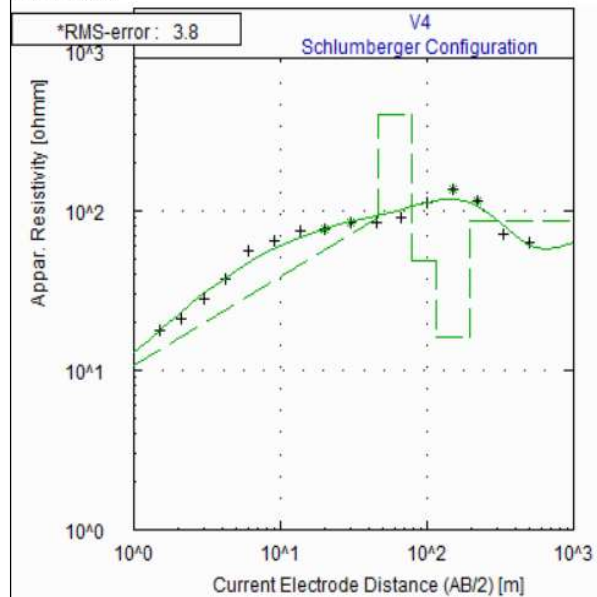
V6	265149	1247265	2103	1.5	500	0.5	45	20
V7	265926	1247482	2100	1.5	500	0.5	45	20
V8	260142	1246824	2096	3	400	1	50	23
V9	260090	1247175	2096	3	400	1	50	23
V10	260136	1247543	2095	3	400	1	50	23
V11	260450	1248446	2091	3	300	1	50	22
V12	260761	1248586	2091	3	400	1	50	23
V13	261044	1248615	2089	3	300	1	50	22
V14	261770	1248500	2085	3	400	1	50	23
V15	261820	1248800	2085	3	400	1	50	23
V16	261807	1249100	2090	3	300	1	50	22
V17	261973	1249410	2080	3	300	1	50	22
V18	262026	1249910	2077	3	400	1	50	23
V19	261575	1250134	2085	3	400	1	50	23
V20	261279	1250100	2084	3	400	1	50	23
V21	260840	1250190	2082	3	400	1	50	23
V22	260828	1250742	2075	3	400	1	50	23
V23	260917	1251093	2073	3	500	1	50	24
V24	265766	1252977.6	2055	1.5	500	0.5	45	20
V25	266190	1252537.6	2042	1.5	750	0.5	45	21
V26	266586	1253581.6	2034	1.5	500	0.5	45	20

V27	267019	1253557.6	2037	1.5	500	0.5	45	20
V28	267331	1253618.6	2039	1.5	750	0.5	45	21
V29	266932	1252943.6	2044	1.5	500	0.5	45	20
V30	267743	1252789.6	2035	1.5	750	0.5	45	21
V31	267176	1253616	1986	1.5	500	0.5	45	20
V32	266854	1252544		1.5	500	0.5	45	20

Appendix 4: 1D-model VES Curves (*next 12 Figures*)



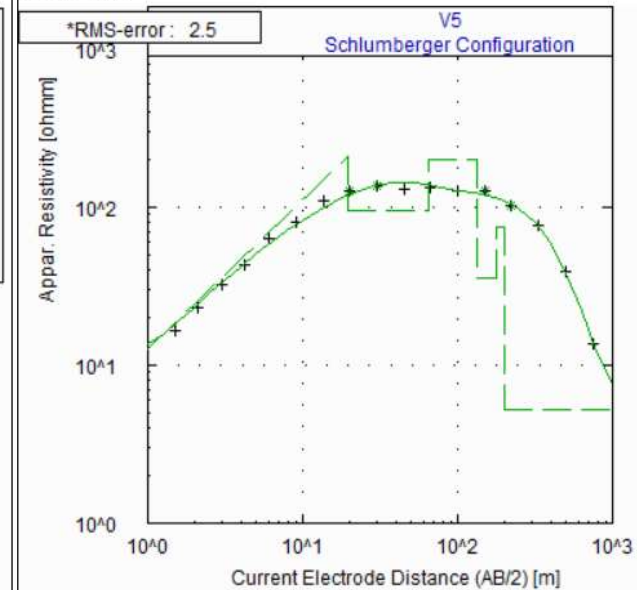
Resist Graph



No	Res	Thick	Depth
1	7.9	0.6	0.6
2	91.3	45.3	45.9
3	399.3	32.6	78.5
4	48.7	35.8	114.3
5	16.0	82.4	196.7
6	86.4	--	--

* RMS on smoothed data

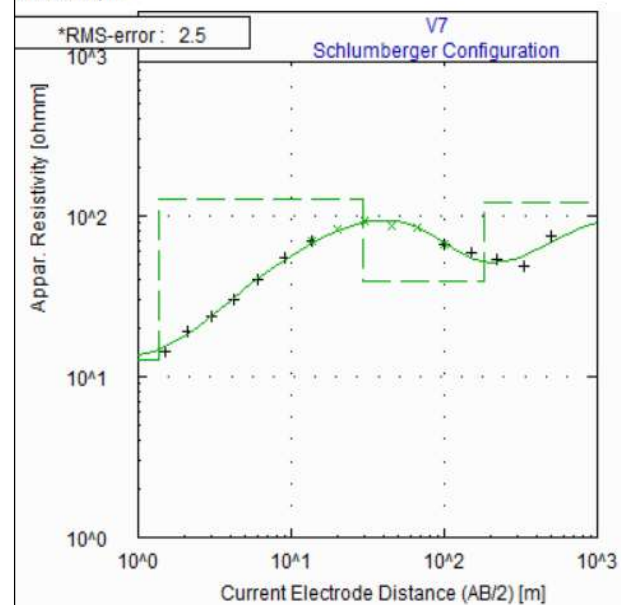
Resist Graph



No	Res	Thick	Depth
1	10.2	0.8	0.8
2	209.5	19.0	19.8
3	95.3	45.9	65.6
4	199.6	69.2	134.8
5	35.8	45.0	179.8
6	75.2	18.7	198.5
7	5.3	--	--

* RMS on smoothed data

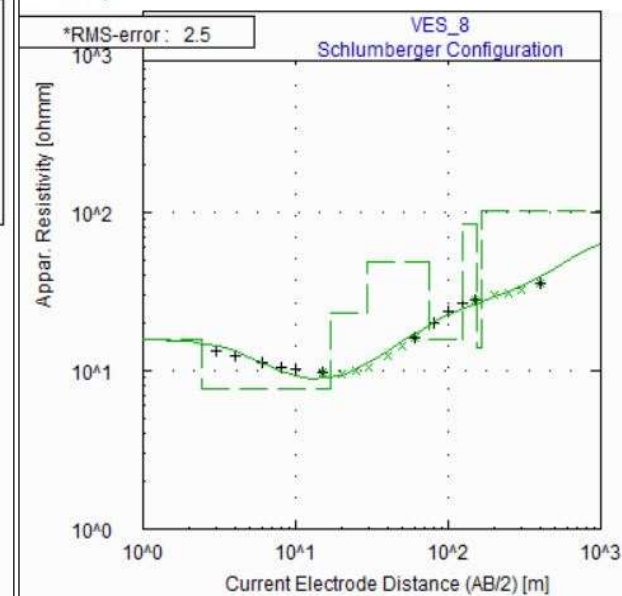
Resist Graph



No	Res	Thick	Depth
1	12.6	1.4	1.4
2	128.1	28.3	29.7
3	39.0	154.2	183.9
4	121.8	--	--

*RMS on smoothed data

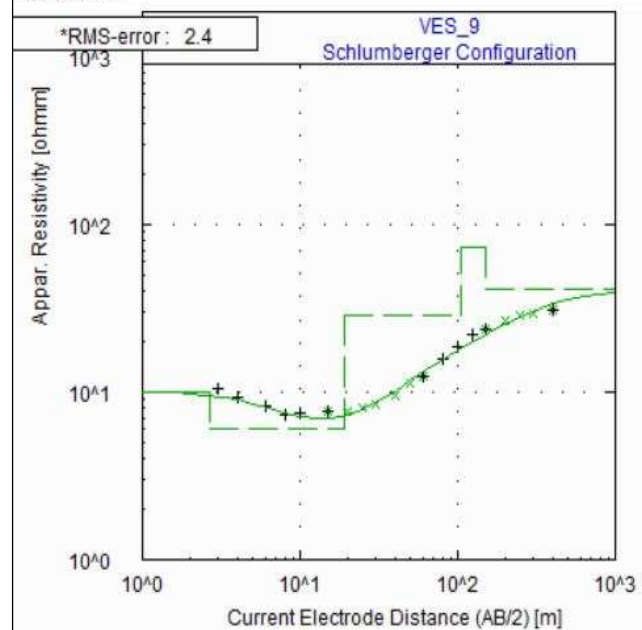
Resist Graph



No	Res	Thick	Depth
1	15.9	2.4	2.4
2	7.6	14.5	16.9
3	23.0	12.6	29.6
4	48.6	44.8	74.3
5	15.7	48.9	123.2
6	84.7	29.9	153.0
7	14.2	12.7	165.7
8	103.4	--	--

*RMS on smoothed data

Resist Graph

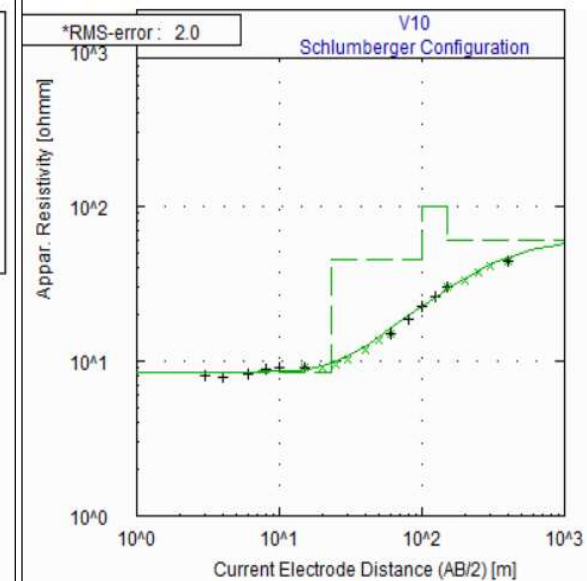


No	Res	Thick	Depth
1	10.0	2.7	2.7
2	6.0	16.3	19.0
3	29.0	86.0	105.0
4	73.0	45.0	150.0
5	41.0	-	-

1	10.0	2.7	2.7
2	6.0	16.3	19.0
3	29.0	86.0	105.0
4	73.0	45.0	150.0
5	41.0	-	-

* RMS on smoothed data

Resist Graph

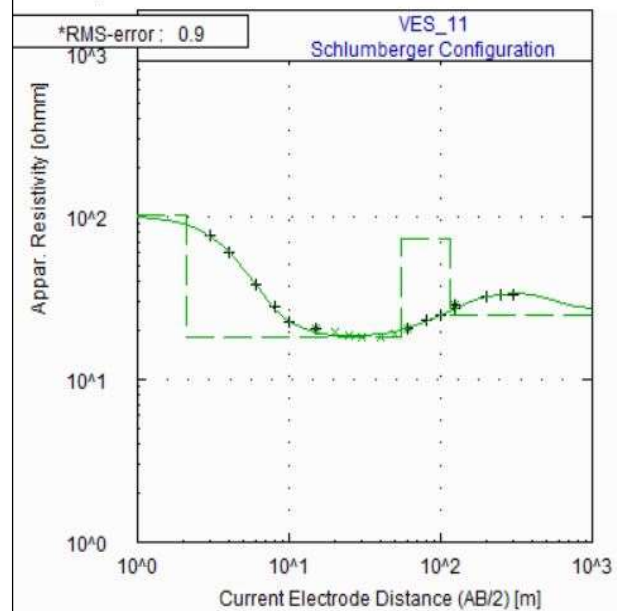


No	Res	Thick	Depth
1	8.5	23.0	23.0
2	45.0	77.0	100.0
3	100.0	50.0	150.0
4	60.0	-	-

1	8.5	23.0	23.0
2	45.0	77.0	100.0
3	100.0	50.0	150.0
4	60.0	-	-

* RMS on smoothed data

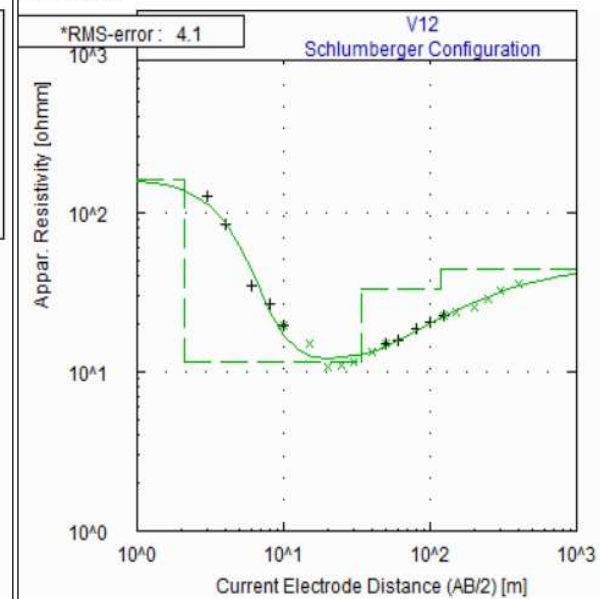
Resist Graph



No	Res	Thick	Depth
1	101.8	2.1	2.1
2	18.1	53.3	55.4
3	73.4	61.0	116.4
4	25.0	--	--

*RMS on smoothed data

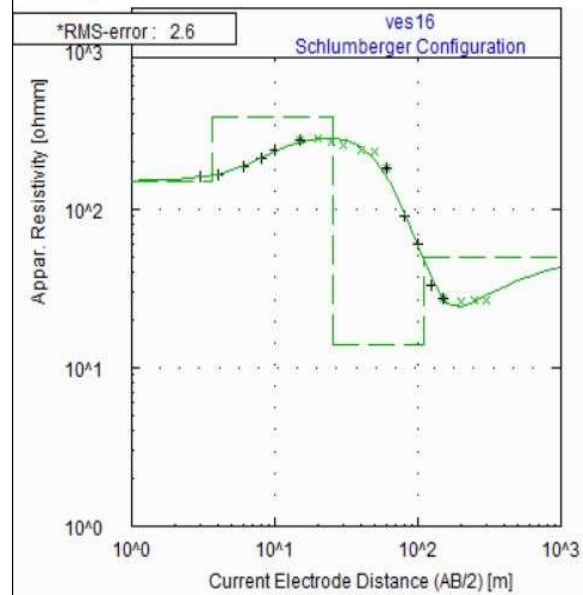
Resist Graph



No	Res	Thick	Depth
1	160.4	2.1	2.1
2	11.4	31.6	33.8
3	33.0	85.0	118.7
4	44.4	--	--

*RMS on smoothed data

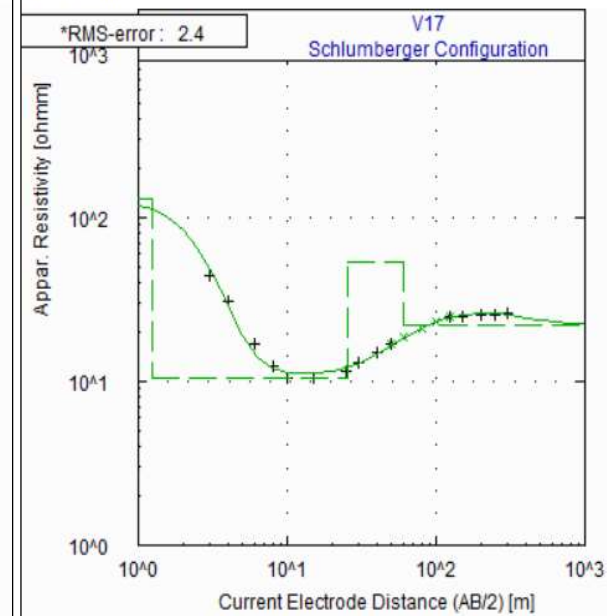
Resist Graph



No	Res	Thick	Depth
1	151.7	3.6	3.6
2	385.4	22.1	25.7
3	14.1	83.1	108.8
4	50.1	--	--

* RMS on smoothed data

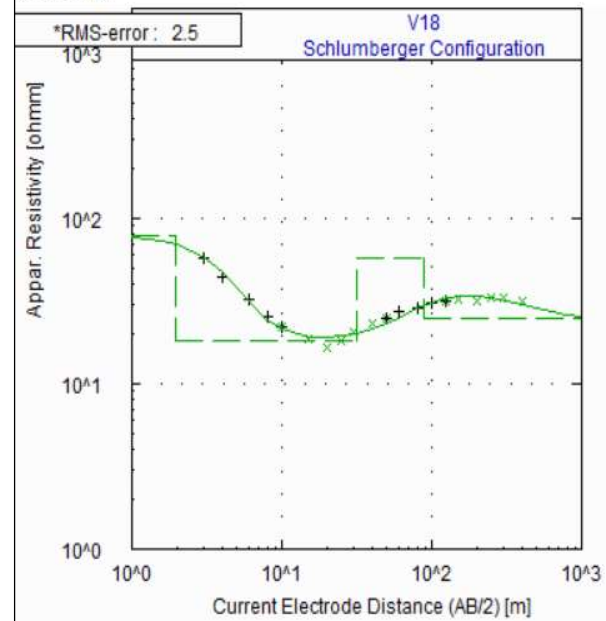
Resist Graph



No	Res	Thick	Depth
1	129.4	1.3	1.3
2	10.6	24.0	25.2
3	53.5	35.1	60.3
4	22.2	--	--

* RMS on smoothed data

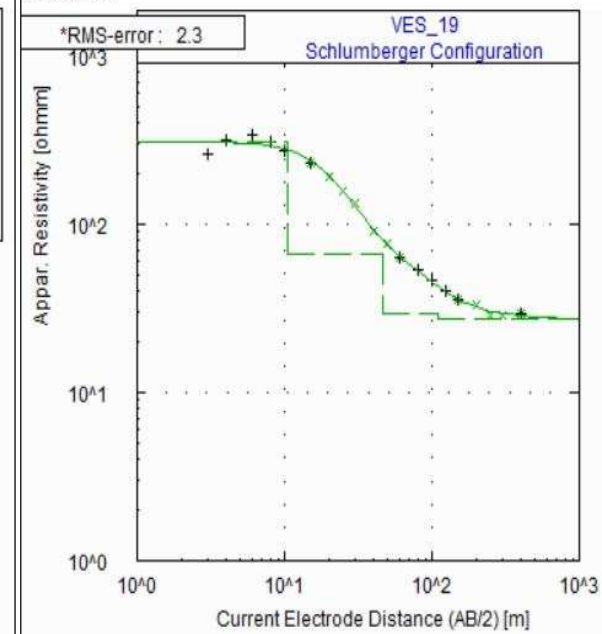
Resist Graph



No	Res	Thick	Depth
1	78.3	1.9	1.9
2	18.1	29.7	31.6
3	58.2	56.3	87.9
4	24.9	-	-

* RMS on smoothed data

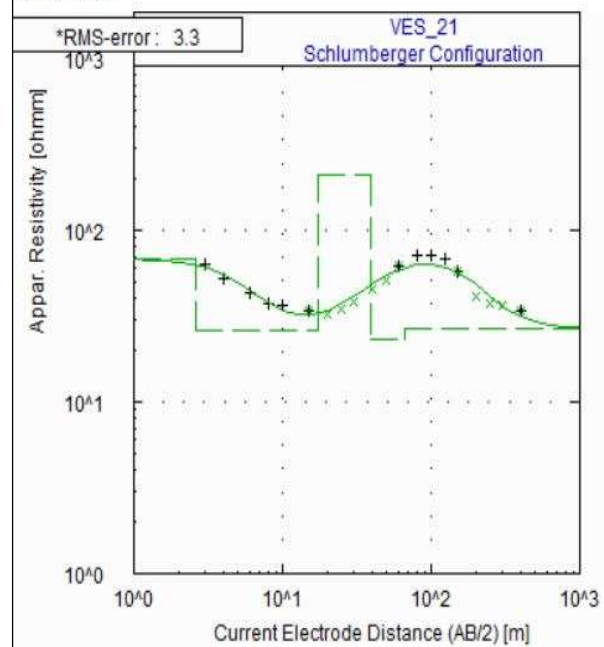
Resist Graph



No	Res	Thick	Depth
1	307.9	10.6	10.6
2	66.2	35.5	46.1
3	29.3	65.0	111.1
4	27.3	-	-

* RMS on smoothed data

Resist Graph

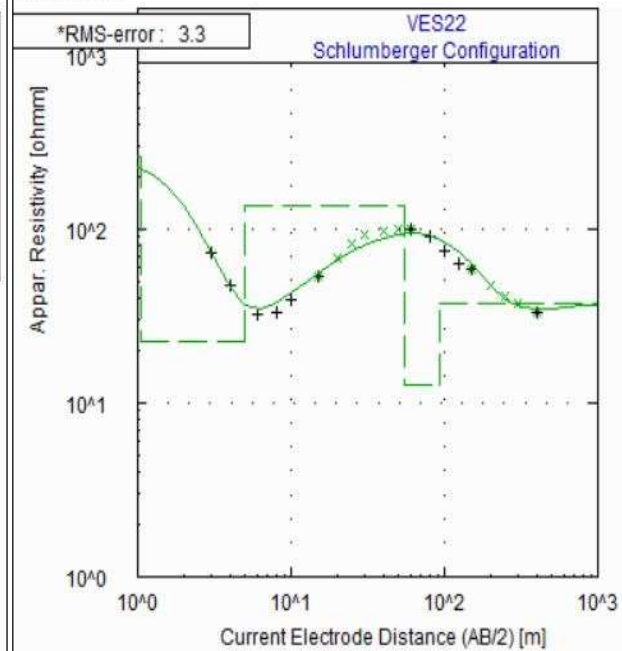


No	Res	Thick	Depth
1	67.7	2.6	2.6
2	26.1	14.9	17.5
3	211.5	22.1	39.5
4	23.3	27.4	66.9
5	26.6	--	--

1	67.7	2.6	2.6
2	26.1	14.9	17.5
3	211.5	22.1	39.5
4	23.3	27.4	66.9
5	26.6	--	--

* RMS on smoothed data

Resist Graph

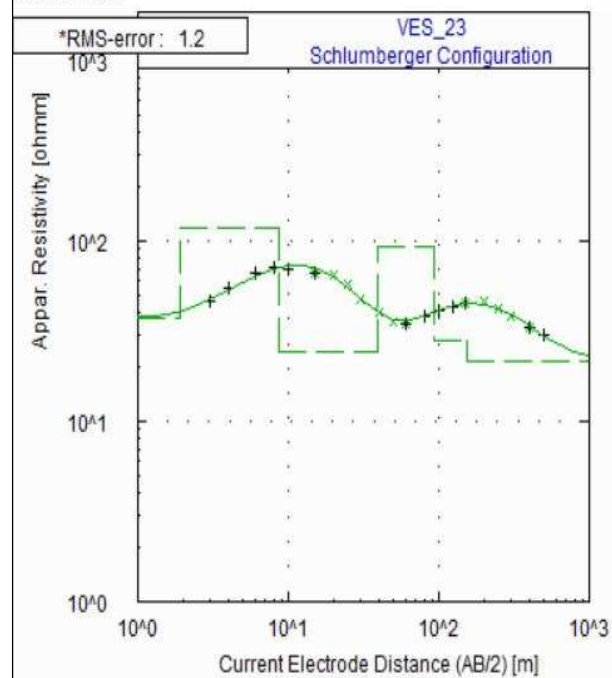


No	Res	Thick	Depth
1	259.1	1.0	1.0
2	22.8	4.0	5.0
3	135.1	50.0	55.0
4	12.7	38.7	93.7
5	37.8	--	--

1	259.1	1.0	1.0
2	22.8	4.0	5.0
3	135.1	50.0	55.0
4	12.7	38.7	93.7
5	37.8	--	--

* RMS on smoothed data

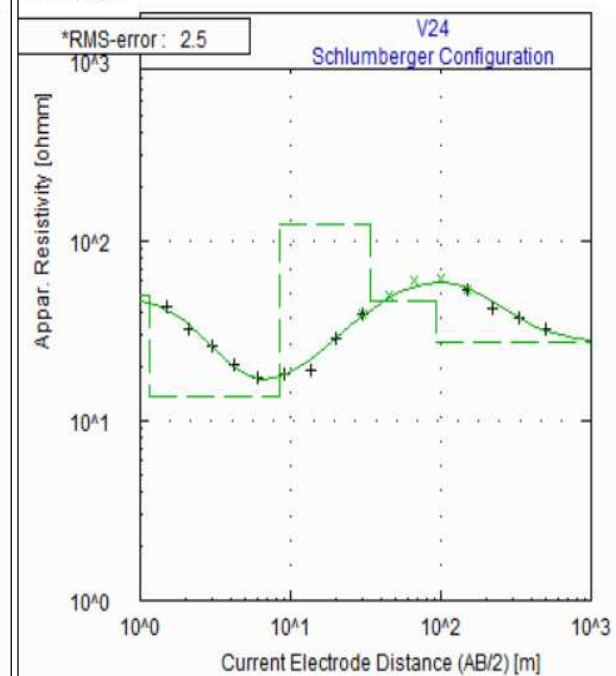
Resist Graph



No	Res	Thick	Depth
1	37.4	1.9	1.9
2	117.5	6.6	8.6
3	24.1	31.0	39.6
4	92.4	53.1	92.7
5	28.2	60.4	153.1
6	21.5	-	-

* RMS on smoothed data

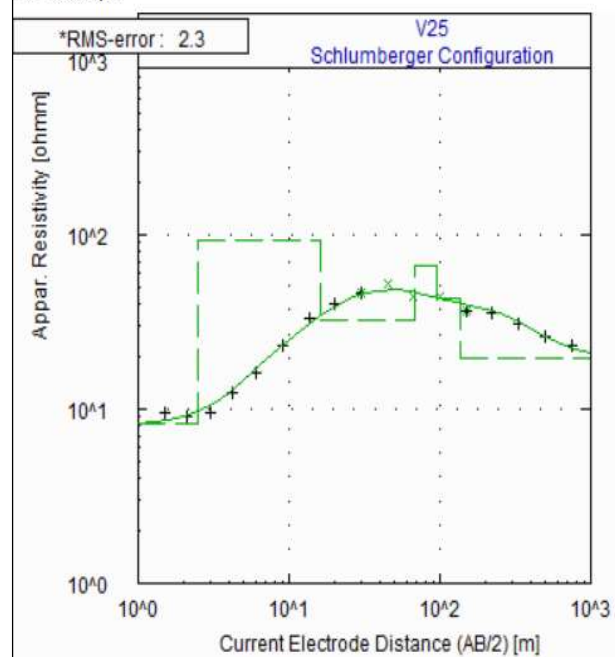
Resist Graph



No	Res	Thick	Depth
1	49.4	1.2	1.2
2	13.8	7.3	8.5
3	124.1	25.7	34.1
4	46.2	59.8	93.9
5	27.6	-	-

* RMS on smoothed data

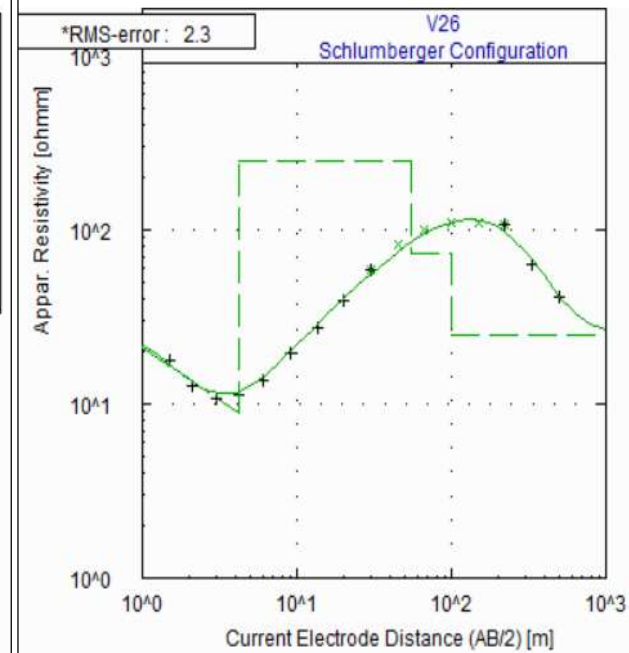
Resist Graph



No	Res	Thick	Depth
1	8.2	2.5	2.5
2	93.8	13.6	16.1
3	32.4	52.6	68.8
4	66.0	25.5	94.2
5	43.1	42.1	136.3
6	19.7	-	-

* RMS on smoothed data

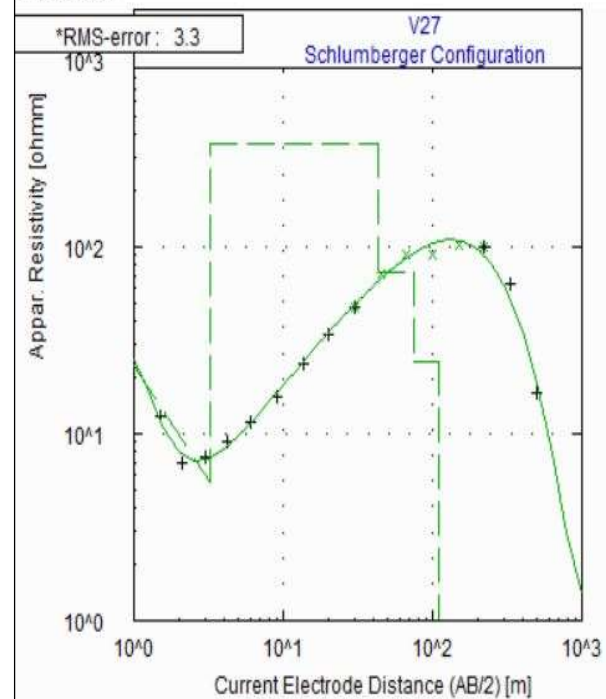
Resist Graph



No	Res	Thick	Depth
1	27.3	0.6	0.6
2	8.8	3.5	4.2
3	250.9	50.2	54.3
4	73.8	46.8	101.1
5	24.9	-	-

* RMS on smoothed data

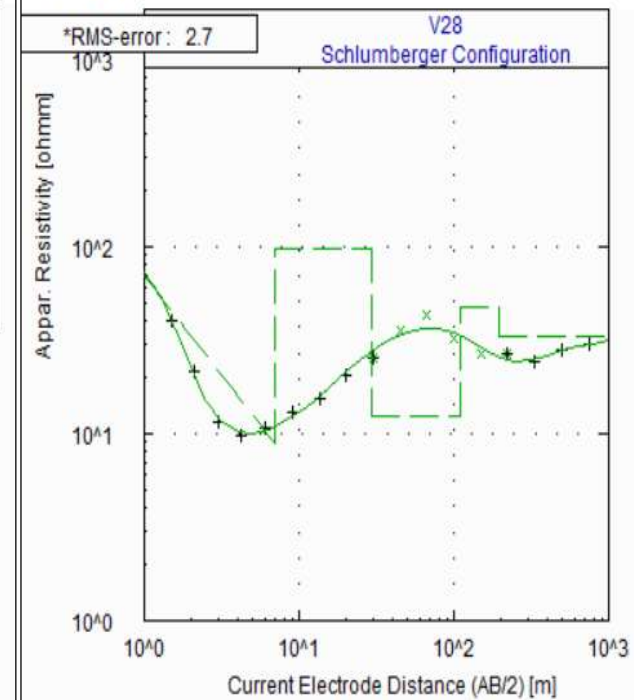
Resist Graph



No	Res	Thick	Depth
1	67.6	0.4	0.4
2	5.5	2.8	3.3
3	355.7	39.6	42.9
4	73.8	32.7	75.5
5	24.1	34.3	109.8
6	1.0	-	-

*RMS on smoothed data

Resist Graph



No	Res	Thick	Depth
1	120.7	0.6	0.6
2	8.8	6.5	7.1
3	96.7	22.3	29.4
4	12.4	81.6	111.0
5	47.1	83.5	194.5
6	32.9	-	-

*RMS on smoothed data

